Volume 4 • Number 3 • 2017 ISSN 2312-4334

East European Journal of Physics

V.N. Karazin Kharkiv National University Publishing

ISSN 2312-4334

MINISTRY OF EDUCATION AND SCIENCE OF UKRAINE

East European Journal of Physics

Volume 4 · Number 3

2017

East European Journal of Physics

EEJP is an international peer-reviewed journal devoted to experimental and theoretical research on the nuclear physics, cosmic rays and particles, high-energy physics, solid state physics, plasma physics, physics of charged particle beams, plasma electronics, radiation materials science, physics of thin films, condensed matter physics, functional materials and coatings, medical physics and physical technologies in an interdisciplinary context.
Published quarterly in hard copy and online by V.N. Karazin Kharkiv National University Publishing.
ISSN 2312-4334 (Print), ISSN 2312-4539 (Online)

The editorial policy is to maintain the quality of published papers at the highest level by strict peer review.
Approved for publication by the Academic Council of the Karazin Kharkiv National University (September 25, 2017, Protocol No. 13).
EEJP registered by the order of Ministry of Education of Ukraine № 747 of 07.13.2015, and is included in the list of scientific specialized editions of Ukraine, which can be published results of dissertations for the degree of doctor and candidate of physical and mathematical sciences.

Editorial office
Department of Physics and Technologies, V.N. Karazin Kharkiv National University
Kurchatov av., 31, office 402, Kharkiv, 61108, Ukraine
Tel: +38-057-335-18-33,
E-mail: eejp@karazin.ua,
Web-pages: http://periodicals.karazin.ua/eejp (Open Journal System), http://eejp.univer.kharkov.ua
Certificate of State registration No.20644-10464P, 21.02.2014

East European Journal of Physics

Volume 4 Number 3 2017

ORIGINAL PAPERS

EAST EUROPEAN JOURNAL OF PHYSICS
East Eur. J. Phys. Vol.4 No.3 (2017) 4-17 DOI:10.26565/2312-4334-2017-3-01

PACS: 64.10.+h, 64.60.an, 67.10.Db, 67.30.ej, 73.21.-b

THERMODYNAMICS OF THE FERMI GAS IN A NANOTUBE

Yu.M. Poluektov[1,2], A.A. Soroka[1]
[1]National Science Center "Kharkov Institute of Physics and Technology"
1, Akademicheskaya Str.,61108 Kharkov, Ukraine
[2]Kharkov V.N. Karazin National University
Sq. Svobody 4, Kharkov, 61022, Ukraine
E-mail: yuripoluektov@kipt.kharkov.ua
Received June 8, 2017

For the ideal Fermi gas that fills the space inside a cylindrical tube, there are calculated the thermodynamic characteristics in general form for arbitrary temperatures, namely: the thermodynamic potential, energy, entropy, equations of state, heat capacities and compressibilities. All these quantities are expressed through the introduced standard functions and their derivatives. The radius of the tube is considered as an additional thermodynamic variable. It is shown that at low temperatures in the quasi-one-dimensional case the temperature dependencies of the entropy and heat capacities remain linear. The dependencies of the entropy and heat capacities on the chemical potential have sharp maximums at the points where the filling of a new discrete level begins. The character of dependencies of thermodynamic quantities on the tube radius proves to be qualitatively different in the cases of fixed linear and fixed total density. At the fixed linear density these dependencies are monotonous and at the fixed total density they have an oscillating character.
KEY WORDS: Fermi particle, nanotube, thermodynamic functions, low-dimensional systems, equation of state, heat capacity, compressibility

ТЕРМОДИНАМІКА ФЕРМІ-ГАЗУ У НАНОТРУБЦІ

Ю.М. Полуектов[1,2], О.О. Сорока[1]
[1]Національний науковий центр "Харківський фізико-технічний інститут"
61108, вул. Академічна, 1, Харків, Україна
[2]Харківський національний університет ім. В.Н. Каразіна
пл. Свободи, 4, м. Харків, 61022, Україна

Для ідеального фермі-газу, який заповнює простір усередині нанотрубки, у загальному вигляді для довільних температур обчислені термодинамічні характеристики, а саме: термодинамічний потенціал, енергія, ентропія, рівняння стану, теплоємності та стисливості. Всі ці величини виражені через введені стандартні функції та їх похідні. Радіус трубки розглядається як додаткова термодинамічна змінна. Показано, що при низьких температурах в квазіодновимірному випадку температурні залежності ентропії та теплоємності залишаються лінійними. В залежностях ентропії та теплоємності від хімічного потенціалу існують різкі максимуми у точках, де починається заповнення чергового дискретного рівня. Характер залежностей термодинамічних величин виявляється якісно відмінним при фіксованій лінійній або повній густині. При фіксації лінійної густини ці залежності монотонні, а при фіксації повної густині мають осциляційний характер.
КЛЮЧОВІ СЛОВА: фермі-частинка, нанотрубка, термодинамічні функції, низькорозмірні системи, рівняння стану, теплоємність, стисливість

ТЕРМОДИНАМИКА ФЕРМИ-ГАЗА В НАНОТРУБКЕ

Ю.М. Полуэктов[1,2], А.А. Сорока[1]
[1]Национальный научный центр "Харьковский физико-технический институт"
61108, Академическая,1, Харьков, Украина
[2]Харьковский национальный университет им. В.Н. Каразина
пл. Свободы, 4, г. Харьков, 61022, Украина

Для идеального ферми-газа, заполняющего пространство внутри цилиндрической трубки, в общем виде для произвольных температур вычислены термодинамические характеристики, а именно: термодинамический потенциал, энергия, энтропия, уравнения состояния, теплоемкости и сжимаемости. Все эти величины выражены через введенные стандартные функции и их производные. Радиус трубки рассматривается как дополнительная термодинамическая переменная. Показано, что при низких температурах в квазиодномерном случае температурные зависимости энтропии и теплоемкости остаются линейными. В зависимостях энтропии и теплоемкости от химического потенциала имеются резкие максимумы в точках, где начинается заполнение очередного дискретного уровня. Характер зависимостей термодинамических величин оказывается качественно различным при фиксированной линейной или полной плотности. При фиксации линейной плотности эти зависимости монотонны, а при фиксации полной плотности имеют осцилляционный характер.
КЛЮЧЕВЫЕ СЛОВА: ферми-частица, нанотрубка, термодинамические функции, низкоразмерные системы, уравнение состояния, теплоемкость, сжимаемость

The model of the ideal Fermi gas is the basis for understanding the properties of electron and other many-fermion systems. In many cases it is also possible to describe with reasonable accuracy the behavior of systems of interacting Fermi particles within the approximation of an ideal gas of quasiparticles whose dispersion law differs from the dispersion law of free particles. It is essential that thermodynamic characteristics of the ideal Fermi gas at arbitrary temperatures in the volume case can be expressed through the special Fermi functions, and thus it is possible to obtain and verify all relations of the phenomenological thermodynamics on the basis of the quantum microscopic model.

In recent time, much attention has been paid to investigation of low-dimensional systems, in particular of properties of the Fermi gas in nanotubes and quantum wells, because apart from purely scientific interest the study of such objects is rather promising for the solid-state electronics [1-6]. Thermodynamics relations for the Fermi gas in the confined geometry have been studied much less than in the volume case [7] and require further investigation. Thermodynamic properties of the Fermi gas at arbitrary temperatures in a quasi-two-dimensional quantum well have been studied in detail by the authors in work [8]. A detailed understanding of the properties of such systems must serve as a basis for the study of low-dimensional systems of interacting particles [9-11].

It is considered that strongly correlated Fermi systems, to which also low-dimensional systems of Fermi particles are attributed, in many respects essentially differ from the usual Fermi liquid systems [12, 13]. At that the properties of quasi-one-dimensional or quasi-two-dimensional systems are often compared with the theory of bulk Fermi liquid [12, 13]. However, as seen even on the examples of the quasi-two-dimensional system of noninteracting particles which was considered by the authors in work [8] and the quasi-one-dimensional system considered in the present work, the properties of low-dimensional systems can substantially differ, especially at low temperatures, from the properties of the bulk system owing to the quantum size effect. For this reason, the theory of Fermi liquid itself in conditions of the confined geometry must, generally speaking, be formulated differently than in the volume case.

The consideration of low-dimensional models of interacting Fermi particles leads to a conclusion about unique properties of such systems [9-11]. It should be kept in mind, however, that real systems are always three-dimensional and their low dimensionality manifests itself only in the boundedness of motion of particles in one, two or three coordinates.

In considering statistical properties of the three-dimensional many-particle systems one usually passes in results to the thermodynamic limit, setting in final formulas the volume and number of particles to infinity at the fixed density. It is of general theoretical interest to study the statistical properties of many-particle systems in which one or two dimensions remain fixed, and the thermodynamic limiting transition is carried out only over remaining coordinates. In this case the coordinates, over which the thermodynamic limiting transition is not performed, should be considered as additional thermodynamic variables. The model of the ideal Fermi gas allows to build the thermodynamics of low-dimensional systems based on the statistical treatment.

The aim of the present work is to develop, within a microscopic approach, the thermodynamics of the ideal Fermi gas that fills the space inside a cylindrical tube. There are calculated its thermodynamic characteristics in general form for arbitrary temperatures, namely: the thermodynamic potential, energy, entropy, equations of state, heat capacities and compressibilities. All these quantities are expressed through the standard functions introduced in the work and their derivatives. It is suggested the representation of thermodynamic quantities in the dimensionless “reduced” form, which is convenient owing to the fact that it does not contain geometric dimensions of the system. The case of low temperatures and tubes of small radius is studied more in detail. It is shown that at low temperatures in the quasi-one-dimensional case under consideration the temperature dependencies of the entropy and heat capacities remain linear, the same as in the quasi-two-dimensional [8] and the volume cases [12,13], except the specific points where the filling of a new discrete level begins. Moreover, the dependencies of the entropy and heat capacities on the chemical potential have sharp maximums at these points. The behavior of thermodynamic quantities with the tube radius proves to be qualitatively different, depending on whether the linear or the total density is fixed. At the fixed linear density these dependencies prove to be monotonous and at the fixed total density they have an oscillating character.

THERMODYNAMICS OF THE FERMI GAS IN A CYLINDRICAL TUBE

The model of the ideal Fermi gas is the basis for studying the bulk properties of Fermi systems of particles of different nature. In the two-dimensional case an analogous role is played by the ideal Fermi gas contained between two parallel planes, whose thermodynamics was considered in detail in [8]. In this work the thermodynamics properties of the ideal Fermi gas enclosed in a cylindrical tube of radius R and length L are studied. The length of the tube is assumed to be macroscopic, and no restrictions are imposed on the radius of the tube. The main attention is paid to studying the properties of tubes of small radius, which corresponds to transition to the quasi-one-dimensional case, at low temperatures. It is everywhere assumed that the spin of the Fermi particle is equal to 1/2. It is also assumed that the potential barrier on the surface of the tube is infinite, so that the wave function of a particle turns into zero at the boundary. The solutions of the Schrödinger equation in this case have the form

$$\varphi_{k,n,\nu}\left(r,\alpha,z\right)=\frac{1}{J_n'\left(\rho_{n\nu}\right)R\sqrt{\pi L}}e^{ikz}e^{\pm in\alpha}J_n\left(\rho_{n\nu}\frac{r}{R}\right), \tag{1}$$

where $\rho_{n\nu}$ are the zeros of the Bessel function of the order n, $J_n\left(\rho_{n\nu}\right)=0$, $n=0,1,\ldots$, $\nu=1,2,\ldots$. The energy of a particle:

$$\varepsilon_{k,n,\nu}=\frac{\hbar^2k^2}{2m}+\rho_{n\nu}^2\frac{\hbar^2}{2mR^2}, \tag{2}$$

and the distribution function has the form

$$f_{k,n,\nu}=\left[\exp\beta\left(\varepsilon_{k,n,\nu}-\mu\right)+1\right]^{-1}, \tag{3}$$

where $\beta = 1/T$ is the inverse temperature. Pay attention that the discrete energy levels with $n = 0$ are nondegenerate, and the levels with $n \geq 1$ are twice degenerate in the projection of angular momentum on the z axis. Thermodynamic functions of the Fermi gas both in the volume case and in the case of lower dimensionality [8] can be expressed through the Fermi function defined by the formula

$$\Phi_s(t) = \frac{1}{\Gamma(s)} \int_0^\infty \frac{z^{s-1} dz}{e^{z-t} + 1}, \tag{4}$$

where s is an integer or half-integer positive number, $\Gamma(s)$ is the gamma function. For calculation of the bulk properties of the Fermi gas it is sufficient to know the functions (4) with half-integer indices $s = 1/2, 3/2, 5/2$, and for the quasi-two-dimensional case – with integer indices $s = 1, 2$. For the quasi-one-dimensional case under consideration in this work the functions with half-integer indices $s = 1/2, 3/2$ are required as well.

It is convenient to introduce the dimensionless temperature $\tau \equiv T/\varepsilon_R$ and the dimensionless chemical potential $\eta \equiv \mu/\varepsilon_R$, with normalization on the energy

$$\varepsilon_R \equiv \frac{\hbar^2}{2mR^2}, \tag{5}$$

and to define the functions of these two dimensionless variables by the following relation

$$\Psi_s(\tau, \eta) \equiv \sum_{n=0}^{\infty} \sum_{\nu=1}^{\infty} g_n \Phi_s(t_{n\nu}) = \sum_{\nu=1}^{\infty} \Phi_s(t_{0\nu}) + 2 \sum_{n=1}^{\infty} \sum_{\nu=1}^{\infty} \Phi_s(t_{n\nu}). \tag{6}$$

Here the parameter $t_{n\nu} \equiv \beta\left(\mu - \rho_{n\nu}^2 \varepsilon_R\right) \equiv \tau^{-1}\left(\eta - \rho_{n\nu}^2\right)$, and the factor $g_n \equiv 2 - \delta_{n0}$ accounts for the degeneracy order of levels. It equals unity for the levels with $n = 0$ and two for the rest of the levels.

After integration over momenta the thermodynamic potential Ω, number of particles N, energy E and entropy S are expressed through the functions (6) by the formulas

$$\Omega = -\frac{2LT}{\Lambda} \Psi_{3/2}(\tau, \eta), \tag{7}$$

$$N = \frac{2L}{\Lambda} \Psi_{1/2}(\tau, \eta), \tag{8}$$

$$E = \frac{LT}{\Lambda} \left[\Psi_{3/2}(\tau, \eta) + 2\frac{\eta}{\tau} \Psi_{1/2}(\tau, \eta) + 2\tau \frac{\partial \Psi_{3/2}(\tau, \eta)}{\partial \tau} \right], \tag{9}$$

$$S = \frac{3L}{\Lambda} \left[\Psi_{3/2}(\tau, \eta) + \frac{2}{3} \tau \frac{\partial \Psi_{3/2}(\tau, \eta)}{\partial \tau} \right], \tag{10}$$

where $\Lambda \equiv \left(\frac{2\pi\hbar^2}{mT} \right)^{1/2}$ is the thermal de Broglie wavelength. The volume $n = N/\pi R^2 L$ and the linear $n_L = N/L$ densities of particles are obviously given as

$$n = \frac{2}{\pi R^2 \Lambda} \Psi_{1/2}(\tau, \eta), \qquad n_L = \frac{2}{\Lambda} \Psi_{1/2}(\tau, \eta). \tag{11}$$

The thermodynamic potential (7) is a function of the temperature, chemical potential, the length of the tube and its radius: $\Omega = \Omega(T, \mu, L, R)$. In contrast to the volume case when Ω is proportional to the volume V, in this case it is proportional to the length L and depends in a complicated manner on the radius R. This circumstance is conditioned by the evident anisotropy of the system under consideration, since here the motions along the tube and in the direction of radius are qualitatively different. In statistical mechanics it is customary to pass in the final formulas to the thermodynamic limit: $V \to \infty, N \to \infty$ at $n = N/V = \text{const}$. In the present case it is more accurate to write down the thermodynamic limit somewhat differently, namely

$$L \to \infty, N \to \infty \quad \text{at} \quad n_L \equiv N/L = \text{const}. \tag{12}$$

It is thereby stressed that the transition to infinite volume occurs only owing to increasing the length of the tube, with its radius R being fixed.

The differential of the thermodynamic potential (7) has the form

$$d\Omega = \frac{\Omega}{L} dL - \frac{4LT}{\Lambda} \left[\frac{\eta}{\tau} \Psi_{1/2} + \tau \frac{\partial \Psi_{3/2}}{\partial \tau} \right] \frac{dR}{R} - \frac{2L}{\Lambda} \Psi_{1/2} d\mu - \frac{L}{\Lambda} \left[3\Psi_{3/2} + 2\tau \frac{\partial \Psi_{3/2}}{\partial \tau} \right] dT. \tag{13}$$

Here it was taken into account that $\partial \Psi_{3/2} / \partial \eta = \tau^{-1} \Psi_{1/2}$ and $d\varepsilon_R = -\left(2\varepsilon_R / R\right) dR$. Naturally, the usual thermodynamic relations hold $S = -\left(\partial \Omega / \partial T\right)_{\mu, L, R}$, $N = -\left(\partial \Omega / \partial \mu\right)_{T, L, R}$, as well as $\Omega = E - TS - \mu N$.

PRESSURES

In a bulk system the pressure is connected with the thermodynamical potential by the known formula $p=-\Omega/V$. In the considered quasi-one-dimensional case the system is anisotropic since the character of motion of particles along the tube and in the direction of its radius is different and, therefore, the usual formula for the pressure is invalid. The force exerted by the gas on the wall perpendicular to the z axis is different from the force exerted on the side wall of the tube. These forces can be calculated in the same way as in the volume case [7]. The pressures on the planes perpendicular to the z axis and on the wall of the tube, on the basis of the relations $p=-\left(\frac{\partial E}{\partial V}\right)_S$ and $V=\pi R^2 L$, are given by the formulas

$$p_{\|}=-\frac{1}{\pi R^2}\left(\frac{\partial E}{\partial L}\right)_{S,R}, \qquad p_R=-\frac{1}{2\pi LR}\left(\frac{\partial E}{\partial R}\right)_{S,L}, \tag{14}$$

or

$$p_{\|}=-\frac{1}{\pi R^2}\left(\frac{\partial \Omega}{\partial L}\right)_{T,\mu,R}, \qquad p_R=-\frac{1}{2\pi LR}\left(\frac{\partial \Omega}{\partial R}\right)_{T,\mu,L}. \tag{15}$$

The differential of the thermodynamic potential (13) can be represented in the form

$$d\Omega=-p_{\|}\pi R^2 dL-p_R 2\pi LRdR-Nd\mu-SdT. \tag{16}$$

Considering the form of the thermodynamic potential (7), we obtain the formulas determining the pressures through the functions (6):

$$p_{\|}=\frac{2T}{\pi R^2\Lambda}\Psi_{3/2}, \qquad p_R=\frac{2T}{\pi R^2\Lambda}\left(\frac{\eta}{\tau}\Psi_{1/2}+\tau\frac{\partial\Psi_{3/2}}{\partial\tau}\right). \tag{17}$$

The energy is connected with the pressures by the formula

$$E=\frac{1}{2}\pi R^2 L\left(p_{\|}+2p_R\right), \tag{18}$$

which in the volume limit $p_{\|}=p_R=p$ turns into the known relation $pV=(2/3)E$ for the Fermi gas [7].

REDUCED FORM OF THERMODYNAMIC QUANTITIES

It is convenient to introduce dimensionless quantities, which we will call "reduced" and designate them by a tilde on top, for the entropy, energy, pressures, volume and linear densities:

$$\begin{gathered}\tilde{S}\equiv\frac{2\sqrt{\pi}}{3}\frac{R}{L}S, \quad \tilde{E}=4\sqrt{\pi}\frac{R^3}{L}\frac{m}{\hbar^2}E, \quad \tilde{p}_{\|}=2\pi^{3/2}R^5\frac{m}{\hbar^2}p_{\|}, \quad \tilde{p}_R=2\pi^{3/2}R^5\frac{m}{\hbar^2}p_R,\\ \tilde{n}=\pi^{3/2}R^3 n, \quad \tilde{n}_L\equiv\sqrt{\pi}Rn_L=\tilde{n}.\end{gathered} \tag{19}$$

The reduced quantities are functions of only two independent dimensionless variables – the temperature τ and the chemical potential η:

$$\begin{gathered}\tilde{S}=\tau^{1/2}\left[\Psi_{3/2}+\frac{2}{3}\tau\frac{\partial\Psi_{3/2}}{\partial\tau}\right], \quad \tilde{E}=\tau^{3/2}\left[\Psi_{3/2}+2\frac{\eta}{\tau}\Psi_{1/2}+2\tau\frac{\partial\Psi_{3/2}}{\partial\tau}\right],\\ \tilde{p}_{\|}=\tau^{3/2}\Psi_{3/2}, \quad \tilde{p}_R=\tau^{3/2}\left(\frac{\eta}{\tau}\Psi_{1/2}+\tau\frac{\partial\Psi_{3/2}}{\partial\tau}\right), \quad \tilde{n}=\tilde{n}_L=\tau^{1/2}\Psi_{1/2}.\end{gathered} \tag{20}$$

The use of the reduced quantities is convenient owing to the fact that they do not contain explicitly geometric dimensions of the system.

HEAT CAPACITIES

An important directly measurable thermodynamic quantity is the heat capacity. In the geometry under consideration heat capacities can be defined under various conditions different from those which take place in the volume case. In order to obtain heat capacities, it is necessary to calculate the quantity $C=T(dS/dT)$. For this purpose, it is convenient to express the differential of the entropy through the reduced quantities:

$$\frac{dS}{S}=\left(\tilde{S}^{-1}\frac{\partial\tilde{S}}{\partial\eta}-\tilde{n}_L^{-1}\frac{\partial\tilde{n}_L}{\partial\eta}\right)d\eta+\left(\tilde{S}^{-1}\frac{\partial\tilde{S}}{\partial\tau}-\tilde{n}_L^{-1}\frac{\partial\tilde{n}_L}{\partial\tau}\right)d\tau. \tag{21}$$

In the volume case at the fixed number of particles, which is assumed here, the equation of state is $p=p(T,V)$. If the chemical potential is used as an independent variable, then the equation of state is defined parametrically by the equations $p=p(T,V,\mu)$ and $N=N(T,V,\mu)$. To obtain the heat capacity as a function of only temperature, one

constraint should be imposed between the pressure and the volume. In the simplest case, it its possible to fix either the volume or the pressure, thus obtaining the heat capacities C_V and C_p.

Under given conditions, owing to anisotropy of the system, there are two equations of state (17) for two pressures $p_R = p_R\left(T,R,L,\mu\right)$ and $p_\parallel = p_\parallel\left(T,R,L,\mu\right)$, which at the fixed average number of particles should be considered together with the equation $N = N\left(T,R,L,\mu\right)$. To obtain the heat capacity as a function of only temperature, two additional constraints should be set between the pressures $p_R, p_\parallel$ and the dimensions of the system R, L, namely $F_1\left(p_R, p_\parallel, R, L\right) = 0$ and $F_2\left(p_R, p_\parallel, R, L\right) = 0$. In the simplest case, two of four quantities $p_R, p_\parallel, R, L$ can be fixed. Then the heat capacity as a function of temperature can be considered under fixation of one of the following pairs of quantities: $\left(R,L\right)$, $\left(p_\parallel, p_R\right)$, $\left(R, p_\parallel\right)$, $\left(R, p_R\right)$, $\left(L, p_\parallel\right)$, $\left(L, p_R\right)$. Fixation of the first of pairs $\left(R,L\right)$ corresponds to the heat capacity at a constant volume in the volume case, and of the second $\left(p_\parallel, p_R\right)$ – to the heat capacity at a constant pressure. In calculations the following relations should be taken into account:

$$\frac{d\tilde{n}_L}{\tilde{n}_L} = \frac{dR}{R} - \frac{dL}{L}, \qquad \frac{d\tau}{dT} = \frac{1}{\varepsilon_R} + \frac{2\tau}{R}\frac{dR}{dT}. \tag{22}$$

Finally, we obtain the formulas for the reduced heat capacities $\tilde{C} \equiv \frac{2\sqrt{\pi}}{3}\frac{R}{L}C$ under different conditions, being valid at arbitrary temperatures:

$$\tilde{C}_{LR} = \tau\left\{\frac{\partial\tilde{S}}{\partial\tau} - \frac{\partial\tilde{S}}{\partial\eta}\frac{\left(\partial\tilde{n}_L/\partial\tau\right)}{\left(\partial\tilde{n}_L/\partial\eta\right)}\right\}, \tag{23}$$

$$\tilde{C}_{p_\parallel p_R} = \tau\frac{\left(\frac{\partial\tilde{S}}{\partial\eta} - \frac{\tilde{S}}{\tilde{n}_L}\frac{\partial\tilde{n}_L}{\partial\eta}\right)\left(\tilde{p}_R\frac{\partial\tilde{p}_\parallel}{\partial\tau} - \tilde{p}_\parallel\frac{\partial\tilde{p}_R}{\partial\tau}\right) + \left(\frac{\partial\tilde{S}}{\partial\tau} - \frac{\tilde{S}}{\tilde{n}_L}\frac{\partial\tilde{n}_L}{\partial\tau}\right)\left(\tilde{p}_\parallel\frac{\partial\tilde{p}_R}{\partial\eta} - \tilde{p}_R\frac{\partial\tilde{p}_\parallel}{\partial\eta}\right)}{\tilde{p}_\parallel\frac{\partial\tilde{p}_R}{\partial\eta} - \tilde{p}_R\frac{\partial\tilde{p}_\parallel}{\partial\eta} + \frac{2}{5}\tau\left(\frac{\partial\tilde{p}_\parallel}{\partial\eta}\frac{\partial\tilde{p}_R}{\partial\tau} - \frac{\partial\tilde{p}_\parallel}{\partial\tau}\frac{\partial\tilde{p}_R}{\partial\eta}\right)}, \tag{24}$$

$$\tilde{C}_{Rp_\parallel} = \tau\left\{\left(\frac{\partial\tilde{S}}{\partial\tau} - \frac{\tilde{S}}{\tilde{n}_L}\frac{\partial\tilde{n}_L}{\partial\tau}\right) - \left(\frac{\partial\tilde{S}}{\partial\eta} - \frac{\tilde{S}}{\tilde{n}_L}\frac{\partial\tilde{n}_L}{\partial\eta}\right)\frac{\left(\partial\tilde{p}_\parallel/\partial\tau\right)}{\left(\partial\tilde{p}_\parallel/\partial\eta\right)}\right\}, \tag{25}$$

$$\tilde{C}_{Lp_\parallel} = \tau\frac{\frac{\tilde{n}_L}{2}\frac{\partial\tilde{p}_\parallel}{\partial\eta}\left(\frac{\partial\tilde{S}}{\partial\tau} - \frac{\tilde{S}}{\tilde{n}_L}\frac{\partial\tilde{n}_L}{\partial\tau}\right) - \frac{\tilde{n}_L}{2}\frac{\partial\tilde{p}_\parallel}{\partial\tau}\left(\frac{\partial\tilde{S}}{\partial\eta} - \frac{\tilde{S}}{\tilde{n}_L}\frac{\partial\tilde{n}_L}{\partial\eta}\right) + \frac{5}{2}\tilde{p}_\parallel\left(\frac{\partial\tilde{S}}{\partial\eta}\frac{\partial\tilde{n}_L}{\partial\tau} - \frac{\partial\tilde{S}}{\partial\tau}\frac{\partial\tilde{n}_L}{\partial\eta}\right)}{\frac{\tilde{n}_L}{2}\frac{\partial\tilde{p}_\parallel}{\partial\eta} - \frac{5}{2}\tilde{p}_\parallel\frac{\partial\tilde{n}_L}{\partial\eta} + \tau\left(\frac{\partial\tilde{n}_L}{\partial\eta}\frac{\partial\tilde{p}_\parallel}{\partial\tau} - \frac{\partial\tilde{n}_L}{\partial\tau}\frac{\partial\tilde{p}_\parallel}{\partial\eta}\right)}. \tag{26}$$

The heat capacities $\tilde{C}_{Rp_R}$ and $\tilde{C}_{Lp_R}$ are determined by formulas (25) and (26) with account of the replacement $p_\parallel \to p_R$. Note that the formulas for the heat capacities (23) – (25) coincide with the corresponding heat capacities of the Fermi gas enclosed between two planes under the replacement therein $R \to L_0$, $\tilde{n}_R \to \tilde{n}_A$, where L_0 is the distance between planes, $\tilde{n}_A$ is the reduced surface density [8]. The heat capacity (26) goes into the formula for the two-dimensional case under the replacement $\tilde{n}_L \to 2\tilde{n}_A$ [8], manifesting the quasi-one-dimensionality of the considered case.

COMPRESSIBILITIES

Another directly observable quantities are compressibilities. We define the "parallel" and the "radial" compressibilities by the relations

$$\gamma_\parallel = \frac{1}{n}\left(\frac{\partial n}{\partial p_\parallel}\right)_R, \qquad \gamma_R = \frac{1}{n}\left(\frac{\partial n}{\partial p_R}\right)_L. \tag{27}$$

The reduced compressibilities will be defined by the relation $\tilde{\gamma} \equiv \left(\hbar^2/2\pi^{3/2}mR^5\right)\gamma$. Compressibilities can be calculated under the condition of both constant temperature (isothermal) and constant entropy (adiabatic). For the reduced compressibilities in isothermal conditions, we obtain:

$$\tilde{\gamma}_{\parallel T} = \frac{1}{\tilde{n}}\frac{\left(\partial\tilde{n}/\partial\eta\right)}{\left(\partial\tilde{p}_\parallel/\partial\eta\right)}, \tag{28}$$

$$\tilde{\gamma}_{RT} = \frac{\left(\partial\tilde{n}/\partial\eta\right)}{\left(\frac{5}{2}\tilde{p}_R - \tau\frac{\partial\tilde{p}_R}{\partial\tau}\right)\frac{\partial\tilde{n}}{\partial\eta} - \left(\frac{\tilde{n}}{2} - \tau\frac{\partial\tilde{n}}{\partial\tau}\right)\frac{\partial\tilde{p}_R}{\partial\eta}}. \tag{29}$$

The adiabaticity condition consists in the invariance of the entropy per one particle (and therefore of the total entropy in the system with a fixed number of particles). In the considered case the adiabaticity condition has the form:

$$\sigma \equiv \frac{S}{N} = \frac{1}{\Psi_{1/2}\left(\tau,\eta\right)}\left[\frac{3}{2}\Psi_{3/2}\left(\tau,\eta\right) + \tau\frac{\partial\Psi_{3/2}\left(\tau,\eta\right)}{\partial\tau}\right] \equiv \Theta\left(\tau,\eta\right) = \text{const}. \tag{30}$$

Together with the equation for the number of particles (8), the equation (30) determines relationships between the density, temperature and pressures in adiabatic processes. The adiabatic compressibilities are given by the formulas:

$$\tilde{\gamma}_{\|\sigma} = \frac{\left(\frac{\partial\Theta}{\partial\eta}\frac{\partial\tilde{n}}{\partial\tau} - \frac{\partial\Theta}{\partial\tau}\frac{\partial\tilde{n}}{\partial\eta}\right)}{\tilde{n}\left(\frac{\partial\Theta}{\partial\eta}\frac{\partial\tilde{p}_\|}{\partial\tau} - \frac{\partial\Theta}{\partial\tau}\frac{\partial\tilde{p}_\|}{\partial\eta}\right)}, \tag{31}$$

$$\tilde{\gamma}_{R\sigma} = \frac{2\left(\frac{\partial\Theta}{\partial\eta}\frac{\partial\tilde{n}}{\partial\tau} - \frac{\partial\Theta}{\partial\tau}\frac{\partial\tilde{n}}{\partial\eta}\right)}{\left[5\tilde{p}_R\left(\frac{\partial\Theta}{\partial\eta}\frac{\partial\tilde{n}}{\partial\tau} - \frac{\partial\Theta}{\partial\tau}\frac{\partial\tilde{n}}{\partial\eta}\right) - \tilde{n}\left(\frac{\partial\Theta}{\partial\eta}\frac{\partial\tilde{p}_R}{\partial\tau} - \frac{\partial\Theta}{\partial\tau}\frac{\partial\tilde{p}_R}{\partial\eta}\right)\right]}. \tag{32}$$

Certainly, at zero temperature the isothermal and adiabatic compressibilities coincide.

ANALYSIS OF FUNCTIONS $\Psi_{1/2}\left(\tau,\eta\right)$ AND $\Psi_{3/2}\left(\tau,\eta\right)$

As shown above, all thermodynamic quantities are expressed through the functions $\Psi_{1/2}\left(\tau,\eta\right)$, $\Psi_{3/2}\left(\tau,\eta\right)$ and their derivatives. In this section we study some properties of these functions. Note that when studying oscillations in the Fermi gas with quantized levels, usually the Poisson formula is used for the extraction of the oscillating part of thermodynamic and kinetic quantities [7]. But a detailed analysis undertaken by the authors shows that it is more convenient to calculate the functions, by which thermodynamic quantities are expressed, without use of the Poisson formula. This, in particular, is connected with the fact that the possibility of extraction of an oscillating part in some function does not at all mean that the total function is oscillating, and the contribution of non-oscillating part should be analyzed as well [8].

At fixed particle number density and at high temperatures, the same as in the volume case, the chemical potential is negative. With decreasing temperature it increases and at some temperature T_0 turns into zero ($\eta = 0$), becoming positive at $T < T_0$. There is one more characteristic temperature T_R, at which $\mu = \rho_{01}^2\varepsilon_R$ ($\eta = \rho_{01}^2$), ρ_{01} is the lowest zero of the Bessel function $J_n\left(\rho_{n\nu}\right) = 0$. The dependencies of the dimensionless chemical potential η on the dimensionless temperature τ are shown in Fig. 1. The characteristic temperatures $\tau_0 = T_0/\varepsilon_R$ and $\tau_R = T_R/\varepsilon_R$ are determined from the equations:

$$\tilde{n}_L = \tau_0^{1/2}\Psi_{1/2}\left(\tau_0,0\right), \qquad \tilde{n}_L = \tau_R^{1/2}\Psi_{1/2}\left(\tau_R,\rho_{01}^2\right). \tag{33}$$

The region where $\mu < \rho_{01}^2\varepsilon_R$ ($\eta < \rho_{01}^2$) will be for convenience called the high temperature region, and the region $\mu > \rho_{01}^2\varepsilon_R$ ($\eta > \rho_{01}^2$) – the low temperature region.

It is convenient to arrange the zeros of the Bessel function in ascending order with the help of a single new index $r \equiv \left(n,\nu\right)$, so that $\rho_{r+1} > \rho_r$, where $1 \equiv \left(0,1\right)$ corresponds to the lowest value at which the Bessel function becomes zero $\rho_1 = \rho_{01}$. The inequalities hold [14]:

$$\rho_{n1} < \rho_{n+1,1} < \rho_{n2} < \rho_{n+1,2} < \rho_{n3} < \rho_{n+1,3} < \ldots. \tag{34}$$

In Table I the ten first zeros of the Bessel function arranged in ascending order are given for reference. In this notation, the functions (6) are written in the form

$$\Psi_s\left(\tau,\eta\right) \equiv \sum_{r=1}^{\infty} g_r\Phi_s\left[\tau^{-1}\left(\eta - \rho_r^2\right)\right], \tag{35}$$

where $g_r = 1$ at $n = 0$ and $g_r = 2$ at $n \geq 1$.

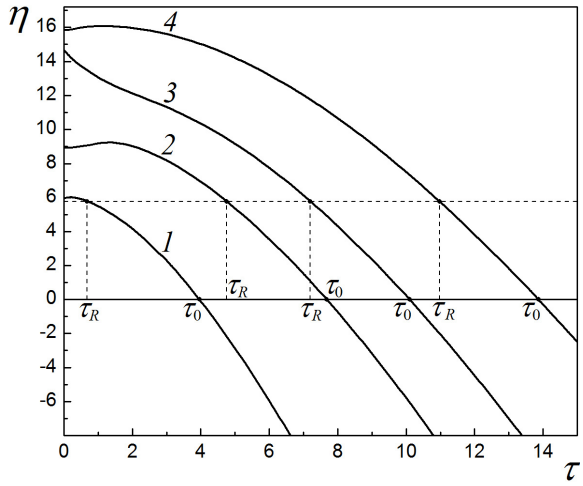

Fig. 1. The dependencies of the chemical potential on temperature $\eta(\tau)$ at different values of the reduced density:

(*1*) $\tilde{n}_L = 0.5\ (\tau_R = 0.68,\ \tau_0 = 3.96)$; (*2*) $\tilde{n}_L = 2.0\ (\tau_R = 4.76,\ \tau_0 = 7.68)$;

(*3*) $\tilde{n}_L = \left(2/\sqrt{\pi}\right)\left(\rho_2^{\,2} - \rho_1^{\,2}\right)^{1/2} = 3.37\ (\tau_R = 7.20,\ \tau_0 = 10.10)$; (*4*) $\tilde{n}_L = 6.0\ (\tau_R = 10.98,\ \tau_0 = 13.87)$.

Table I

The ten first zeros of the Bessel function

$\rho_1 = \rho_{0,1}$	$\rho_2 = \rho_{1,1}$	$\rho_3 = \rho_{2,1}$	$\rho_4 = \rho_{0,2}$	$\rho_5 = \rho_{3,1}$
2.40	3.83	5.14	5.52	6.38
$\rho_6 = \rho_{1,2}$	$\rho_7 = \rho_{4,1}$	$\rho_8 = \rho_{2,2}$	$\rho_9 = \rho_{0,3}$	$\rho_{10} = \rho_{5,1}$
7.02	7.59	8.42	8.65	8.77

In the high temperature region $\eta \le \rho_1^2$ the functions (6) can be calculated by the formula

$$\Psi_s(\tau,\eta) = \sum_{k=1}^{\infty} \frac{(-1)^{k+1}}{k^s} \sum_{r=1}^{\infty} g_r e^{\frac{k}{\tau}\left(\eta - \rho_r^2\right)}. \tag{36}$$

In the low temperature region $\eta > \rho_1^2$ there can be obtained asymptotic expansions for the functions (6), valid in the limit $\tau \to 0$. Let us represent the functions (6) in the form

$$\Psi_s(\tau,\eta) = \sum_{r=1}^{r_0-1} g_r \Phi_s\left[\tau^{-1}\left(\eta - \rho_r^2\right)\right] + \sum_{r=r_0+2}^{\infty} g_r \Phi_s\left[\tau^{-1}\left(\eta - \rho_r^2\right)\right] + g_{r_0}\Phi_s\left[\tau^{-1}\left(\eta - \rho_{r_0}^2\right)\right] + g_{r_0+1}\Phi_s\left[\tau^{-1}\left(\eta - \rho_{r_0+1}^2\right)\right]. \tag{37}$$

Here the index r_0, enumerating zeros, is defined by the condition: $\rho_{r_0}^2 < \eta < \rho_{r_0+1}^2$. We singled out the third and the fourth terms, important at $\eta \ge \rho_{r_0}^2$ and $\eta \le \rho_{r_0+1}^2$. At $\tau \ll 1$ the contribution of the second term is exponentially small, and for calculation of the first sum one should make use of the expansion being valid to within exponential corrections:

$$\Phi_s(t) = \frac{t^s}{s\Gamma(s)}\left\{1 + 2\sum_{k=0}^{\infty} \frac{s(s-1)\ldots(s-2k-1)\left(1-2^{-2k-1}\right)\zeta(2k+2)}{t^{2k+2}}\right\}. \tag{38}$$

Finally, we obtain the asymptotic expansion valid in the limit $\tau \to 0$:

$$\begin{aligned}\Psi_s(\tau,\eta) = \frac{1}{s\Gamma(s)\tau^s} Z_s^{(r_0-1)}(\eta) + \frac{2}{\Gamma(s)} \sum_{k=0}^{\infty} b_s(2k+1)\left(1-2^{-2k-1}\right)\zeta(2k+2)\tau^{2k+2-s} Z_{s-2k-2}^{(r_0-1)}(\eta) + \\ + g_{r_0}\Phi_s\left[\tau^{-1}\left(\eta - \rho_{r_0}^2\right)\right] + g_{r_0+1}\Phi_s\left[\tau^{-1}\left(\eta - \rho_{r_0+1}^2\right)\right],\end{aligned} \tag{39}$$

where

$$Z_s^{(r_0)}(\eta) \equiv \sum_{r=1}^{r_0} g_r\left(\eta - \rho_r^2\right)^s, \tag{40}$$

$b_s(m) = \prod_{l=1}^{m}(s-l)$ at $m \ge 1$, and $b_s(0) = 1$. In particular, for the functions required in calculation of thermodynamic quantities, at $\tau \to 0$ it is sufficient to use the following approximations:

$$\Psi_{1/2}(\tau,\eta)=\frac{2}{\sqrt{\pi\tau}}Z_{1/2}^{(r_0-1)}(\eta)+g_{r_0}\Phi_{1/2}\left[\tau^{-1}\left(\eta-\rho_{r_0}^2\right)\right]+g_{r_0+1}\Phi_{1/2}\left[\tau^{-1}\left(\eta-\rho_{r_0+1}^2\right)\right],$$
$$\Psi_{3/2}(\tau,\eta)=\frac{4}{3\sqrt{\pi}\tau^{3/2}}\left[Z_{3/2}^{(r_0-1)}(\eta)+\frac{\pi^2}{8}\tau^2 Z_{-1/2}^{(r_0-1)}(\eta)\right]+g_{r_0}\Phi_{3/2}\left[\tau^{-1}\left(\eta-\rho_{r_0}^2\right)\right]+g_{r_0+1}\Phi_{3/2}\left[\tau^{-1}\left(\eta-\rho_{r_0+1}^2\right)\right]. \quad (41)$$

In fact, at $\tau\le 1$ these formulas approximate well the exact functions defined by the formula (6). Thus, at $\tau=0.1$ the error does not exceed 0.01%, and even at $\tau=1$ – 1%. The dependencies of these functions and their derivatives on the chemical potential are shown in Fig. 2. As seen (Fig. 2b), the function $\Psi_{3/2}(\tau,\eta)$ and its derivative monotonically increase with increasing the chemical potential. The function $\Psi_{1/2}(\tau,\eta)$ also monotonically increases but the behavior of its derivative has an oscillating character, besides the derivative has sharp maximums at the points corresponding to the zeros of the Bessel function (Fig. 2a). Note also that, since $\tilde{n}=\tilde{n}_L=\tau^{1/2}\Psi_{1/2}(\tau,\eta)$, the function $\Psi_{1/2}(\tau,\eta)$ describes the dependence of the reduced density, divided by $\tau^{1/2}$, on the chemical potential.

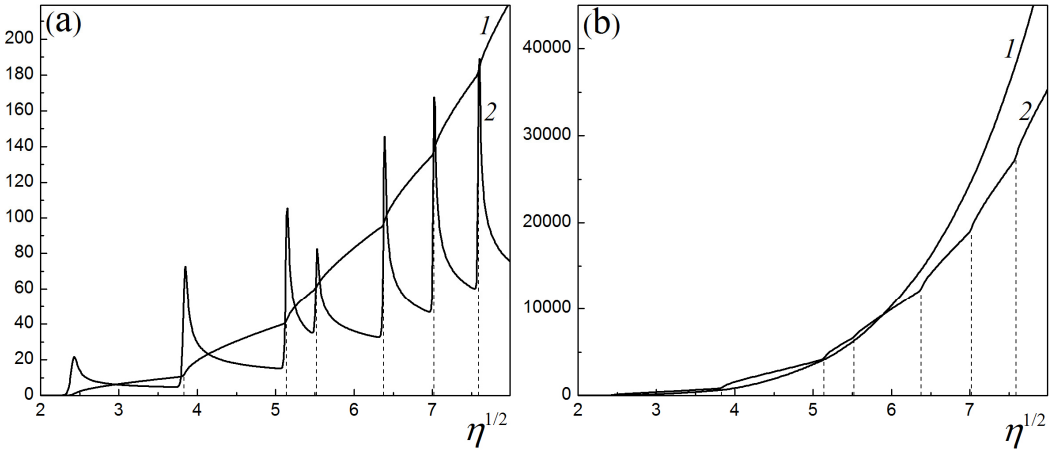

Fig. 2. Graphs of the functions $\Psi_{1/2}(\tau,\eta),\Psi_{3/2}(\tau,\eta)$ and their derivatives at $\tau=0.1$.
(a) The functions $\Psi_{1/2}(\tau,\eta)$ (*1*) and $\partial\Psi_{1/2}(\tau,\eta)/\partial\eta^{1/2}$ (*2*); (b) The functions $\Psi_{3/2}(\tau,\eta)$ (*1*) and $\partial\Psi_{3/2}(\tau,\eta)/\partial\eta^{1/2}$ (*2*).
The dashed lines correspond to the zeros of the Bessel function $\eta^{1/2}=\rho_r$.

THERMODYNAMIC QUANTITIES AT LOW TEMPERATURES

The most interesting range where the quantum effects may manifest themselves on the macroscopic level in the behavior of thermodynamic characteristics is the range of low temperatures. Let us consider the behavior of observable quantities at low temperatures such that $\tau\ll 1$ using the formulas (41). For the reduces densities of particles we have

$$\tilde{n}=\tilde{n}_L=\tau^{1/2}\Psi_{1/2}(\tau,\eta)=$$
$$=\frac{2}{\sqrt{\pi}}Z_{1/2}^{(r_0-1)}(\eta)+\tau^{1/2}\left\{g_{r_0}\Phi_{1/2}\left[\tau^{-1}\left(\eta-\rho_{r_0}^2\right)\right]+g_{r_0+1}\Phi_{1/2}\left[\tau^{-1}\left(\eta-\rho_{r_0+1}^2\right)\right]\right\}. \quad (42)$$

Here with a good accuracy the density can be considered independent of temperature and the formula $\tilde{n}=\tilde{n}_L\approx\left(2/\sqrt{\pi}\right)Z_{1/2}^{(r_0)}(\eta)$ can be used. The reduced entropy is determined by the formula

$$\tilde{S}=\frac{2\pi^{3/2}}{9}Z_{-1/2}^{(r_0-1)}(\eta)\tau+\tau^{1/2}\left\{g_{r_0}\Phi_{3/2}\left[\tau^{-1}\left(\eta-\rho_{r_0}^2\right)\right]-\frac{2}{3}\tau^{-1}\left(\eta-\rho_{r_0}^2\right)g_{r_0}\Phi_{1/2}\left[\tau^{-1}\left(\eta-\rho_{r_0}^2\right)\right]+\right.$$
$$\left.+g_{r_0+1}\Phi_{3/2}\left[\tau^{-1}\left(\eta-\rho_{r_0+1}^2\right)\right]-\frac{2}{3}\tau^{-1}\left(\eta-\rho_{r_0+1}^2\right)g_{r_0+1}\Phi_{1/2}\left[\tau^{-1}\left(\eta-\rho_{r_0+1}^2\right)\right]\right\}. \quad (43)$$

The terms which contain the functions Φ_s in (43) can be significant when $\eta\approx\rho_{r_0}^2$ or $\eta\approx\rho_{r_0+1}^2$. It should be noted that in the quasi-one-dimensional case, the same as in the volume and the quasi-two-dimensional [8] cases, nearly everywhere except the specific points there remains the linear dependence of the entropy on temperature (see Fig. 3), and the following formula can be used

$$\tilde{S}\approx\left(2\pi^{3/2}/9\right)Z_{-1/2}^{(r_0)}(\eta)\tau. \quad (44)$$

The slope of the lines (44) and the width of the range where this formula is valid depend on the closeness of the chemical potential value to the square of the Bessel function zero. As the chemical potential approaches the square of the Bessel function zero from the side of greater values $\eta\to\rho_{r_0}^2+0$ the slope angle of a line increases (curve 2 in Fig. 3)

and at the very point $\eta = \rho_{r_0}^2$, as it follows from the formula (43), $\tilde{S} \sim \sqrt{\tau}$ (curve 1 in Fig. 3). As the chemical potential approaches the square of the Bessel function zero from the side of smaller values $\eta \to \rho_{r_0}^2 - 0$ the slope angle of a line tends to a finite value (curve 3 in Fig. 3), at that, however, the temperature range where the linear dependence is realized proves to be quite narrow.

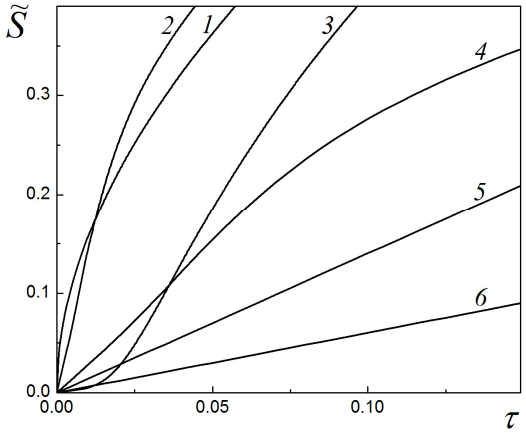

Fig. 3. The dependence of the reduced entropy $\tilde{S}(\tau,\eta)$ on the temperature τ at a fixed value of the chemical potential:
(*1*) $\eta = \rho_2{}^2 = \rho_{1,1}^2 = 14.68$ $(\tilde{n}_L = 3.37)$; (*2*) $\eta = 14.72$ $(\tilde{n}_L = 3.81)$; (*3*) $\eta = 14.60$ $(\tilde{n}_L = 3.35)$;
(*4*) $\eta = 5.98$ $(\tilde{n}_L = 0.5)$; (*5*) $\eta = 20.0$ $(\tilde{n}_L = 9.46)$; (*6*) $\eta = 10.0$ $(\tilde{n}_L = 2.32)$. The density $\tilde{n}_L$ is given at $\tau = 0$.

The dependence of the reduced entropy on the dimensionless chemical potential is presented in Fig. 4. As we see, the entropy has sharp maximums at the points where the chemical potential equals the square of the Bessel function zero. At calculation by means of the approximate formula (44) while approaching the point $\eta = \rho_{r_0}^2$ from the right there is the root singularity $\tilde{S} \sim \left(\eta - \rho_{r_0}^2\right)^{-1/2}$, and while approaching this point from the left the entropy takes a finite value. The calculation by the more accurate formula (43) eliminates the singularity and allows to obtain the entropy value at the maximum $\tilde{S}_{\max}$, which with a good accuracy is determined by the formula

$$\tilde{S}_{\max} \approx \tilde{S}\left(\tau, \eta_{r_0}\right) \approx \frac{2\pi^{3/2}}{9} Z_{-1/2}^{(r_0-1)}\left(\eta_{r_0}\right)\tau + g_{r_0}\left(1-2^{-1/2}\right)\zeta(3/2)\sqrt{\tau}\,, \tag{45}$$

where $\zeta(3/2) \approx 2.612$ is the Riemann zeta function. Pay attention that the values of maximums for the nondegenerate levels with $n = 0$ turn out to be less than the appropriate values for the neighboring levels with the two-fold degeneracy at $n \neq 0$ (see Fig. 4).

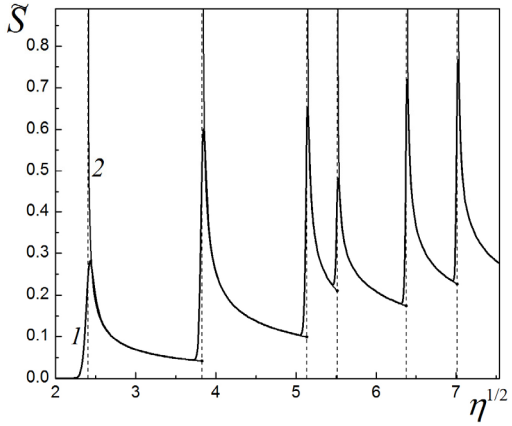

Fig. 4. The dependence of the reduced entropy $\tilde{S}(\tau,\eta)$ on the chemical potential.
The curve *1* is plotted by means of the formula (43), and the curve *2* – by the formula (44) at $\tau = 0.1$.
The dashed lines correspond to the zeros of the Bessel function $\eta^{1/2} = \rho_r$.

In the quasi-one-dimensional case under study the dependence of the entropy on the chemical potential is qualitatively different from the quasi-two-dimensional case [8], i.e. the entropy has a sharp maximum rather than undergoes a jump at the beginning of the filling of a new discrete level. One more difference of the given system from

the quasi-two-dimensional case is the irregularity of the values of chemical potential, specified by the Bessel function zeros, at which the entropy has peculiarities [8].

In the main approximation all introduced above heat capacities (23) − (26), as it had to be expected, prove to be identical and coinciding with the entropy. Thus, in the quasi-one-dimensional case, in the same way as in the quasi-two-dimensional [8] and the volume cases, all heat capacities prove to be proportional to temperature:

$$\tilde{C} = \frac{2\pi^{3/2}}{9} Z_{-1/2}^{(r_0)}(\eta)\tau \,. \tag{46}$$

Only at the specific points, at $\eta \to \rho_{r_0}^2 + 0$, similarly to the entropy case, there appears the dependence $\tilde{C} \sim \sqrt{\tau}$. The temperature dependence of heat capacities and their dependence on the chemical potential are similar to the dependencies for the entropy shown in Figs. 3 and 4.

It is interesting to consider the transition from the formulas (44), (46) to the volume case, when the radius of the tube becomes large as compared with the de Broglie wavelength. It can be done, if one takes into account that in order to make the transition from the dispersion law of particles in the tube (2) to the dispersion law of free particles it is necessary to make the substitution

$$\rho_{nv}^2 \frac{\hbar^2}{2mR^2} \to \frac{\hbar^2\left(k_x^2 + k_y^2\right)}{2m}. \tag{47}$$

The same rule of transition to the continuous spectrum can be obtained by means of the asymptotic expression for the Bessel functions.

Performing formally the same substitution at calculation of the functions (41) and replacing the summation over the Bessel function zeros by the integration over the wave vector in the (x, y) plane, we obtain

$$Z_{1/2}(\eta) = \frac{\sqrt{2}\, m^{3/2}\mu^{3/2}R^3}{3\hbar^3}, \qquad Z_{-1/2}(\eta) = \frac{m^{1/2}\mu^{1/2}R}{\sqrt{2}\hbar}. \tag{48}$$

Finally, we come to the known volume expressions for the particle number density $n = \left(2m\mu\right)^{3/2}/3\pi^2\hbar^3$ and also the entropy and the heat capacity $S = C = \left(m^{3/2}(2\mu)^{1/2}/3\hbar^3\right)VT$.

Let us give the results of calculation of the reduced pressures at zero temperature. In this case the pressures are determined by the formulas:

$$\tilde{p}_{\parallel} = \frac{4}{3\sqrt{\pi}} Z_{3/2}^{(r_0)}(\eta), \tag{49}$$

$$\tilde{p}_R = \frac{2}{\sqrt{\pi}}\left[\eta Z_{1/2}^{(r_0)}(\eta) - Z_{3/2}^{(r_0)}(\eta)\right]. \tag{50}$$

The dependencies of the pressures (49) and (50) on the chemical potential are shown in Fig. 5. As seen, the parallel pressure smoothly increases with increasing the chemical potential, and the radial pressure undergoes breaks (discontinuities in the derivative) at the points where the filling of a new discrete level begins. In the volume case, considering the formula $Z_{3/2}(\eta) = 2^{3/2} m^{5/2}\mu^{5/2}R^5/5\hbar^5$, the both formulas (49) and (50) lead to the known expression for the pressure of the Fermi gas at zero temperature: $p = \left(2^{5/2}/15\pi^2\right)m^{3/2}\mu^{5/2}/\hbar^3$.

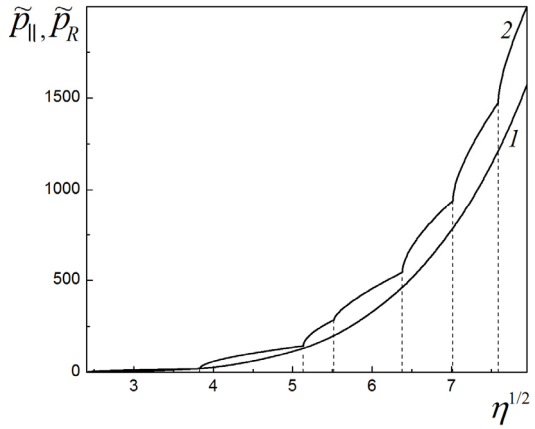

Fig. 5. The dependencies of the reduced pressures on the chemical potential at zero temperature: (*1*) $\tilde{p}_{\parallel}(\eta)$; (*2*) $\tilde{p}_R(\eta)$. Dashed lines correspond to the zeros of the Bessel function.

Let us proceed to consideration of the compressibilities. The reduced compressibilities at zero temperature are determined be the formulas:

$$\tilde{\gamma}_{\|}=\frac{\sqrt{\pi}}{4}\frac{Z_{-1/2}^{(r_0)}(\eta)}{\left[Z_{1/2}^{(r_0)}(\eta)\right]^2},\qquad \tilde{\gamma}_{R}=\frac{\sqrt{\pi}Z_{-1/2}^{(r_0)}(\eta)}{4\eta Z_{1/2}^{(r_0)}(\eta)Z_{-1/2}^{(r_0)}(\eta)-5Z_{3/2}^{(r_0)}(\eta)Z_{-1/2}^{(r_0)}(\eta)+\left[Z_{1/2}^{(r_0)}(\eta)\right]^2}. \tag{51}$$

The dependencies of the compressibilities (51) on the chemical potential are shown in Fig. 6.

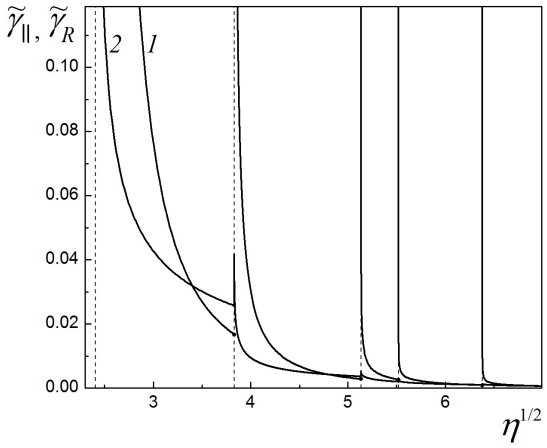

Fig. 6. The dependencies of the compressibilities on the chemical potential at zero temperature: (*1*) $\tilde{\gamma}_{\|}(\eta)$; (*2*) $\tilde{\gamma}_R(\eta)$. Dashed lines correspond to the zeros of the Bessel function.

While approaching the point where the filling of a new level begins from the side of smaller values of the chemical potential the parallel compressibility has a finite value, and while approaching the specific point from the side of greater values of the chemical potential – it tends to infinity. The radial compressibility has finite maximums in the specific points, such that the magnitude of peaks rapidly decreases with increasing the chemical potential. In the volume limit the both compressibilities coincide, being given by the formula

$$\gamma_{\|}=\gamma_R=\frac{9\pi^2}{4\sqrt{2}}\frac{\hbar^3}{m^{3/2}\mu^{5/2}}. \tag{52}$$

Since the square of speed of sound $u^2=m^{-1}\left(\partial p/\partial n\right)$ and the compressibility are connected by the relation $u^2=1/mn\gamma$, then from (52) it follows the known formula for the speed of sound in the Fermi gas at zero temperature: $u^2=(2/3)(\mu/m)$.

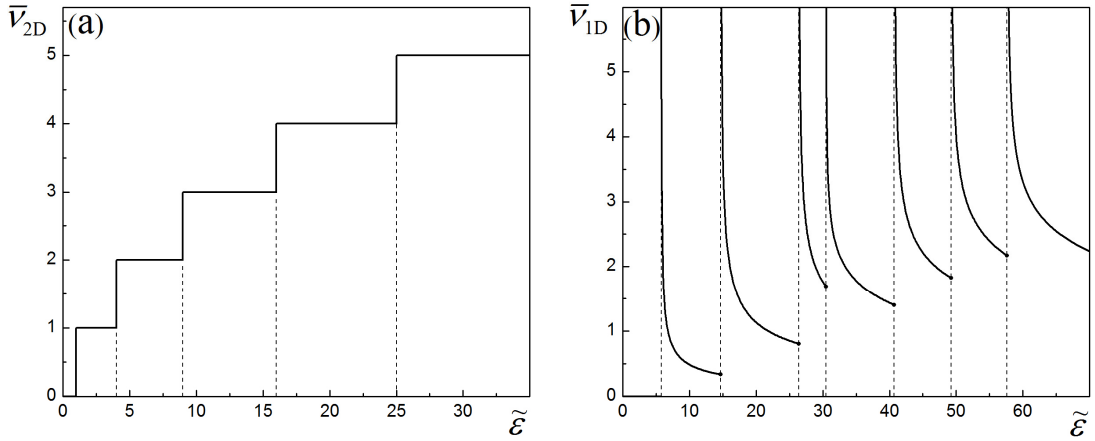

Fig. 7. The density of states for the quasi-two-dimensional quantum well and the nanotube:

(a) $\bar{\nu}_{2D}(\tilde{\varepsilon})=\nu_{2D}(\tilde{\varepsilon})\left(\frac{mA}{\pi\hbar^2}\right)^{-1}=\sum_{n=1}^{\infty}\theta\left(\tilde{\varepsilon}-n^2\right)$, $\tilde{\varepsilon}=\varepsilon/\varepsilon_L$, $\varepsilon_L\equiv\pi^2\hbar^2/2mL_0^2$, A is the area, L_0 is the distance between planes [8];

(b) $\bar{\nu}_{1D}(\tilde{\varepsilon})=\nu_{1D}(\tilde{\varepsilon})\left(\frac{2mLR}{\pi\hbar^2}\right)^{-1}=Z_{-1/2}^{(r_0)}(\tilde{\varepsilon})$ at $\rho_{r_0}^2<\tilde{\varepsilon}\le\rho_{r_0+1}^2$, $\tilde{\varepsilon}=\varepsilon/\varepsilon_R$. The dashed lines correspond to $\tilde{\varepsilon}=\rho_r^2$.

The peculiarities considered above in the behavior of the entropy, heat capacities, pressures and compressibilities of the quasi-one-dimensional system and their difference from those of the quasi-two-dimensional system are connected with the form of the density of states $\nu(\varepsilon)$, which is shown in Fig. 7 for the quasi-two-dimensional quantum well and the quasi-one-dimensional tube. In the case of the quantum well the density of states is constant and changes by a jump at the beginning of the filling of a new level (Fig. 7a). In the quasi-one-dimensional case the density of states tends to

infinity $\nu(\varepsilon) \sim \left(\varepsilon - \rho_r^2 \varepsilon_R\right)^{-1/2}$ at $\varepsilon \to \rho_r^2 \varepsilon_R + 0$ (Fig. 7b). Such a dependence of the density of states on the energy is similar to that which takes place for electrons in magnetic field. The difference consists in that in magnetic field the peculiarities are distributed regularly with the intervals multiple of odd numbers of half the cyclotron frequency. In the considered case the distribution of the peculiarities is irregular and is determined by the zeros of the Bessel function.

DEPENDENCIES OF THERMODYNAMIC QUANTITIES ON THE TUBE RADIUS

If thermodynamic quantities are taken in the reduced form (19), and the dimensionless chemical potential η and the dimensionless temperature τ are used as independent variables, then as it was shown the geometrical dimensions fall out of the thermodynamic relations, in particular the radius of the tube R falls out. Meanwhile, exactly the dependencies of the observable quantities on the tube radius are of interest in experiment. To obtain such dependencies, the relations derived above should be presented in the dimensional form. At that, the form of dependence of the thermodynamic quantities on the radius will essentially depend on what quantity is being fixed when studying such dependence: the total density n or the linear density n_L. Let us show it on the example of dependence of the chemical potential on the tube radius. In the dimensional form the formulas for the densities can be presented as follows

$$\pi^{3/2} R^3 n = \pi^{1/2} R n_L = \frac{2}{\sqrt{\pi}} Z_{1/2}^{(r_0)}(\eta), \tag{53}$$

and, according the definition, the chemical potential is expressed through the parameter η by the formula

$$\mu = \frac{\hbar^2}{2mR^2}\eta\,. \tag{54}$$

The formulas (53) and (54) define parametrically the dependence of the chemical potential on the radius in the domain of variation of the parameter $\rho_{r_0}^2 < \eta < \rho_{r_0+1}^2$. As we see, the dependence of R on the parameter η will be different depending on what is fixed – the volume or the linear density.

At the fixed linear density $n_L = \text{const}$ in the domain $\rho_{r_0}^2 < \eta < \rho_{r_0+1}^2$ the dependence of the chemical potential on the radius is parametrically defined by the equations

$$\bar{\mu} = \frac{\eta}{\left[Z_{1/2}^{(r_0)}(\eta)\right]^2}, \qquad \bar{R} = Z_{1/2}^{(r_0)}(\eta), \tag{55}$$

where

$$\bar{R} = \frac{\pi n_L}{2} R, \qquad \bar{\mu} = \mu \frac{2m}{\hbar^2}\left(\frac{2}{\pi n_L}\right)^2. \tag{56}$$

At the fixed total density $n = \text{const}$ the similar dependence is defined by the equations

$$\bar{\mu} = \frac{\eta}{\left[Z_{1/2}^{(r_0)}(\eta)\right]^{2/3}}, \qquad \bar{R} = \left[Z_{1/2}^{(r_0)}(\eta)\right]^{1/3}, \tag{57}$$

where

$$\bar{R} = \left(\frac{\pi^2 n}{2}\right)^{1/3} R, \qquad \bar{\mu} = \mu \frac{2m}{\hbar^2}\left(\frac{2}{\pi^2 n}\right)^{2/3}. \tag{58}$$

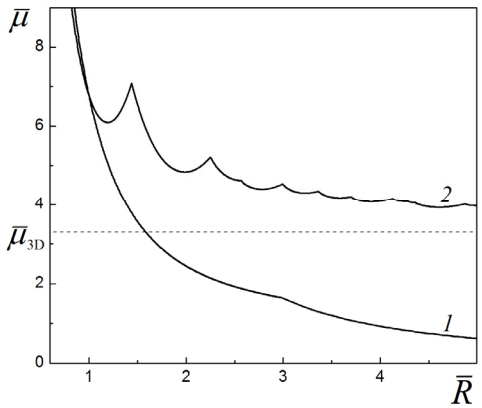

Fig. 8. The dependencies of the chemical potential on the tube radius:
(*1*) at the fixed linear density n_L ($\bar{\mu}, \bar{R}$ are defined by formulas (56); (*2*) at the fixed volume density n ($\bar{\mu}, \bar{R}$ are defined by formulas (58)). The dashed line shows the chemical potential $\bar{\mu}_{3D} = \lim_{\bar{R}\to\infty} \bar{\mu} = 6^{2/3}$ of volume system of density n.

The dependencies of the chemical potential on the tube radius are shown for both cases in Fig. 8. As seen, at the fixed linear density the chemical potential monotonically decreases with increasing the radius (curve *1* in Fig. 8). The oscillation dependence on the radius is realized at the fixed total density (curve *2* in Fig. 8). The amplitude of oscillations rapidly decreases with increasing the radius, at that the chemical potential quite slowly approaching its volume value $\overline{\mu}_{3\mathrm{D}} = \lim\limits_{\overline{R}\to\infty} \overline{\mu} = 6^{2/3}$.

Let us also give the dependencies on the radius of such a directly measurable quantity as the pressure. At the fixed linear density $n_L = \mathrm{const}$ in the domain $\rho_{r_0}^2 < \eta < \rho_{r_0+1}^2$ the dependencies of the radial and the parallel pressures on the parameter η are defined by the formulas:

$$\overline{p}_R = \frac{\eta Z_{1/2}^{(r_0)}(\eta) - Z_{3/2}^{(r_0)}(\eta)}{\left[Z_{1/2}^{(r_0)}(\eta)\right]^5}, \qquad \overline{p}_{\parallel} = \frac{2}{3}\frac{Z_{3/2}^{(r_0)}(\eta)}{\left[Z_{1/2}^{(r_0)}(\eta)\right]^5}, \tag{59}$$

where

$$\overline{p}_{R,\parallel} = \pi^2 \frac{m}{\hbar^2}\left(\frac{2}{\pi n_L}\right)^5 p_{R,\parallel} \tag{60}$$

and the dependence of the radius on η is given by the formulas (55), (56). At the fixed total density $n = \mathrm{const}$ the similar dependencies are defined by the equations

$$\overline{p}_R = \frac{\eta Z_{1/2}^{(r_0)}(\eta) - Z_{3/2}^{(r_0)}(\eta)}{\left[Z_{1/2}^{(r_0)}(\eta)\right]^{5/3}}, \qquad \overline{p}_{\parallel} = \frac{2}{3}\frac{Z_{3/2}^{(r_0)}(\eta)}{\left[Z_{1/2}^{(r_0)}(\eta)\right]^{5/3}}, \tag{61}$$

where

$$\overline{p}_{R,\parallel} = \pi^2 \frac{m}{\hbar^2}\left(\frac{2}{\pi^2 n}\right)^{5/3} p_{R,\parallel}, \tag{62}$$

and the dependence of the radius on η is given by the formulas (57), (58). The dependencies of the pressures on the tube radius are shown for both cases in Fig. 9.

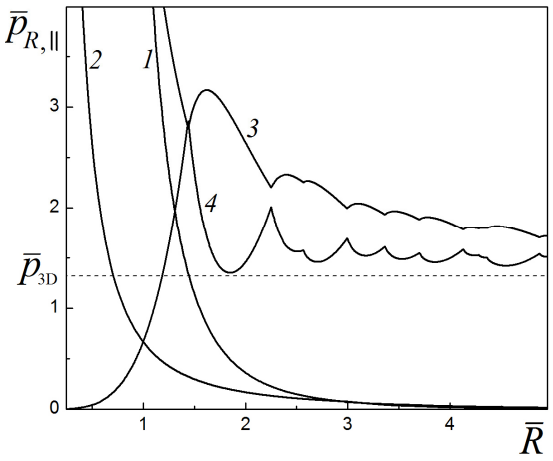

Fig. 9. The dependencies of the pressures on the tube radius:
(*1*) $\overline{p}_R = \overline{p}_R(\overline{R})$ and (*2*) $\overline{p}_{\parallel} = \overline{p}_{\parallel}(\overline{R})$ at the fixed linear density n_L;
(*3*) $\overline{p}_R = \overline{p}_R(\overline{R})$ and (*4*) $\overline{p}_{\parallel} = \overline{p}_{\parallel}(\overline{R})$ at the fixed volume density n.
The dashed line shows the pressure $\overline{p}_{3\mathrm{D}} = \lim\limits_{\overline{R}\to\infty} \overline{p}_{R,\parallel} = (2/5)6^{2/3}$ of volume system of density n.

Here also, the oscillations exist only under condition of the fixed total density, so that qualitatively the situation in this quasi-one-dimensional case is similar to that which takes place in the quasi-two-dimensional quantum well [8]. At the fixed linear density n_L with increasing the radius the total density n approaches zero, so that the both pressures approach zero as well. In the opposite case $R \to 0$ the total density increases unlimitedly and therefore the pressures also tend to infinity (curves *1*, *2* in Fig. 9). At the fixed total density n with increasing the radius the both pressures approach, oscillating, their volume value $\overline{p}_{3\mathrm{D}} = \lim\limits_{\overline{R}\to\infty} \overline{p}_{R,\parallel} = (2/5)6^{2/3}$. In the limit $R \to 0$ it should be $L \to \infty$, and so the linear density $n_L \to 0$. Hence the parallel pressure also approaches zero $p_{\parallel} \to 0$. The radial pressure with decreasing the tube radius tends to infinity $p_R \to \infty$ due to the zero-point oscillations in the radial direction (curves *3*, *4* in Fig. 9).

CONCLUSION

The exact formulas for calculation of the thermodynamic functions of the ideal Fermi gas that fills the tube of an arbitrary radius at arbitrary temperature have been derived in the work. It is shown that all thermodynamic quantities, written in the dimensionless reduced form not containing geometric dimensions, can be expressed through some standard functions (6) of the dimensionless temperature and chemical potential and their derivatives. The thermodynamic potential, energy, density, entropy, equations of state, heat capacities and compressibilities of the Fermi gas at arbitrary temperatures in the considered quasi-one-dimensional case are calculated through the introduced standard functions. It is shown that owing to the anisotropy of the system the Fermi gas has two equations of state since the pressures along the tube and in the direction of its radius are different. Due to the same reason the system is characterized by more number of heat capacities than in the volume case.

At low temperatures the entropy and all heat capacities are linear in temperature everywhere except the specific points where the chemical potential coincides with the square of the Bessel function zero and the filling of a new discrete level begins. At these specific points the root dependence of the entropy and heat capacities on temperature appears. The dependencies of the entropy and heat capacities on the chemical potential have sharp maximums at the specific points. This differs the quasi-one-dimensional case from the the quasi-two-dimensional where the heat capacities and entropy undergo jumps at the beginning of the filling of a new discrete level. The dependencies of the pressures and compressibilities on the chemical potential at zero temperature are calculated. It is shown that the character of dependence of thermodynamic quantities on the tube radius essentially depends on whether this dependence is considered at the fixed linear or the fixed total density. At the fixed linear density the thermodynamic quantities vary monotonically with the radius, and at the fixed total density they undergo oscillations. We believe that the results of this work and work [8] devoted to the quasi-two-dimensional system can serve as a basis for further consistent study of low-dimensional systems of interacting Fermi particles.

REFERENCES

1. Ando T., Fowler A.B., Stern F. Electronic properties of two-dimensional systems // Rev. Mod. Phys. – 1982. – Vol. 54. – P. 437-672.
2. Komnik Y.F. Physics of metal films. – Moscow: Atomizdat, 1979. – 264 p. (in Russian)
3. Dragunov V.P., Neizvestnyj I.G., Gridchin V.A. Fundamentals of nanoelectronics. – Moscow: Fizmatkniga, 2006. – 496 p. (in Russian)
4. Vagner I.D. Thermodynamics of two-dimensional electrons on Landau levels // HIT J. of Science and Engineering A. – 2006. – Vol. 3. – P. 102-152.
5. Freik D.M., Kharun L.T., Dobrovolska A.M. Quantum-size effects in condensed systems. Scientific and historical aspects // Phys. and Chem. of Solid State. – 2011. – Vol. 12. – P. 9-26.
6. Shaginyan V.R., Popov K.G. Strongly correlated Fermi-systems: theory versus experiment // Nanostuctures. Mathematical physics and modeling. – 2010. – Vol. 3. – P. 5-92.
7. Landau L.D., Lifshitz E.M. Statistical physics, Vol. 5. – Oxford: Butterworth-Heinemann, 1980. – 544 p.
8. Poluektov Yu.M., Soroka A.A. Thermodynamics of the Fermi gas in a quantum well // East Eur. J. Phys. – 2016. – Vol. 3, No.4. – P. 4-21; arXiv:1608.07205 [cond-mat.stat-mech].
9. Tomonaga S., Remarks on Bloch's method of sound waves applied to many-fermion problems // Progr. Theor. Phys. – 1950. – Vol. 5. – P. 544-569.
10. Luttinger J.M. An exactly soluble model of a many-fermion system // J. Math. Phys. – 1963.– Vol. 4. – P. 1154-1162.
11. Deshpande V.V., Bockrath M., Glazman L.I., Yacoby A. Electron liquids and solids in one dimension // Nature. – 2010. – Vol. 464 (11). – P. 209-216.
12. Landau L.D., The theory of a Fermi liquid // Sov. Phys. JETP. – 1957. – Vol. 3. – P. 920-925.
13. Pines D., Nozières P. The theory of quantum liquids, Vol. I. – New York: Benjamin, 1966. – 149 p.
14. Abramowitz M., Stegun I. (Editors), Handbook of mathematical functions. – Moscow: Nauka, 1979. – 832 p.

EAST EUROPEAN JOURNAL OF PHYSICS
East Eur. J. Phys. Vol.4 No.3 (2017) 18-25 DOI:10.26565/2312-4334-2017-3-02

PACS: 13.85.Hd, 13.85.-t, 13.66.Bc, 84.35+I, 07.05.Tp.

EMPIRICAL EQUATION USING GMDH METHODOLOGY FOR THE CHARGED PARTICLES MULTIPLICITY DISTRIBUTION IN HADRONIC POSITRON-ELECTRON ANNIHILATION

E.A. El-Dahshan[1,2], S.Y. El-Bakry[1]
[1]*Department of Physics, Faculty of Sciences, Ain Shams University*
Abbassia, Postal Code: 11566, Cairo, Egypt
[2]*Egyptian E-Learning University (EELU)*
33 Elmesah Street, Eldoki, Postal Code: l1261, El-Geiza
e_eldahshan@yahoo.com, seldahshan@eelu.edu.eg, salahyaseen_elbakry@sci.asu.edu.eg
Received April 12, 2017, revised June 7, 2017, accepted August 23, 2017

Multiplicity distributions are the most general characteristics of hadronic multiparticle production processes. The multiplicity distribution of hadronic positron-electron annihilation is investigated using group method data handling (GMDH) technique up to the highest available center of mass energy ($\sqrt{s}$) (from 14 GeV to 206 GeV). We have obtained an empirical physical equation for the multiplicity distribution as a function of $\sqrt{s}$ and the charged multiplicity (n_{ch}) i. e. $P\left(n_{ch},\sqrt{s}\right)$. Based on the obtained equation, we have also calculated the energy dependence of average multiplicity ($\overline{n}$) i.e. $\overline{n}=\overline{n}\left(\sqrt{s}\right)$. Our results are compared with the available experimental and theoretical values.
KEYWORDS: hadronic positron-electron annihilation, charged-particles multiplicity distribution, empirical modeling, neural networks, group method of data handling (GMDH).

The charged particle multiplicity (the total number of charged particles produced in an event) in positron-electron annihilation into multi-hadron final states is one of the most fundamental observables in the fragmentation process during which quark-antiquark pairs are produced [1-5]. For example, the interactions among the elementary particles are represented by Feynman diagrams such as those in the following Figure [1].

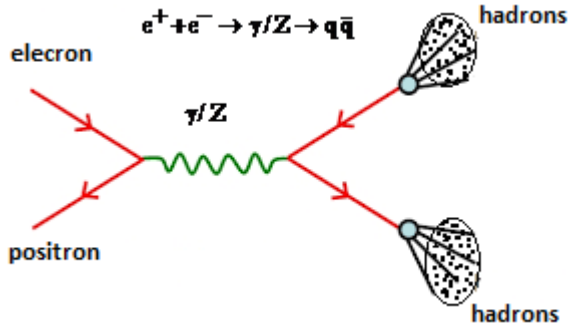

Fig. 1. Feynman diagrams for the annihilation of an electron-positron (e^+e^-) pair into a virtual γ photon or **Z** boson and its decay into a quark-antiquark ($q\bar{q}$) pair: $e^+e^- \rightarrow (Z_o/\gamma) \rightarrow q+\bar{q}$ [1] .

The e^+e^- annihilation process is well understood by the creation of a quark-antiquark pair, branching of these pairs in accordance to perturbative quantum chromo-dynamics (QCD) and finally hadronization [5]. The analysis and investigation of multiplicity production is the first step for understanding the particle production mechanism, especially in e^+e^- annihilation, it can provide additional information on hadronic final states [6-11]. Multiplicity distributions can be characterized either in terms of probability, P_n , of producing , n_{ch}, charged particles at energy ,E, i.e. $P_n(E)$, or by the moments of these distributions. The normal method of studying the charged-particle multiplicity distribution and its shape, is to calculate its moments. The common behaviors of the charged-particle multiplicity distribution are obtained using low-order moments, such as the mean, $\overline{n}$, the dispersion, D, which estimates the width of the distribution, the skewness, S, which measures how symmetric the distribution is, and the kurtosis, K, which measures how sharply peaked the distribution is [8]. The multiplicity distribution are treated experimentally (see **e**.g. [12-20]) and theoretically [21-24]. However, due to the lacking of fundamental theory, a number of phenomenological models have been proposed to characterize the charged-particle multiplicity in high energy hadron processes [1, 9], starting with early investigations by W. Heisenberg and E. Fermi [19, 20]. Furthermore, because of the shortage of the fundamental theory to describe the experimental data on multiplicity distribution, the investigation of charged particles production in

hadronic collisions is still phenomenological and based on a wide class of models and some theoretical principles. We shall study the distribution of the number of charged particles produced in positron-electron hadronic annihilation i. e. the charged multiplicity distribution and the average multiplicity (first order moment). The probability of producing a given number of charged prongs in an inelastic collision can be written as [1, 8]:

$$P = \frac{\sigma_n}{\sigma_{inel}} = \frac{\sigma_n}{\sum_n \sigma_n}, \tag{1}$$

where σ_n = the topological cross-section for n-prong events, and σ_{inel} = the total inelastic cross-section.

The average charged multiplicity , $\overline{n}$, is defined by [9-11]:

$$\overline{n} = \sum_{n=1}^{\infty} nP . \tag{2}$$

Recently, computational intelligence (CI) methodologies have become one of the most efficient techniques for the analysis of the charged particles in positron-electron annihilation (High energy physics "HEP" particle interactions) [25-31]. Generally, CI is a broad term covering a wide range of computational methodologies and approaches (such as artificial neural networks (ANNs), Genetic Programming (GP), ……) and most of them are nature-inspired algorithms. CI approaches have been used in many fields in particles and nuclear physics as in the other fields, such as studies of event selection problems with Genetic programming (J. M. Link; et.al. 2005) [25], re-discover certain laws of physics-such as Hamiltonian, Lagrangian, and other laws of geometric and momentum conservation (M. Schmidt, H. Lipson, 2009) [26], estimation of the fission barrier heights of the nuclei (A. Serkan, and T. Bayram, 2014) [27], estimations of beta-decay energies through the Nuclidic Chart (S. Akkoyun et al., 2014) [28] and searching for exotic particles in high-energy physics (P. Baldi et al.2016 and 2014) [30, 31].

In the light of this, ANNs are considered as nonlinear and highly flexible models that successfully model and analyze any nonlinear problem such as particle physics problems. Given enough data, they can approximate the underlying function for the given problem with high precision [32]. However, the main drawback of ANN approach is concentrated on the neural network architecture. In addition to that, the required time of learning causes difficulties for using ANN in real time system for modeling and regression. Group method data handling (GMDH) type Neural Networks enables restoring the unknown nonlinear regression in parametric form (as an empirical equation). The basic idea of the GMDH is the utilizing of feed-forward networks depending on short-term polynomial transfer functions whose coefficients are obtained utilizing regression combined with the self organizing activity behind neural network [33-36].

The ANN and the GMDH are inductive algorithms able to build non-linear connections between a set of input data and the output, without need for complex theory [36]. The two algorithms (GMDH and ANN) are combined to develop GMDH-Neural Network paradigm. The GMDH can be used for demonstrating and approximating any nonlinear complex system. It has been found that, the GMDH is an accurate simplified model for inaccurate or noisy data sets.

In the present work, we have used the GMDH-neural network (to obtain empirical physical equation) to model and analyze the charged distribution in hadronic positron-electron annihilation at center of mass energy, $\sqrt{s}$, i.e. $P\left(n_{ch}, \sqrt{s}\right)$, ranging from 14 to 206 GeV [12-20] as well as the energy dependence of average multiplicity, $\overline{\mathrm{n}}$. The obtained results are compared with the ones from other models [21-24]. The success of the approach used here is promising for modeling systems for which the relationships between the interaction parameters are not well understood and for which precise data is not available.

The paper is organized as follows: section **GROUP METHOD DATA HANDLING (GMDH)** gives brief introduction on the GMDH approach. Details of the polynomial model for charged particles multiplicity distribution in hadronic e^+e^- annihilation are described in section **PROPOSED MODEL FOR THE CHARGED-PARTICLES MULTIPLICITY DISTRIBUTION IN HADRONIC POSITRON-ELECTRON ANNIHILATION**. The results obtained are presented in section **RESULTS AND DISCUSSION**. Finally, the main conclusions of this study are formulated in section **CONCLUSIONS**.

GROUP METHOD DATA HANDLING (GMDH)

One of the potential issues of using ANN based approaches in any domain is the possible choice of different architectures, network types, learning paradigm, layer topologies and sizes. Trials and errors paradigm are often used to choose the type and topology of a network for a given problem, and this can give poor performance. The utilization of GMDH neural networks can guide users with these choices and diminish the requirement for a priori knowledge about the model for the problem to be solved [33-36]. The GMDH is able to extract knowledge about the system under observation directly from data sampling. GMDH was developed by A.G. Ivakhnenko in the end of 1960s for identifying non-linear relation between input and output variables. A.G. Ivakhnenko was inspired by the form of Kolmogorov-Gabor polynomials which is the discrete analogue of Volterra Function series [33-36]. The central idea behind the GMDH technique is that it tries to build a mathematical function (called polynomial model) that behaves as closely as possible to the way the predicted and the actual values of the output would. The GMDH problem consists of

constructing a polynomial function $\hat{f}$ that could simulate and model the actual one, f, in order to predict output $\hat{y}$ for a given input vector $X = (x_1, x_2, x_3, ...x_n)$; as close as possible to its actual output y. Therefore, given M observations of "multi-input single-output" pairs, the problem consists of finding y_i as follows:

$$y_i = f(x_{i1}, x_{i2}, x_{i3}, ...x_{in}) \qquad (i = 1, 2, ...M) \tag{3}$$

In the next step, GMDH-type neural network is trained in order to approximate the output values for a given input vector:

$$\hat{y} = \hat{f}(x_{i1}, x_{i2}, x_{i3}, ...x_{in}) \ (i = 1, 2, ...M) \tag{4}$$

The function $\hat{f}$ is determined so that the sum of square difference between predicted values and actual ones is minimized as follows:

$$\sum_{i=1}^{M} [\hat{f}(x_{i1}, x_{i2}, x_{i3}, ...x_{in}) - y_i]^2 \rightarrow \min \tag{5}$$

Ivakhnenko employed Kolmorovo-Gaborov sentence [33], which proves that every function $y_n = f(x)$ can be represented by an infinite Volterra-Kolmogorov-Gabor (VKG) polynomial [33-36] of the form:

$$y = f(x_{i1}, x_{i2}, x_{i3}, ..., x_{in}) = a_0 + \sum_{i=1}^{n} a_i x_i + \sum_{i=1}^{n}\sum_{j=1}^{n} a_{ij} x_i x_j + \sum_{i=1}^{n}\sum_{j=1}^{n}\sum_{k=1}^{n} a_{ijk} x_i x_j x_k + ... \tag{6}$$

where $X = (x_1, x_2, x_3, ...x_M)$ is the vector input variables and $A = (a_i, a_{ij}\, a_{ijk}, ...)$ is the vector of coefficients of weights. This mathematical form can be characterized by a system of partial quadratic polynomials (referred to as Partial descriptor "PD") consisting of only two variables (neurons: each neuron is considered as the partial model) as follows:

$$\hat{y} = G(x_i, x_j) = a_0 + a_1 x_i + a_2 x_i + a_3 x_i x_j + a_4 x_i^2 + a_5 x_j^2 \tag{7}$$

Thus, such PD is recursively utilized in the network of connected neuron to establish the general mathematical form of the inputs and outputs variables given in equation (6). The coefficients a_i in equation (7) are calculated using regression techniques during the learning process. Also, the GMDH network model is constructed during the learning process based on the experimental data. The experimental data, including inputs "independent variables" ($x_1, x_2, x_3, ...x_n$) and output (one dependent variable "y") is split into a training and testing set. During a learning process a forward multi-layer neural network is developed (see Fig. 2). The GMDH network learns in an inductive manner and builds a function (called a polynomial) model) that results in the minimum error between the predicted value and expected output. The resulting network can be represented as a polynomial of polynomial system in the form of explicit mathematical equation. This inductive approach to determining the model structure notably reduces the amount of a priori knowledge required from the user and allows selecting structure that best follows the given dataset. For further details, the authors refer to read [33-36].

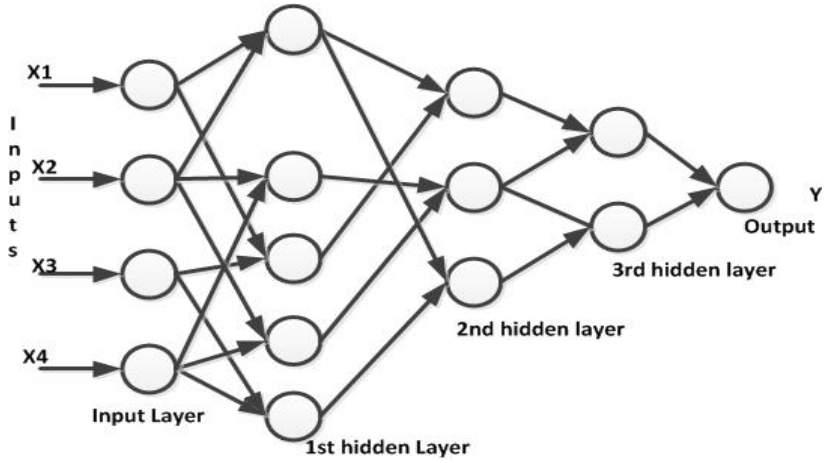

Fig. 2. General structure of GMDH polynomial neural network

PROPOSED MODEL FOR THE CHARGED-PARTICLES MULTIPLICITY DISTRIBUTION IN HADRONIC POSITRON-ELECTRON ANNIHILATION

The analysis of hadronic positron-electron annihilation founded by a mathematical models based on the traditional methods is complicate. Today, advances in information technology and data analysis approaches have forced the physicists to use the computational intelligence (CI) in modeling and analyzing physical phenomena, especially in high energy physics (HEP). Moreover, computational intelligence methodologies have become one of the most efficient

techniques for the analysis of the charged particles in positron-electron annihilation. CI, such as ANN, was first proposed by Bezdek [37] and it has gained much attention. CI is a set of "nature-inspired" computational algorithms and paradigms to model complex real-world problems for which conventional mathematical modeling can be useless. It also offers us automatic modeling techniques using the measurements of system behavior.

In the last few years, GMDH neural network has become one of the most efficient inductive learning algorithms in the family of computational intelligent techniques for computer-based mathematical modeling of non-linear complex phenomena. GMDH neural network tends to automatically generate a computer program in the form of polynomial equations when it is applied to estimate highly nonlinear complex phenomena. This approach has many privileges: it gives the user knowledge about the system and the way of verification of models constructed by human experts, as well as it saves a lot of time used for manual derivation of model equations.

GMDH models developed in the present work mainly aim to generate the mathematical functions for the prediction and analysis of multiplicity distributions, $P\left(n_{ch},\sqrt{s}\right)$, of positron-electron hadronic annihilation. According to this model, we have obtained empirical physical equation to calculate and predict the charged-particle multiplicity distribution which takes the form $P\left(n_{ch},\sqrt{s}\right)$ leading to the calculation of $\overline{n}$. Once we obtain the equation for $P\left(n_{ch},\sqrt{s}\right)$, it is easy to obtain the calculation of $\overline{n}$, since $\overline{n}$ is a function of $\sqrt{s}$.

In order to demonstrate the prediction ability and evaluate the generality of GMDH type neural networks, experimental data from several collaboration [12-20] has been used to construct the $P\left(n_{ch},\sqrt{s}\right)$ model (GMDH) (empirical physical equation). In the present study, experimental data from different Collaborations [12-20] has been used for the model development. The experimental data are divided into training (calibration) set and testing (validation) set (A 10-fold cross-validation method [32] was used to evaluate the estimation error, that is, all the experimental data are randomly divided into 10 folds. 9 of them are used to train the model and the remaining one is used to test it). When the learning stage is finished, the built model is utilized to calculate and predict the output values for data which never been seen during the training stage.

Three different classes of polynomials, namely linear, quadratic, and cubic are utilized, resulting in the proposed model. The functions used in the network are as follows:

Quadratic: 2 variables $y = q_1 + q_2x_1 + q_3x_1^2 + q_4x_2 + q_5x_2^2 + q_6x_1x_2$

Logarithm: 1 variable $y = q_1 + q_2\log(x_1 + q_3)$

Exponential: 1 variable $y = q_1 + q_2\exp(q_3(x_1 + q_4))$

Where, q_1, q_2, …, are the coefficients of the polynomial functions (estimated the GMDH model during the learning process) and x_1, x_2 are the variables. Some network parameters (free parameters) must be specified before the learning process (e.g. the maximum number of layers, polynomial type and order). In this study; the number of layers in the neural network that the model may contain is specified as 20, and the polynomial order of a variable that a polynomial may contain is specified as 16). Convergence tolerance that will stop the training algorithm from adding a new layer when it reaches the specified value and detects from adding a layer will not improve the model. The number of neurons in each layer of the network is specified as the same number of neurons in the input layer. Network layer connections method controls how neurons in the network are connected together. In this paper, only the type of connection to the previous layer is chosen (This tells DTREG [38] that the inputs to one layer may come only from outputs generated by the next lower layer).

Based on minimum error performance in validation sets the corresponding polynomial representation of the present GMDH model for $P\left(n_{ch},\sqrt{s}\right)$ is obtained (empirically) as:

$$P = P(n_{ch},\sqrt{s}) = a_1 + b_1\, e^{\left(c_1(d_1+g_1(h-I\frac{n_{ch}}{\sqrt{s}})N_1)+k_1\right)}, \tag{8}$$

where,

$$N_1 = a_2 + b_2\, e^{\left(c_2(d_2+g_2(h-I\frac{n_{ch}}{\sqrt{s}})N_2)+k_2\right)}$$

$$N_2 = a_3 + b_3\, e^{\left(c_3(d_3+g_3(h-I\frac{n_{ch}}{\sqrt{s}})N_3)+k_3\right)}$$

$$N_3 = -0.042996 + 0.286515\, e^{\left(\frac{-((N_4)-0.267503)^2}{0.040062}\right)}$$

$$N_4 = -0.116698 + 4.027115N_5 - 32.31281N_5^2 + 1.599191N_6 + 4.039759N_6^2 - 16.22014N_5N_6$$

$$N_5 = -0.193252 - 0.027337\log(\sqrt{s} + 37.73184)$$

$$N_6 = -0.008245 + 11.02105 N_7 N_8$$

$$N_7 = 0.168889 + 2.940838 N_{10} - 88.85973 N_{10}^2 + 6.973632 N_{11} + 22.60074 N_{11}^2 + 102.1841 N_{10} N_{11}$$

$$N_8 = a_4 + b_4 + (h - I\frac{n_{ch}}{\sqrt{s}}) - c4(h - I\frac{n_{ch}}{\sqrt{s}})^2 d_4 N_9 + g_4 N_9^2 + k_4(h - I\frac{n_{ch}}{\sqrt{s}})N_9$$

$$N_9 = a_5 + b_5 + n_{ch} c_5 n_{ch}^2 + d_5(h - I\frac{n_{ch}}{\sqrt{s}}) - g_4(h - I\frac{n_{ch}}{\sqrt{s}})^2 + k_5 n_{ch}(h - I\frac{n_{ch}}{\sqrt{s}})$$

$$N_{10} = -0.072627 - 0.002561\frac{\sqrt{s}}{n_{ch}^2}$$

$$N_{11} = 0.06004 + 0.002546 n_{ch} - 0.000082 n_{ch}^2$$

a_1 = -1.296707, b_1= 1.298148, c_1 = 0.722543, d_1 = -0.000534, g_1 = 16.88877, h = 0.061227, I = 0.004658,
k_1= 0.097891, a_2= -1.273491, b_2= 1.274938, c_2= 0.735137, d_2 = -0.000559, g_2= 16.89868, k_2= 0.098519,
a_3= -1.358375, b_3= 1.359726, c_3= 0.692116, d_3 = 0.00059, g_3= 16.90984, k_3 = 0.099141,
a_4= -19.93856, b_4= 684.3732, c_4= -5870.185, d_4= 17.87208, g_4= 7.419097, k_4= 308.3482,
a_5= -10.78599, b_5= 0.244696, c_5= -0.000064, d_5= 453.8323, g_5=4544.448, k_5= 4.099441.

The center-of-mass energy dependence of the average charged-particle multiplicity, $\overline{n}$, according to our model GMDH is obtained as:

$$\overline{n} = Ae^{-13} + (B + C\{D + G\log(\sqrt{s} + H)\}) - k\{D + G\log(\sqrt{s} + H)\}^2, \quad (9)$$

where
A = -1.921449, B = - 0.17183, C = 1.019804, D = - 24.50703, G = 9.628115, H = 9.628115, K = 0.000532.

The criteria of root mean square error (MSE) and coefficient of determination (R^2) are used for evaluating the performance of the GMDH models.

RESULTS AND DISCUSSION

Hadron production in positron-electron annihilation is created from the yield of quark-antiquark pairs which can generate gluons, the exchange particle of the field theory of the strong interactions and QCD. The produced gluon depends on the center of mass energy. Based on the GMDH, the general form empirical equation can be represented by a system of particle description using some type of order polynomial such as, linear, equations, quadratic equations and cubic equations (see equations (8) and (9)).

We investigate the general features of hadronic decays in $e^+e^- \to (Z_o/\gamma) \to q + \overline{q}$ reactions at the highest available centre-of-mass energies. We analyzed the multiplicity distribution of hadronic decays in $e^+e^- \to (Z_o/\gamma) \to q + \overline{q}$ reactions up to the highest available centre-of-mass energies $\sqrt{s} = 206\,GeV$. Due to the physical phenomena correlated with the non-linear characteristics of multiplicity distribution of the e^+e^- hadronic collision, it may be tricky to establish explicit mathematical equation for multiplicity distribution. By adequate operations of mathematical analysis, deduction of highly nonlinear physical equations for multiplicity distribution is of utmost interest.

In this paper, by using group method of data handling (GMDH), we have constructed mathematical functional form for the charged particle multiplicity distribution of e^+e^- hadronic annihilation

The GMDH model is developed by running DTREG software [38]. The simulation results are conducted on a pentium4, with 1.4 GHZ, 2G RAM and Windows XP. With these configurations, the predictive results are obtained in few seconds. A 10-fold cross-validation is used to create and test the model [32].

The proposed GMDH model is tested after training. As shown in Fig. 3, the GMDH technique was able to perfectly model and simulate the charged particles multiplicity distribution, $P(n_{ch}, \sqrt{s})$ as well as the center-of-mass energy dependence of the average multiplicity distribution, $\overline{n} = \overline{n}(\sqrt{s})$ of the e^+e^- interactions at high energies. This gives the GMDH the proven ability of wide usage in the modeling of high energy physics.

Figure 3 demonstrates the calculated charged multiplicity distribution at $\sqrt{s} = 14, 29, 34.8, 43.6, ..., 206\ GeV$ which have been compared with the corresponding experimental and theoretical ones [21-24]. The comparison between the charged particle multiplicity distribution calculated by the generalized multiplicity distribution (GMD) model for e^+e^- collisions at $\sqrt{s}$ =14, and 206 GeV is shown in Fig. 3. This Figure shows that the proposed model gives a good agreement with the experimental [12-20] and theoretical [21-24] data especially at 183 and 206 GeV.

Fig. 4 demonstrates the comparison between the multiplicity distributions for different $\sqrt{s}$. From this figure, we

notice that the maximum probability of production "n_{ch}" charged particles decreases with the increase of $\sqrt{s}$ as well as shifts towards the increase of "n_{ch}". Further, we notice that the width of the distribution is broadened with the increase of $\sqrt{s}$.

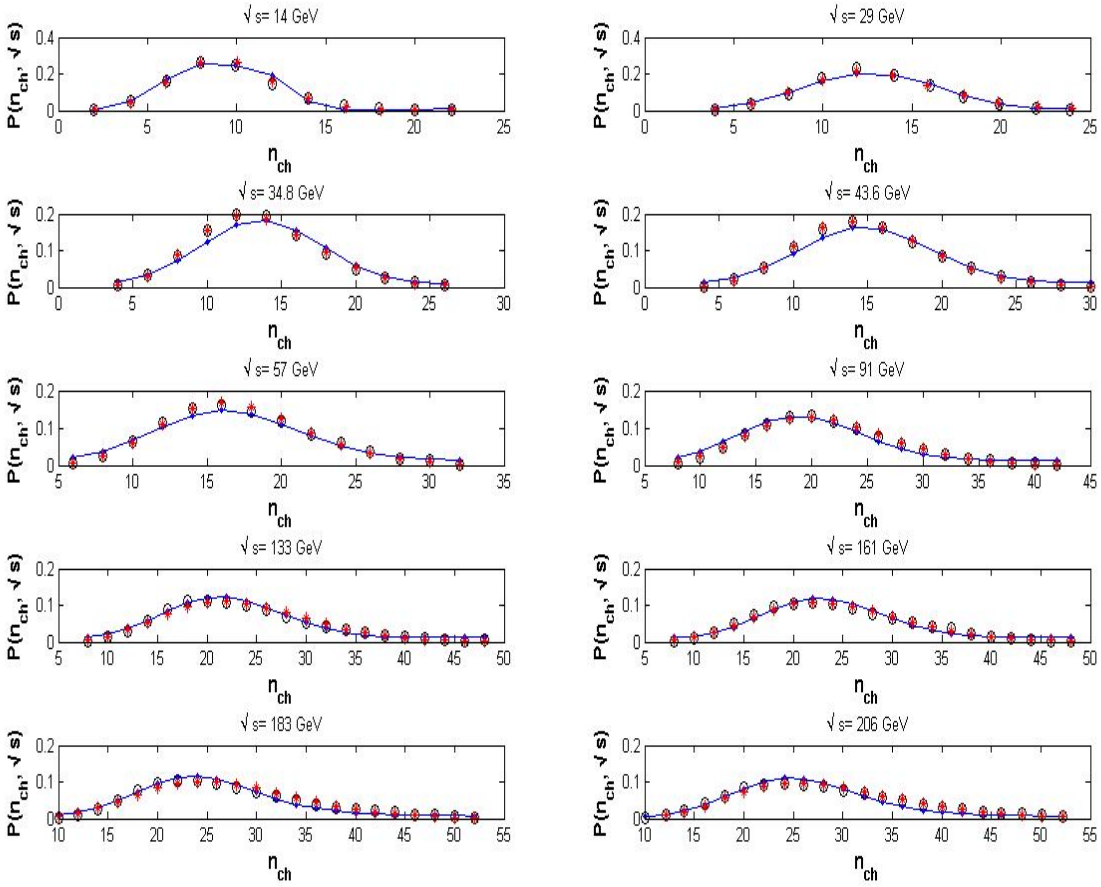

Fig. 3. Demonstrates the calculated charged multiplicity distribution $P\left(n_{ch},\sqrt{s}\right)$ at $\sqrt{s}=14,29,34.8,43.6,....,206\ GeV$ those have been compared with experimental [12-20] and theoretical ones "GMD Model" [21-24]. (-) GMDH model, experimental data (o) and (*) theoretical ones.

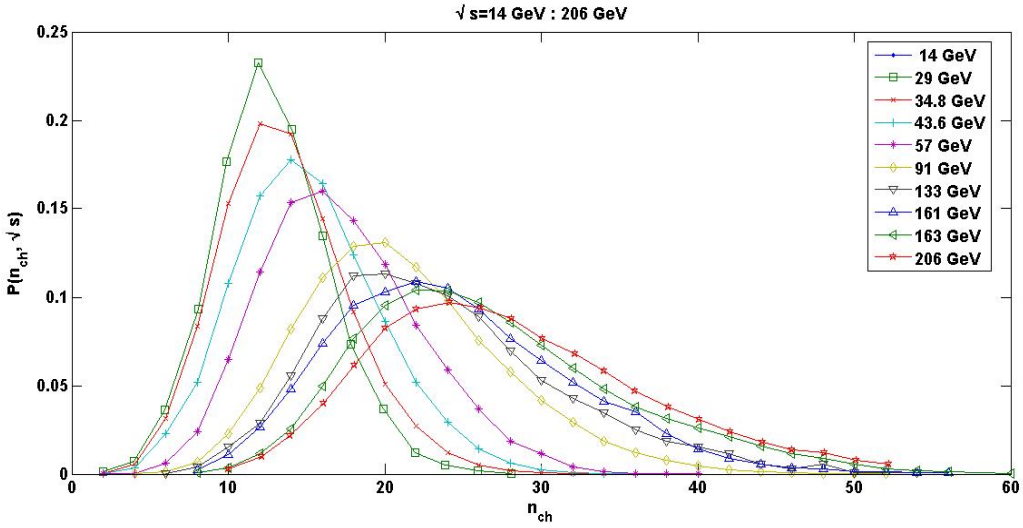

Fig. 4. The calculated charged multiplicity distribution $P\left(n_{ch},\sqrt{s}\right)$ at $\sqrt{s}=14,29,34.8,43.6,....,206\ GeV$.

Based on the obtained equations (eqs. (8) and (9)), the values of energy dependence of the average charged multiplicity in $e^{+}e^{-}$ collision for $\sqrt{s}$ ranging from 14 to 206 GeV are calculated and compared with corresponding experimental and theoretical results as shown in Fig. 5. Also, From Fig.5 we notice that, $\overline{n}$, increase with the increase

of $\sqrt{s}$ which shows the same trend as the experiment.

The average multiplicity of charged particles at a hadronic energy at the highest centre of mass energies in e^+e^- interactions, up to 206 GeV has been calculated to be $\bar{n}$. When compared to other models, the value calculated is consistent with the evolution predicted by GMD method [21-24]. When $\sqrt{s}$ =206 GeV $\bar{n}$ =27.5, and so on for the lower energies. The results prove that the proposed GMDH model has impressively learned well the nonlinear behavior of the charged multiplicity distribution and the average charged multiplicity in e^+e^- collision.

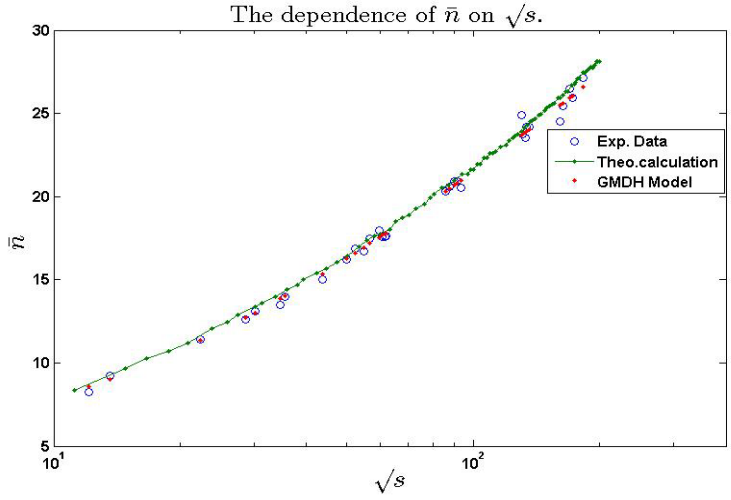

Fig. 5. The comparison between the experimental and theoretical values of the energy dependence of the average charged multiplicity in e^+e^- annihilation: (o) experimental data, (♦) GMDH model, and (-♦-) theoretical ones [21-24].

CONCLUSIONS

We have obtained an empirical physical equation for the description of the charged particles multiplicity distribution in hadronic positron-electron annihilation based on GMDH approach. We have used the obtained equation to calculate and predict $P\left(n_{ch},\sqrt{s}\right)$ through the energy range 14 GeV to 206 GeV. The average multiplicity, $\bar{n}$, is calculated using our empirical physical equation. The comparison between our results and the experimental and theoretical ones explores a good agreement. Based on our GMDH model, we present an empirical equation corresponding to physical phenomenon in a mathematical form, we are still faced with the challenge of justifying and giving words to their meaning. These models define input-output relations based on experimental data and use mathematical and statistical concepts to link input to model the output. Our results are in a good agreement with the experimental and theoretical ones. These results confirm the reliability of our models. Scientists may use such approaches to focus on interesting phenomena more rapidly and to interpret their meaning. This represents one of the key challenges for computational Intelligence techniques in high energy physics modeling.

ACKNOWLEDGEMENTS

The authors are very grateful to the Editor-in-Chief and the anonymous referees for their helpful comments and for the kind suggestions that improved the manuscript seriously.

REFERENCES

1. Zheng H.W., Perez P., Auchincloss P., Blanis D., Bodek A., Budd H., Kim Y.K. Charged-particle multiplicities in e+e− annihilations at $\sqrt{S}$ = 50− 61.4 GeV // Phys. Rev. D. – 1990. – Vol. 42. – P. 737.
2. Ghaffary T. Charged Particles Multiplicity and Scaling Violation of Fragmentation Functions in Electron-Positron Annihilation // Advances in High Energy Physics. – 2016. – Vol. 2016. – Article ID 4506809. – P.8; doi:10.1155/2016/4506809.
3. Bzdak A. Universality of multiplicity distribution in proton-proton and electron-positron collisions. – 2015 // e-Print: arXiv:1507.01608 [hep-ph].
4. Biebel O. Experimental tests of the strong interaction and its energy dependence in electron–positron annihilation // Phys. Rev. – 2001. – Vol. 340. – P.165-289.
5. Derrick M., Gan K.K., Kooijman P., Loos J.S., Musgrave B., Price L.E., Wood D.E. Study of quark fragmentation in e+e− annihilation at $\sqrt{S}$ =29 GeV: Charged-particle multiplicity and single-particle rapidity distributions // Phys. Rev. D. – 1986. – Vol. 34. – P.3304-3320.
6. Wyatt T. High-energy colliders and the rise of the standard model // Nature. – 2007. – Vol.448. – P. 274-280.
7. Ackerstaff K., Alexander G., Allison J., Altekamp N., Ametewee K., Anderson K.J., Azuelos G. QCD studies with e+ e- annihilation data at $\sqrt{S}$ =161 GeV // Z. Phys. C Part. Fields. – 1997. – Vol. 75. – P.193-207.

8. Beggio P.C., Luna E.G.S. Cross sections, multiplicity and moment distributions at the LHC // Nucl. Phys. A,. – 2014. – Vol. 929. – P. 230-245.
9. Acton P.D., Alexander G., Allison J., Allport P.P., Anderson K.J., Arcelli S., Bahan G.A. A study of charged particle multiplicities in hadronic decays of the Z0 // Z. Phys. C Part. Fields. – 1992. – Vol. 53. – P. 539-554.
10. Abreu P., Adam W., Adami F., Adye T., Alexeev G.D., Allen P., Anassontzis E. Charged particle multiplicity distributions in Z0 hadronic decays // Z. Phys. C Part. Fields. – 1991. – Vol. 50. – P.185-194.
11. Dremin I.M. QCD and models on multiplicities in e+e− and interactions // Phys Atom Nucl+. – 2005. – Vol. 68. – P. 758-770.
12. ALEPH Collaboration, DELPHI collaboration, L3 Collaboration, OPAL Collaboration, & LEP Electroweak Working Group. Electroweak measurements in electron–positron collisions at W-boson-pair energies at LEP // Phys. Rept. – 2013. – Vol. 532. – P. 119-244.
13. Braunschweig W., Gerhards R., Kirschfink F.J., Martyn H.U., Fischer H.M., Hartmann H., Foster B. Charged multiplicity distributions and correlations in e+e− annihilation at PETRA energies // Z. Phys. C Part. Fields. C45. – 1989. – Vol. 45. - P. 193-208.
14. Achard P., Adriani O., Aguilar-Benitez M., Alcaraz J., Alemanni G., Allaby J., Anselmo F. Studies of hadronic event structure in e+e- annihilation from 30 to 209GeV with the L3 detector // Phys. Rept. – 2004. – Vol. 399. – P. 71-174.
15. Alexander G., Allison J., Altekamp N., Ametewee K., Anderson K.J., Anderson S., Ball A.H. QCD studies with e+e− annihilation data at 130 and 136 GeV // Z. Phys. C Part. Fields. – 1996. – Vol. 72. – P. 191-206.
16. Radchenko N.V. About agreement of PYTHIA and the experimental results in e+e- annihilation to hadrons. – 2007. e-print: arXiv:0706.3453 [hep-ph].
17. Abbiendi G. QCD studies with annihilation data at $\sqrt{S}$ = 172-189 GeV // The Eur. Phys. J. C. – 2000. – Vol. 16. – P. 185-210.
18. Abreu P., Adam W., Adye T., Agasi E., Ajinenko I., Aleksan R., Amaldi U. Charged particle multiplicity in e+e− interactions at $\sqrt{S}$ = 130 GeV // Phys. Lett. B. – 1996. – Vol. 372. – P.172-180.
19. Heisenberg W. Production of meson showers // Nature. – 1949. – Vol. 164. - No. 4158. – P. 65-65.
20. Fermi E. High energy nuclear events // Prog. Theor. Phys. – 1950. – Vol. 5. – P. 570-583.
21. Dewanto A., Chan A.H., Oh C.H., Chen R., Sitaram K. Lee-Yang circle analysis of e+e− and generalized multiplicity distribution // Eur. Phys. J. C. – 2008. – Vol. 57. – P. 515-523.
22. Chew C.K., Kiang D., Zhou H. A generalized non-scaling multiplicity distribution // Phys Lett. B. – 1987. – Vol. 186. – P. 411-415.
23. Chan A.H., Chew C.K. e+e− multiplicity distribution from branching process // Z. Phys. C Part. Fields. – 1992. – Vol. 55. – P. 503-508.
24. Zborovský I. Multiplicity distributions in proton-(anti) proton and electron-positron collisions with parton recombination. – 2011. e-print arXiv:1106.4697 [hep-ph].
25. Link J.M., Yager P.M., Anjos J.C., Bediaga I., Castromonte C., Göbel C., Pepe I.M. Application of genetic programming to high energy physics event selection // Nucl. Instr. Meth. Phys. Res. A. – 2005. – Vol. 55. – P. 504-527.
26. Schmidt M., Lipson H. Distilling free-form natural laws from experimental data // Science. – 2009. – Vol. 324. – P. 81-85.
27. Akkoyun S., Bayram T. Estimations of fission barrier heights for Ra, Ac, Rf and Db nuclei by neural networks // Int. J. Mod. Phys. E. – 2014. – Vol. 23. – P. 1450064.
28. Akkoyun S., Bayram T., Turker T. Estimations of beta-decay energies through the nuclidic chart by using neural network // Radiat. Phys. Chem. – 2014. – Vol. 96. – P. 186-189.
29. Bhat P., Lonnblad L., Meier K., Sugano K. Using neural networks to identify jets in hadron-hadron collisions. / Research directions for the decade: Proceedings of the 1990 summer study on high energy physics. – 1992.
30. Baldi Pierre, Cranmer K., Faucett T., Sadowski P., Whiteson D. Parameterized neural networks for high-energy physics // Eur. Phys. J. C. – 2016. – Vol. 76:235.
31. Alves A. Stacking machine learning classifiers to identify Higgs bosons at the LHC. (2016). e-print arXiv:1612.07725 [hep-ph].
32. Haykin S.S. Neural networks and learning machines (Vol. 3). – 2009. Uppr Saddle River, NJ, USA. Pearson.
33. Ivakhnenko A.G. Polynomial theory of complex systems // IEEE Trans. on Systems, Man and Cybernetics SMC. – 1971. – Vol. 1. – P. 364-378.
34. Madala H.R., Ivakhnenko A.G. Inductive learning algorithms for complex systems modeling // Boca Raton. – 1994. – 368p. – CrC Press.
35. Mueller J.A., Ivachnenko A.G., Lemke F. GMDH algorithms for complex systems modeling // Math. Comput. Model. Dyn. Syst. – 1998. – Vol. 4. – P. 275-316.
36. Farlow S.J. Self-organizing methods in modeling: GMDH type algorithms. – 1984. – Vol. 54. – CrC Press.
37. Bezdek J.C. On the relationship between neural networks, pattern recognition and intelligence // Int J Approx Reason. – 1992. – Vol. 6. – P. 85-107.
38. Sherrod P.H. DTREG Predictive Modeling Software. – 2008. – Manual for software available online: www.dtreg.com.

EAST EUROPEAN JOURNAL OF PHYSICS
East Eur. J. Phys. Vol.4 No.3 (2017) 26-30 DOI:10.26565/2312-4334-2017-3-03

PACS: 52.25.Os, 52.20.Dq, 52.55.Fa

SPECTRA ANALYSIS OF RUNAWAY ELECTRON SYNCHROTRON RADIATION FOR THE RECENT EAST RUNAWAY EXPERIMENT

I.M. Pankratov[1,2], V.Y. Bochko[2]

[1]*Institute of Plasma Physics, NSC "Kharkiv Institute of Physics and Technology"*
Academicheskaya Str.1, 61108 Kharkiv, Ukraine
[2]*Department of Physics and Technology, V.N. Karazin Kharkiv National University*
Svobody Sq.4, 61022 Kharkiv, Ukraine
E-mail: pankratov@kipt.kharkov.ua

Received June 26, 2017

The energy of disruption generated runaway electrons can reach as high as tens of megaelectronvolt and they can cause a serious damage of plasma-facing-component surfaces in large tokamaks like International Thermonuclear Experimental Reactor (ITER). The synchrotron radiation diagnostic allows a direct observation of such runaway electrons and an analysis of their parameters and promotes the safety operation of present day large tokamaks and future ITER. Only this diagnostic will be applied in ITER. In the paper detail analysis of the synchrotron radiation spectra of runaway electrons for the recent Experimental Advanced Superconducting Tokamak (EAST, Institute of Plasma Physics of Chinese Academy of Sciences) experiment parameters has been presented. The calculations are carried out on the base of precise expression for synchrotron radiation spectral density. They make more precise spectra analysis of the previous paper by Zhou R.J., Pankratov I.M., Hu L.Q., et al. (Physics of Plasmas, 2014, Vol. 21, No. 6, 063302). Obtained results are important for correct interpretation of runaway EAST experiments and runaway experiments in other tokamaks.

KEYWORDS: synchrotron radiation, diagnostic runaway electrons, tokamak safety operation, EAST tokamak

АНАЛИЗ СПЕКТРОВ СИНХРОТРОННОГО ИЗЛУЧЕНИЯ УБЕГАЮЩИХ ЭЛЕКТРОНОВ ДЛЯ НЕДАВНЕГО ЭКСПЕРИМЕНТА НА ТОКАМАКЕ EAST

И.М. Панкратов[1,2], В.Ю. Бочко[2]

[1]*Институт физики плазмы, ННЦ "Харьковский физико- технический институт"*
ул. Академическая 1, 61108 Харьков, Украина
[2]*Физико- технический факультет, Харьковский национальный университет имени В.Н. Каразина*
пл. Свободы 4, 61022 Харьков, Украина

Энергия убегающих электронов, образующихся при срывах разряда, может достигать десятков мегаэлектронвольт, что приводит к серьезным повреждениям элементов поверхности первой стенки в больших токамаках, это - потенциальная угроза для Международного термоядерного экспериментального реактора (ИТЭР). Диагностика, основанная на синхротронном излучении убегающих электронов, позволяет как непосредственное их наблюдение, так и анализ параметров этих электронов, что способствует безопасной работе существующих больших токамаков и будущего токамака-реактора ИТЭР. Именно эта диагностика будет использована в ИТЭРе. Предоставлен детальный анализ спектров синхротронного излучения убегающих электронов для параметров недавнего эксперимента на токамаке EAST (Институт физики плазмы Академии наук Китая). Расчеты проведены на основе точного выражения для спектральной плотности синхротронного излучения. Они уточняют анализ спектров статьи Zhou R.J., Pankratov I.M., Hu L.Q., et al. (Physics of Plasmas, 2014, Vol. 21, No. 6, 063302). Полученные результаты важны для правильной интерпретации эксперимента на EAST и экспериментов с убегающими электронами на других токамаках.

КЛЮЧЕВЫЕ СЛОВА: синхротронное излучение, диагностика убегающих электронов, безопасность работы токамака, токамак EAST

АНАЛІЗ СПЕКТРІВ СИНХРОТРОННОГО ВИПРОМІНЮВАННЯ ЕЛЕКТРОНІВ – ВТІКАЧІВ ДЛЯ НЕЩОДАВНЬОГО ЕКСПЕРИМЕТУ НА ТОКАМАЦІ EAST

І.М. Панкратов[1,2], В. Ю. Бочко[2]

[1]*Інститут фізики плазми, ННЦ "Харківський фізико-технічний інститут"*
вул. Академічна 1, 61108 Харків, Україна
[2]*Фізико- технічний факультет, Харківський національний університет імені В.Н. Каразіна*
м. Свободи 4, 61022 Харків, Україна

Енергія електронів-втікачів, які утворюються під час зривів розряду, може досягати десятків мегаелектронвольт, що призводить до серйозних пошкоджень елементів поверхні першої стінки у великих токамаках, це є потенційною загрозою для Міжнародного термоядерного експериментального реактора (ІТЕР). Діагностика, що базується на синхротронному випромінюванні електронів - втікачів, дозволяє як безпосереднє їх спостереження, так і аналіз параметрів цих електронів, що сприяє безпечній роботі сучасних токамаків та майбутнього токамаку-реактора ІТЕР. Саме ця діагностика буде використана в ІТЕРі. Представлено детальний аналіз спектрів синхротронного випромінювання електронів-втікачів для параметрів нещодавнього експерименту на токамаці EAST (Інститут фізики плазми Академії наук Китаю). Розрахунки проведені на основі точного виразу для спектральної густини потужності синхротронного випромінювання. Вони уточнюють аналіз спектрів статті Zhou R.J., Pankratov I.M., Hu L.Q., et al. (Physics of Plasmas, 2014, Vol. 21, No. 6, 063302). Отримані результати важливі для правильної інтерпретації експерименту на EAST та експериментів з електронами-втікачами на інших токамаках.

КЛЮЧОВІ СЛОВА: синхротронне випромінювання, діагностика електронів – втікачів, безпека роботи токамака, токамак EAST

Runaway electrons can be a potential threat to the safe operation of large tokamaks, especially ITER. The strong electric fields induced during the tokamak disruption can generate a lot of runaways. The energy of these electrons can reach as high as tens of MeV and they can cause a serious damage of plasma-facing-component (PFC) surfaces in large tokamaks like ITER [1]. Therefore an effective monitoring of the runaway electrons is an important task.

The synchrotron radiation is a powerful tool for direct observation and investigation of runaway electrons in large tokamaks [2]. For the first time, this diagnostic was used in the TEXTOR tokamak [3]. The established methods of runaway electron monitoring (HXR, photoneutron emission) will be difficult to apply in large machines like ITER because of the high gamma and neutron background and the very thick wall (vessel shielding). Only the diagnostic based on the runaway electron synchrotron radiation measurements will be possible in ITER [4]. The theoretical bases of the analysis of synchrotron radiation spectra of runaway electrons in the curved magnetic field with the finite value of the transverse velocity were considered in [5].

The experiments on investigations of runaway electrons are carrying out in JET (Joint European Torus), JT-60U (Japan), DIII-D (USA), Tore Supra (France), KSTAR (Republic of Korea), etc. (see for example [6-9]). Recently the investigation of runaway electron generation was started in the EAST tokamak (China) [10-11] and the synchrotron radiation diagnostic detecting the runaway electrons is used there. The aim of these experiments is to find tokamak operation scenarios that will reduce runaway current as much as possible (or fully suppress) to avoid damage of PFC.

This paper is a continuation of paper [12], where spectrum analysis was done only for expected runaway electron parameters in EAST. They are differing from parameters obtained in recent runaway EAST experiment [10]. The aim of this work is to provide more detail analysis of synchrotron radiation spectra for this recent runaway EAST experiment (shot #28957).

MONITORING OF RUNAWAY ELECTRONS

In Ref. [5], the theoretical analysis of the synchrotron radiation spectra of runaway electrons was carried out. The features of the relativistic electron motion in a tokamak (the motion along the tokamak helical magnetic field, the cyclotron gyration motion around the guiding center with a frequency $\omega_B = eB/mc\Gamma$ and the vertical centrifugal drift of guiding center motion with velocity $v_{dr} = v_\parallel^2 / R\omega_B$) were taken into account. The local nature of electron orbits was involved: only a small part of the electron trajectory in a tokamak is effective to produce the radiation observed in the detector. Recall that highly relativistic particles emit radiation in the direction of their velocity vector. Here B is the local value of confinement magnetic field, $\Gamma >>1$ is the relativistic factor, R is the major radius of runaway electron position, $v_\parallel, v_\perp$ are the longitudinal and transversal components of velocity with respect to the confinement magnetic field, $v_\parallel >> v_\perp$, e and m are the charge and rest mass of electron, c is the light velocity. In case of the EAST tokamak, the confinement magnetic field was taken in the form

$$\mathbf{B}(r,\theta) = [-B_0 \mathbf{e}_\varsigma + B_\theta(r)\mathbf{e}_\theta]/R, \tag{1}$$

where B_0/R and $B_\theta(r)$/R are the toroidal and poloidal magnetic field components, respectively, $R = 1 - (r/R_0)cos\theta$, r and R_0 are the magnetic surface minor and major radii, respectively, θ is the poloidal angle.

In Ref. [5] the expression for instantaneous spectral density of the emitted power was derived (λ is the wavelength):

$$P_{full}(\lambda) = i\frac{2\pi ce^2}{\lambda^3\Gamma^2}\left\{\int_C \frac{du}{u}\left(1-2u^2\right) I_0\left(au^3\right)\exp\left[-\frac{3}{2}\xi\left(u-\frac{u^3}{3}\right)\right] - \right.$$
$$\left. -\frac{4\eta}{1+\eta^2}\int_C du\cdot u I_1\left(au^3\right)\exp\left[-\frac{3}{2}\xi\left(u-\frac{u^3}{3}\right)\right]\right\}, \tag{2}$$

where

$$a = \frac{\xi\eta}{1+\eta^2}, \quad \xi = \frac{4\pi R}{3\lambda\Gamma^3\sqrt{1+\eta^2}}. \tag{3}$$

The integration path is taken along the line of steepest descent from a saddle point [13], $I_{0,1}(z)$ is the modified Bessel function. A key parameter of the radiation analysis is

$$\eta = \frac{v_\perp}{v_{dr}} \approx \frac{eBR\theta_p}{m_e c^2\Gamma}, \tag{4}$$

where the pitch angle θ_p is defined as:

$$\theta_p = v_\perp / v_{||}\,. \tag{5}$$

Correct estimation of the ratio $\theta_p = v_\perp / v_{||}$ during the experiment is an important part of spectra analysis. Uncertainties during measurement of the ratio $v_\perp / v_{||}$ may cause large errors during spectra analysis.

The single-electron spectral density of the synchrotron radiation $P(\lambda, \alpha)$ depends on cyclotron gyration phase α ($\dot{\alpha} \approx -\omega_B$) and oscillates strongly with α. In tokamaks the radiation of many runaway electrons is observed in the detector simultaneously. In this case, it is possible to introduce an averaged spectral density of the emitted power:

$$P(\lambda) = \frac{1}{2\pi} \int_0^{2\pi} d\alpha P(\lambda, \alpha). \tag{6}$$

There is a difference between Eq. (2) and Schwinger's result [14]:

$$P_{Sch}(\lambda) = \frac{4\pi c e^2}{\sqrt{3}\lambda^3 \Gamma^3} \int_w^{\infty} K_{5/3}(x) dx, \tag{7}$$

where

$$w = 4\pi R_{curv} / 3\lambda\Gamma^3. \tag{8}$$

Here R_{curv} is the instantaneous curvature radius. Equation (7) describes the emission of a single electron, meanwhile Eq. (2) describes the radiation of many runaway electrons whose distribution function is independent on the phase of cyclotron gyration α i.e., distribution function has the form $f(p_{||}, p_\perp, t)$.

The asymptotic approximation of integral (2) simplifies the spectra analysis. Integral (2) can be easily integrated by saddle point method (see, e.g. [13]) when $\xi >> 1$,

$$\xi = \left(4\pi/3\right)\left(R/\lambda\Gamma^3\right)\left(1/\left(1+\eta^2\right)^{1/2}\right) >> 1. \tag{9}$$

Two limit cases are possible (see [5]). In the first case (the saddle point is $u_0 = (1, 0)$)

$$P_{as1}(\lambda) \approx \pi c e^2 \sqrt{\frac{2\sqrt{1+\eta^2}}{\lambda^5 R\Gamma}} \left[I_0(a) + \frac{4\eta}{1+\eta^2} I_1(a) \right] \exp\left(-\frac{4\pi}{3} \frac{R}{\lambda\Gamma^3} \frac{1}{\sqrt{1+\eta^2}} \right) \tag{10}$$

when

$$a = \left(4\pi/3\right)\left(R/\lambda\Gamma^3\right)\left(\eta/\left(1+\eta^2\right)^{3/2}\right) \lesssim 1. \tag{11}$$

The asymptotic expression (10) for $P_{as1}(\lambda)$ is valid for $\eta >> 2$ or $\eta << 0.5$ as it follows from the inequalities (9) and (11).

In the second case (the saddle point is $u_0 = (\sqrt{1+\eta^2} / (1+\eta), 0)$)

$$P_{as2}(\lambda) \approx \frac{\sqrt{3}}{2} \frac{c e^2 \Gamma (1+\eta)^2}{\lambda^2 R\sqrt{\eta}} \exp\left(-\frac{4\pi}{3} \frac{R}{\lambda\Gamma^3} \frac{1}{1+\eta} \right) \tag{12}$$

when

$$a u_0^3 = \left(4\pi/3\right)\left(R/\lambda\Gamma^3\right)\left(\eta/\left(1+\eta\right)^3\right) > 1. \tag{13}$$

Expressions (10) and (12) have a maximum values at λ_m [5]. The asymptotic expressions Eq. (10) and Eq. (12) describe correctly the features of the spectrum in the range $\lambda < \lambda_m$ only, where the value of ξ is large, $\xi >> 1$.

When η is the order of several units ($\eta \sim (1 - 2)$), equation (12) has to be used. The analysis of experimental conditions (runaway shot #28957) shows that it is just a case of the EAST tokamak. Note that an application of Eq. (10) is discussed only in the review paper [2].

In Eqs. (2-4) and Eqs. (9-13) the value of major radius R corresponds to the runaway electron positions. Note that for simplicity of analysis in Ref. [5] and Ref. [11] the value of R_0 was used in the same expressions. The spectrum is shifted toward shorter wavelengths with increasing of parameter η. Recall that the experimental measurement of the spectrum in the region $\lambda < \lambda_m$, where $P(\lambda)$ decreases exponentially fast, is very important because it allows estimating the maximum energy of runaways in the discharge.

The integral (2) can be taken numerically without additional simplifications. It has been taken numerically along the contour C (a hyperbola x^2-$y^2/3$=1 passing through the saddle point (x=1, y=0), where x and y are real and imaginary

parts of the complex number respectively) in the complex plane to calculate accurately the spectrum near the maximum position. This integration path provides the most rapid convergence of the integral.

RUNAWAY INVESTIGATION IN EAST

The EAST tokamak is a non-circular advanced steady state experimental device. The EAST first plasma discharge was successfully achieved in 2006. The scientific mission of the EAST project is to study the physical issues involved in steady state advanced tokamak devices. The engineering mission of the EAST project is to establish the technology basis of fully superconducting tokamaks in support of future reactors.

The investigated runaway discharge was an ohmic discharge #28957 [10, 11] and was performed in the limiter configuration, with toroidal magnetic field B_0 = 2 T, plasma current I_p = 250 kA, central line-averaged density $<n_e>$ = 2.2 × 10^{19} m^{-3}, plasma major radius R_0 = 1.86 m and minor radius a = 0.45 m. At the plasma center, electron temperature $T_e \approx 0.55$ keV was obtained from a soft x-ray pulse height analysis (PHA) system during the plasma current flat-top phase. Runaway electrons were created during the start-up phase of the discharge by the ohmic coil. Runaway electrons were located around the q = 2 rational magnetic surface (ring-like runaway electron beam), where q is the safety factor. A visible CMOS camera of the EAST tokamak operates in the narrow (0.38 – 0.75) μm wavelength range. The camera was located in the equatorial plane looking tangentially into the direction of runaway electron approach.

In Ref. [11] on the base of synchrotron radiation spectra and synchrotron radiation spot shape joint analysis the values of runaway electron parameters were obtained. It was deduced that the energy E of runaways was E=30 MeV and pitch angle θ_p was θ_p =0.16 (Fig.9-11 in Ref. [11]). But in Ref. [11] for this runaway shot #28957 the analysis of runaway electron parameters was carried out on the basis of the asymptote Eq. (12) only.

ANALYSIS OF SYNCHROTRON RADIATION SPECTRA FOR THE EAST SHOT #28957

The presented calculation of the synchrotron radiation spectra was based on precise expression for spectral density Eq. (2) for parameters of runaway electrons obtained in the recent EAST experiment (shot #28957, [11]). The numerical integration of P_{full} was carried out by the method of the steepest descent [13]. For these parameters, the comparison of radiation spectra obtained from precise expression Eq. (2) with data of asymptotic expressions Eq. (12) was carried out. Results of comparison for energy E = (26, 30) MeV and for pitch angles θ_p = 0.16, 0.18 are shown in Fig. 1. The wavelength operation range detected by the EAST visible light camera (0.38 – 0.75 μm) is shown in these figures also. The spectrum moves to the smaller values of wavelength not only with energy increasing but also with pitch angles increasing [5]. In the case of runaway energy E = 30 MeV, the intensity of synchrotron radiation is much higher in comparison with energy E = 26 MeV.

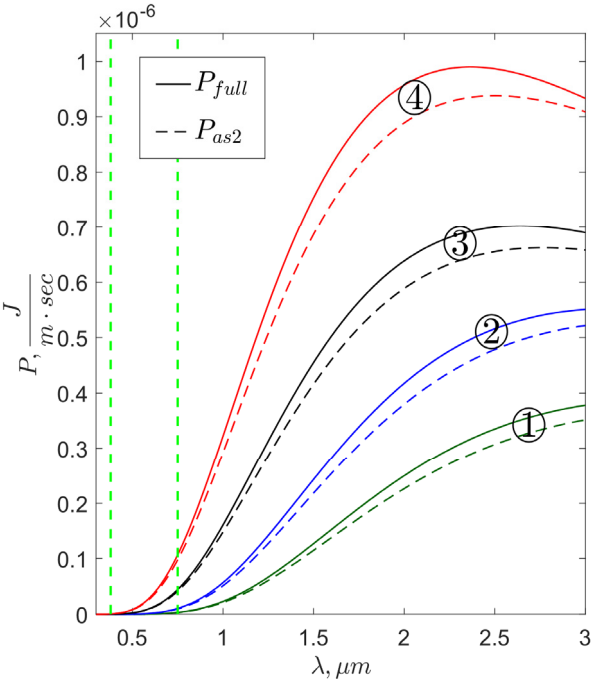

Fig. 1. Synchrotron radiation spectra analysis for runaway electron parameters in the EAST experiment: (1) E = 26 MeV, θ_p = 0.16, (2) E = 26 MeV, θ_p = 0.18, (3) E = 30 MeV, θ_p = 0.16, (4) E = 30 MeV, θ_p = 0.18. The wavelength operation range for the visible light camera (0.38 – 0.75) μm is marked with vertical dashed lines.

For wavelength region $\lambda << \lambda_m$ (λ_m is the wavelength at which spectrum of runaway electrons has a maximum) the

precise (P_{full}) and asymptotic (P_{as2}) curves practically are coincided for all cases. Hence, the validity of using asymptotic expression Eq. (12) in Ref. [11] for analyzing of synchrotron radiation spectra during recent runaway EAST experiment near the wavelength operation range (0.38 – 0.75) μm of the CMOS visible light camera has been confirmed, it is the main conclusion from data presented in Fig. 1. When the energy of runaway electrons is E = 30 MeV this difference between P_{full} and P_{as2} is a little bigger but still negligible. As it was declared in Ref. [11], the synchrotron radiation is barely visible for runaway electrons with E = 26 MeV.

However, we notice that with increasing of wavelength the difference between asymptote and precise expression increases. A comparison of precise expression for synchrotron radiation spectrum of runaway electrons Eq. (2) with asymptotic expression Eq. (12) for wide wavelength range shows that the difference between P_{full} and P_{as2} becomes more significant when the wavelength is approaching to λ_m. Hence, for wavelengths in the range of $\lambda \sim \lambda_m$ precise expression Eq. (2) should be used instead of asymptote Eq. (12) for investigation of runaway electron parameters.

CONCLUSIONS

For recent the runaway EAST experiment parameters (Ref. [11]) detail analysis of synchrotron radiation spectra of runaway electrons using precise expression for spectral density Eq. (2) has been presented. For wavelengths $\lambda << \lambda_m$ the validity of using asymptotic expression Eq. (12) for analyzing of synchrotron radiation spectra parameters in wavelength operation range of the EAST visible light camera (0.38 – 0.75 μm) has been confirmed, λ_m is the wavelength at which spectrum of runaway electrons has a maximum. It is emphasized that if for analysis to use the wavelength range near maximum value of spectra, where λ is close to λ_m, the precise expression of spectral power density P_{full} should be used.

Obtained results are important for correct interpretation of runaway EAST experiments and runaway experiments in other tokamaks.

REFERENCES

1. Progress in the ITER physics basis. Chapter 3: MHD stability, operational limits and disruptions // Nuclear Fusion. – 2007. – Vol. 47. – No. 6. – P. 128-202.
2. Jaspers R., Lopes Cardozo N.J., Donne A.J.H., et al. A synchrotron radiation diagnostic to observe relativistic runaway electrons in tokamak plasma // Review Sci. Instruments.– 2001.– Vol. 72-II. – No.1.– P. 466-470.
3. Finken K.H., Watkins J.G., Rusbuldt D., et al. Observation of infrared synchrotron radiation from tokamak runaway electrons in TEXTOR // Nuclear Fusion.– 1990.– Vol. 30. – No.5.– P. 859-870.
4. ITER physics basis, chapter 7: measurement of plasma parameters // Nuclear Fusion.– 1999.– Vol.39. – No. 12.– P. 2541-2575.
5. Pankratov I.M. Analysis of the synchrotron radiation spectra of runaway electrons // Plasma Physics Reports.– 1999.– Vol. 25. – No. 2.– P. 145-148.
6. Reux C., Plyusnin V., Alper B., et al. Runaway electron beam generation and mitigation during disruptions at JET-ILW // Nuclear Fusion. – 2015. – Vol. 55. –No. 9. – 093013.
7. Yoshino R., Tokudo S., Kawano Y. Generation and termination of runaway electrons at major disruptions in JT-60U // Nuclear Fusion. – 1999. – Vol. 39. – No. 2. – P. 151-161.
8. Yu J.H., Hollmann E.M., Commaux N., et al. Visible imaging and spectroscopy of disruption runaway electrons in DIII-D // Physics of Plasmas. – 2013. – Vol. 20. – No. 4. – 042113.
9. England A.C., Chen Z.Y., Seo D.C., et al. Runaway electron suppression by ECRH and RMP in KSTAR // Plasma Science and Technology. – 2013. – Vol. 15. – No. 2. – P. 119-122.
10. Zhou R.J., Hu L.Q., Li E.Z. et al. Investigation of ring-like runaway electron beams in the EAST tokamak // Plasma Phys. Control. Fusion.– 2013.– Vol.55. – No. 5.– 055006.
11. Zhou R.J., Pankratov I.M., Hu L.Q., et al. Synchrotron radiation spectra and synchrotron radiation spot shape of runaway electrons in Experimental Advanced Superconducting Tokamak // Physics of Plasmas. – 2014. – Vol. 21. – No. 6. – 063302.
12. Pankratov I.M., Pavlenko I.V., Pomazan O.A. Analysis of synchrotron radiation emitted by runaway electrons in tokamaks // The Journal of Kharkiv National University, physical series "Nuclei, Particles, Fields". – 2013. – No.1059. – Iss. 39. – P. 39-45.
13. Olver F.W. Asymptotics and Special Functions.– Natick: A K Peters, 1997.– 592 p.
14. Schwinger J. On the classical radiation on accelerated electrons // Phys. Review.– 1949.– Vol. 75. – No. 12.– P. 1912-1925.

East Eur. J. Phys. Vol.4 No.3 (2017) 31-35 DOI:10.26565/2312-4334-2017-3-04

PACS: 25.20.-x.

INVESTIGATION OF (γ,n) REACTIONS IN THE CHANNEL OF MULTIPARTICLE PHOTODISINTEGRATION OF ^{12}C AND ^{16}O NUCLEI

S.N. Afanas'ev
National Scientific Center "Kharkiv Institute of Physics and Technology", Kharkiv, Ukraine
1, Akademicheskaya st., Kharkiv, Ukraine, 61108
E-mail: afanserg@kipt.kharkov.ua
Received May 26, 2017

The reactions $^{12}C(\gamma,n)^3He2\alpha$ and $^{16}O(\gamma,n)^3He3\alpha$ is investigated by a method that employs a diffusion chamber placed in a magnetic field and irradiated by a beam of bremsstrahlung photons with an end-point energy of 150 MeV. In the excitation curve for the 2α system, a resonance is found, and this resonance identified as the ground state of the ^{8}Be nucleus. The parameters of the γ-quantum and neutron are calculated, and the partial channels $^{12}C(\gamma,n)^3He^8Be_0$ and $^{16}O(\gamma,n)^3He\alpha^8Be_0$ reactions are singled out. It is shown that these reactions proceed according a sequential-type scheme with the formation of one or several unresolved excited states of ^{11}C and ^{15}O nuclei at the first step. The total cross section of the reactions was determined and a similarity in their behavior was found for E_γ > 55 MeV. A jumplike change in the dependence of the kinetic energy of the neutron on E_γ in different energy intervals of the γ-quantum was observed.
KEY WORDS: diffusion chamber, photodisintegration, the excitation energy, ground state of the ^{8}Be nucleus

ДОСЛІДЖЕННЯ (γ,n)-РЕАКЦІЙ У КАНАЛІ БАГАТОЧАСТИНКОВОГО ФОТОРОЗЩЕПЛЕННЯ ЯДЕР ^{12}C ТА ^{16}O

С.М. Афанасьєв
Національний Науковий Центр «Харківський фізико-технічний інститут», Харків, Україна
вул. Академічна 1, м. Харків, Україна, 61108

Виконано аналіз реакцій $^{12}C(\gamma,n)^3He2\alpha$ та $^{16}O(\gamma,n)^3He3\alpha$, отриманих методом дифузійної камери в магнітному полі на пучку гальмівних фотонів з $E_\gamma^{макс}$=150 МеВ. У кривій збудження системи 2 α-частинок виявлено резонанс, ідентифікований як основний стан ядра ^{8}Be. Обчислено кінематичні параметри γ-кванта і нейтрона, та виділено парціальні канали $^{12}C(\gamma,n)^3He^8Be_0$ та $^{16}O(\gamma,n)^3He\alpha^8Be_0$. Було показано, що реакції мають послідовний двочастинковий тип розпаду з утворенням одного або декількох нероздільних збуджених станів ядер ^{11}C і ^{15}O на першому етапі розвалу. Визначено повний перетин реакцій і виявлена подоба в їхньому поводженні при E_γ > 55 МеВ. Виявлено різку зміну залежності кінетичної енергії нейтрона від E_γ у різних інтервалах енергії γ-кванта.
КЛЮЧОВІ СЛОВА: дифузійна камера, фоторозщеплення, енергія збудження, основний стан ядра ^{8}Be

ИССЛЕДОВАНИЕ (γ,n)-РЕАКЦИЙ В КАНАЛЕ МНОГОЧАСТИЧНОГО ФОТОРАСЩЕПЛЕНИЯ ЯДЕР ^{12}C И ^{16}O

С.Н. Афанасьев
Национальный Научный Центр «Харьковский физико-технический институт», Харьков, Украина
ул. Академическая 1, г. Харьков, Украина, 61108

Выполнен анализ реакций $^{12}C(\gamma,n)^3He2\alpha$ и $^{16}O(\gamma,n)^3He3\alpha$, полученных методом диффузионной камеры в магнитном поле на пучке тормозных фотонов с $E_\gamma^{макс}$=150 МэВ. В кривой возбуждения системы 2α-частиц обнаружен резонанс, идентифицированный как основное состояние ядра ^{8}Be. Вычислены кинематические параметры γ-кванта и нейтрона, и выделены парциальные каналы $^{12}C(\gamma,n)^3He^8Be_0$ и $^{16}O(\gamma,n)^3He\alpha^8Be_0$. Было показано, что в реакциях происходит последовательный двохчастичный тип распада с образованием одного или нескольких неразделенных возбужденных состояний ядер ^{11}C и ^{15}O на первом этапе распада. Определено полное сечение реакций и обнаружено подобие в их поведении при E_γ > 55 МэВ. Обнаружено резкое изменение зависимости кинетической энергии нейтрона от E_γ в разных интервалах энергии γ-кванта.
КЛЮЧЕВЫЕ СЛОВА: диффузионная камера, фоторасщепление, энергия возбуждения, основное состояние ядра ^{8}Be

The development of models for the photodisintegration of light nuclei with knockout of one nucleon fell to its way from the model of the direct mechanism in base of which lie one-particle currents and impulse approximation to the absorption models of the γ-quantum by nuclear substructures: quasideutron and quasiα-particle. However, the reaction mechanism for nucleon knockout from a nucleus has yet to be clarified conclusively.

Calculations in the nonrelativistic approximation [1] revealed that the direct-knockout mechanism cannot explain the equality of the cross sections for (γ,p) and (γ,n) reactions or an identifiable shape of the angular distributions in these reactions. It was concluded [2] that, at intermediate energies, a dominant contribution comes from the process of photon interaction with a nucleon pair. In addition, it was concluded that the role of exchange currents is small if the residual nucleus is in the ground state and increases with growth of energy of its excitation. However, this conclusion is at odds with the results of the calculations performed in the relativistic approximation [3], where it was shown that the direct-mechanism contribution to (γ,N) reactions is greater than that in the nonrelativistic approximation, ensuring agreement with experimental data.

Therefore, the experimental data on photoproduction of high-excited states of nuclei were important. As a rule,

these nuclei break up to hadrons forming multiparticle photonuclear reactions. Analyzing decay modes it is possible to select a certain excited states of residual nuclei almost without a background. The problem of exclusive event selection could be solved by means of a track 4π-detector registering all charged particles in a final state. The decay products have small energies. The diffusion chamber combining a gas target with a detector became the effective instrument for research of multiparticle photonuclear reactions. The reactions $^{12}C(\gamma,n)^3He2\alpha$ and $^{16}O(\gamma,n)^3He3\alpha$ (in what follows, they will shortly be designated as $^{12}C(\gamma,n)$ and $^{16}O(\gamma,n)$ reactions, respectively), which are studied here, proceed with the formation of highly excited states of the residual nucleus.

At present, there are no calculations have been performed so far for the ^{12}C and ^{16}O nucleus photodisintegration accompanied by neutron escape and the formation of a final nucleus in a highly excited state. However, in a line of experimental studies on the "mirror" reactions of $^4He(\gamma,p)^3H$ and $^4He(\gamma,n)^3He$ [4, 5], $^{12}C(\gamma,p\alpha)^7Li$ and $^{12}C(\gamma,n\alpha)^7Be$ [6], $^{12}C(\gamma,p)^3H2\alpha$ and $^{12}C(\gamma,n)^3He2\alpha$ [7], the cross sections of the (γ,p) and (γ,n) reactions were found to be equal. The experimental data of the "mirror" reactions were compared with the calculations for (γ,p) reactions. Further, in work [8] a comparison is made between the asymmetry coefficients of the differential cross sections in the $^{12}C(\gamma,p)^{11}C$ and $^{16}O(\gamma,p)^{15}N$ reactions and also their similarity was found as a function of the energy of the γ-quantum. But comparisons of (γ,n) reactions on different nuclei in channels with the formation of several particles in the final state have not been carried out at the present time.

Thus, the $^{12}C(\gamma,n)$ and $^{16}O(\gamma,n)$ reactions proposed for the study corresponds to several criteria for testing the models of interaction of the γ-quantum with the nucleus:

- similar channels of multiparticle decays on different nuclei,
- the formation of photoneutrons in a channel with highly excited states of residual nuclei,
- formation of a system $(n+^3He)$ corresponding to a quasiαparticle.

Here we present the results from studies into the reaction $^{12}C(\gamma,n)$ and $^{16}O(\gamma,n)$. The experiments were made using a diffusion chamber in the magnetic field, exposed to bremsstrahlung γ-quanta that had a maximum energy of 150 MeV [9]. The chamber combined a target and a detector with a large-acceptance solid angle. The reactions $\gamma+^{12}C\rightarrow3\alpha$ and $\gamma+^{16}O\rightarrow4\alpha$, respectively, was the main source of background. Events featuring doubly charged particles were measured simultaneously. The reactions being studied was separated on the basis of the transverse momentum $P_\perp$, which is equal to the sum of the transverse momenta of the final particles involved. The procedure used to separate the $\gamma+^{12}C\rightarrow3\alpha$ and $\gamma+^{16}O\rightarrow4\alpha$ reactions in question was described previously in [10, 11].

The aim of this work is the comparisons of (γ,n) reactions on different nuclei (^{12}C and ^{16}O) in channels with the formation of several particles in the final state. This information is an important component of information for understanding the γ-quanta absorption processes at energies below giant resonance.

EXPERIMENTAL RESULTS

Ground state of the ^{8}Be nucleus

We will touch upon special features of the detection of the relevant the $^{12}C(\gamma,n)^3He2\alpha$ and $^{16}O(\gamma,n)^3He3\alpha$ reactions. The chamber used operated in a mode that made it possible to separate singly and doubly charged particles visually and to compare the ionization density and the width of a track after measuring its radius of curvature. However, we were unable to identify ^{3}He and ^{4}He nuclei by this method. The error in measuring the photon energy and the angle of neutron escape is determined by the error in measuring the momenta of visible particles and the error because of the indistinguishability of ^{3}He and ^{4}He particles. Therefore, a method was proposed for identifying α- particles from the formation of the ground state (GS) of the ^{8}Be nucleus. The resonance corresponding to the formation of a GS in experimental data is manifested in the form of a narrow near-threshold resonance and in many-particle nuclear reactions with several α-particles in the final state [12, 13] its formation is most probable in the intermediate stage.

The excitation energy of a system of two α-particles was determined as [14]:

$$E_x(\alpha\alpha) = M^{eff}(^8Be) - 2m_\alpha, \quad (1)$$

where $M^{eff}(^8Be)$ is the effective mass equal to the total energy of the system in the rest reference system, m_α is the rest mass of α-particles.

In this and the following figures, the experimental results are presented: for the $^{12}C(\gamma,n)$ reaction by light circles (○), for the $^{16}O(\gamma,n)$ reaction by dark circles (●).

It is not possible to select from of several combination of α-particles pairs of every event a pair that was produced as a result of ^{8}Be disintegration. Therefore, for the distribution of the in-pair relative energy of two α-particles, all values of $E_x(\alpha\alpha)$ for every event are plotted in Fig. 1a at energy $E_x(\alpha\alpha) < 0.5$ MeV. The histogramming step was 0.025 MeV, and the points were placed in the middle of intervals; the displayed errors are pure statistical. Data on the reaction $^{12}C(\gamma,n)$ are normalized to the $^{16}O(\gamma,n)$ reaction in area.

The concentration of events in the 0.1 MeV regions can be explained by the formation of the ground state of ^{8}Be. The width observed experimentally is of instrumental origin. It is well known from [15] that the mass of the ^{8}Be nucleus

exceeds the mass of two alpha particles by 0.092 MeV and that the resonance FWHM is Γ = 6.8 eV. Because of insufficient energy resolution and low statistical validity, this experiment does not attempt to refine the parameters of the excited states of the ^{8}Be nucleus. The resonance observed in the αα-system is identified with the known data. Two α-particles corresponding to the formation of the GS are reliably identified. Subsequently, only the partial channels for the formation of the GS of the ^{8}Be nucleus (^{12}C(γ,n)^{3}He^{8}Be$_0$ and ^{16}O(γ,n)^{3}Heα^{8}Be$_0$) will be analyzed.

For the ^{12}C(γ,n) reaction, all particles are identified. In the case of the ^{16}O(γ,n) reaction, there are two particles that do not form the ^{8}Be nucleus. The particle momentum determined from the track curvature is independent of the particle mass. Therefore, arbitrary assignments of a particle type to a track lead to the same total momentum P. By consecutively identifying the particle with the final nucleus ^{3}He, we arrive at two values for the of E_γ and P_n: E_γ^1, E_γ^2 and P_n^1, P_n^2. The average value of these two is taken to be the result of a measurement.

The photon energy was determined by the formula:

$$E_\gamma = \frac{m^2 + P^2 - (M-E)^2}{2 \cdot (M - E + P_x)}, \tag{2}$$

where m and M are the neutron and target-nucleus masses (^{12}C or ^{16}O), E and P are, respectively, the total energy and the total momentum of the visible particles in final state; and P_x is the projection of this total momentum onto the direction of the photon momentum.

Excitation-energy distribution in the system of charged particles

For both reactions, we have measured the excitation-energy distribution in the system of visible particles (^{3}He+^{8}Be$_0$ for the ^{12}C(γ,n) reaction and ^{3}He+α+^{8}Be$_0$ for the ^{16}O(γ,n) reaction), defining as:

$$E_x = M^{eff} - M, \tag{3}$$

where M^{eff} is the effective mass of charged particles and M is the ground-state mass of the ^{11}C or ^{15}O, respectively. For comparison of distributions in Fig. 1b are represented the value of $E_{sum} = E_x - Q$, where Q is the threshold of the decay of ^{11}C or ^{15}O. The excitation functions of the excitations have a similar form.

The curves (1 is ^{12}C(γ,n) reaction, 2 is ^{16}O(γ,n) reaction) in Fig. 1b represent phase-space distribution [14]:

$$f(E_{sum}) \propto E_{sum}^{\frac{3}{2}k-\frac{5}{2}} \cdot (E_{sum}^{max} - E_{sum})^{\frac{3}{2}(n-k)-1}, \tag{4}$$

where n is the number of final particles, k is the number of particles forming a resonance (k < n), E_{sum}^{max} is the maximum possible excitation energy of a system of k particles equal to the maximum energy of a γ-quantum in a given interval minus the reaction threshold. For a continuous photon spectrum, phase-space distributions were calculated step by step. First, this was done for photon-energy intervals 1 MeV wide. The area under the curve was normalized to the number of events per interval. After that, summation of probabilities was performed for identical intervals of energies E_{sum}.

A comparison of the distributions in question with the phase-space distributions is indicate of the formation of one or several unresolved excited states of the ^{11}C or ^{15}O nuclei. It is well known from [16, 17] that, at such energies ^{11}C and ^{15}O nuclei have broad levels decaying to final state involving ^{3}He and ^{4}He nuclei. However, the observed resonances do not coincide with some specific level. Therefore, the reactions being studies are of a sequential type: the initial step involves nucleon knockout and the formation of excited states of the ^{11}C or ^{15}O nuclei.

The total cross section for the reactions ^{12}C(γ,n)^{3}He^{8}Be$_0$ and ^{16}O(γ,n)^{3}Heα^{8}Be$_0$

We have measured the total cross section for the reactions ^{12}C(γ,n) and ^{16}O(γ,n) in the photon-energy range between the energy threshold of the reaction and 120 MeV with a variable step – specifically, with a step of 2 MeV at E_γ < 60 MeV and a step of 5 MeV at higher energy. The results are shown in Fig. 2a at the midpoint of a step. The displayed errors are purely statistical.

The measured cross sections exhibit a broad maximum at the near-threshold area. The rate of decrease in cross section undergoes a change in the region around 55 MeV. The histogram represents the total cross section for the ^{4}He(γ,n)^{3}He [5] reaction, and the measurement results are normalized around 40 MeV. The experimental cross section at different nuclei (^{4}He, ^{12}C and ^{16}O) have the same slope at E_γ > 55 MeV (Fig. 2b). The change in the rate of decrease in the cross section may possibly be due to a change the mechanism interaction of γ-quantum with nuclei.

No cross-section calculations have been performed so far for carbon and oxygen nuclei photodisintegration accompanied by neutron escape and the formation of a final nucleus in a highly excited state; therefore, a comparison with data on the "mirror" reaction ^{12}C(γ,p)^{3}H2α [7]. The total cross section was obtained within the mechanism of direct proton knockout from the s-shell [18]. After normalization at the maximum cross section for the reaction ^{12}C(γ,n), it is represented by curve 1 in Fig. 2b. The calculation within the model assuming photon absorption by an alpha-particle

cluster [19] is shown by curve 2. The total cross section for the relevant $^{12}C(\gamma,n)^{11}C$ reaction was calculated in [2] within the self consistent random-phase approximation. The nucleon–nucleon interaction was simulated by Skyrme forces (Sk3). The cross section obtained after normalization in the region around 40 MeV is represented by curve 3. All calculations at $E_\gamma > 55$ MeV decreases faster than its experimental counterpart.

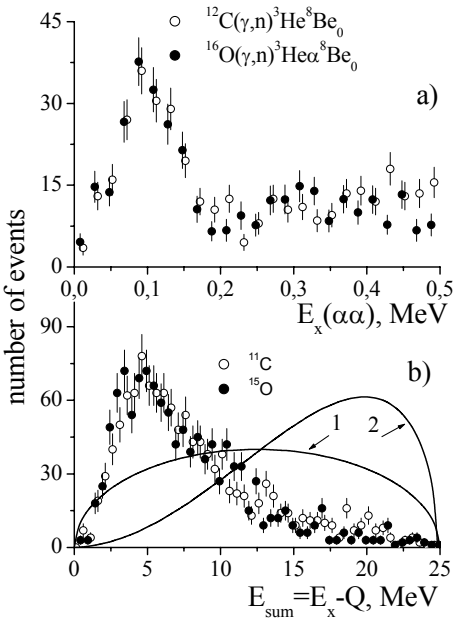

Fig. 1. Distribution of events with respect to the excitation energy: a) system of two α-particles at $E_x(\alpha\alpha) < 0.5$ MeV, b) system of visible particles. The notation is explained in the main body of the text.

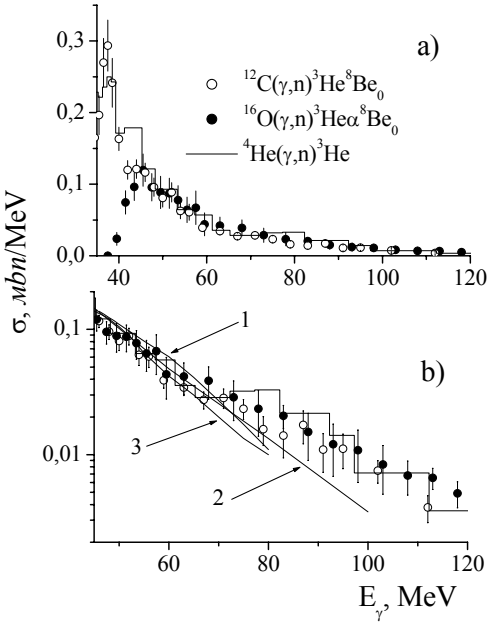

Fig. 2. Total cross section for the reactions $^{12}C(\gamma,n)$ and $^{16}O(\gamma,n)$ as a function of the photon energy: a) all spectr, b) at $E_\gamma > 45$ MeV. The histogram is the reaction $^4He(\gamma,n)^3He$ [5]. The displayed curves in the main body of the text.

The dependence of the average energy of the neutron on the total energy

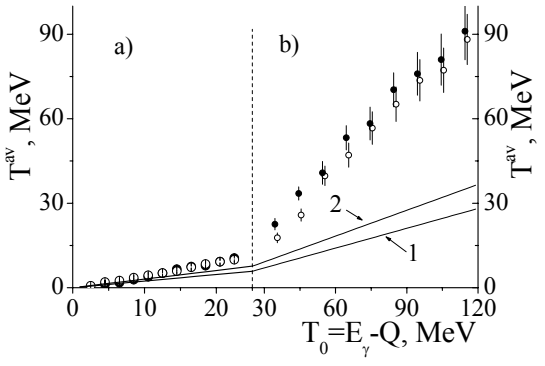

Fig. 3. The dependence of the average energy of the neutron (T^{av}) on the total energy $T_0 = (E_\gamma - Q)$. The displayed curves were calculated in (5).

In Fig. 3 we show the dependence of the average kinetic energy (T^{av}) of the neutron on the total kinetic energy equal to $T_0 = E_\gamma - Q$ (Q is the energy threshold of the reaction). The average energy T^{av} was determined for particles corresponding to an interval T_0 of 1 MeV. The results are shown in Fig. 3 by points placed at the midpoint of a step. The displayed errors are purely statistical. We have measured T^{av} in the T_0 range with a variable step – specifically, with a step of 2 MeV at $T_0 <$ 24 MeV (zone a) and a step of 10 MeV at $T_0 > 24$ MeV (zone b).

There is agreement in the form of distributions for both (γ,n) reactions. Also, we should note a fast increase in the dependence at $T_0 > 24$ MeV. The lines (1 for the $^{12}C(\gamma,n)$ reaction, 2 for the $^{16}O(\gamma,n)$ reaction), shown in Fig. 3, are corresponded to the statistical distribution [20]:

$$T^{av} = \frac{A\text{-}M}{(n\text{-}1)\cdot A}\cdot T_0, \qquad (5)$$

where A, M – are the atomic number of the target and of the neutron, respectively, and n is the number of particles in the final state. In the case of direct knockout of a compound nucleus, the energy distributions of the particles must correspond to the statistical distribution calculated on the assumption of a "symmetric" distribution of the total energy between all reaction products.

The distribution of the neutron T^{av} above the statistical distribution (lines 1 and 2, respectively, for the reactions $^{12}C(\gamma,n)$ and $^{16}O(\gamma,n)$) in both energy intervals.

A fit by the linear function $T^{av} = a\cdot T_0$ to the experimental data is executed and the coefficients a_1 ($^{12}C(\gamma,n)$ reaction) and a_2 ($^{16}O(\gamma,n)$ reaction) were determined for both reactions in two energy intervals. At $T_0 < 24$ MeV (zone a): $a_1^a = 0.503 \pm 0.012$, and $a_2^a = 0.465 \pm 0.011$. At $T_0 > 24$ MeV (zone b): $a_1^b = 0.891 \pm 0.065$, $a_2^b = 0.923 \pm 0.059$. Qualitatively, the results for the first energy interval have been explained on the basis of the model of photon absorption

by a quasi-deuteron pair. Upon its decay, the neutron escapes from the ^{12}C or ^{16}O nucleus with half the energy ($T_0/2$), while the remaining particles form an excited the ^{11}C or ^{15}O nucleus, which is observed experimentally. In the case of the second energy interval, the data can be explained within the framework of the direct knockout mechanism of the nucleon, where by (5) $T^{av} = T_0 (A-1) / A$. Here, it can be expected that is for the $^{12}C(\gamma,n)$ reaction is $T^{av} = 11T_0 / 12$, and for the $^{16}O(\gamma,n)$ reaction is $T^{av} = 15T_0 / 16$. Qualitatively, the experimental data consistent with this assumption.

CONCLUSION

A detector of large acceptance in solid angle has been employed to study the multi-particle photodisintegration of carbon nuclei (the reactions $^{12}C(\gamma,n)^3He2\alpha$) and oxygen ($^{16}O(\gamma,n)^3He3\alpha$).

The distribution of events with respect to the excitation energy of the subsystem of two alpha particles has been measured. A resonance that has a maximum at $E_0 = 0.1$ MeV has been found and was identified as a ground state of ^8Be. Events have been separated into channels of ground state formation ($^{12}C(\gamma,n)^3He^3He^8Be_0$ and $^{16}O(\gamma,n)^3He\alpha^8Be_0$ reactions). The photon energy and kinematic parameters of the neutrons was determined.

The energy dependence of the total cross section for the partial reaction $^{12}C(\gamma,n)^3He^8Be_0$ and $^{16}O(\gamma,n)^3He\alpha^8Be_0$ has been measured in the photon-energy range between the energy threshold of the reaction and 120 MeV. The measured cross sections exhibit a broad resonance at the near-threshold area. The rate of decrease in cross section undergoes a change in the region around 55 MeV.

The dependence of the average kinetic energy of the neutron (T^{av}) on the total kinetic energy of the system (T_0) is measured. The data on the $^{12}C(\gamma,n)^3He^8Be_0$ and $^{16}O(\gamma,n)^3He\alpha^8Be_0$ reactions behave identically. At $T_0 < 24$ MeV – $T^{av} \sim 0.5T_0$, with the growth of T_0, the neutron carries away most of the total energy. This behavior can be explained by a change in the mechanism of interaction of the γ-quantum with the nucleus.

ACKNOWLEDGMENTS

Author is grateful to A.F. Khodyachikh and L.G. Levchuk for stimulating discussions and a number of enlightening comments.

REFERENCES

1. Hebach H., Wortberg A., Gari M. Photonuclear reactions at intermediate energies // Nucl. Phys. – 1976. – Vol. A267. – P. 425-460.
2. Cavinato M., Marangoni M., Saruis A.M. Photoreactions of ^{12}C, ^{16}O and ^{40}Ca in self-consistent RPA theory: (II). Unpolarized (γ,p) and (γ,n) angular distributions below pion threshold // Nucl. Phys. – 1984. – Vol. A422. – P. 237-272.
3. Johansson J.I., Sherif H.S. Importance of the direct knockout mechanism in relativistic calculations for (γ,p) reactions // Phys. Rev. – 1997. – Vol. C56. – P. 328-338.
4. Feldman G., Balbes M.J., Kramer L.H., et al. $^3H(p,\gamma)^4He$ reaction and the (γ,p)/(γ,n) ratio in ^4He // Phys. Rev. – 1990. – Vol. C42. – R1167-R1170.
5. Arkatov Yu.M., Vatset P.I., Voloshchuk V.I., et al. Photodisintegration of ^4He nucleus down to threshold of meson production // Ukrainskij Fizicheskij Zhurnal. – 1978. – Vol. 23. – P. 1818-1840 (in Russian).
6. Kirichenko V.V., Khodyachikh A.F., Vatset P.I., et al. Study of reactions $^{12}C(\gamma,p\alpha)^7Li$ and $^{12}C(\gamma,n\alpha)^7Be$ at $E_{\gamma max} = 120$ MeV // Yad. Fiz. – 1979. – Vol. 29. – P. 572-581 (in Russian).
7. Afanas'ev S.N., Gorbenko E.S., Khodyachikh A.F. Investigation of the reaction mechanism for the four-particle photodisintegration of a carbon nucleus // Yad. Fiz. – 2007. – Vol. 70. – P. 873-881 (in Russian).
8. Khodyachikh A.F. Photonuclear reactions on p-shell nuclei at intermediate energies // PAST. Series: Nucl. Phys. Invest. – 2003. – Vol. 2. – P. 45-49 (in Russian).
9. Ayzatskiy N.I., Afanas'ev S.N., Buki A.Yu., et al. Investigation of atomic nuclei by electrons and protons with energies up to 300 MeV. – Kharkiv: Mis'kdruk, 2017. – 388 p. (in Russian).
10. Afanas'ev S.N., Khodyachikh A.F. On the mechanism of formation of excited states of the ^8Be nucleus in the reaction $^{12}C(\gamma,3\alpha)$ // Yad. Fiz. – 2008. – Vol. 71. – P. 1859-1869 (in Russian).
11. Afanas'ev S.N. The ^8Be ground state formation in $^{16}O(\gamma,4\alpha)$ reaction // The Journal of Kharkiv National University. Physical Series: «Nuclei, Particles, Fields». – 2012. – Vol. 1025. – P. 4-9 (in Russian).
12. Alcorta M., Borge M.J.G., Cubero M., et al. Properties of ^{12}C resonances determined from the $^{10}B(^3He,p\alpha\alpha\alpha)$ and $^{11}B(^3He,d\alpha\alpha\alpha)$ reactions studied in complete kinematics // Phys. Rev. – 2012. – Vol. C86. – 064306 [6 pages].
13. Curtis N., Almaraz-Calderon S., Aprahamian A., et al. $^8Be+^8Be$ and $^{12}C+\alpha$ breakup states in ^{16}O populated via the $^{13}C(^4He,4\alpha)n$ reaction // Phys. Rev. – 2016. – Vol. C94. – 034313 [10 pages].
14. Baldin A.M., Gol'danski V.I., Maksimenko V.M., Rozental' I.L. Kinematics of Nuclear Reactions. – Moscow: Atomizdat, 1968. – 456 p. (in Russian).
15. Tilley D.R., Kelley J.H., Godwin J.L., et al. Energy levels of light nuclei A = 8, 9, 10 // Nucl. Phys. – 2004. – Vol. A745. – P. 155-362.
16. Kelley J.H., Kwan E., Purcell J.E., et al. Energy levels of light nuclei A=11 // Nucl. Phys. – 2012. – Vol. A880. P. 88-195.
17. Ajzenberg-Selove F. Energy levels of light nuclei A =13-15 // Nucl. Phys. – 1991. – Vol. A523. – P. 1-196.
18. Balashov V.V., Fetisov V.N. Role of nucleon clusters in deep photo-disintegration of light nuclei // Nucl. Phys. – 1961. – Vol. 27. – P. 337-343.
19. Mamasahlisov V.M., Dzibuti R.I. High energy photodesintegration of ^9Be and ^{12}C nuclei // JETF. – 1961. – Vol. 41. – P. 1493-1497 (in Russian).
20. Maikov V.N. Some photoreactions on light nuclei // JETP. – 1958. – Vol. 6. – P. 973-982 (in Russian).

EAST EUROPEAN JOURNAL OF PHYSICS
East Eur. J. Phys. Vol.4 No.3 (2017) 36-42 DOI:10.26565/2312-4334-2017-3-05

PACS: 28.41.Qb, 81.40 Ef, 61.10.Nz

INFLUENCE OF COLD ROLLING TO THE TEXTURE PARAMETER OF PURE HAFNIUM AND ZIRCONIUM

G.P. Kovtun, K.V. Kovtun, D.G. Malykhin, T.S. Yurkova, T.Yu. Rudycheva
National scientific center "Kharkov Institute of Physics and Technologies"
1, Akademicheskaya st., Kharkov, Ukraine, 61108
E-mail: dmitr.malykhin@gmail.com
Received August 12, 2017

Results of X-ray investigations of dependence of the crystallographic texture of hafnium and zirconium on degrees of cold rolling are presented. To obtain numerical principles, the method of inverse pole figures (IPF) with calculation of the texture parameters of Kearns (TP) for a chosen direction has been used. Measuring was carried out in the plane of the plates, as well as in the other two directions relating to rolling. The trigonal diagram of TP changes with degrees of deformation was built. Two stages of TP changes with deformation degrees are revealed: rate of the TP changes at the initial stage and, in part, characteristics of the subsequent stage depend on the initial texture of the materials. The second stage is characterized either by achievement of a minimum of TP in the rolling direction of the plates, or by moderate and even slight changes of them. In an example of hafnium, it has established that the increased rate of initial changes in TP is exclusively associated with intensive twinning predominantly by the $\{10\bar{1}2\}\langle\bar{1}011\rangle$ system. Arguments for dominance of twinning in the texture formation in hafnium and zirconium on the subsequent stage of rolling deformation are given.
KEYWORDS: X-ray analysis, texture, inverse pole figures, texture parameter, cold rolling, hafnium, zirconium, twinning

ВПЛИВ ХОЛОДНОЇ ПРОКАТКИ НА ТЕКСТУРНИЙ ПАРАМЕТР ЧИСТОГО ГАФНІЮ ТА ЦИРКОНІЮ

Г.П. Ковтун, К.В. Ковтун, Д.Г. Малихін, Т.С. Юркова, Т.Ю. Рудичева
Національний науковий центр «Харківський фізико-технічний інститут»
Україна, 61108, м. Харків, вул. Академічна, 1

Наведено результати рентгенівських досліджень залежності кристалографічної текстури гафнію і цирконію від ступеня холодної деформації прокаткою. Для отримання численних закономірностей використано метод зворотних полюсних фігур (ЗПФ) з розрахунком текстурних параметрів Кернса (ТП). Зйомки проведено в площині пластин, а також в двох інших напрямках, пов'язаних з прокаткою. Побудовано тригональну діаграму змін ТП зі ступенем деформації. Виявлено дві стадії змін ТП зі ступенем деформації: темп змін ТП на першій стадії і, почасти, характеристики другої стадії залежать від початкової текстури матеріалів. Друга стадія характеризується досягненням мінімуму ТП, виміряних у напрямку прокатки пластин, або помірною чи слабкою їх зміною. На прикладі гафнію встановлено, що підвищений темп початкових змін ТП виключно пов'язаний з інтенсивним двійникуванням переважно за системою $\{10\bar{1}2\}\langle\bar{1}011\rangle$..Наведено аргументи на користь домінування двійникування у формуванні текстури гафнію і цирконію на другій стадії деформації прокаткою.
КЛЮЧОВІ СЛОВА: рентгеноструктурний аналіз, текстура, зворотні полюсні фігури, текстурний параметр, холодна прокатка, гафній, цирконій, двійникування

ВЛИЯНИЕ ХОЛОДНОЙ ПРОКАТКИ НА ТЕКСТУРНЫЙ ПАРАМЕТР ЧИСТОГО ГАФНИЯ И ЦИРКОНИЯ

Г.П. Ковтун, К.В. Ковтун, Д.Г. Малихін, Т.С. Юркова, Т.Ю. Рудичева
Национальный Научный центр «Харьковский физико-технический институт»
Украина, 61108, г. Харьков, ул. Академическая, 1

Приведены результаты рентгеновских исследований зависимости кристаллографической текстуры гафния и циркония от степени холодной деформации прокаткой. Для получения численных закономерностей использован метод обратных полюсных фигур (ОПФ) с расчётом текстурных параметров Кернса (ТП). Съёмки проведены в плоскости пластин, а также в двух других направлениях, связанных с прокаткой. Построена тригональная диаграмма изменений ТП со степенью деформации. Выявлено две стадии изменений ТП со степенью деформации: темп изменений ТП на начальной стадии и, отчасти, характеристики последующей стадии зависят от исходной текстуры материалов. Вторая стадия характеризуется достижением минимума ТП, измеренных в направлении прокатки пластин, либо умеренным или даже слабым их изменением. На примере гафния установлено, что повышенный темп начальных изменений ТП исключительно связан с интенсивным двойникованием преимущественно по системе $\{10\bar{1}2\}\langle\bar{1}011\rangle$. Приведены аргументы в пользу доминирования двойникования в формировании текстуры гафния и циркония на последующей стадии деформации прокаткой.
КЛЮЧЕВЫЕ СЛОВА: рентгеноструктурный анализ, текстура, обратные полюсные фигуры, текстурный параметр, холодная прокатка, гафний, цирконий, двойникование

Zirconium and hafnium are the basis of materials intended for use in the construction of nuclear reactors. Products made of such materials, especially from zirconium-niobium alloys, undergo a special thermo-mechanical treatment aimed to maximize their satisfactory performance. Their crystallographic texture is an important characteristic on which the mechanical and radiation properties of these materials depend, as well as concerning to other hcp metals. Obtaining skills to predict its development after a necessary cycle of treatments is of practical interest. Study of principles of its changes after elementary processing cycles and analysis of the structural mechanisms responsible for these changes is

of scientific interest.

The aim of these studies is to reveal principles of changes in the crystallographic texture of pure hafnium and zirconium in process of cold rolling deformation, starting from annealed state of their plates. An exceptional feature is the subject of research – the Kearns texture parameter (TP) [1], which characterizes the general directionality of the crystallographic axes "c" of grains in hcp metals towards the investigated direction of the sample.

The world experience of research of this kind is practically absent. At present, the X-ray method of direct pole figures (DPF) is widely used for crystallographic texture research. The advantages of this method is simplicity of texture representing – in the form of a spatial distribution of orientations of the "c" axes, and the disadvantages are the difficulties of obtaining them due to limitations in the orientation of the samples and other technical reasons. This greatly reduces accuracy in the event of subsequent data processing. In fact, the DPF is a qualitative result of such studies.

In contrast, the suggested approaches described below make it possible to determine with satisfactory accuracy the TP as a characteristic convenient for both quantitative analysis and revealing numerical principles. This aspect also has no precedents and is therefore of especial interest.

The second exceptional feature of the research is the determination of TP in three orthogonal directions associated with rolling of plates.

Results will obtained can give some information about laws of rolling texture developments in the materials, and about accompanying structural mechanisms of it.

TECHNIQUE AND MATERIALS

To determine the TPs of hafnium and zirconium plates, the X-ray analysis of their texture by inverse pole figures (IPF) is used [2-4]. In contrast to the DPF method, in this approach, a usual X-ray optical scheme with Bragg-Brentano focusing is used. In particular, the present investigations were carried out using an X-ray diffractometer DRON4-07 in the radiation of CuK_α. To eliminate the vertical divergence of the X-ray beam, the pair of Soller slits was used.

According to this method, for the selected measuring direction (*j*), the pole density values P_{ji} (i.e. $P_{j,(hkl)}$) are calculated – this is an analogue of the distribution of crystallographic orientations (*hkil*) in this direction. These quantities are proportional to the experimental values of the integral intensity I_{ji}. The corresponding coefficient (R_j), in turn, is proportional to the flux of radiation incident on the sample. In general, the values of P_{ji} may be determined according to the following formulas:

$$P_{ji} = \frac{1}{R_j}\frac{I_{ji}}{I_{0i}}; \quad R_j = \sum_i A_i \frac{I_{ji}}{I_{0i}}; \tag{1}$$

where I_{0i} is the standard set of integrated intensities of reflection from an ideally non-textured (crystallographically isotropic) sample of such material; A_i is the quote of own orientation space (of a grain) for the *i*-th reflection, is used as the statistical weight [4]. In fact, the pole density is normalized to unity and would equal to unity for such non-textured material. Values I_{0i} either may be measured in advance, if there is a non-textured sample, or calculated [5].

The TP may be determined on the basis of the calculations of P_{ji} (1) using the following formula:

$$f_j = \left\langle \cos^2 \alpha_i \right\rangle_j = \sum_i A_i P_{ji} \cos^2 \alpha_i; \tag{2}$$

where α_i (α_{ij}) is the angle between the "c" axes of crystallites and the normals (*hkil*) in their reflecting position, i.e. in the direction of measuring. The meaning of the TP can be explained by an elementary example: the TP of a grain is equal to 1, if its axis "c" is oriented in the measuring direction, – is equal to 0 if it is perpendicular to them, and takes intermediate values in other cases. The TP of the material is averaged over all the plurality of grains.

The method was tested at its application to the Zr-2.5% Nb alloy texture investigations. So, the refined intensities I_{0i} were obtained by averaging the results for the samples of this alloy, obtained in three projections [6]. After comparing the results with the calculated values, the final set of values was obtained, the error of each of them is estimated at a limit of 5%. The values of A_i were calculated mathematically. Their set may be applicable to titanium, hafnium, zirconium and its industrial alloys.

Texture measurements of hafnium and zirconium samples were carried out in the rolling plane (normal direction, – ND), in the cross-section (rolling direction, – RD), and in the longitudinal section of the plates (transverse direction, – TD).

As samples for three-dimensional studies, hafnium plates HFE-1 (of Ukrainian specification) 2 mm thick annealed at 850°C for 1 hour, with a residual zirconium content of less than 0.2 wt. %, and other impurities – less than 0.1 wt. % are used. For the studies, samples were obtained by subsequent rolling up to 5, 15 and 30%.

Plates of iodide zirconium (99.9 mass%) with a thickness of 5 mm are also investigated in “3D” after both annealing at 600°C for 1 hour and subsequent deformation by 6, 10, 15, 20, 30 and 50%. Measurements in RD and TD were carried out from the surfaces of the central cut of plates to eliminate the boundary effect of rolling.

Additionally, the TP parameter in the normal direction of hafnium plates 5 mm thick, of the same kind and annealing mode, deformed to 5, 10, 15, 20, 30 and 50%, is investigated. For this material, the designation “$Hf^{(2)}$” will be further used, as well as “$Hf^{(1)}$” for its previous analogue.

The investigated surfaces of the plates were preliminary processed by grinding and etching.

RESULTS

In Figure 1, the IPFs of the $Hf^{(1)}$ plates are shown in three measuring directions. The values of the pole density (0002), $(10\bar{1}0)$ and $(11\bar{2}0)$ are displayed.

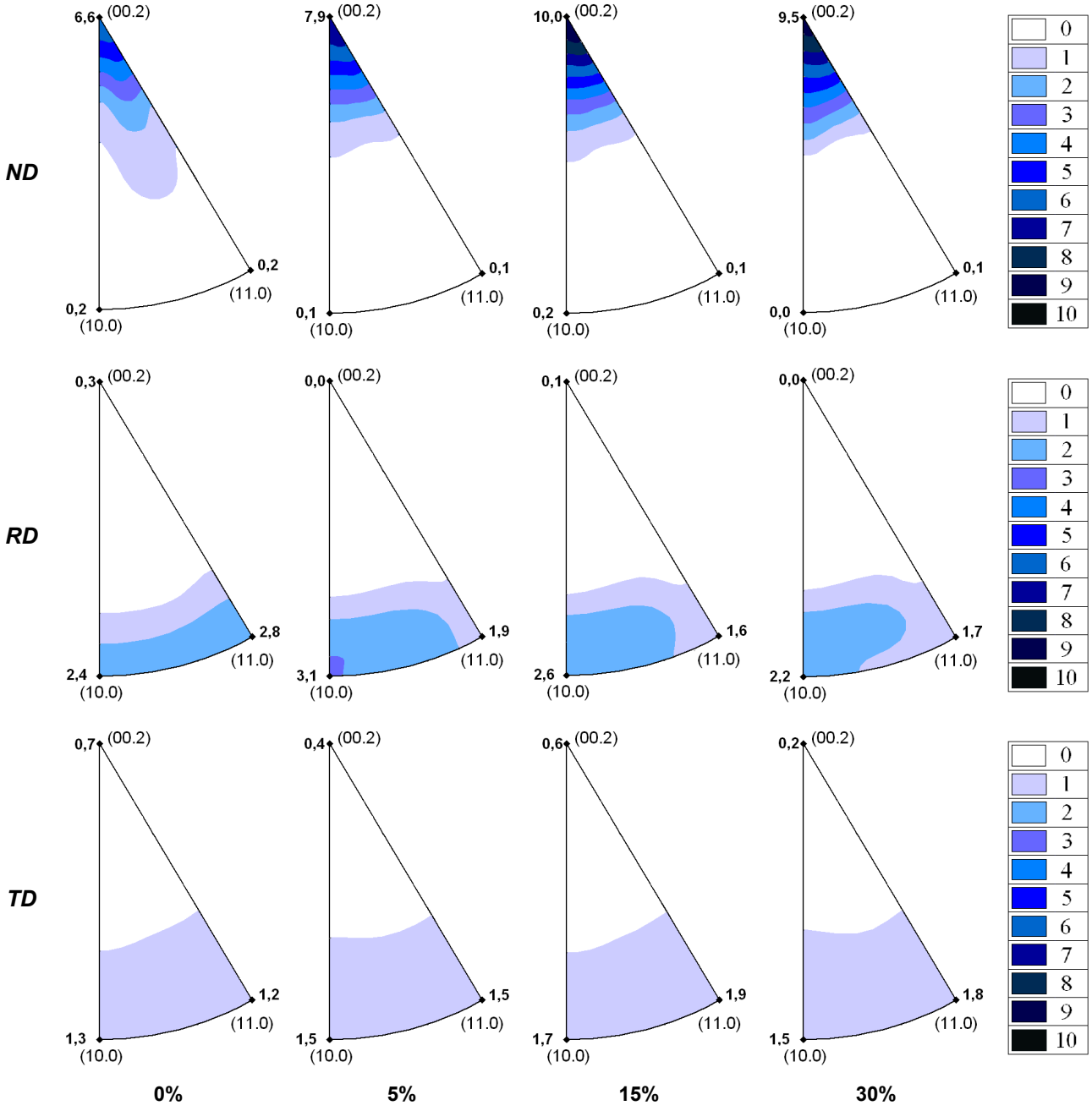

Fig.1. IPFs in three measuring directions for the original and deformed $Hf^{(1)}$ plates. The directions and the degree of deformation are indicated.

In Figure 2, with the same designations, IPFs of zirconium plates are given.

Based on the results of measurements from the plane of the initial and deformed $Hf^{(1)}$, $Hf^{(2)}$, and Zr plates, the graphs are given for the TP values in the ND direction (f_{ND}, Fig. 3) calculated by the formula (2).

The TP values determined for the three directions of the $Hf^{(1)}$ and Zr plates are displayed using a trigonal diagram (to be continued in the context). The diagram is built according to the principle of representing sections of ternary phase diagrams. The basis of this building is the trigonometric regularity:

$$\sum_j \cos^2 \alpha_{ji} = 1 \rightarrow \sum_j f_j = 1 \quad (j = 1, 2, 3). \tag{3}$$

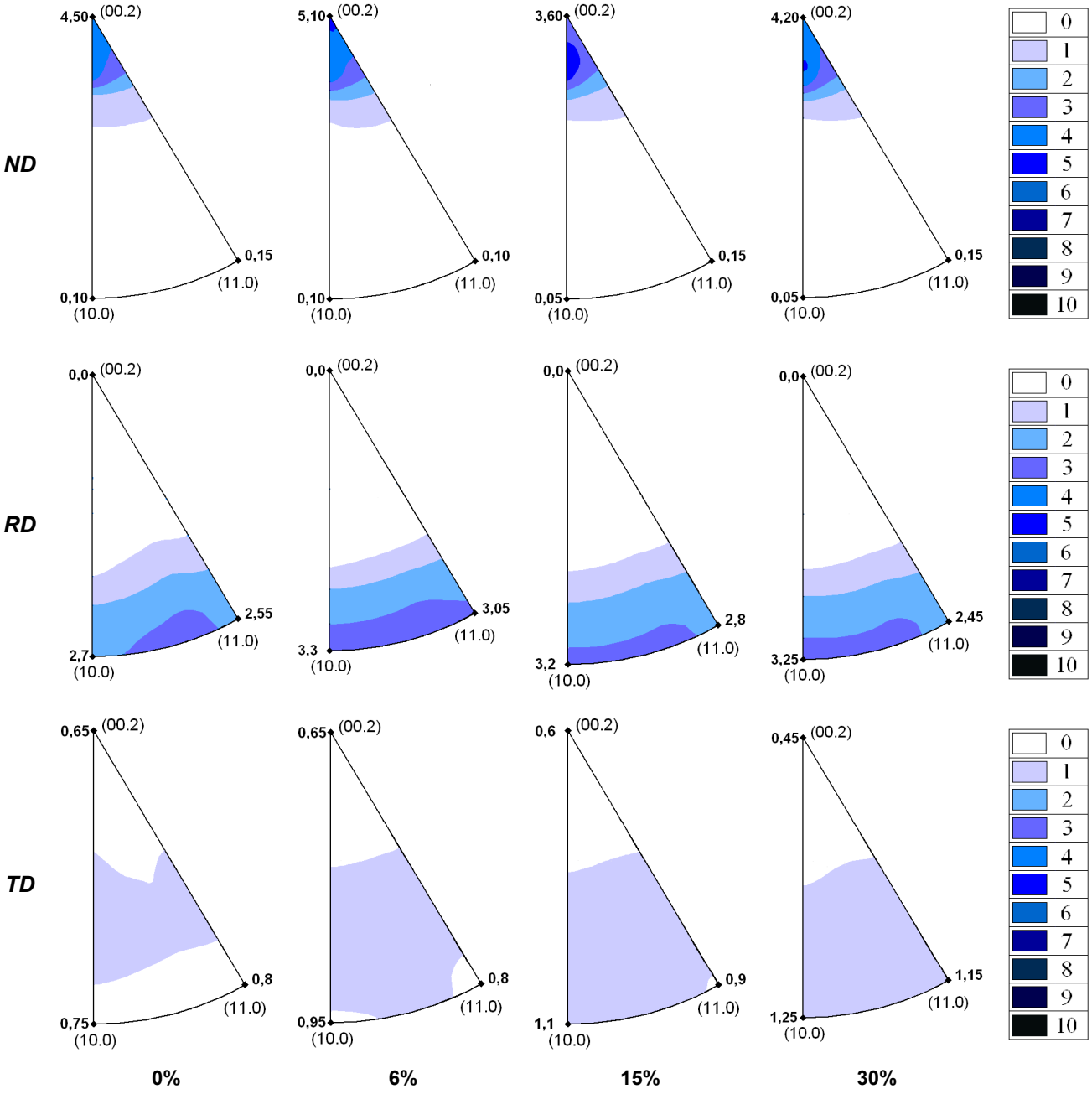

Fig.2. IPFs in three directions for the original and deformed plates of zirconium with indication the directions and the deformation degrees.

ANALYSIS OF THE RESULTS AND DISCUSSION

First of all, an ambiguity of the results obtained on the $Hf^{(1)}$ and $Hf^{(2)}$ samples (Fig. 3) attracts an attention. This circumstance, apparently, is due to differences in the making of the original plates.

A common principle of the graphs (Fig. 3) is moderate changes of the TPs for deformations of more than 5%. In the region below it and somewhat higher, the commonality of the graphs run is absent. The rate of the changes at up to 5%, as can be seen, depends on the initial values of the TPs. Partially, this also relates to changes at increased deformations, as can be seen in the example of the $Hf^{(1)}$.

Existence of such differences is confirmed by figure 4, where the arrows indicate the direction of the changes, starting from the initial state. So, on the one hand, it can be seen from the figure that the texture parameters of the original Zr plate fit in the direction of their further change, although at the same time, there is an increased initial rate. In part, this circumstance can also be noted for the $Hf^{(2)}$ (Fig. 3). Probably, the original plates of the $Hf^{(2)}$ and Zr were made by rolling, as well as subsequent samples, and at the same time – with achievement of high texture. On the other hand, for the $Hf^{(1)}$ (Fig. 4), the initial stage is more clearly detected, due to both the lower initial f_{ND} value (Fig. 3) and the increased TP in the RD (f_{RD}; Fig. 4).

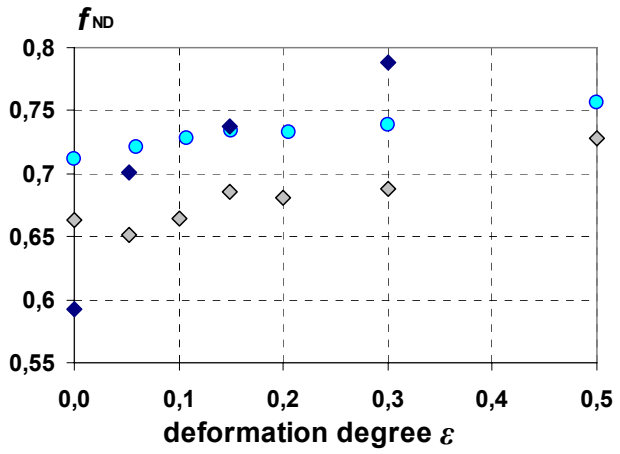

Fig.3. Changes of the f_{ND} with deformation degrees of the Hf$^{(1)}$ (◆) [7], Hf$^{(2)}$ (◆) and zirconium plates (○).

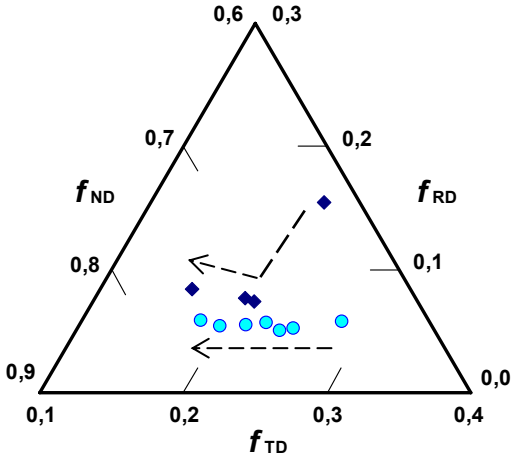

Fig.4. Diagram of the TPs changes for the Hf$^{(1)}$ (◆) [7] and zirconium plates (○) at the cold rolling.

In general, there are two principles in the obtained results. Firstly, in the changes of TPs with deformation degree of hafnium and zirconium, the stationary (moderate) stage exists. Its feature is small changes in f_{RD} (Fig. 4). In zirconium, for example, this parameter at such stage practically does not change, taking on value 0.06. Secondly, in the changes of TPs, at depending on their initial values, the initial stage as a rule can exist, differing by an accelerated run and a differed direction on the texture diagram. Partly, it is observed on the plates of Zr and is especially obvious for the Hf$^{(1)}$ plates (Fig. 3.4), and even is noticeable for Hf$^{(2)}$ (Fig. 3).

To define the structural nature of changes of TPs, first of all, their evaluation was carried out from the standpoint of homogeneous deformation at the scales of grains and higher. It was understood that such deformation is provided by the dislocation slip mechanisms. It was assumed that the contribution of slip to the formation of a typical rolling texture, if this could be, can be due to the binding of both the basal planes (0002) of the crystallites and their "c" normals – to the geometry of such kind deformation. According to this principle, during deformation, these planes are permanently approaching to the rolling plane by their orientation. In this calculation, changes of the normals "c" incline are taken: $\alpha_{ij} \rightarrow \alpha'_{ij}$. The texture features of the initial and deformed plates allow us to use for estimation such formula: $\tan\alpha'_{ij} = k\tan\alpha_{ij}$, – where k depends on the deformation degree ε and takes the value $(1 - \varepsilon)^n$. The value n is equal to 2 for the longitudinal section of the plates (RD↔ND), and to unit for the cross section (TD↔ND) [7].

According to this scheme, the evaluation was carried out on a sequence of values of the pole density $(h0\bar{h}l)$, aligned along the $\cos^2\alpha$ scale. In this regard, in Fig. 5, the deformation dynamics of the experimental sequence of values $P_i(\cos^2\alpha_i)$ and calculated one – $P_i(\cos^2\alpha'_i)$ – are given. The values of $P_i(\cos^2\alpha'_i)$ were calculated on the basis of the data for the initial sample.

As can be seen from figure 5, the experimental and calculated data significantly differ. In view of this, it should be assumed that at the rolling process of the plates, dislocation slipping in the grain body is distributed irregularly. In such cases one considers that it develops a tendency to localize in the grain boundary region. Such a state, apparently, has little effect on the changes in the crystallographic orientations of grains. The reason of the texture changes in this case remains to be attributed to twinning. Data from other studies confirm formation of twins in zirconium during rolling [8].

From what has been said, in particular, it follows that in the initial changes in the Hf$^{(1)}$ texture, which are the most evident in comparison with other ones (Fig. 3, 4), preference should also be attributed to twinning.

For a detailed explanation of this, a calculation of the $f_{RD}(hki0)$ values, characterizing the directionality of normals to the prismatic planes along the RD (instead of the "c" axes, as is accepted for TP), has been carried out. Practically it has taken in account the directions within 30º around the RD. An analogue of formula (2) has been used with the replacement $\cos^2\alpha_{ij} \rightarrow \sin^2\alpha_{ij}$:

$$f_{RD}(hki0) = \sum_i A'_i P_i \sin^2 \alpha_i , \tag{4}$$

where A'_i is the statistical weight of the poles, additionally bounded by the such angular limits and so equal to either A_i, or zero, or intermediate values. All values refer to the RD.

The meaning of this task is to analyze the juxtaposition of quotes of prismatic – $(hki0)$ – and basal (axis "c") orientations along RD, and their changes during deformation.

In this regard, in Figure 6 the graph of correlation of f_{RD} with $f_{RD}(hki0)$ for all deformation degrees of the Hf$^{(1)}$ plates is presented. As can be seen, the graph obviously represents a linear correlation of these values. Significantly, its course is extrapolated to coordinates (1; 0). So, if $f_{RD}(hki0)$ could reached its maximum, i.e. unit, then the parameter f_{RD} (i.e. $f_{RD}(0002)$) according to formula (3) would vanish.

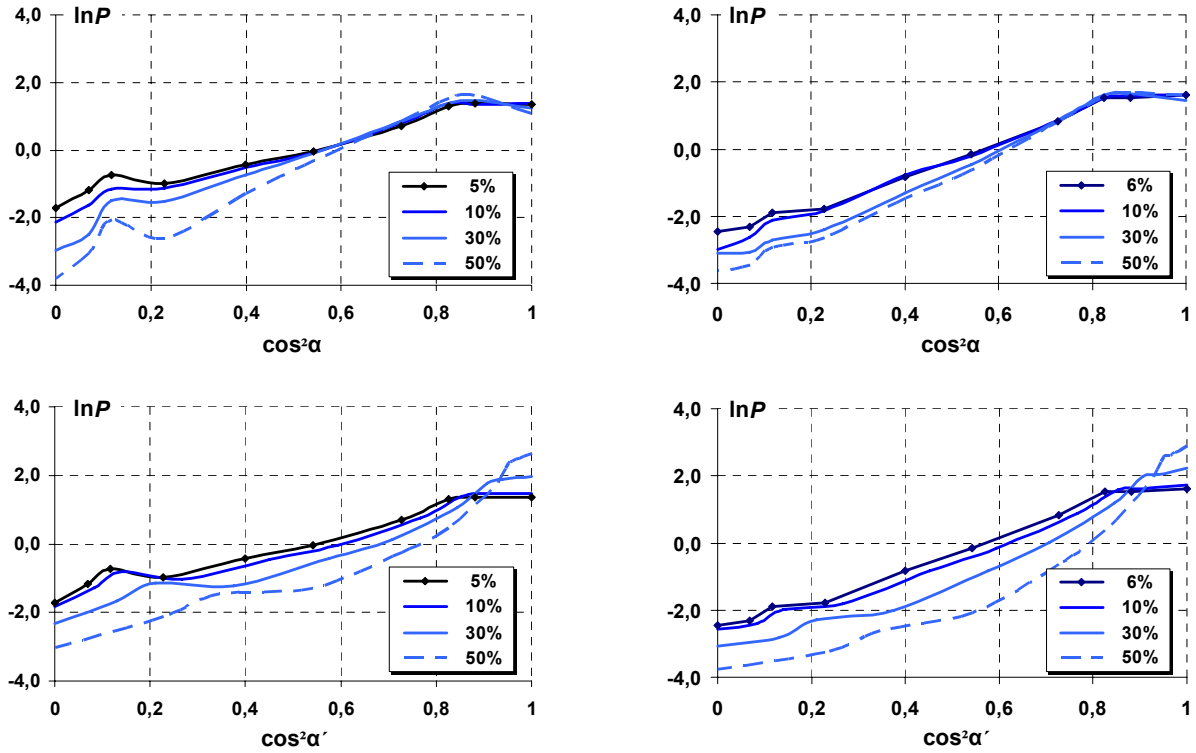

Fig. 5. Graphs of changes in the experimental (upper figures) and calculated sequences of values of the pole density (lower figures) measured in normal direction of the deformed Hf(2) (left) and Zr samples (right-hand).

It follows from this that the initial rotation of the "c" axes from the RD towards the ND (and a slight reverse for deformations above 5%) is done with immediate exchanges (0002) ↔ (*hki*0). In other words, the turn acts are made practically on 90°. It is meant, intermediate orientations do not participate in this. By the way, they are practically absent (Fig.1, RD).

This shows that the changes of the TPs at the initial stage of deformation of the Hf(1) are carried out exclusively by intensive twinning, and predominantly by the $\{10\bar{1}2\}\langle\bar{1}011\rangle$ system, which rotates the axes by 85° [9.10].

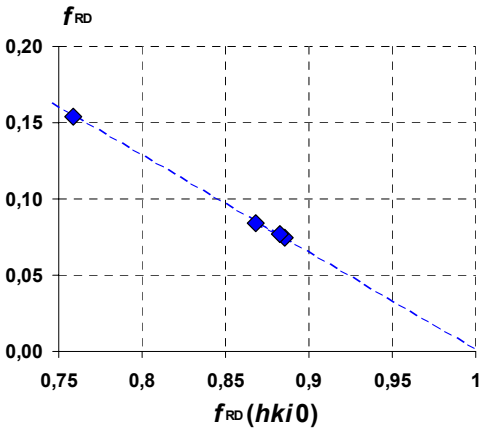

Fig.6. Correlation between f_{RD} and $f_{RD}(hki0)$ parameters at all the deformation degrees for the Hf(1).

For the Hf(2) and zirconium, the conditions for this are insufficient. Evidently, such a process in these materials could end at the stage of making the original plates. An initial stage of TPs changes in pre-annealed zirconium plates can be expected if the initial f_{RD} parameter will noticeably exceed a value of 0.06.

The results obtained are in general consistent with existing concepts, according to which twinning exhibits high activity at deformation of hcp metals [11], significantly affects their texture [10-12] and plays an exclusive role in texture formation in zirconium alloys [13]. Moreover, it does a significant contribution to the mechanical properties of hcp metals [14].

CONCLUSIONS

By the method of inverse pole figures, X-ray studies of dependence of the crystallographic texture of hafnium and zirconium plates, in particular, the texture parameter of Kearns (TP) on degree of cold deformation by rolling are carried out. Measurements are done in the rolling plane of plates and in two other orthogonal directions.

In the changes of TPs with the degree of deformation of hafnium and zirconium, the presence of two stages has been revealed. Unlike the initial one, the subsequent stage is characterized by a moderate rate of change of TPs, in particular, by small changes in the rolling direction.

The level and rate of changes of the TPs at the initial and, in part, the characteristics of the subsequent stage depends on the initial state of the material, in this case on degree of difference of the initial TPs from their expected values in the subsequent stage.

Using the example of hafnium, which is characterized by a relatively high value of the initial TP in the rolling

direction, it is found that the increased rate of initial changes of this parameter is exclusively associated with intensive twinning, predominantly of its $\{10\bar{1}2\}\langle\bar{1}011\rangle$ system. The arguments for dominance of twinning in formation of the texture of hafnium and zirconium in the subsequent stage are given.

REFERENCES

1. Kearns J. Thermal expansion and preferred orientation in Zircaloy // USAEC WAPD-TM-472. Nov. 1965.
2. Ageyev N.V., Babareko A.A., Betsofen S.Ya. Method of inverse pole figures // Izvestiya AN SSSR. Ser.: Metals. – 1974. – No. 1. – P. 94-103.
3. Harris. G.B. Quantitative measurement of preferred orientation in rolled uranium bars // Phil. Mag. – 1952. – Vol. 43. – No. 336. – P. 113-123.
4. Morris P.R. Reducing the effects of non-uniform pole distribution in inverse pole figure studies // J. Appl. Physics. – 1959. – Vol. 30. – No. 4. – P. 595 -596.
5. Mirkin L.I. Reference book on X-ray analysis of policrystals. Red. prof. Umanskij. Moscow. State ed. phys.-mat. liter. – 1961. – 864 P.
6. Grytsyna V., Stukalov A., Chernyayeva T. et al. Destruction of crystallographic texture in zirconium alloy tubes // Fourteenth International Symposium: Zirconium in Nuclear Industry. Stockholm, Sweden, June 13-17, 2005. ASTM Stock. Number: STP1467. Bridgeport, NJ. – 2006. – P. 305-329.
7. Malykhin D.G., Kovtun G.P., Potina T.S. Features of texture, microhardness and deformation mechanisms in cold-rolled hafnium // Voprosy atomnoi nauki i tehniki. Ser.: «Vacuum, pure metals, superconductors (21)». – 2016. – No.1(101). – P. 35-40.
8. Luan B.-F., Ye Q., Chen J.-W. et al. Deformation twinning and textural evolution of pure zirconium during rolling at low temperature // Trans. Nonferr. Met. Soc. China. – 2013. – No. 23. – P. 2890-2895.
9. Chernyayeva T.P., Grytsyna V.M. Characteristics of HCP metals defining its behavior at mechanical, thermal and radiation treatment // Voprosy atomnoi nauki i tehniki. Ser.: «Physics of radiation damages and radiation material science» (92). – 2008. – No. 2. – P. 15-27.
10. E. Tenckhoff. Review of deformation mechanisms, texture and mechanical anisotropy in zirconium and zirconium base alloys // Proceedings of XVI International Symposium «Zirconium in Nuclear Industry». West Conshohocken, ASTM STP1467. – 2006. – P. 25-50.
11. Vishnyakov Ya.D., Babareko A.A., Vladimirov S.A. et. al. Theory of formation of textures in metals and alloys. Moscow.: Nauka, 1979. – 345p.
12. Calnan E.A., Clews C.J.B. // Phil. Mag. – 1952. – Vol. 42A. – No. 328. – P. 919-931.
13. Tome C.N., Lebensohn R.A., Kocks U.F. A model for texture development dominated by deformation twinning: application to zirconium alloys // Acta Metall Mater. – 1991. – Vol. 39. – No. 11. – P. 2667-2680.
14. Tome C.N., Agnew S.R., Blumenthal W.R. et al. The relation between texture, twinning and mechanical properties in hexagonal aggregates // Materials Science Forum. – 2002. – Vol. 408-412. – P. 263-268.

East Eur. J. Phys. Vol.4 No.3 (2017) 43-47 DOI:10.26565/2312-4334-2017-3-06

PACS: 61.80.Ba

THE FORMATION OF SURFACE LAYERS IN Zr-Fe ALLOYS UNDER ION IRRADIATION

V.G. Kirichenko, V.A. Kobylnik, T.A. Kovalenko, O.A. Usatova
V. N. Karazin Kharkiv National University
4. Svobody Sq., 61022, Kharkiv, Ukraine
E-mail: val.kir.248@gmail.com
Received April 25, 2017

The study of phase transformations in intermetallic phases, which are released in the form of fine-dispersed inclusions in binary alloys based on zirconium Zr - 1.03 at. % Fe; Zr - 0.51 at. % Fe; after ion irradiation and subsequent isothermal annealing was carried out. Mössbauer spectroscopy on ^{57}Fe nuclei in backscattering geometry with registration of internal conversion electrons, X-ray spectral analysis, X-ray diffraction analysis and electron microscopy were used. As a result, the observed segregation and phase composition of the intermetallic phases in the surface layer change under ion irradiation. Subsequent isothermal annealing after irradiation leads to a change in the concentration of inclusions of intermetallic phases and phase modification in the surface layer.
KEY WORDS: zirconium, alloys, phases, segregation, ion, irradiation

ФОРМУВАННЯ ПОВЕРХНЕВИХ ШАРІВ В Zr-Fe **СПЛАВАХ ПРИ ІОННОМУ ОПРОМІНЮВАННІ**
В.Г. Кіріченко, В.А. Кобильник, Т.О. Коваленко, О.О. Усатова
Харківський національний університет імені В.Н. Каразіна
61022, Харків, м. Свободи, 4
У роботі проведено дослідження фазових перетворень в інтерметалічних фазах, які виділяються у вигляді дрібнодисперсних включень в бінарних сплавах на основі цирконію після іонного опромінення і подальшого ізотермічного відпалу. Використовували мессбауерівську спектроскопію на ядрах ^{57}Fe в геометрії зворотного розсіювання з реєстрацією електронів внутрішньої конверсії, рентгеноспектральний аналіз, рентгеноструктурний аналіз і електронну мікроскопію. В результаті виявлена сегрегація і фазовий склад интерметаллических фаз в поверхневому шарі змінюється при іонному опроміненні. Подальший ізотермічний відпал після опромінення призводить до зміни концентрації включень интерметаллических фаз і модифікації фаз в поверхневому шарі.
КЛЮЧОВІ СЛОВА: цирконій, сплави, фази, зріст, сегрегація, іон, опромінення

ФОРМИРОВАНИЕ ПОВЕРХНОСТНЫХ СЛОЕВ В Zr-Fe СПЛАВАХ ПРИ ИОННОМ ОБЛУЧЕНИИ
В.Г. Кириченко, В.А. Кобыльник, Т.А. Коваленко, О.А. Усатова
Харьковский национальный университет имени В.Н. Каразина
61022, г. Харьков, пл. Свободы, 4
В работе проведено исследование фазовых превращений в интерметаллических фазах , которые выделяются в виде мелкодисперсных включений в бинарных сплавах на основе циркония после ионного облучения и последующего изотермического отжига. Использовали мессбауэровскую спектроскопию на ядрах ^{57}Fe в геометрии обратного рассеяния с регистрацией электронов внутренней конверсии, рентгеноспектральный анализ, рентгеноструктурный анализ и электронную микроскопию. В результате обнаруженная сегрегация и фазовый состав интерметаллических фаз в поверхностном слое изменяется при ионном облучении. Последующий изотермический отжиг после облучения приводит к изменению концентрации включений интерметаллических фаз и модификации фаз в поверхностном слое.
КЛЮЧЕВЫЕ СЛОВА: цирконий, сплавы, сегрегация, ион, облучение

Zirconium alloys such as E-110M, E-125, E-635, Zry-2, Zry-4, M5, ZIRLO have been widely used in nuclear power engineering [1]. The basic problems in the operation of zirconium alloys under irradiation are due to the presence of radiation growth and radiation creep due to anisotropy of α - zirconium. Used zirconium alloys differ with radiation growth, radiation creep, corrosion resistance, high temperature strength [2]. The experimental results on the formation of gradient corrosion-resistant structural-phase states in materials and fuel claddings of thermal reactors have been considered and summarized [3]. The action by high-temperature pulsed plasma flows is effective for changing the surface layer of materials. For example, as applied to E110 and E635 zirconium alloys, new structural-phase states formed by the method of "ion mixing" [3].

Such effects are associated with recently discovered gradient materials with high technological properties [4]. Optimization of gradient materials is realized by introducing nanoparticles into the surface layers. In [5] it is found that an increase in the surface concentration of iron atoms in zirconium alloys in a layer up to 0.3 μm thick is associated with an increase in the size of inclusions with an increase in the annealing temperature of the deformed alloys. The amorphization alloys based on zirconium under ion irradiation was observed [6]. The formation of amorphous intermetallic phases on the surface of zirconium alloys after ion irradiation can be attributed to the viscosity of zircaloys and the influence of the viscosity of the metallic matrix on the crystallization of amorphous phases during annealing after irradiation [6].

The purpose of this work is the research after ion irradiation of surface layers of zirconium alloys with Fe^{57} additions by Mossbauer spectroscopy on Fe^{57} nuclei.

EXPERIMENTAL METHODS

For the study alloys Zr - 1.03 at. % Fe, Zr - 0.51 at. % Fe was made. The procedure for their preparation is described in [6]. Mössbauer spectroscopy on ^{57}Fe nuclei was used in the backscattering geometry with registration of internal conversion electrons (CEMS). An X-ray spectral analysis of the surface of annealed zirconium alloy samples was carried out on a Camebax MBX 268 spectrometer. X-ray study of alloys was carried out on the DRON-3.0. X-ray diffraction analysis showed that at all stages of thermo mechanical processing of alloys the matrix phase composition is represented by the alpha-phase of Zr.

RESULTS AND DISCUSSION

The solubility limit of Fe in α-Zr decreases from value 0.015±0.001 % at 943 K to value 0.004±0.001 % at 713 K [7,8]. Consequently, when doping zirconium with iron in the metallic matrix of alloys the precipitates of intermetallic phases of complex composition are formed. In a binary Zr-Fe system 5 intermetallic compounds was found: Zr_4Fe, Zr_3Fe, Zr_2Fe, $ZrFe_2$ and $ZrFe_3$ [9].The equilibrium Zr-Fe phase diagram is shown in Fig. 1 [10].

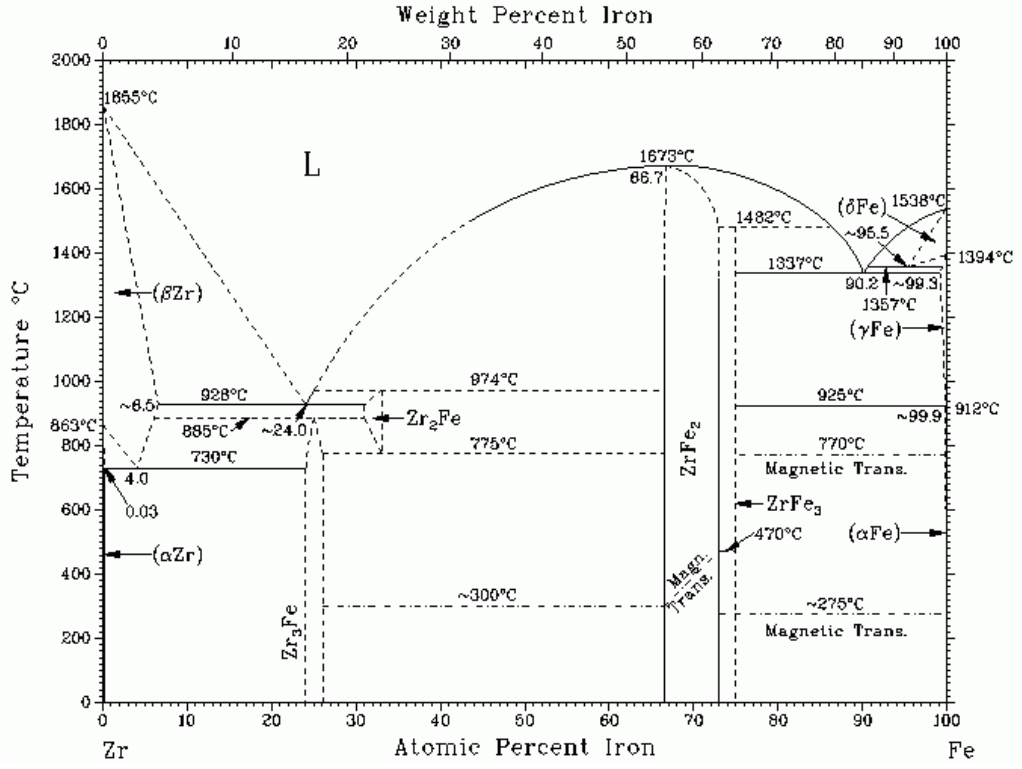

Fig. 1. The equilibrium Zr-Fe phase diagram

Parameters of Mossbauer spectra of formed intermetallic phases in Zr-Fe system are given in the Table.

Table

The Mossbauer parameters of the phases in the binary system Zr-Fe

Phase	Isomer shift, δ, mm/s	Quadruple splitting, Δ, mm/s	Composition, at. % Fe	Crystal structure
$ZrFe_2$	- 0.22(1)	0.46(1)	67	C15 type
Zr_2Fe	- 0.31(1)	0.75(1)	33	$CuAl_2$ type
Zr_2Fe	- 0.12(1)	0.30(1)	33	Ti_2Ni type
Zr_3Fe	- 0.33(1)	0.91(1)	25	Re_3B type
α-Zr_4Fe	- 0.34(1)	0.85(1)	20	hexagonal structure
β-Zr_4Fe	- 0.3(1)	0.75(1)	20	orthorhombic structure
ZrFe (solid solution)	0.04(1)	-	0.02	α-phase

CEMS scattering spectrum of the surface of the Zr-1.03 aт % Fe alloy after annealing at 970 K for 5 h is shown on Fig. 2. The spectrum has a doublet structure with doublet parameters characteristic for the phase Zr_3Fe.

According to experimental data the stable phase Zr_3Fe is formed after high temperature annealing (1100-1200 K) and has the orthorhombic Re_3B type structure with a=3.326 Å, b=10.988 Å, c=8.807 Å. Fe atoms in this structure have only one position and with 6 Zr atoms as nearest neighbors [9].

Deformed alloys characterized broadened X-ray reflexes due to the increase in the dislocation density in the surface layer, furthermore, the formation of segregations of a second phase on the formed defects.

Analysis of the scattering spectra of annealed deformed alloys in the Zr-Fe system leads to the conclusion that the surface layer is enriched with intermetallic inclusions, which contain in its composition Fe atoms.

The degree of enrichment of the surface layer due to the creation of a gradient layer as a result of thermal annealing of deformed alloy is shown in Fig. 3. Experimental data are presented as the diagram in the coordinates C-T to describe the surface segregation of intermetallic phases inclusions, where C – concentration ^{57}Fe atoms composed of intermetallic phase; T – the annealing temperature (Fig. 3). The concentration of ^{57}Fe atoms increase with temperature of annealing emphasizing the greatest increase in iron concentration and consequently the presence of gradient of intermetallic phases in the surface layer.

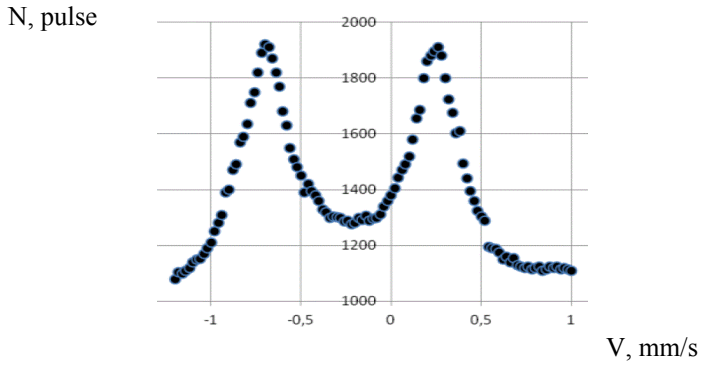

Fig. 2. CEMS scattering spectrum of the surface of the Zr-1,03 ат% Fe alloy after annealing at 970 K for 5 h

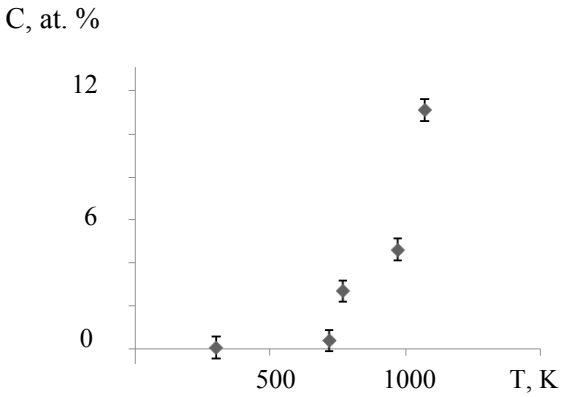

Fig. 3`. Dependence of iron concentrations in the surface layer Depth 300 nm of the alloy from the thermal annealing temperature of the deformed layer Zr-1.03 at.% Fe

The results of calculations using the program SRIM-2008.04 of damages cascade and ion profile of the distribution of iron atoms in the Zr-1.03 at. % alloy under irradiated with iron ions with an energy of 600 keV are shown in Fig. 4,5.

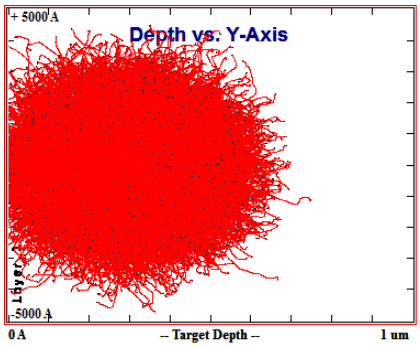

Fig. 4. Damage cascade with energy of 600 keV ions

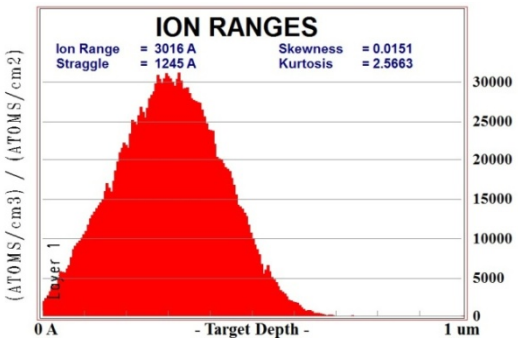

Fig. 5. Ion distribution under energy of 600 keV ions

The results of the calculations indicate that there is a weak dependence of the diameter of the cascade band d and the energy ranges R on the alloy composition and the strong dependence on the ion energy.

The calculations carried out with the help of the SRIM-2008.04 program will make it possible to make an effective choice of ion irradiation regimes in imitation experiments. The results of calculations of the effect of ion irradiation of a layer of zirconium-iron alloy which contain 12 at% iron in a layer 300 nm and 600 nm deep, respectively, are shown in Fig. 6,7.

CEMS spectrum of Zr-1.03 at% Fe alloy surface layer, which enriched up to 12 at. % Fe, after iron ion irradiation with an energy of 600 keV and after addition annealing at 970 K for 5 h is shown in Fig. 8. This spectrum consists of two components belonging to the amorphous phase (with a smaller value of quadruple splitting), which was formed after irradiation and the crystalline phase into which the amorphous phase turns during annealing. The spectrum of the crystalline phase has a higher value of quadruple splitting.

The dependence of the concentration change ΔC in the 300 nm layer on the iron content C in the layer and the additional annealing temperature T after irradiation is shows In Fig. 9. This 3D –diagram demonstrate the dependence

of the iron content on the annealing temperature in the surface layer 300 nm deep after ion irradiation and after additive annealing. This data demonstrate the possibility of the controlled formation of gradient layers after thermal annealing and ion irradiation. Additional annealing reduces the spatial scale of the created gradient structures in the concentration range of 14-16% and the annealing temperature range of 670-720 K.

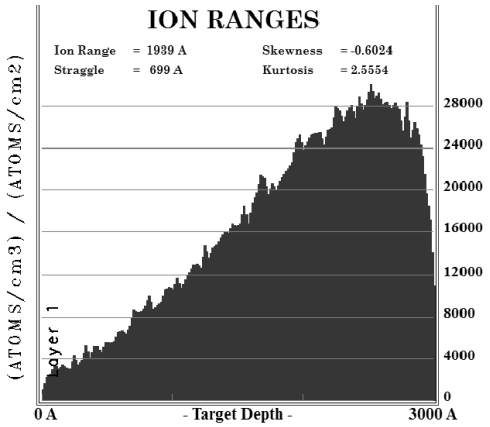

Fig. 6. Distribution of iron ions in the zirconium-iron alloy layer with a layer depth of 300 nm

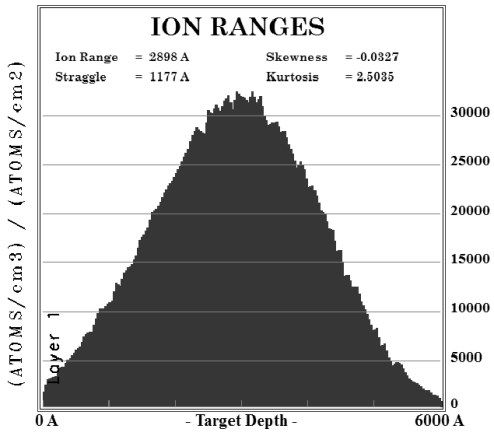

Fig. 7. Distribution of iron ions in the zirconium-iron alloy layer with a layer depth of 600 nm

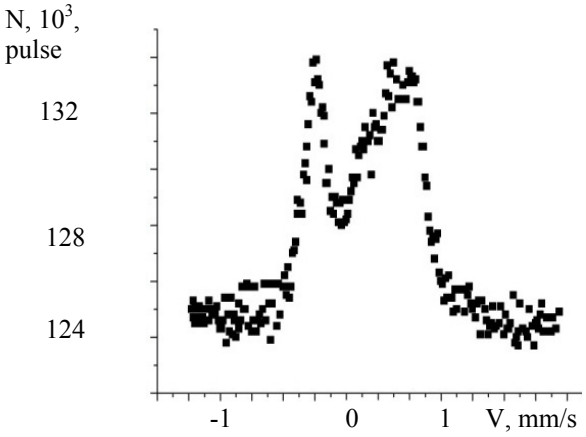

Fig. 8. CEMS spectrum of surface of Zr-1.03 at% Fe alloy after iron ion irradiation with an energy of 600 keV and after annealing at 970 K for 5 h

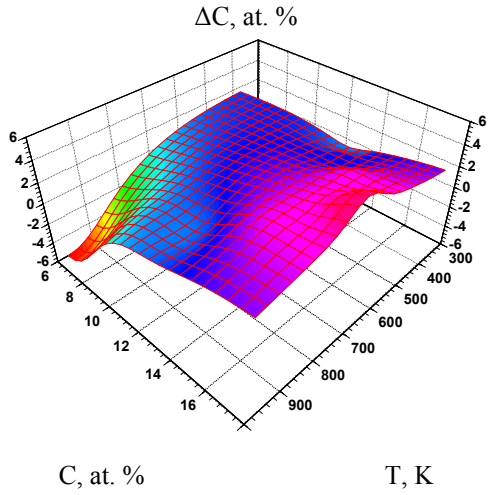

Fig. 9. The dependence of the concentration change in the 300 nm layer on the iron content in the layer and the additional annealing temperature after irradiationture

Another important problem is the amorphization of intermetallic phases in surface layer under the irradiation by ions of the amorphous state of alloys, metastable and crystalline phases are formed after further annealing, while the crystallization temperatures and the entropy of crystallization activation depend on the composition of the alloy.

CONCLUSIONS

Thus, a layer of 300 nm depth enriched with intermetallic inclusions before irradiation of the surface of the zirconium-iron alloy was created by thermal annealing of the deformed alloys. Irradiation by Fe^{4+} ions with energy 600 keV of surface enriched layer leads to transformation of crystalline Zr_3Fe to amorphous phase. It is possible to create multi component gradient structures under ion irradiation of the alloy surface. The growth and disintegration of inclusions under thermal annealing after irradiation is not controlled by bulk diffusion and the migration of iron atoms can be associated with the presence of inter phase boundaries was found

REFERENCES

1. Solonin M.I., Reshetnikov F.G., Nikulina V.A. New Construction Materials for Active Zone in Nuclear Power Plants // Nucl. Mater. – 2004. – Vol. 25. – P.12–14.
2. Rogerson A. Irradiation growth in zirconium and its alloys // J. Nucl. Mater. – 1988. – Vol.159. – P.43-61.
3. Kalin B.A., Volkov N.V., Yakushin V.L. Radiation-beam action as a method to form gradient structural-phase state in materials of nuclear engineering // Problems of Atomic Science and Technology. Series: Physics of Radiation Damage and Radiation Material Science. – 2007. – No.2 (90). – P.164-171.

4. Na K.S., Kim J.H. Optimization of volume fractions for functionally graded panels considering stress and critical temperature // Composite structures. – 2009. – Vol.89. – P. 509-516.
5. Kirichenko V.G., Yampolsky A.A. Features of the formation of surface gradient layers in zirconium alloys // Problems of Atomic Science and Technology. Series: Physics of Radiation Damage and Radiation Material Science. – 2017. – No. 2 (108). - P. 114-116.
6. Kirichenko V.G., Azarenkov N.A. Nuclear physics of zirconium alloys. – Kharkiv: KHNU imeni V.N. Karazina, 2012. – 336p. (In Russian)
7. Stupel M.M., Weiss B.Z. Determination of Fe solubility in α-Zr by Mossbauer spectroscopy // Scr. Met. – 1985. – Vol. 19. – No. 6. – P. 739–740.
8. Filippov V.P., Kirichenko V.G., Salomasov V.A., Khasanov A.M. Phase transformations in intermetallic phases in zirconium alloys // Hyperfine Interact. (2017) 238:23. – DOI 10.1007/s10751-016-1377-3. Springer International Publishing Switzerland 2017.
9. Aubertin F., Gonser U., Campbell S. An appraisal of the phases of the Zirconium-Iron system // Z. Metallkunde. – 1985. – Bd. 76. – No. 4. – S. 237–244.
10. http://www.himikatus.ru/art/phase-diagr1/Fe-Zr.php

EAST EUROPEAN JOURNAL OF PHYSICS
East Eur. J. Phys. Vol.4 No.3 (2017) 48-53 DOI:10.26565/2312-4334-2017-3-07

PACS: 52.40.Hf

PHASE STATES OF MACROPARTICLES IN PLASMA WITH HOT ELECTRONS AT PRESENCE OF ION BEAM

O.A. Bizyukov, O.D. Chibisov, O.I. Kutenko
V. N. Karazin Kharkiv National University
4. Svobody Sq., 61022, Kharkiv, Ukraine
e-mail: alekx0930741952@gmail.com
Received September 1, 2017

The evaporation possibility of micro sized metallic particles during them passage through the region of a magnetized plasma with a Maxwellian velocity distribution with the electron temperature in the range T_e=1...100eV at presence of an ion beam with the energy in the range ε_b=1...6keV is studied theoretically. The floating potential of a macroparticle is obtained using the OML theory, the effect of the electron temperature and the energy of the ion beam on its magnitude is studied. The equation of energy balance on the macroparticle surface is obtained, such energy exchange mechanisms as collisions of particles of an ion beam and plasma particles with the macroparticle, thermal radiation of the macroparticle, as well as cooling due to the evaporation of substance from the macroparticle surface are taken into account. The effect of the temperature of plasma electrons and the ion beam energy on the stationary temperature of the macroparticle is studied. It is shown that for the given plasma and ion beam parameters, the temperature of the copper macroparticle is below the boiling point so that the evaporation of the macroparticle occurs at temperatures below the boiling point. The dependences of the macroparticle evaporation time on the electron temperature and the energy of the ion beam have been obtained.
KEYWORDS: macroparticles, dusty plasma, ion beam, evaporation, electric potential

ФАЗОВЫЕ СОСТОЯНИЯ МАКРОЧАСТИЦ В ПЛАЗМЕ С ГОРЯЧИМИ ЭЛЕКТРОНАМИ В ПРИСУТСТВИИ ИОННОГО ПУЧКА

А.А. Бизюков, А.Д. Чибисов, А.И. Кутенко
Харьковский национальный университет имени В.Н. Каразина
61022, г. Харьков, пл. Свободы, 4

Теоретически изучается возможность испарения металлических макрочастиц микронных размеров при прохождении через область замагниченной плазмы с электронами, имеющими Максвелловское распределение по скоростям с температурой в диапазоне T_e=1…100 эВ, и в присутствии ионного пучка с энергией в диапазоне ε_b=1…6 кэВ. В приближении OML теории вычисляется плавающий потенциал макрочастицы, изучается влияние температуры электронов а также энергии ионного пучка на его величину. Получено уравнение баланса энергий на поверхности макрочастицы, при этом принимаются во внимание такие механизмы обмена энергией, как столкновение частиц ионного пучка и частиц плазмы с макрочастицей, тепловое излучение макрочастицы, а также охлаждение за счет испарения вещества с поверхности макрочастицы. Изучается влияние температуры плазменных электронов и энергии ионного пучка на стационарную температуру макрочастицы. Показано, что при заданных параметрах плазмы и ионного пучка такая равновесная температура медной макрочастицы находится ниже точки кипения, так что испарение макрочастицы происходит при температурах ниже температуры кипения. Получены зависимости времени испарения медных макрочастиц от температуры электронов и энергии ионного пучка.
КЛЮЧЕВЫЕ СЛОВА: макрочастицы, пылевая плазма, ионный пучок, испарение, электрический потенциал

ФАЗОВІ СТАНИ МАКРОЧАСТОК В ПЛАЗМІ З ГАРЯЧИМ ЕЛЕКТРОНАМИ В ПРИСУТНОСТІ ІОННОГО ПУЧКА

О.А. Бізюков, О.Д. Чібісов, О.І. Кутенко
Харківський національний університет імені В.Н. Каразіна
61022, Харків, м. Свободи, 4

Теоретично вивчається можливість випаровування металевих макрочасток мікронних розмірів при проходженні через область замагніченої плазми з електронами, що мають розподіл максвела за швидкостями з температурою в діапазоні T_e = 1 ... 100 еВ, і в присутності іонного пучка з енергією в діапазоні ε_b = 1 ... 6 кеВ. У наближенні OML теорії обчислюється плаваючий потенціал макрочастки, вивчається вплив температури електронів а також енергії іонного пучка на його величину. Отримано рівняння балансу енергій на поверхні макрочастки, при цьому беруться до уваги такі механізми обміну енергією, як зіткнення частинок іонного пучка і частинок плазми з макрочасткою, теплове випромінювання макрочастки, а також охолодження за рахунок випаровування речовини з поверхні макрочастки. Вивчається вплив температури плазмових електронів і енергії іонного пучка на стаціонарну температуру макрочастки. Показано, що при заданих параметрах плазми і іонного пучка така рівноважна температура мідної макрочастки знаходиться нижче точки кипіння, так що випаровування макрочастки відбувається при температурах нижче температури кипіння. Отримано залежності часу випаровування мідних макрочасток від температури електронів і енергії іонного пучка.
КЛЮЧОВІ СЛОВА: макрочастки, пилова плазма, іонний пучок, випаровування, електричний потенціал

Plasma which contains micron sized particles of a substance (dust plasma) in the laboratory is mainly formed as a result of plasma sources operation, as well as a result of erosion of surfaces of a vacuum chamber. In technological processes, such as deposition of coatings, plasma treatment of surfaces, at creating of microelectronic devices, etc., the

presence of dust particles (macroparticles or MPs) in plasma is a negative factor, as it leads to deterioration of such properties of the treated surfaces as porosity of coatings, adhesion of coatings and surface roughness [1-3]. In practice, the most of ways of decreasing the droplet flow on the processed surface are based on separation of the ion flow and the droplet flow by the magnetic fields [3-7].

The aim of this paper is the considering of the possibility of decreasing of the droplets flow due to evaporation of the macroparticles by the heating of plasma electrons at presence of the ion beam.

CHARGING OF THE MP

It is known that the MP immersed in the plasma is charged as a result of absorption of electrons and ions of plasma, as well as various types of electron emission from the MP surface. The magnitude of the charge determines which way MP interacts with the plasma and is one of the key parameters affecting on the energy balance of the MP. Charge of the MP is determined by the condition that the sum of the electrical currents on the surface of the MP is equal to zero. Calculation of the currents from plasma on the MP at presence of the magnetic field is a difficult problem, however in some cases various approximations are used successfully. In particular, if the magnetic field is not strong enough such the condition

$$r_g >> \lambda_d >> a\ , \tag{1}$$

is correct, where r_g is the Larmor radius of electron, λ_d is the Debye length, a is the MP radius, in a collisionless plasma, for describing of the ion and electron currents on the MP Orbital-Motion-Limited (OML) theory is used [8]. In this paper we consider plasma with the magnetized electrons which temperature T_e is in the range 10-100eV, ion temperature T_i is 1eV, plasma density n_0 is $10^{10}-10^{11} cm^{-3}$. Ion beam energy varies in the range 1-6000eV. Strength of the magnetic field B is such that the condition (1) is correct and we can use the OML theory.

According to the OML theory, electron and ion currents from the plasma to the MP surface have the form:

$$I_{i(e)} =< en_0 v_{i(e)} \sigma_{i(e)}^{OML} >= e \cdot \Gamma_{i(e)}\ , \tag{2}$$

where $\sigma_{i(e)}^{OML} = \pi a^2 \left(1 \pm \frac{2e\varphi_a}{m_{i(e)} v_{i(e)}^2}\right)$ is the absorption cross section of ions (electrons) in the OML theory,

$$\Gamma_i = \sqrt{8\pi} a^2 n_0 v_{Ti} \left(1 - e\varphi_a / T_i\right),$$

and

$$\Gamma_e = \sqrt{8\pi} a^2 n_0 v_{Te} \exp\left(-e\varphi_a / T_e\right)$$

are the flows of the ions and electrons on the MP surface, φ_a is the potential of the MP surface, $v_{Ti(e)} = \sqrt{T_{i(e)} / m_{i(e)}}$ is the ion (electron) thermal velocities. Electric current of a secondary electron from the MP surface can be found by averaging over all energies of the electrons:

$$I_e^{e-e} =< n_0 e v_e \sigma_e^{OML} \delta^{e-e} >\ , \tag{3}$$

where

$$\delta^{e-e} = \delta_{\max} \frac{E - e\varphi_a}{E_m} \exp\left(2(1 - \sqrt{\frac{E + e\varphi_a}{E_m}})\right)$$

is the secondary emission yield, E is the kinetic energy of primary electron, E_m is the electron energy which corresponds to the maximum of secondary emission yield $\delta_{\max}$. Ion beam current in terms of OML theory is:

$$I_i^b = en_0 v_i \sigma_j^{OML} = e\Gamma_b\ , \tag{4}$$

where v_i is the ion velocity, Γ_b is the flow of the ions on the MP surface.

Secondary electron emission produced by the ion impact (for energies about 1 keV) we can express through the emission yield γ as:

$$I_e^{i-e} = e\gamma\Gamma_b\ . \tag{5}$$

Taking into account the charging processes described above (2) - (5), the MP potential can be found by solving the equation of electric currents balance:

$$I_e^{e-e}(\varphi_a) + I_e^{i-e}(\varphi_a) + I_i^{pl}(\varphi_a) + I_i^b(\varphi_a) - I_e^{pl}(\varphi_a) = 0\ . \tag{6}$$

Results of numerical solution of the equation (6) for cooper MP is shown in the Fig. 1,2. From the Fig. 1 it can be seen, that when the electron temperature is increasing, absolute value of MP potential is increasing as well. It can also be seen, that curve 4 has a local minimum which is caused by the increasing of electron yield from the MP surface. Fig. 2 shows, that when ion beam energy increases, absolute value of MP potential decreases. Thus, increasing of the ion beam energy leads to increasing of electron flow onto MP surface.

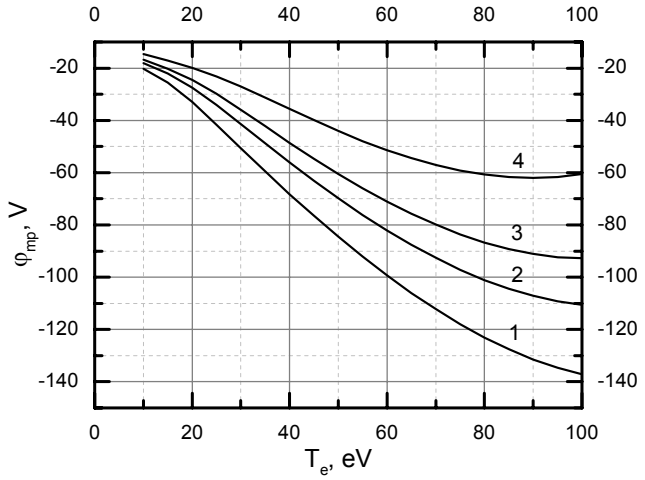

Fig. 1. The dependencies of the MP potential on the electron temperature at different energies of the ion beam (1 - $\varepsilon_b = 1$keV , 2 - $\varepsilon_b = 2$keV , 3 - $\varepsilon_b = 3$keV ,4 - $\varepsilon_b = 6$keV)

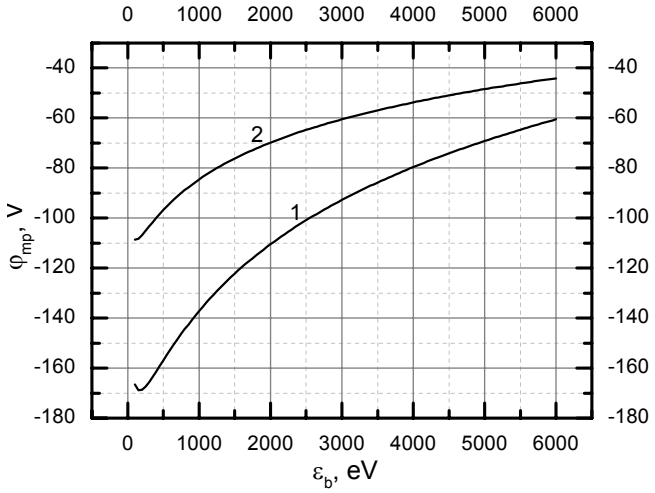

Fig. 2. The dependence of the MP potential on the ion beam energy at different electron temperatures (1-T_e=100 eV, 2-T_e=50 eV)

HEATING AND EVAPORATION OF THE MP

Absorption of the plasma ions and electrons as well as beam ions leads not only to charge transferring but also energy transferring from the plasma and ion beam that causes intensive heating of the MP. Consider the processes that are involved in energy exchange. In plasma with a Maxwellian velocity distribution of particles in the OML theory, energy flows are described by:

$$P_i = \Gamma_i \cdot (2T_i + e\varphi_a + I)\,, \tag{7}$$

$$P_b = \Gamma_b \cdot (\varepsilon_b + e\varphi_a + I)\,, \tag{8}$$

$$P_e = \Gamma_e \cdot 2T_e\,, \tag{9}$$

where I is the ionization energy of an atom. The power radiated from the MP surface is described by the Stefan–Boltzmann law:

$$P_r = 4\pi a^2 \sigma T_a^4\,, \tag{10}$$

where σ is the Stefan-Boltzmann constant. Energy flow due to evaporation of MP substance is described by:

$$P_{evpr} = \Gamma_a \cdot (2k_B T_a + p)\,, \tag{11}$$

where

$$\Gamma_a = 4\pi a^2 n' \sqrt{\frac{k_B T_a}{2\pi m_a}} \exp\left(-\frac{p}{k_B T_a}\right)$$

is the flow of the evaporated atoms from the MP surface, n' is the concentration of the atoms in the metal, p is the heat of evaporation of an atom.

Stationary temperature of the MP T_a^{st} can be found as a result of solution of the balance energy (7)-(11) equation on the MP surface:

$$P_i(\varphi_a, T_i) + P_e(\varphi_a, T_e) + P_b(\varphi_a, \varepsilon_b) - P_r(T_a^{st}) - P_{evpr}(T_a^{st}) = 0 . \quad (12)$$

Equation (12) have been solved numerically. There were obtained dependences of stationary temperature of the MP as a function of electron temperature (Fig. 3) and ion beam energy (Fig. 4).

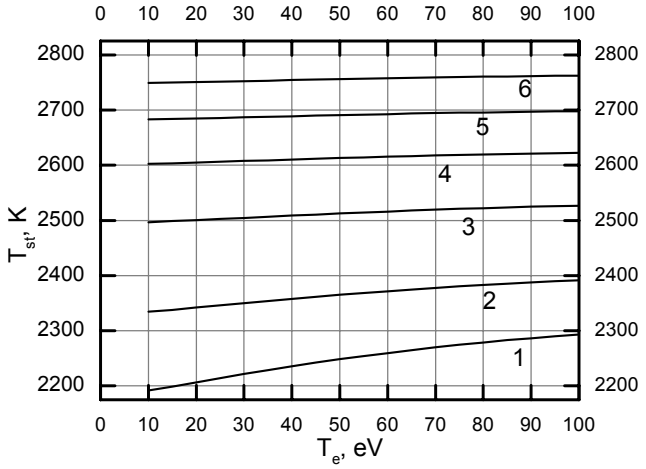

Fig. 3. Stationary temperature of the MP as a function of the electron temperature
(1- $\varepsilon_b = 1$keV , 2- $\varepsilon_b = 2$keV , 3- $\varepsilon_b = 3$keV , 4- $\varepsilon_b = 4$keV , 5- $\varepsilon_b = 5$keV , 6- $\varepsilon_b = 6$keV)

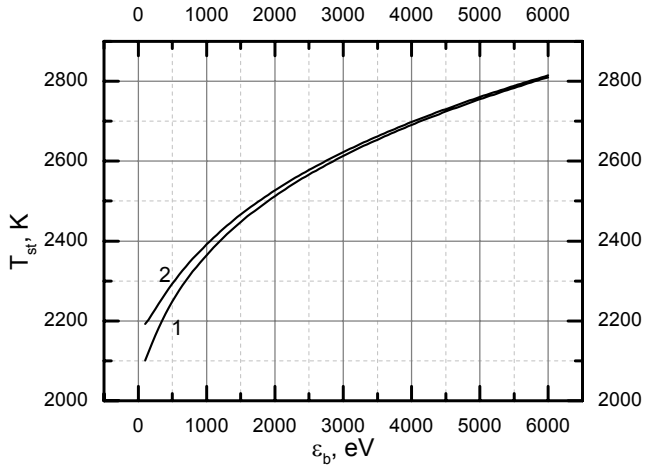

Fig. 4. Stationary temperature of the MP as a function of the ion beam energy
(1- $T_e = 50$eV , 2- $T_e = 100$eV)

Numerical calculations of (12) were performed for copper, however similar results can be obtained for other metals. Fig. 3,4 show that stationary temperature strongly depends on the ion beam energy and slightly depends on the electron temperature at current parameters. The performed calculations show, that at all energies of the ion beam and electron temperatures, stationary temperature does not reach the boiling point (for cooper). Such strong cooling is achieved due to the intensive evaporation of the MP substance.

During the evaporation (vaporization), changing of the mass of the MP substance is described by the equation:

$$dm = \frac{P_{evpr}(\varphi_a, T_a^{st}) \cdot dt}{H}, \tag{13}$$

where $P_{evpr}(\varphi_a, T_a^{st},) = P_i(\varphi_a, T_i) + P_e(\varphi_a, T_e) + P_b(\varphi_a, \varepsilon_b) - P_r(T_a^{st})$ is the power which is spent to evaporation of the MP substance, H is the heat of evaporation. Time of evaporation of the MP with a radius a is calculated by integrating of the equality (13):

$$t_{evpr} = \frac{4\pi a^3 \rho H}{3P_{evpr}(\varphi_a, T_a^{st})}. \tag{14}$$

Results of the numerical calculations of (14) are shown in the Fig. 5,6.

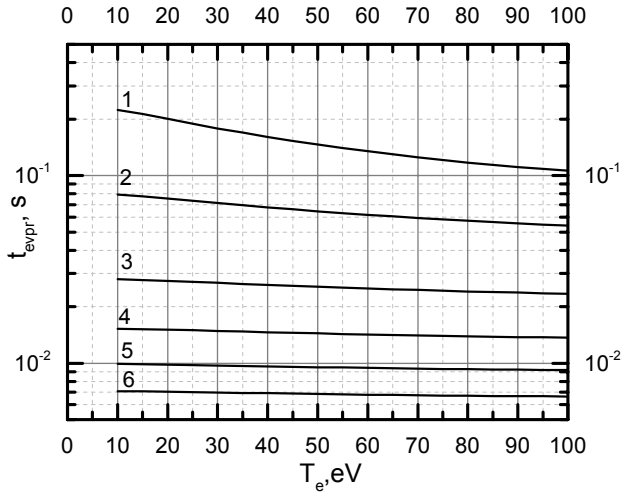

Fig.5. Dependence of the evaporation time of the MP ($a = 10\mu m$) on the electron temperature
(1- $\varepsilon_b = 1$keV , 2- $\varepsilon_b = 2$keV , 3- $\varepsilon_b = 3$keV , 4- $\varepsilon_b = 4$keV , 5- $\varepsilon_b = 5$keV , 6- $\varepsilon_b = 6$keV)

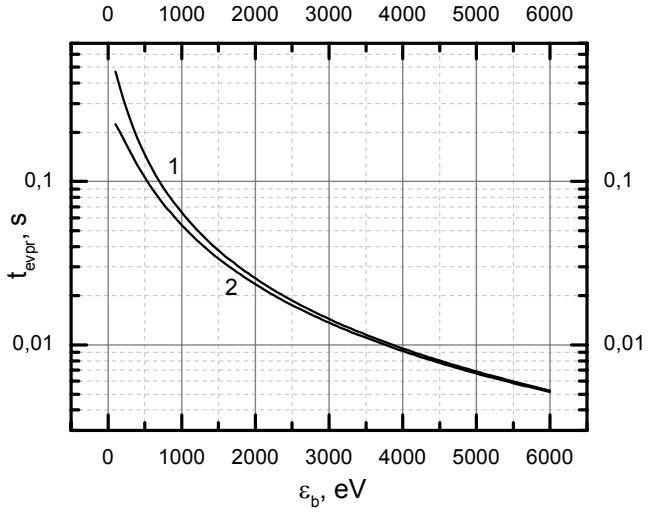

Fig. 6. Dependence of the evaporation time of the MP ($a = 10\mu m$) on the ion beam energy
(1- $T_e = 100$eV , 2- $T_e = 50$eV)

The obtained results show that total evaporation time of 10mkm cooper MP is in the range $4 \cdot 10^{-1}$-$5 \cdot 10^{-3}$s and depending on the electron temperature and ion beam energy. Evaporation of the MP takes place at temperatures below boiling point at all values of ion beam energy as well as electron temperature. Increasing of the ion beam energy significantly decrease the MP evaporation time, whereas increasing of the electron temperature gives the slight effect

on the evaporation time at considered parameters. The ion beam provides heating of the MP by two ways: by direct transferring of ion kinetic energy due to impact with the MP surface and the following recombination; indirect way due to decrease of MP electric potential and consequently increasing energy transfer caused by the electron flow.

CONCLUSIONS

The possibility of evaporation of micro sized metallic particles in the magnetized high temperature technological plasma at presence of an ion beam in terms of OML theory has been studied. The dependencies of electric potential of the MP on the electron temperature as well as energy of the ion beam have been obtained. It has been shown that increasing of the ion beam energy leads to increases of electron flow onto MP surface since absolute value of MP potential is decreasing. The interaction of the MP with the particles of the plasma and ion beam causes intensive heating and following evaporation of the MP. Evaporation of the MP takes place at temperatures below boiling point at all considered values of ion beam energy as well as electron temperature due to intensive cooling by the evaporated atoms flow. It has been shown that total evaporation time of 10mkm cooper MP is in the range $4\cdot10^{-1}$-$5\cdot10^{-3}$s and depends on the electron temperature and ion beam energy. Increasing of the ion beam energy significantly decrease the MP evaporation time, whereas increasing of the electron temperature without ion beam gives the slight effect on the evaporation time at considered parameters.

REFERENCES

1. Eds.R.L. Boxman, D.M. Sanders, Martin P.J. Handbook of Vacuum Arc Science and Technology: Fundamentals and Applications. NJ: Noyes Publ. 1995, P. 742.
2. Anders A. Cathodic Arcs: From Fractal Spots to Energetic Condensation. Springer Science Business Media, LLC, 2008, p.540.
3. Aksenov I.I., Andreyev A.A., et. al. Vacuum arc: sources of plasma, deposition of coatings, surface modification. – Kiev: Naukova dumka, 2012. – P. 238-273. (in Russian)
4. Anders A., Anders S., Brown I. G. Transport of vacuum arc plasmas through magnetic macroparticle filters // Plasma Sources Sci. Technol. – 1995. – Vol. 4. – No. 1. – P. 1-12.
5. Karpov D.A. Cathodic arc sources and macroparticle filtering // Surf. Coat. Techol. – 1997. – Vol. 96. – No. 1. – P. 22-33.
6. Khoroshikh V.M. Stationary vacuum arc in technological systems for surface treatment // Physical surface engineering – 2003. – Vol. 1. – No. 1. – P. 19-26. (in Russian)
7. Aksenov I.I., Belous V.A., Padalka V.G., Khoroshikh V.M. Transportation of plasma flows in a curvilinear plasma-optical system // Plasma physics. – 1978. – Vol. 4. – No. 6. – P. 758-763. (in Russian)
8. Fortov V.E., Khrapak A.G., et. al. Dusty plasma // UFN. – 2004. – Vol. 174. – No. 5. – P. 495-544.

EAST EUROPEAN JOURNAL OF PHYSICS
East Eur. J. Phys. Vol.4 No.3 (2017) 54-62 DOI:10.26565/2312-4334-2017-3-08

PACS: 87.14.Cc, 87.16.Dg

MOLECULAR DYNAMICS STUDY OF CYTOCHROME *C* – LIPID COMPLEXES

V. Trusova, G. Gorbenko, U. Tarabara, K. Vus, O. Ryzhova
Department of Nuclear and Medical Physics, V.N. Karazin Kharkiv National University
4 Svobody Sq., Kharkiv, 61022, Ukraine
e-mail: valerija.trusova@karazin.ua
Received August 1, 2017

The interactions between a mitochondrial hemoprotein cytochrome *c* (cyt *c*) and the model lipid membranes composed of zwitterionic lipid phosphatidylcholine (PC) and anionic lipids phosphatidylglycerol (PG), phosphatidylserine (PS) or cardiolipin (CL) were studied using the method of molecular dynamics. It was found that cyt *c* structure remains virtually unchanged in the protein complexes with PC/PG or PC/PS bilayers. In turn, protein binding to PC/CL bilayer is followed by the rise in cyt *c* radius of gyration and root-mean-square fluctuations. The magnitude of these changes was demonstrated to increase with the anionic lipid content. The revealed effect was interpreted in terms of the partial unfolding of polypeptide chain in the region Ala15-Leu32, widening of the heme crevice and enhancement of the conformational fluctuations in the region Pro76-Asp93 upon increasing the CL molar fraction from 5 to 25%. The results obtained seem to be of utmost importance in the context of amyloidogenic propensity of cyt *c*.
KEYWORDS: cytochrome c; protein-lipid interactions; amyloid, molecular dynamics

МОЛЕКУЛЯРНО-ДИНАМІЧНЕ ДОСЛІДЖЕННЯ КОМПЛЕКСІВ ЦИТОХРОМУ *С* З ЛІПІДАМИ
В. Трусова, Г. Горбенко, У. Тарабара, Е. Вус, О. Рижова
Кафедра ядерної та медичної фізики, Харківський національний університет імені В.Н. Каразіна
пл. Свободи 4, Харків, 61022, Україна
Методом молекулярної динаміки досліджено взаємодію мітохондріального гемопротеїну цитохрому *с* з модельними мембранами, що складались із цвіттеріонного ліпіду фосфатидилхоліну (ФХ) та аніонних ліпідів фосфатидилгліцерину (ФГ), фосфатидилсерину (ФС) чи кардіоліпіну (КЛ). Показано, що структура цитохрому *с* залишається практично незмінною у комплексах білка з ФХ/ФГ чи ФХ/ФС бішарами. У свою чергу, зв'язування білка із ФХ/КЛ бішарами супроводжується збільшенням радіусу інерції та середньоквадратичних флуктуацій цитохрому *с*. Продемонстровано, що величина цих змін зростає із вмістом аніонного ліпіду. Винайдені ефекти були інтерпретовані у рамках часткового розгортання поліпептидного ланцюга в області Ala15-Leu32, розширення гемового карману та посилення конформаційних флуктуацій на ділянці Pro76-Asp93 при зростанні молярної частки КЛ від 5 до 25%. Отримані результати важливі у контексті амілоїдогенної здатності цитохрому *с*.
КЛЮЧОВІ СЛОВА: цитохром *с*, білок-ліпідні взаємодії, амілоїд, молекулярна динаміка

МОЛЕКУЛЯРНО-ДИНАМИЧЕСКОЕ ИССЛЕДОВАНИЕ КОМПЛЕКСОВ ЦИТОХРОМА *С* С ЛИПИДАМИ
В. Трусова, Г. Горбенко, У. Тарабара, Е. Вус, О. Рыжова
Кафедра ядерной и медицинской физики, Харьковский национальный университет имени В.Н. Каразина
пл. Свободы 4, Харьков, 61022, Украина
Методом молекулярной динамики исследовано взаимодействие митохондриального гемопротеина цитохрома *с* с модельными мембранами, состоящими из цвиттерионного липида фосфатидилхолина (ФХ) и анионных липидов фосфатидилглицерина (ФГ), фосфатидилсерина (ФС) или кардиолипина (КЛ). Показано, что структура цитохрома *с* остается практически неизменной в комплексах белка с ФХ/ФГ или ФХ/ФС бислоями. В свою очередь, связывание белка с ФХ/КЛ бислоями сопровождается увеличением радиуса инерции и величины среднеквадратичных флуктуаций цитохрома *с*. Продемонстрировано, что величина этих изменений возрастает с содержанием анионного липида. Выявленные эффекты были интерпретированы в рамках частичного разворачивания полипептидной цепи в области Ala15-Leu32, расширение гемового кармана и усиление конформационных флуктуаций на участке Pro76-Asp93 при возрастании молярной доли КЛ от 5 до 25%. Полученные данные важны в контексте амилоидогенной способности цитохрома *с*.
КЛЮЧЕВЫЕ СЛОВА: цитохром *с*, белок-липидные взаимодействия, амилоид, молекулярная динамика

One-dimensional crystallization of the proteins and peptides into highly ordered fibrillar structures, termed amyloids, is a key factor in etiology of a number of disorders, including Alzheimer's, Parkinson's, Huntingtons diseases, type II diabetes, rheumatoid arthritis, spongiform encephalophaties, etc [1]. Amyloid fibrils are distinguished by a core cross-β-sheet structure in which β-strands run perpendicularly to the long axis of the fibril, while β-sheets propagate in its direction [2]. Amyloid assembly is a hierarchical process that is currently regarded as alternative folding [3], since both the intrachain and interchain contacts are governed by the common forces, *viz.* hydrophobic effect, hydrogen-bonding, charge attraction and van der Waals interactions [4]. Protein oligomerization followed by amyloid formation is commonly initiated by the transition of polypeptide chain into unstable aggregation-competent conformation [5]. Since the compactness of native state is compromised by the loss of configurational entropy during polypeptide folding and repulsive electrostatic interactions, the native protein structure is only marginally stable and any variation in physicochemical properties of polypeptide environment may prove critical for protein transition from monomeric to aggregated state [6]. In vitro, fibrillization-favoring conditions are created by lowering pH, elevating temperature,

adding organic solvents or denaturants, etc., while in vivo, aggregation-competent conformation may arise from mutations, oxidative or heat stress, or destabilization of the protein structure upon its adsorption at interfaces. It is the presence of large amount of interface, formed by cellular membranes, that determines the principal difference between in vitro and in vivo amyloid growth. Lipid bilayer, a basic structural element of biological membranes, may act as an effective catalyst of fibrillogenesis, providing an environment where protein molecules accumulate and adopt conformation and orientation promoting their assembly into protofibrillar and fibrillar structures. The problem of membrane-mediated fibrillogenesis has been approached in a number of works, demonstrating the complexity and multiplicity of factors which may control fibrillogenesis in membrane systems [7-9]. It has been hypothesized that anionic phospholipids represent the main membrane component responsible for the enhancement of fibril formation, as shown, particularly, for α-synuclein [10], Aβ peptide [7], amylin [11], tau [12], lysozyme, transthyretin, cytochrome c, insulin, myoglobin [13]. An increasing number of studies provides support to the idea that lipid bilayer can lower the activation energy barrier for protein unfolding [14]. Partial unfolding in a membrane environment has been reported, for instance, for phospholipase A2, bacterial toxins, acetylcholinesterase, pheromone-binding protein, recombinant human prion protein, etc [15]. The role of lipids as a structure-forming environment is not restricted to electrostatic phenomena (lowered interfacial pH or neutralization of the protein surface charge by anionic headgroups), other bilayer characteristics may have an impact on the protein structure as well. It is becoming increasingly apparent that development of effective anti-amyloid strategies is impossible without elucidating the mechanisms by which lipids promote transition of the protein molecule into aggregation-competent conformation. One of the powerful modern tools to address this problem is the method of molecular dynamics (MD). This method is highly suitable for uncovering the atomistic level details of polypeptide conformational changes in solution and in a membrane environment [16,17], protein folding and misfolding [18,19], the assembly of prefibrillar and fibrillar aggregates [20], etc.

The aim of the present study involves the use of MD simulation to gain insight into the role of acidic phospholipids in the occurrence of potentially amyloidogenic conformations of cytochrome *c* (cyt *c*), a basic protein playing an essential role in the electron transfer in the respiratory chain of the inner mitochondrial membrane and programmed cell death, apoptosis [21,22]. It has been demonstrated that cyt *c* is capable of forming amyloid fibrils in vitro, although the physiological significance of this property is not clear [23-25]. Nevertheless, α-synuclein and cyt *c* have been found to be colocalized in Lewy bodies of patients with Parkinson's disease [26]. It has been hypothesized that there exists yet unknown link between apoptosis and neurodegeneration [23,26]. Therefore, examining the conformational dynamics of cyt *c* in various environments is of great importance for understanding the determinants and physiological role of amyloidogenic propensity of this protein.

MATERIALS AND METHODS

Molecular dynamics simulations were performed with GROMACS software (version 5.1) using the CHARMM36 force field [B33]. The calculations were done at a temperature of 310 K and a pressure of 1 bar. The crystal structure of horse heart cytochrome c (PDB ID: 1HRC) was used as a starting structure for simulations. The orientation of the protein with respect to the lipid/water interface was predicted using the PPM server [B34]. The input files for MD calculations were prepared using the web-based graphical interface CHARMM-GUI [B35]. The lipid bilayers were built from phosphatidylcholine (PC) and varying proportions of one of the anionic phospholipids, cardiolipin (CL, 5, 11 and 25 mol%), phosphatidylglycerol (PG, 10, 20 and 40 mol %) or phosphatidylserine (PS, 10, 20 and 40 mol %). The protein was solvated in the rectangular box with a minimum distance of 10 Å to the edges of the box. The TIP3P water model was used. To obtain a neutral total charge of the system a necessary number of counterions was added. For correct treatment of long-range electrostatic interactions, Particle Mesh Ewald algorithm was employed [B36]. The minimization and equilibration of the system were performed during 100 ps and 1 ns, respectively. The time step for MD simulations was 2 fs. The trajectories and coordinates were saved every 2 ps for further analysis. The whole time interval for MD calculations was 100 ns. The analysis tools included in GROMACS were used to calculate the root-mean-square deviations (RMSD), root-mean-square fluctuations (RMSF) and radius of gyratio (Rg). The evolution of the secondary structure was followed using the VMD program. The contact maps were generated with the CMView software [B37]. The analysis of cyt *c* three-dimensional structure after the simulation was performed using PyMOL.

RESULTS AND DISCUSSION

Cytochrome *c* is a globular protein composed of 104 amino acid residues, with a high α-helical content and minimal β-sheet structure (Fig. 1). Under physiological conditions there exists an equilibrium between a soluble native and membrane-bound states of cyt *c* [32]. Biological functions of cyt *c* are mediated by its interaction with cardiolipin, an anionic mitochondrial phospholipid with unique physicochemical properties [33]. The cyt *c* molecule has been assumed to contain two types of binding sites for anionic phospholipids, accounting for electrostatic interactions between the residues Lys72, Lys73 and deprotonated phosphate group (A-site) and hydrogen bonding between Asn52 and protonated phosphate (C-site) [34].

Moreover, it has been supposed that upon cyt *c* – CL association through C-site one of four CL acyl chains extends outwards from the lipid bilayer into the protein hydrophobic channel close to Asn52, thereby ensuring the hydrophobic protein-lipid interactions [34]. The idea of extended lipid anchorage initially put forward by Rytomaa &

Kinnunen [35], was further developed by Kalanxni & Wallace who proposed that CL acyl chain accommodates in the nonpolar pocket situated in the vicinity of Met80 loop [36], while Sinibaldi et al. suggested the insertion of two fatty acid chains of CL into two different hydrophobic channels of cyt *c* surrounding Met80 and Asn52 [37]. Along with the diversity of the binding modes, another characteristic feature of cyt *c* – CL interaction is the heterogeneity of the protein conformational states [38-40]. CL was reported to produce the loosening of cyt *c* tertiary structure, destabilization of the secondary structure, loss of Met_{80} – iron ligation and opening of the heme crevice, eventually leading to the increase of the protein peroxidase activity [41-43].

Fig. 1. Crystal structure of the horse heart cytochrome c (PDB code 1HRC). Shown in red is the heme group

Recent studies provided evidence for the existence of multiple conformations of CL-bound cyt *c* differing in the degree of protein unfolding and undergoing the conformational exchange between the extended and compact subpopulations [38,44]. Remarkably, the alterations in the protein structure are strongly coupled with the molecular reorganization of CL-containing lipid bilayers [45-47]. Similar to other basic proteins, cyt *c* is capable of gathering the anionic phospholipids into microdomains, but cyt *c* – CL systems display particular behavior due to decreased energetic barrier for the formation of the inverted hexagonal (H_{II}) phase [46] and toroidal lipid pores [47]. All the above phenomena are conjectured to be of importance for both electron transfer and apoptotic functions of cyt *c* and may contribute to its amyloidogenic propensity. Notwithstanding considerable advances in molecular-level understanding of cyt *c* – CL interactions, the precise mechanisms of this process still remain to be fully elucidated. One of the unresolved questions is how specific features of CL distinguishing it from other anionic phospholipids operate in determining the structural and functional peculiarities of cyt *c* – CL complexes. To address this question, we performed the molecular dynamics simulation of cyt *c* complexes with PC/CL, PC/PS and PC/PG bilayers. Fig. 2 illustrates the disposition of cyt *c* molecule relative to the negatively charged lipid/water interface predicted by the PPM server. Remarkably, the protein orients in such a way that the residues Lys72 and Lys73 face the membrane surface and this orientation is generally retained during the MD simulation.

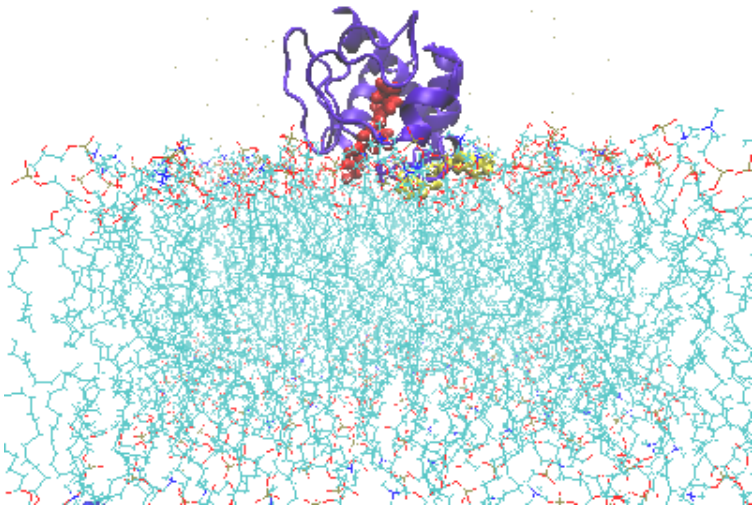

Fig. 2. Schematic illustration of the disposition of cyt *c* with respect to the lipid/water interface predicted by the PPM server. Shown in red is the heme group, while Lys72 and Lys73 are colored in yellow.

Figs. 3 and 4 represent the time course evolution of the two structural parameters of cyt *c* in the presence of lipid membranes – the radius of gyration (R_g) and root-mean-square fluctuations (RMSF) of C_α-atoms.

Notably, another parameter commonly used in the analysis of MD data, the backbone root-mean-square deviation (RMSD), did not show any significant difference between PC/CL, PC/PS and PC/PG systems suggesting that cyt *c* structure does not undergo considerable changes in a membrane environment within the examined time interval. At the same time, the radius of gyration was higher in CL-containing membranes, with the magnitude of this effect being increased with the molar content of CL (Fig. 3). Specifically, for the weakly charged lipid bilayers R_g was by ~7% higher in the presence of PC/CL membranes compared to PC/PG and PC/PS systems (Fig. 3A). The increase of the membrane charge resulted in ~11% (Fig. 3B) and ~14% (Fig. 3C) differences between CL- and PG/PS-containing bilayers. Similar tendencies were revealed while analyzing the root-mean-square fluctuations.

Concentrating on Fig. 4, it is clearly seen that: i) the residues Ala15-Leu32 experience much more pronounced

fluctuations compared to the other residues; ii) for CL-containing systems this effect is more conspicuous than for PC/PG or PC/PS bilayers; iii) the difference in RMSF values for the above protein region gradually increases with elevating the CL molar fraction, iv) the rise in CL content results in the enhancement of fluctuations in the region Pro76-Asp93. These findings led us to some preliminary conclusions: i) cyt *c* undergoes local conformational transitions in the region of Ala15-Leu32 and, to a lesser extent, in the region Pro76-Asp93; ii) these transitions are more specific for PC/CL lipid bilayers, as judged from the behavior of RMSF and R_g .

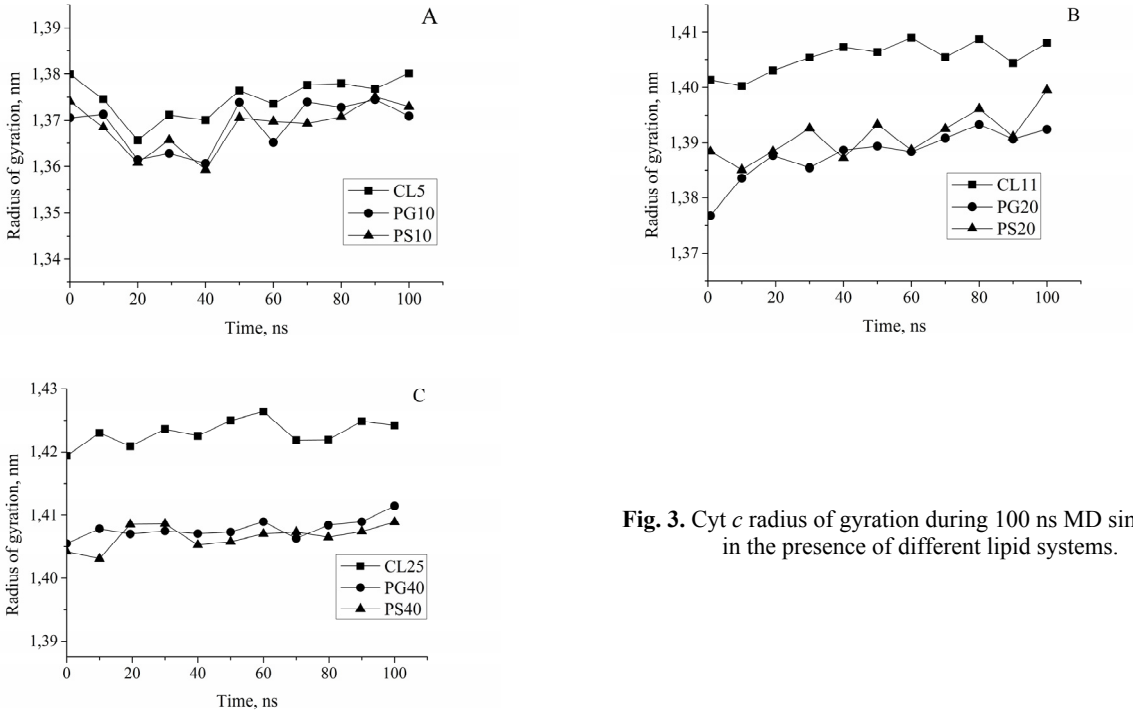

Fig. 3. Cyt *c* radius of gyration during 100 ns MD simulations in the presence of different lipid systems.

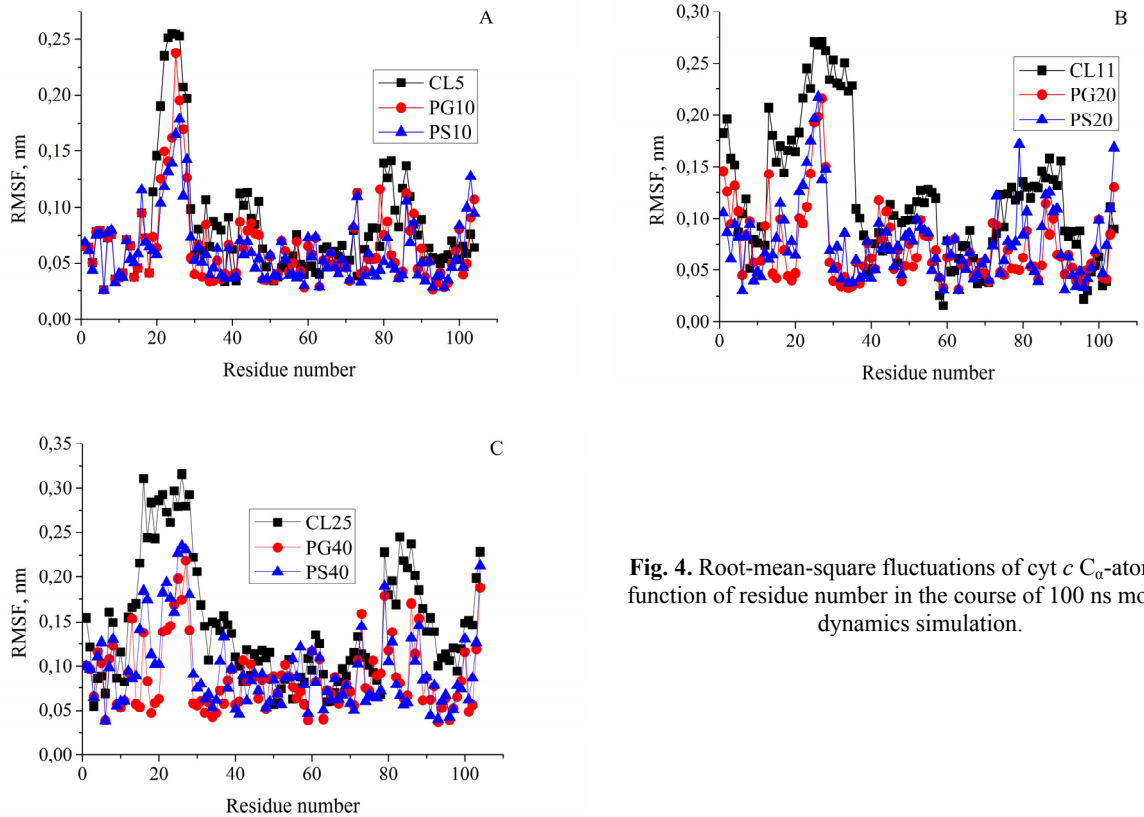

Fig. 4. Root-mean-square fluctuations of cyt *c* C_α-atoms as a function of residue number in the course of 100 ns molecular dynamics simulation.

In order to clarify what mechanism may be responsible for the aforesaid structural reorganization of polypeptide chain, we analyzed the time course of the changes in cyt *c* secondary structure. The representative plots are given in Fig. 5.

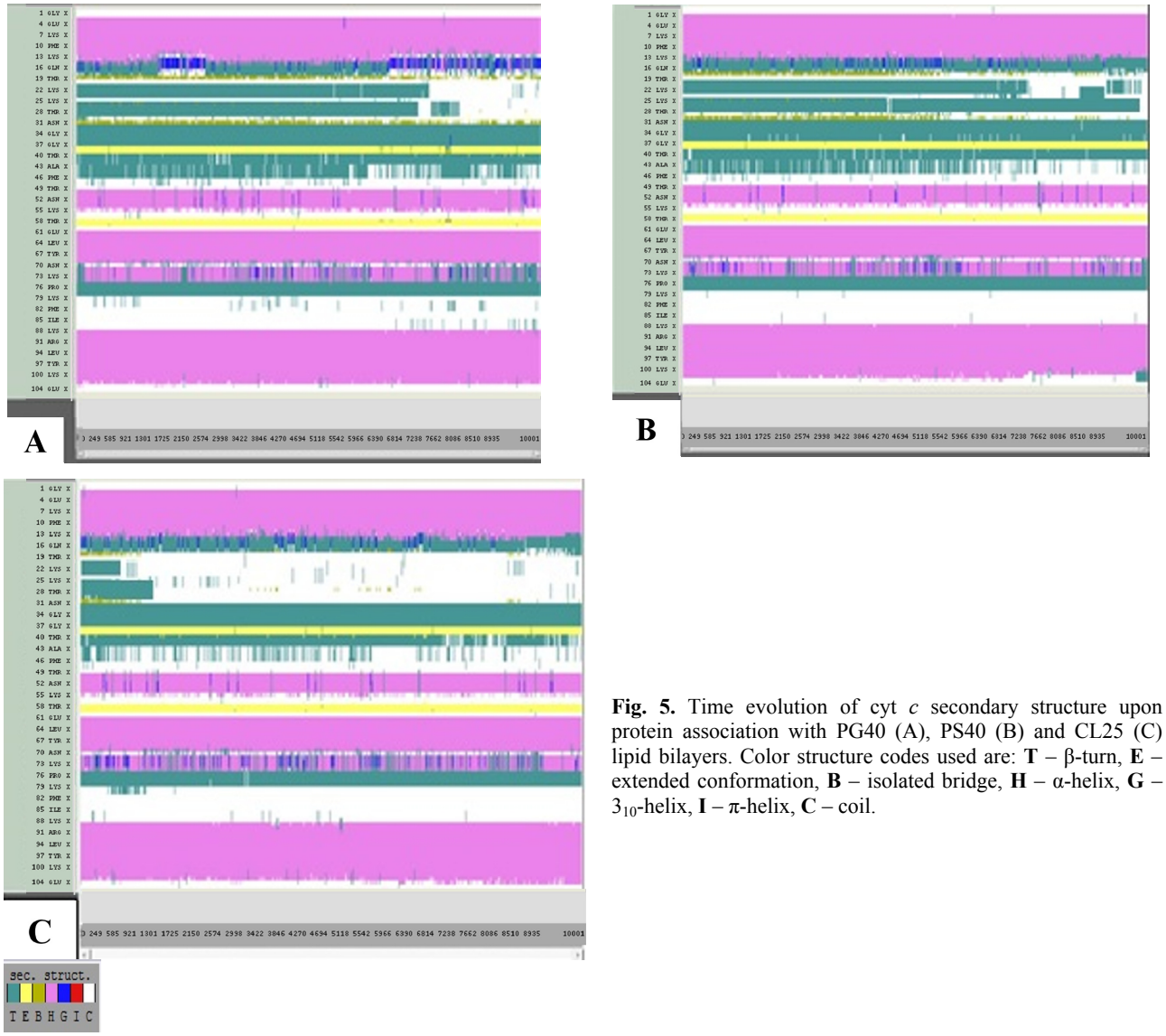

Fig. 5. Time evolution of cyt *c* secondary structure upon protein association with PG40 (A), PS40 (B) and CL25 (C) lipid bilayers. Color structure codes used are: **T** – β-turn, **E** – extended conformation, **B** – isolated bridge, **H** – α-helix, **G** – 3_{10}-helix, **I** – π-helix, **C** – coil.

It appeared that secondary structure of cyt *c* bound to PC/CL membranes differs from that observed in the presence of PC/PG or PC/PS lipid bilayers. Remarkably, the main difference involves the region Gln16-Asn31, the same fragment that was revealed by RMSF measurements. More specifically, in all cyt *c* – PC/PG(PS) systems the protein fragment Gln16-Asn31 adopts mostly turn conformation, while in cyt *c* – PC/CL complexes the unstructured (coiled) conformation of this region is predominant. Likewise, the content of coiled structures in the region Gln16-Asn31 increases with the molar fraction of CL, while in the presence of PC/PG(PS) membranes cyt *c* secondary structure was virtually independent of the proportion of anionic lipid. Furthermore, the comparison of timeline plots for cyt *c* free in solution (Fig. 5A) and those in the complexes with either PG- or PS-containing lipid bilayers (Figs. 5B and C) showed that the protein secondary structure undergoes slight alterations in these types of model membranes.

Notably, the peculiar features of CL-cyt *c* interactions have been revealed in the earlier studies [41,48,49]. More specifically, the affinity of cyt *c* for anionic phospholipids assessed by the surface plasmon resonance was found to decrease in the row: CL > PS > PC [49,50]. The solid-state ^{31}P NMR studies of cyt *c* interactions with CL, PS and PG bilayers showed that regardless the main driving force of all these interactions is electrostatic in nature, the structural alterations of the bound protein are lipid dependent [41,]. PS and CL were found to produce significant destabilization of cyt *c* structure, while in complexes with PG the protein retains a native-like conformation [41]. The resemblance between CL and PS in their effect on the structural state of cyt *c* was established in the early Raman [51,52] and ^{31}P NMR [50] studies. The two different conformational states of cyt *c* adsorbed on the negatively charged surfaces have been identified – the native-like state I and state II, with the opened heme crevice. The equilibrium between these two

states was supposed to be governed by the electrostatic interactions between lysine residues located around the heme crevice and the lipid phosphate groups. It was found that CL and PS promote the conformational equilibrium over the same temperature interval, while PG turned out to be less efficient in this respect, suggesting that cyt *c* conformation in complexes with PG is close to native [50]. A thorough recent work of Pandiscia & Schweitzer-Stenner provides evidence for an equilibrium between partially unfolded and native-like conformers of cyt *c* adsorbed on CL-containing bilayers, one of which forms electrostatic contacts with CL headgroups while the other one associates with lipids either via hydrogen bonding or hydrophobic interactions [40].

Overall, the MD data strongly suggest that lipid-induced conformational changes are specific for CL and involve the destabilization of the cyt *c* structure and partial unfolding of polypeptide chain in the region Gln16-Asn31, adjacent to the heme pocket. As indicated above, a great deal of experimental works provide evidence for partial unfolding of cyt *c* and opening of the heme crevice on the surface of CL-containing membranes [53-55]. One of the main mechanism underlying this phenomenon is assumed to involve the breakage of His26-Pro44 hydrogen bond [53,56]. It was shown that this bond plays a critical role in the stabilization of cyt *c* molecule [57], and its disruption triggers the destruction of Met80-heme ligation and opening of the heme crevice, the process resulting eventually in the loosening of the overall protein structure.

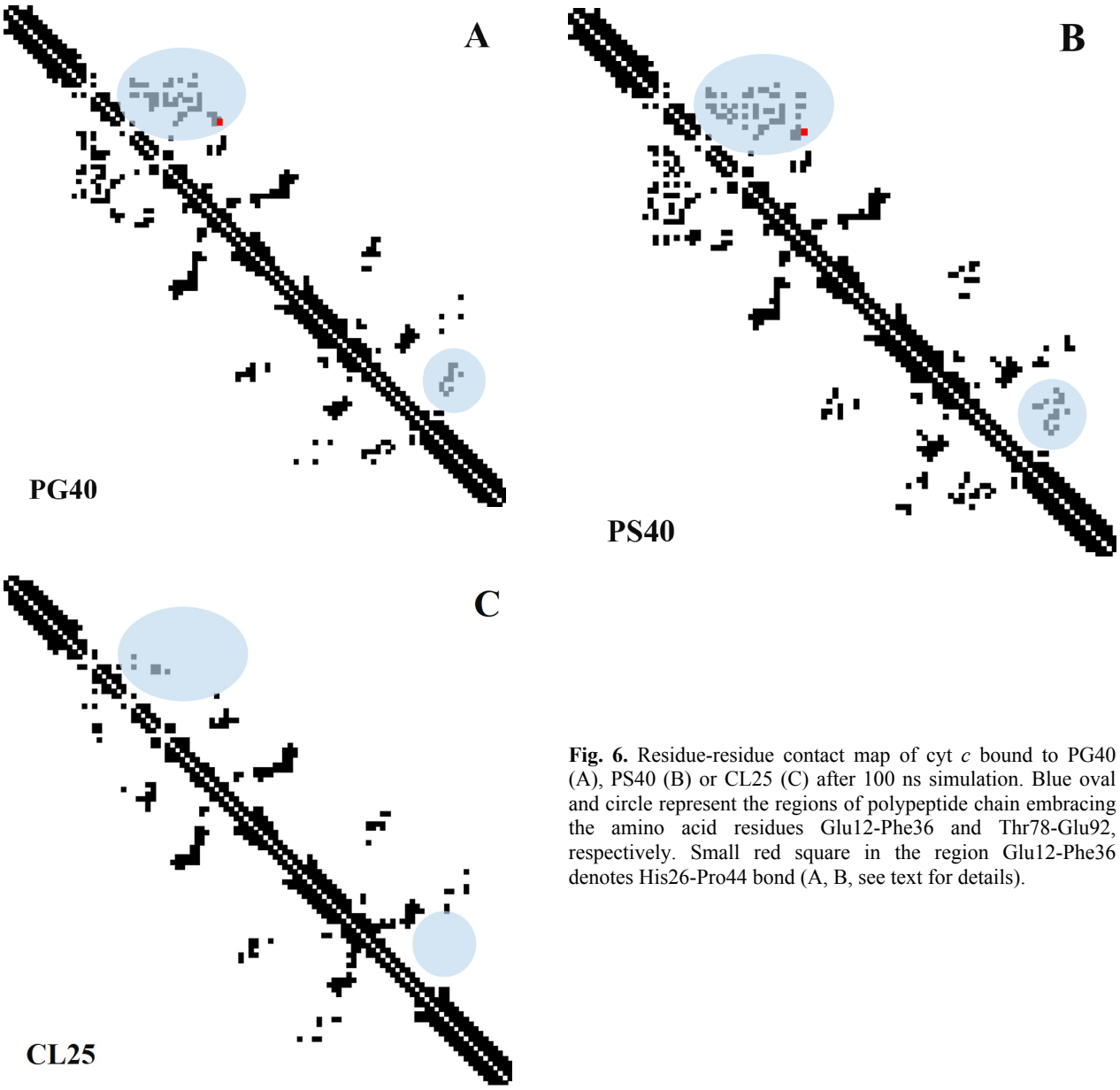

Fig. 6. Residue-residue contact map of cyt *c* bound to PG40 (A), PS40 (B) or CL25 (C) after 100 ns simulation. Blue oval and circle represent the regions of polypeptide chain embracing the amino acid residues Glu12-Phe36 and Thr78-Glu92, respectively. Small red square in the region Glu12-Phe36 denotes His26-Pro44 bond (A, B, see text for details).

Apparently, the described scenario manifests itself in the profiles of secondary structure evolution of cyt *c* recovered from the MD simulation of PC/CL lipid bilayers. Indeed, the comparison of cyt *c* inter-residue contact maps showed that His26-Pro44 bond is present in PC/PG or PC/PS (Figs. 6A and B) membranes, but disrupts when cyt *c*

binds to PC/CL bilayers (Fig. 6C). Furthermore, the contact maps are virtually identical for PC/PG and PC/PS systems, while cyt *c* complexation with PC/CL bilayers is accompanied by the reduction of the number of contacts, predominantly in the regions Glu12-Phe36 and Thr78-Glu92. The breaking of the contacts points to the perturbation of three-dimensional compactness of cyt *c* and adoption of more labile conformation in the aforementioned fragments of polypeptide chain. Notably, these findings are in excellent harmony with the results of RMSF calculations depicted in Fig. 4. Additional proofs in favor of the above conclusion come from the analysis of cyt *c* spatial structure after the simulation which showed that the width of the heme pocket increases from 0.91 nm in PG40 bilayers up to 1.07 nm in CL25 systems.

CONCLUSIONS

Cumulatively, the molecular dynamics simulation of the examined protein-lipid systems provided evidence for the local destabilization of cyt *c* structure, specific for CL-containing membranes. The analysis of 100 ns trajectories showed that:

- cyt *c* structure does not undergo noticeable perturbations upon its association with either PC/PG or PC/PS lipid bilayers;
- the complexation of cyt *c* with CL-containing membranes is followed by the protein transition into a more labile conformation arising from the widening of the heme crevice and partial unfolding of polypeptide chain mainly in the region Ala15-Leu32;
- increase of CL proportion from 5 to 25 mol% results in the enhancement of fluctuations in the region Pro76-Asp93.

The revealed specific features of cyt *c* – CL interactions may not only be a means of modulating the biological functions of this protein, but may also underlie its transition to the conformations favoring the oligomerization and fibrillization in a membrane-bound state.

ACKNOWLEDGEMENTS

This work was supported by the grant № 0116U000937 for Young Scientists from the Ministry of Science and Education of Ukraine.

REFERENCES

1. Chiti F., Dobson C.M. Protein misfolding, amyloid formation, and human disease: a summary of progress over the last decade // Annu. Rev. Biochem. – 2017. – Vol. 86. – P. 27-68.
2. Kelly J.W. Towards an understanding of amyloidogenesis // Nat. Struct. Biol. – 2002. – Vol. 9. – P. 323-325.
3. Zbilut J. P., Colosimo A., Conti F., Colafranceschi M., Manetti C., Valerio M., Webber Jr. C. L., Giuliani A. Protein aggregation/folding: the role of deterministic singularities of sequence hydrophobicity as determined by nonlinear signal analysis of acylphosphatase and Aβ (1-40) // Biophys. J. – 2003. – Vol. 85. – P. 3544-3557.
4. Seelig J. Thermodynamics of lipid-peptide interactions // Biochim. Biophys. Acta. – 2004. – Vol. 1666. – P. 40-50.
5. Gsponer J., Vendruscolo M. Theoretical approaches to protein aggregation // Protein Pept. Lett. – 2006. – Vol. 13. – P. 287-293.
6. Dill K. A. Dominant forces in protein folding // Biochemistry. – 1990. – Vol. 29. – P. 7133-7155.
7. Bokvist M., Lindstrom F., Watts A., Grobner G. Two types of Alzheimer's β-amyloid (1–40) peptide membrane interactions: aggregation preventing transmembrane anchoring versus accelerated surface fibril formation // J. Mol. Biol. – 2004. – Vol. 335. – P. 1039–1049.
8. Sharp J.S., Forrest J.A., Jones R.A.L. Surface denaturation and amyloid fibril formation of insulin at model lipid-water interfaces // Biochemistry – 2002. – Vol. 41. – P. 15810–15819.
9. Zhao H., Jutila A., Nurminen T., Wickstrom S.A., Keski-Oja J., Kinnunen P.K.J. Binding of endostatin to phosphatidylserine-containing membranes and formation of amyloid-like fibers // Biochemistry. – 2005. – Vol. 44. – P. 2857–2863.
10. Jo E., Darabie A.A., Han K., Tandon A., Frazer P.E., McLaurin J. α-synuclein – synaptosomal membrane interactions. Implications for fibrillogenesis // Eur. J. Biochem. – 2004. – Vol. 271. – P. 3180–3189.
11. Knight J.D., Miranker A.D. Phospholipid catalysis of diabetic amyloid assembly // J. Mol. Biol. – 2004. – Vol. 341. – P. 1175–1187.
12. Chirita C.N., Necula M., Kuret J. Anionic micelles and vesicles induce tau fibrillization *in vitro* // J. Biol. Chem. – 2003. – Vol. 278. – P. 25644–25650.
13. Zhao H., Tuominen E.K.J., Kinnunen P.K.J. Formation of amyloid fibers triggered by phosphatidylserine-containing membranes // Biochemistry. – 2003. – Vol. 43. – P. 10302–10307.
14. Uversky V.N., Fink A.L. Conformational constraints for amyloid fibrillation: the importance of being unfolded // Biochim. Biophys. Acta. – 2004. – Vol. 1698. – P. 131–153.
15. Gorbenko G. P., Kinnunen P. K. J. The role of lipid-protein interactions in amyloid-type protein fibril formation // Chem. Phys. Lipids. – 2006. – Vol. 141. – P. 72-82.
16. Wei G., Mousseau N., Derreumaux P. Computational simulations of early steps of protein aggregation // Prion. – 2007. – Vol. 1. – P. 3-8.
17. Avila C., Drechsel N., Alcantara R., Viila-Freixa J. Multiscale molecular dynamics of protein aggregation // Current Protein and Peptide Science. – 2011. – Vol. 12. – P. 221-234.
18. Beck D., Daggett V. Methods for molecular dynamics simulations of protein folding/unfolding in solution // Methods. – 2004. – Vol. 34. – P. 112-120.

19. Miao Y., Feixas F., Eun C., McCammon J.A. Accelerated molecular dynamics simulations of protein folding // J. Computat. Chem. – 2015. – Vol. 36. – P. 1536-1549.
20. Lemkul J.A., Bevan D.R. Assessing the stability of Alzheimer's amyloid protofibrils using molecular dynamics // J. Phys. Chem. B. – 2010. – Vol. 114. – P. 1652-1660.
21. Diaz-Moreno I., Garcia-Heredia J.M., Diaz-Quitana A., De la Rosa M.A. Cytochrome c signalosome in mitochondria // Eur. Biophys. J. – 2011. – Vol. 40. – P. 1301–1315.
22. Goodsell D.S. The molecular perspective: cytochrome c and apoptosis // The Oncologist. – 2004. – Vol. 9. – P. 226–227.
23. Haldar S., Sil P., Thangamuniyandi M., Chattopadhyay K. Conversion of amyloid fibrils of cytochrome c to mature nanorods through a honeycomb morphology // Langmuir. – 2015. – Vol. 31. – P. 4213–4223.
24. Groot N.S., Ventura S. Amyloid fibril formation by bovine cytochrome c // Spectroscopy. – 2005. – Vol. 19. – P. 199–205.
25. Furkan M., Fazili N.A., Afsar M., Naeem A. Analysing cytochrome c aggregation and fibrillation upon interaction with acetonitrile: an in vitro study // J. Fluoresc. – 2016. – Vol. 26. – P. 1959–1966.
26. Hashimoto M., Takeda A., Hsu L.J., Takenouchi T., Masliah E. Role of cytochrome c as a stimulator of alpha-synuclein aggregation in Lewy body disease // J. Biol. Chem. – 1999. – Vol. 274. – P. 28849−28852.
27. Huang J., MacKerell A. CHARMM36 all-atom additive protein force field: validation based on comparison to NMR data // J. Comput. Chem. – 2013. – Vol. 34. – P. 2135–2145.
28. Lomize M., Pogozheva I., Joo H., Mosberg H., Lomize A. OPM database and PPM web server: resources for positioning of proteins in membranes // Nucl. Acids Res. – 2012. – Vol. 40. – P. 370–376.
29. Jo S., Lim J., Klauda J., Im W. CHARMM-GUI Membrane builder for mixed bilayers and its application to yeast membranes // Biophys. J. – 2009. – Vol. 97. – P. 50–58.
30. Darden T., York D., Pedersen L. Particle mesh Ewald: An N log(N) method for Ewald sums in large systems // J. Chem. Phys. – 1993. – Vol. 98. – P. 10089–10092.
31. Vehlow C., Stehr H., Winkelmann M., Duarte J., Petzold L., Dinse J., Lappe M. CMView: Interactive contact map visualization and analysis // Bioinformatics. – 2011. – Vol. 27. – P. 1573–1574.
32. Cortese J.D., Voglino A.L., Hackenbrock C.R. Multiple conformations of physiological membrane-bound cytochrome c // Biochemistry. – 1998. – Vol. 37. – P. 6402−6409.
33. Lewis R.N.A., McElhaney R.N. The physicochemical properties of cardiolipin bilayers and cardiolipin-containing lipid membranes // Biochim. Biophys. Acta. – 2009. – Vol. 1788. – P. 2069–2079.
34. Rytömaa M., Kinnunen P.K.J. Evidence for two distinct acidic phospholipid-binding sites in cytochrome *c* // J. Biol. Chem. – 1994. – Vol. 269. – P. 1770–1774.
35. Rytömaa M., Mustonen P., Kinnunen P.K.J. Reversible, nonionic, and pH-dependent association of cytochrome c with cardiolipin-phosphatidylcholine liposomes // J. Biol. Chem. – 1992. – Vol. 267. – P. 22243–22248.
36. Kalanhni E., Wallace C.J.A. Cytochrome c impaled: investigation of the extended lipid anchorage of a soluble protein to mitochondrial membrane models // Biochem. J. – 2007. – Vol. 407. – P. 179–187.
37. Sinibaldi F., Howes B.D., Droghetti E., Polticelli F., Piro M.C., Di Pierro D., Fiorucci L., Coletta M., Smulevich G., Santucci R. Role of lysines in cytochrome c–cardiolipin interaction // Biochemistry. – 2013. – Vol. 52. – P. 4578–4588.
38. Hanske J., Toffey J.R., Morenz A.M., Bonilla A.J., Schiavoni K.H., Pletneva E.V. Conformational properties of cardiolipin-bound cytochrome c // Proc. Natl. Acad. Sci. USA. – 2012. – Vol. 109. – P. 125–130.
39. Muenzner J., Pletneva E. Structural transformations of cytochrome c upon interaction with cardiolipin // Chem. Phys. Lipids. – 2014. – Vol. 179. – P. 57–63.
40. Pandiscia L.A., Schweitzer-Stenner R. Coexistence of native-like and non-native partially unfolded ferricytochrome *c* on the surface of cardiolipin-containing liposomes // J. Biol. Chem. B. – 2015. – Vol. 119. – P. 1334–1349.
41. Pinheiro T.J.T., Watts A. Lipid specificity in the interaction of cytochrome c with anionic phospholipid bilayers revealed by solid-state 31P NMR // Biochemistry. – 1994. – Vol. 33. – P. 2451–2458.
42. Pinheiro T.J.T., Cheng H., Seeholzer S.H., Roder H. Direct evidence for the cooperative unfolding of cytochrome c in lipid membranes from H-2H exchange kinetics // J. Mol. Biol. – 2003. – Vol. 303. – P. 617–626.
43. Belikova N.A., Vladimirov Y.A., Osipov A.N., Kapralov A.A., Tyurin V.A., Potapovich M.V., Basova L.V., Peterson J., Kurnikov I.V., Kagan V.E. Peroxidase activity and structural transitions of cytochrome c bound to cardiolipin-containing membranes // Biochemistry. – 2006. – Vol. 45. – P. 4998–5009.
44. Hong Y., Muenzner J., Grimm S.K., Pletneva E.V. Origin of the conformational heterogeneity of cardiolipin-bound cytochrome c // J. Amer. Chem. Soc. – 2012. – Vol. 134. – P. 18713–18723.
45. Brown L., Wuthrich K. NMR and ESR studies of the interactions of cytochrome c with mixed cardiolipin-phosphatidylcholine vesicles // Biochim. Biophys. Acta. – 1977. – Vol. 468. – P. 389–410.
46. De Kruijff B., Cullis P.R. Cytochrome c specifically induces non-bilayer structures in cardiolipin-containing model membranes // Biochim. Biophys. Acta. – 1980. – Vol. 602. – P. 477–490.
47. Bergstrom C.L., Beales P.A., Lv Y., Vanderlick T.K., Groves J.T. Cytochrome c causes pore formation in cardiolipin-containing membranes // Proc. Natl. Acad. Sci. USA. – 2013. – Vol. 110. – P. 6269–6274.
48. Spooner P.J.R., Watts A. Reversible unfolding of cytochrome c upon interaction with cardiolipin bilayers. 2. Evidence from phosphorus-31 NMR measurements // Biochemistry. – 1991. – Vol. 30. – P. 3880–3885.
49. Stepanov G., Gnedenko O., Mol'nar A., Ivanov A., Vladimirov Y., Osipov A. Evaluation of cytochrome c affinity to anionic phospholipids by means of surface plasmon resonance // FEBS Lett. – 2009. – Vol. 583. – P. 97–100.
50. Pinheiro T.J.T. The interaction of horse heart cytochrome c with phospholipid bilayers. Structural and dynamic effects // Biochimie. – 1994. – Vol. 76. – P. 489–500.
51. Hildebrandt P., Heimburg T., Marsh D. Quantitative conformational analysis of cytochrome c bound to phospholipid vesicles studied by resonance Raman spectroscopy // Eur. Biophys. J. – 1990. – Vol. 18. – P. 193–201.
52. Heimburg T., Hildebrandt P., Marsh D. Cytochrome c-lipid interactions studied by resonance Raman and 31P NMR spectroscopy. Correlation between the conformational changes of the protein and lipid bilayer // Biochemistry. – 1991. – Vol.

30. – P. 9084–9089.
53. Muenzner J., Toffey J., Hong Y., Pletneva E. Becoming a peroxidase: cardiolipin-induced unfolding of cytochrome c // J. Phys. Chem. B. – 2013. – Vol. 117. – P. 12878–12886.
54. Mandal A., Hoop C., DeLucia M., Kodali R., Kagan V., Ahn J., Wel P. Structural changes and proapoptotic peroxidase activity of cardiolipin-bound mitochondrial cytochrome c // Biophys. J. – 2015. – Vol. 109. – P. 1873–1884.
55. O'Brien E., Nucci N., Fuglestad B., Tommos C., Wand A.J. Defining the apoptotic trigger the interaction of cytochrome c and cardiolipin // J. Biol. Chem. – 2015. – Vol. 290. – P. 30879–30887.
56. Balakrishnan G., Hu Y., Spiro T. His26 protonation in cytochrome c triggers microsecond β-sheet formation and heme exposure: implications for apoptosis // J. Am. Chem. Soc. – 2012. – Vol. 134. – P. 19061–19069.
57. Bandi S., Bowler B. Probing the dynamics of a His73–heme alkaline transition in a destabilized variant of yeast iso-1-cytochrome c with conformationally gated electron transfer methods // Biochemistry. -2011. – Vol. 50. – P. 10027–10040.

East Eur. J. Phys. Vol.4 No.3 (2017) 63-70 DOI:10.26565/2312-4334-2017-3-09

PACS: 87.14.C++c, 87.16.Dg

AURAMINE O AS POTENTIAL AMYLOID MARKER: FLUORESCENCE AND MOLECULAR DOCKING STUDIES

K. Vus[1], U. Tarabara[1], K. Semenova[1], V. Viter[2], O. Nikitina[2], V. Trusova[1], G. Gorbenko[1]

[1]Department of Nuclear and Medical Physics, [2]Department of Molecular and Medical Biophysics
V.N. Karazin Kharkiv National University
4 Svobody Sq., Kharkiv, 61022, Ukraine
e-mail: kateryna_vus@yahoo.com
Received August 23, 2017

The applicability of Auramine O to the detection and characterization of lysozyme and serum albumin amyloid fibrils has been assessed using the fluorimetric titration and molecular docking. The parameters of the dye binding to native and fibrillar proteins were estimated in terms of the Langmuir adsorption model. It was found that Auramine O displays the high affinity for amyloid fibrils, being of the same order of magnitude as that of the classical amyloid markers. The dye also showed greater fluorescence response to lysozyme fibrils and lower sensitivity to the native protein, than Thioflavin T. Furthermore, unlike Thioflavin T, Auramine O was able to detect the morphological differences between lysozyme and albumin fibrils due to the shifts in the position of the emission maxima of the fibril-incorporated fluorophore. The molecular docking studies revealed that Auramine O and Thioflavin T form the most stable complexes with the G54_L56/S60_W62 groove of lysozyme fibrils, running parallel to the fibril axis. The results obtained suggest the contribution of both hydrophobic and electrostatic interactions to the stabilization of the dye complexes with amyloid fibrils.
KEYWORDS: Auramine O, Thioflavin T, amyloid marker, association constant, fluorescence quantum yield, molecular rotor, lysozyme, serum albumin, amyloid fibrils

АУРАМИН О КАК ПОТЕНЦИАЛЬНЫЙ АМИЛОИДНЫЙ МАРКЕР: ФЛУОРЕСЦЕНТНОЕ ИССЛЕДОВАНИЕ И МОЛЕКУЛЯРНЫЙ ДОКИНГ

Е. Вус[1], У. Тарабара[1], Е. Семенова[1], В. Витер[2], О. Никитина[2], В. Трусова[1], Г. Горбенко[1]

[1]Кафедра ядерной и медицинской физики, [2]Кафедра молекулярной и медицинской биофизики
Харьковский национальный университет имени В.Н. Каразина
пл. Свободы 4, Харьков, 61022, Украина

С помощью методов флуориметрического титрования и молекулярного докинга проведена оценка возможности использования аурамина О для детектирования и характеризации амилоидных фибрилл лизоцима и сывороточного альбумина. С использованием модели адсорбции Ленгмюра получены параметры связывания зондов с нативными и фибриллярными белками. Выявлена высокая афинность аурамина О к амилоидным фибриллам, одного порядка с аффинностью классических амилоидных маркеров. Краситель также имел более значительный флуоресцентный ответ в присутствии амилоидных фибрилл лизоцима и более низкую чувствительность к нативному белку, чем тиофлавин Т. Кроме того, аурамин О, в отличие от тиофлавина Т, проявил способность детектировать фибриллы различной морфологии благодаря сдвигам положений максимума эмиссии связанного зонда. Методом молекулярного докинга показано, что аурамин О и тиофлавин Т образуют наиболее стабильные комплексы с желобком G54_L56/S60_W62 фибрилл лизоцима, который простирается параллельно ее главной оси. Полученные результаты свидетельствуют о вкладе как гидрофобных, так и электростатических взаимодействий в стабилизацию комплексов красителей с амилоидными фибриллами.
КЛЮЧЕВЫЕ СЛОВА: аурамин О, тиофлавин Т, амилоидный маркер, константа ассоциации, квантовый выход флуоресценции, молекулярный ротор, лизоцим, сывороточный альбумин, амилоидные фибриллы

АУРАМІН О ЯК ПОТЕНЦІЙНИЙ АМІЛОЇДНИЙ МАРКЕР: ФЛУОРЕСЦЕНТНЕ ДОСЛІДЖЕННЯ ТА МОЛЕКУЛЯРНИЙ ДОКІНГ

К. Вус[1], У. Тарабара[1], К. Семенова[1], В. Вітер[2], О. Нікітіна[2], В. Трусова[1], Г. Горбенко[1]

[1]Кафедра ядерної та медичної фізики, [2]Кафедра молекулярної та медичної біофізики
Харківський національний університет імені В.Н. Каразіна
пл. Свободи 4, Харків, 61022, Україна

За допомогою методів флуориметричного титрування та молекулярного докінгу проведена оцінка можливості застосування аураміну О для детектування та характеризації амілоїдних фібрил. З використанням моделі адсорбції Ленгмюра отримано параметри зв'язування зондів з нативними та фібрилярними білками. Виявлена висока афінність аураміну О до амілоїдних фібрил, що була одного порядку з афінністю класичних амілоїдних маркерів. Барвник також мав більш високу інтенсивність флуоресценції у присутності амілоїдних фібрил лізоциму та більш низьку чутливість до нативного білка, ніж тіофлавін Т. Крім того, аурамін О, на відміну від тіофлавіну Т, проявив здатність до детектування фібрил різної морфології, завдяки зсувам положення максимуму емісії. Методом молекулярного докінгу показано, що аурамін О та тіофлавін Т утворюють найбільш стабільні комплекси з жолобком G54_L56/S60_W62 фібрили лізоциму, що простягається паралельно її головній осі. Отримані результати свідчать про внесок як гідрофобних, так і електростатичних взаємодій у стабілізацію комплексів барвників з амілоїдними фібрилами.

КЛЮЧОВІ СЛОВА: аурамін О, тіофлавін Т, амілоїдний маркер, константа асоціації, квантовий вихід флуоресценції, молекулярний ротор, лізоцим, сироватковий альбумін, амілоїдні фібрили

A wide variety of human disorders, viz. Alzheimer's, Parkinson's diseases, systemic amyloidosis, type II diabetes, etc. are characterized by the deposition of the specific protein aggregates, amyloid fibrils, in the extracellular matrix followed by functional disturbances in various tissues and organs [1]. Amyloid fibrils are the β-sheet-rich protein assemblies of *ca.* 5–10 nm in width and up to several micrometers in length [2]. Despite significant progress in understanding the molecular basis of amyloid fibril formation, a number of essential issues remain unclear. In particular, a great morphological heterogeneity of amyloids may hamper the medical diagnostics and development of anti-amyloid drugs, suggesting the necessity of the improved fibril detection strategies [2]. Furthermore, considering the amyloids as a new class of nanomaterials, the fabrication of the nanostructured amyloid films with the desired physical properties requires elucidating the effects of the environmental conditions on amyloid morphology. One of the most effective approaches to addressing these problems is based on the use of amyloid-specific fluorescent dyes. Of these, a fluorescent dye, Thioflavin T (ThT), has been widely employed for the identification and quantification of amyloid aggregates, and for the monitoring the fibrillization kinetics in real-time [13]. ThT association with the β-sheets composed of minimum 5 β-strands (that is typical for amyloid structures) results in a drastic increase in its fluorescence and significant red shift of the absorption maximum [14–16]. Despite the remarkable amyloid-specific spectral response of ThT, this dye may show false positive results in the presence of native proteins and lipids, sensitivity to the pH of the bulk, weak binding to the positively charged fibrils, etc. [17,18]. The above drawbacks of ThT strongly suggest the necessity of designing the novel amyloid markers. To exemplify, another dye, Auramine O (AuO) has been successfully employed to detect insulin aggregates [19]. Furthermore, unlike ThT, AuO "recognized" insulin fibrils due to the appearance of additional red-shifted emission band. However, the potential of Auramine O as amyloid marker is not yet fully assessed.

In view of this, the aim of the present study was to gain further insights into amyloid specificity of AuO through evaluating its applicability for the detection and characterization of lysozyme and albumin amyloid fibrils. Specifically, our goals were: i) to evaluate the quantitative parameters of the dye-protein binding using the fluorimetric titration; ii) to compare AuO and ThT responses to the presence of amyloid fibrils and native proteins; iii) to uncover the advantages of AuO over ThT; iv) to ascertain possible location of AuO within fibril structure using the molecular docking. Lysozyme is a small cationic protein, possessing antibacterial activity [4]. Lysozyme misfolding and aggregation is associated with the hereditary amyloidoses [5]. Hen egg white lysozyme (HEWL) is a structural analogue of the human variant, that is widely employed as a model protein in the amyloid studies [6,7]. The characterization of the interactions between lysozyme fibrils and small ligands, including the fluorescent dyes, may be useful for the design of the drugs against amyloidoses. Moreover, the HEWL amyloid films prepared *in vitro* showed remarkable mechanical properties, suitable for the development of the amyloid-based multifunctional materials [8].

Serum albumin is an all-α-anionic protein, acting as a carrier from blood stream to tissues and playing a key role in the regulation of osmotic pressure, thrombosis and coagulation [9]. Similar to HEWL, bovine serum albumin has been widely employed as a model protein in the studies of the protein fibrillization [10]. However, to the best of our knowledge, the structure of the serum albumin fibrils and the precise mechanisms of the protein aggregation are so far poorly understood. For example, the residues, which form the core cross-β-structure of the albumin fibrils have not yet been identified. Furthermore, serum albumin was reported to inhibit the Aβ-peptide and transthyretin fibril growth by the stabilization of the Aβ monomers [11,12]. Therefore, further investigation of albumin fibrillization and its effects on the amyloid fibril formation by the other proteins and peptides may prove of importance for the improvement of anti-amyloid strategies.

EXPERIMENTAL SECTION

Materials

Hen egg white lysozyme (Lz) and bovine serum albumin (BSA) were from Sigma (St. Louis, MO, USA). All other chemicals were of analytical grade and used without further purification.

Preparation of amyloid fibrils

The reaction of amyloid fibril formation by the lysozyme and bovine serum albumin was carried out in 10 mM glycine buffer at pH 2 and 60 ºC for 14 days. Protein concentration in the stock solutions was 10 mg/ml. Hereafter, the native protein forms are designated as LzN and BSAN, while the fibrillar forms – as LzF and BSAF.

Fluorescence measurements

Fluorescence spectra of ThT and AuO were measured with the spectrofluorimeter Shimadzu RF-6000 (Japan) at 25 ºC using 10 nm excitation and emission slit widths. The excitation wavelength for both dyes was 440 nm.

Binding model

The quantitative characteristics of the dye-protein complexation were determined from the fluorimetric titration of ThT and AuO solutions by the native or fibrillar proteins. Specifically, the dependence of the dye fluorescence intensity increase (ΔI) on the protein concentration (P) was analyzed in terms of the Langmuir adsorption model [22]:

$$\Delta I = 0.5\alpha \left[Z_0 + nP + \frac{1}{K_a} - \sqrt{(Z_0 + nP + \frac{1}{K_a})^2 - 4nPZ_0} \right], \quad (1)$$

where Z_0 is the total dye concentration, K_a and n are the association constant and stoichiometry of the dye-protein complexes, α is a coefficient proportional to the difference of ThT and AuO quantum yields in a buffer and protein-associated state. To make a more precise comparison of the dye sensitivity and specificity to the fibrils, fluorescence intensity increases of the fibril-/native protein-bound dyes ($I_{fibr/nat} / I_0$) with respect to buffer, and those of the fibril-bound probes (I_{fibr} / I_{nat}) with respect to the native proteins, have been estimated. The value of the binding parameters, K_a, n, α, derived from the fit of eq. 1 to the experimental data are presented in Table 1 for the fixed dye and protein concentrations 2 and 10 μM, respectively.

Moleculardocking studies

The molecular docking was implemented to identify the possible binding sites of the native and fibrillar proteins for AuO and ThT. Lysozyme and albumin structures with PDB IDs 3A8Z and 4F5S, respectively, were chosen for the docking. The model amyloid fibril of lysozyme was constructed from the K-peptide (the residues 54-62 of wild-type protein) using the CreateFibril tool [23]. ThT and AuO structures were built in Avogadro [24], followed by the geometry optimization of the ground states of the dyes with the 6-31G(d,p) basis set using the GAMESS software [25]. The protein-dye complexes possessing a good shape complementarity and the lowest desolvation energy were obtained using the PatchDock web server [26]. Next, 10 best structures generated by the PatchDock, were refined with the FireDock, an algorithm, which optimizes the intermolecular binding by allowing the flexibility of the side chains and small rigid-body movements [27]. The results obtained from the FireDock were reported to be in a good agreement with the experimental data. The most stable dye-protein complexes were visualized by the Visual Molecular Dynamics software [28].

RESULTS AND DISCUSSION

As seen in Fig. 1, AuO and ThT are the small cationic dyes, possessing the electron-donating amino moieties on the aromatic groups. These dyes belong to the molecular rotor family due to the internal rotation of their fragments upon excitation, followed by the transition from the fluorescent locally excited (LE) state to the nonfluorescent twisted internal charge transfer (TICT) state [19,20]. In turn, steric restriction of the intramolecular twisting results in the dramatic increase in the fluorescence quantum yield of these fluorophores. The above mechanism was suggested to underlie the high sensitivity of ThT to amyloid fibrils due to the dye embedding into the fibril grooves, running parallel to the fibril axis, giving rise to significant increase in the potential energy of relative rotation of the benzothiazole and phenyl moieties [21].

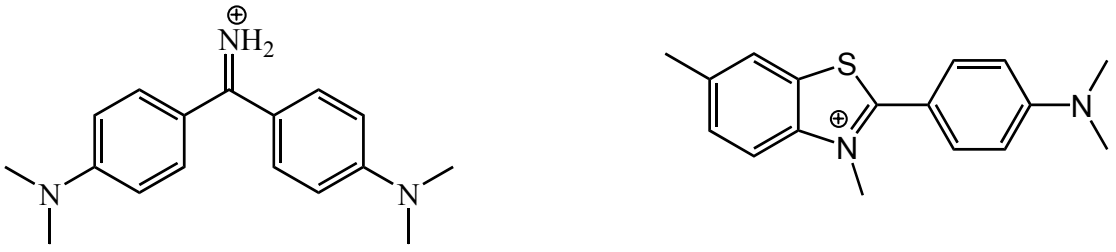

a b

Fig. 1. Chemical structures of the fluorescent dyes: a – Auramine O; b – Thioflavin T

As shown in Fig. 2, the binding of AuO to the amyloid fibrils and native proteins manifests itself in the increase of the dye fluorescence intensity with the protein concentration. Likewise, emission maxima of the BSA-incorporated fluorophore showed *ca.* 10–12 nm shifts to the shorter wavelengths ($\lambda_{fibr/nat} - \lambda_0$, Table 1), suggesting the decreased polarity of the dye environment [29]. On the contrary, BSA-bound ThT did not show noticeable spectral shifts. Furthermore, emission maxima of the both dyes remained almost invariable in the presence of native and fibrillar lysozyme. According to these results, AuO seems to be more sensitive to the solvent polarity than ThT. The above spectral properties of AuO resemble those of Nile Red, another fluorescent amyloid marker, which showed the dependence of the emission maximum on the local polarity of amyloid binding sites [30].

To obtain the quantitative characteristics of the dye-protein binding the experimental dependences $\Delta I(P)$ were approximated by eq. (1) (Fig. 3). As seen in Table 1, AuO showed similar affinity for native and fibrillar proteins, and higher stoichiometry for BSAF, BSAN, than that of ThT. In turn, ThT possessed 10-fold higher K_a value in the presence of lysozyme fibrils, as compared to that of lysozyme monomers. The greater K_a values characteristic of the

AuO- and ThT-BSA complexes may arise from the enhanced hydrophobic dye-protein interactions. Likewise, at pH 7.4 BSA has a negative electric charge, while AuO and ThT are positively charged, assuming the increased electrostatic stabilization of the dye-protein complexes, as well [31]. The K_a value characterizing the AuO-BSAN binding also suggests the formation of fibrils of a certain morphology, differing from that observed by other authors. For instance, in the Mudliar's work BSA (100 μM) was incubated at 65 ºC for 2 hours resulting in the fibril formation and the K_a value lower by 2 orders of magnitude compared to that obtained in the present study [32].

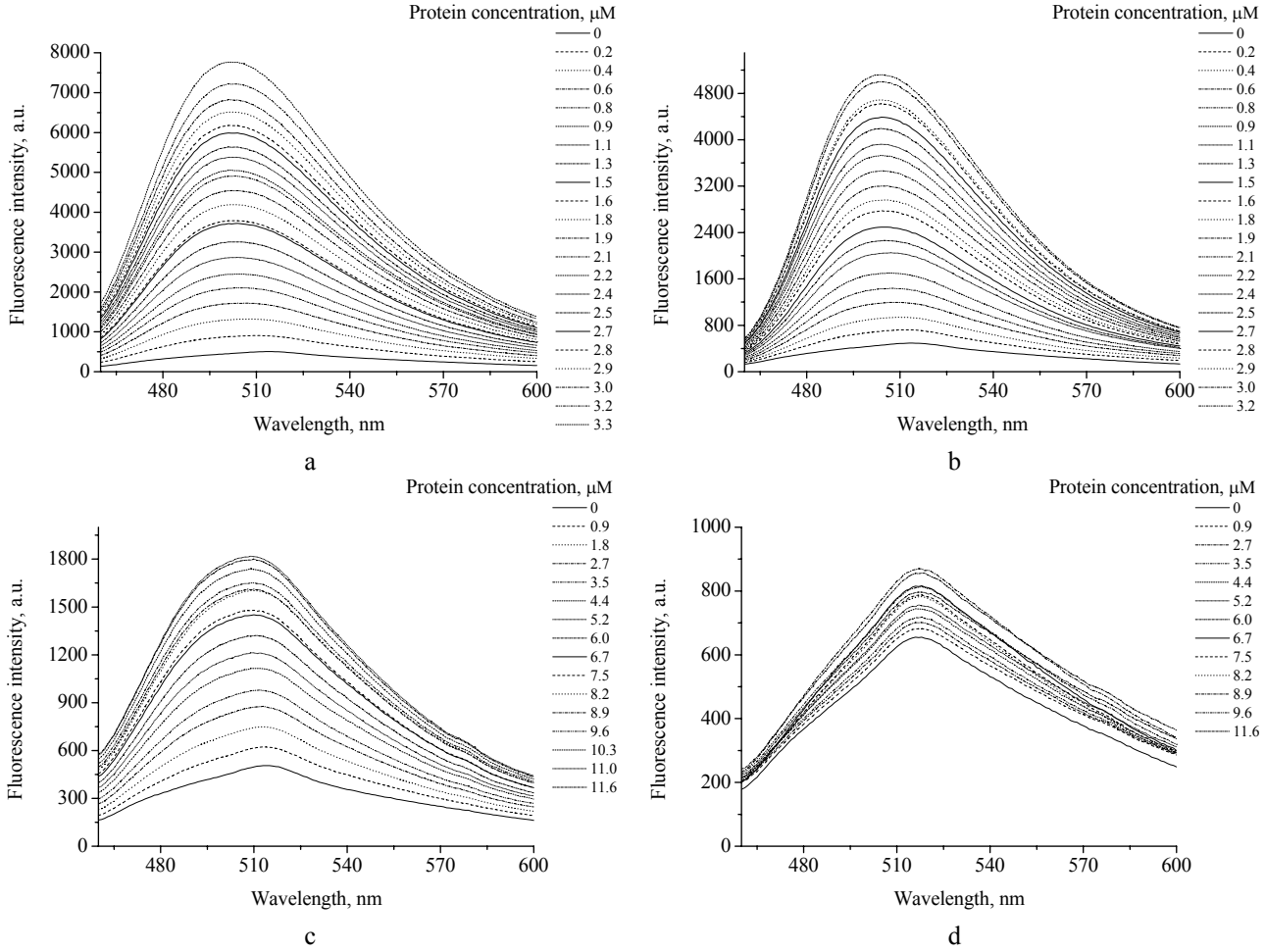

Fig. 2. Fluorescence spectra of AuO in the presence of proteins
a - fibrillar albumin; b - native serum albumin; c - fibrillar lysozyme; d - native lysozyme. Dye concentration was 15 μM

Interestingly, unlike lysozyme, BSAN and BSAF have similar number of the dye binding sites, supposedly with different morphology. The large molecule of serum albumin possesses about 24 residues of the different subdomains with the very high aggregation propensity, estimated with AGGRESCAN [33], Zyggregator [34] and TANGO [35]. These residues presumably form fibril core, enabling the dye association with various fibril grooves that may increase the number of the dye binding sites. Indeed, Holm et al. reported drastic increase in the β-sheet content during BSA fibrillization, followed by ThT and Congo Red complexation with the different subtypes of the aggregates formed in parallel [36].

The comparison of the α values for the dye complexes with fibrillar and native proteins revealed higher fluorescence responses of the fluorophores to the presence of amyloid fibrils (Table 1). Furthermore, LzF-bound AuO showed greater signal-to noise ratio ($I_{fibr/nat} / I_0$) compared to that of the BSAF-associated dye. In turn, ThT showed higher specificity for BSAF than that of LzF. Interestingly, the examined dyes possess up to 15-fold greater quantum yields in the presence of fibrillar and native BSA, as compared to LzN. In the case of BSAN this could be explained by the dye incorporation into the protein hydrophobic patches, viz. sites I and II [37]. In turn, stabilization of the locally excited state and the concomitant increase in the ThT quantum yield are predominantly due to the dye interactions with the long β-sheets, resulting in the lowered sensitivity of the fluorophore to hydrophobic pockets of BSAN [14]. Analysis of the quantitative characteristics of the dye-protein complexation revealed that AuO could be used as alternative to ThT for LzF detection.

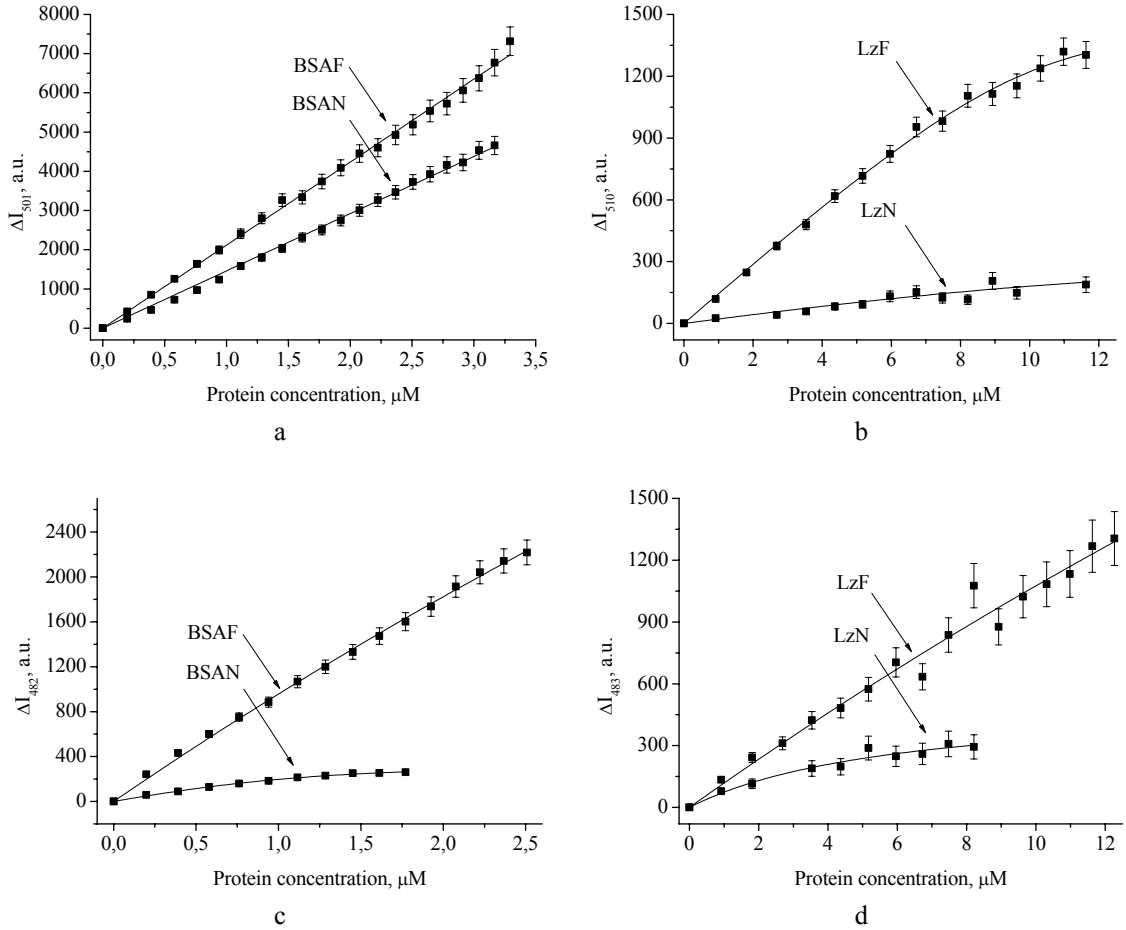

Fig. 3. The isotherms of the dye binding to serum albumin and lysozyme
a ,b – AuO; c,d – ThT. AuO and ThT concentrations were 15 μM and 2 μM, respectively

Finally, the molecular docking was used to identify the possible protein binding sites for AuO and ThT. It appeared that AuO and ThT tend to associate with the similar sites on the native or fibrillar proteins (Figure 4). It can be assumed that both dyes associate with G54_L56/S60_W62 fibril groove of the anti-parallel β-sheet of the lysozyme

Table 1.

Quantitative characteristics of the dye-protein binding

Dye	Protein	λ_0 *, nm	$\lambda_{fibr/nat} - \lambda_0$ **, nm	K_a, μM^{-1}	n	α, μM^{-1}	$I_{fibr/nat} / I_0$	I_{fibr} / I_{nat}
AuO	BSAF	514	-12	1.20±0.25	2.60±0.51	800	26.7	1.5
	BSAN		-10	2.00±0.41	2.90±0.32	500	17.7	-
	LzF		-4	1.40±0.30	1.50±0.30	102	3.9	2.8
	LzN		0	0.40±0.08	1.20±0.24	21	1.4	-
ThT	BSAF	480	-2	0.73±0.15	0.35±0.07	4800	17.5	3
	BSAN		0	1.70±0.37	1.90±0.03	174	2.0	-
	LzF		-3	0.20±0.04	0.11±0.02	4020	3.5	1.9
	LzN		0	0.02±0.00	7.50±0.15	260	1.8	-

*Emission maximum of the free dye in buffer; **Difference between the emission maxima of the protein-bound and free dye fibril via hydrophobic interactions [38]. According to our quantum-chemical calculations, AuO length is *ca.* ~1.3 nm, being shorter than that of ThT (*ca.* ~1.5 nm). Therefore, AuO may associate with 4 β-strands of the β-sheet, while ThT is likely to associate with 5 β-strands [39].

Furthermore, AuO and ThT tend to associate with the IB domain of BSAN (the residues L115, P117, L122, E125, F133, K136, Y137, E140, Y160, R185) and the active center of LzN (the residues I58, N59, W62, W63, I98, D101, N103, A107, W108) [40,41]. Interestingly, Mudliar et al. reported AuO binding to the hydrophobic IIA domain of BSA, i.e. to the specific ligand-binding site [32,42]. These discrepancies could be due to the fact that Mudliar employed Auto Dock software, while the simple PatchDock/FireDock tools used in the present study give less precise results. The

above data support our suggestion about the contribution of both hydrophobic and electrostatic dye-protein interactions in the stabilization of the dye-protein complexes [43].

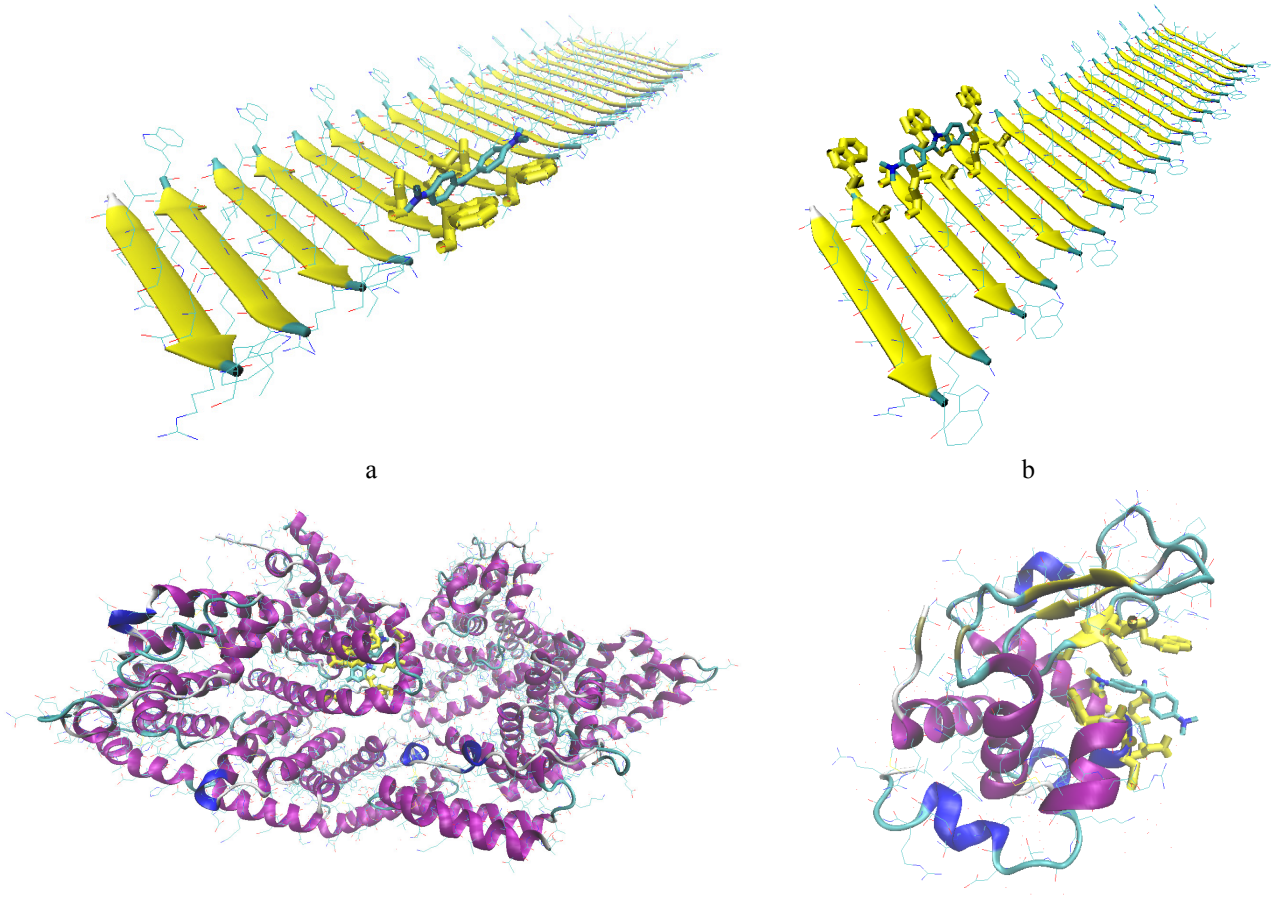

Fig. 4. Schematic representation of the most stable dye-protein complexes obtained by the molecular docking
a – AuO associated with the lysozyme fibril represented by the β-sheet formed from the K-peptide. The dye is bound to the G54_L56/S60_W62 fibril groove of the anti-parallel β-sheet; b – ThT associated with the same lysozyme fibril groove as AuO; c – AuO bound to the native serum albumin. The residues L115, P117, L122, E125, F133, K136, Y137, E140, Y160, R185 represent the protein binding site for the dye; d - AuO bound to the native lysozyme. The residues I58, N59, W62, W63, I98, D101, N103, A107, W108 represent the protein binding site for the dye.

CONCLUSIONS

- The quantitative parameters for the Auramine O binding to fibrillar and native lysozyme and bovine serum albumin have been estimated, revealing the possibility of the dye application for the detection and characterization of amyloid fibrils;
- Auramine O showed the dependence of the position of the emission maximum on the polarity of the amyloid binding sites. This feature could be employed for the structural differentiation of lysozyme and serum albumin amyloid fibrils;
- Simple docking studies revealed that Auramine O associates with the specific fibril binding sites, viz. the grooves, running parallel to the fibril axis.
- Both fluorescence and docking studies indicate that hydrophobic and electrostatic dye-protein interactions play an essential role in the stabilization of the dye-protein complexes.

REFERENCES

1. Hill S.E., Robinson J., Matthews G., Muschol M. Amyloid protofibrils of lysozyme nucleate and grow via oligomer fusion // Biophys. J. – 2009. – Vol. 96. – P. 3781–3790.
2. Toyama B.H., Weissman J.S. Amyloid structure: conformational diversity and consequences // Annu. Rev. Biochem. – 2011. – Vol. 80. – 10.1146/annurev-biochem-090908-120656.
3. Cho W.H., Stahelin R.V. Membrane–protein interactions in cell signaling and membrane trafficking // Annu. Rev. Biophys. Biomol. Struct. – 2005. – Vol. 34. – P. 119–151.
4. Laible N.J., Germaine G.R. Bactericidal activity of human lysozyme, muramidase-inactive lysozyme, and cationic polypeptides against Streptococcus sanguis and Streptococcus faecalis // Infect Immun. – 1985. – Vol. 48. – P. 720–728.
5. Granel B., Valleix S., Serratrice J., Chérin P., Texeira A., Disdier P., Weiller P.J., Grateau G. Lysozyme amyloidosis: report of 4 cases and a review of the literature // Medicine (Baltimore). – 2006. – Vol. 85. – P. 66–73.

6. Sivalingam V., Prasanna N.L., Sharma N., Prasad A., Patel B.K. Wild-type hen egg white lysozyme aggregation in vitro can form self-seeding amyloid conformational variants // Biophys. Chem. – 2016. – Vol. 219. – P. 28–37.
7. Morozova-Roche L.A., Zurdo J., Spencer A., Noppe W., Receveur V., Archer D.B., Joniau M., Dobson C.M. Amyloid fibril formation and seeding by wild-type human lysozyme and its disease-related mutational variants // J. Struct. Biol. – 2000. – Vol. 130. – P. 339–351.
8. Knowles T.P.J., Oppenheim T.W., Buell A.K., Chirgadze D.Y., Welland M.E. Nanostructured films from hierarchical self-assembly of amyloidogenic proteins // Nature Nanotechnology. – 2010. – Vol. 5. – P. 204 – 207.
9. Taboada P., Barbosa S., Castro E., Mosquera V. Amyloid fibril formation and other aggregate species formed by human serum albumin association // J. Phys. Chem. B. – 2006. – Vol. 110. – P. 20733–20736.
10. Holm N.K., Jespersen S.K., Thomassen L.V., Wolff T.Y., Sehgal P., Thomsen L.A., Christiansen G., Andersen C.B., Knudsen A.D., Otzen D.E. Aggregation and fibrillation of bovine serum albumin // Biochim. Biophys. Acta. – 2007. – Vol. 1774. – P. 1128–38.
11. Milojevic J., Raditsis A., Melacini G. Human serum albumin inhibits Aβ fibrillization through a "monomer-competitor" mechanism // Biophys. J. – 2009. – Vol. 97. – P. 2585–2594.
12. Kugimiya T., Jono H., Saito S., Maruyama T., Kadowaki D., Misumi Y., Hoshii Y., Tasaki M., Su Y., Ueda M., Obayashi K., Shono M., Otagiri M., Ando Y. Loss of functional albumin triggers acceleration of transthyretin amyloid fibril formation in familial amyloidotic polyneuropathy // Lab. Invest. – 2011. – Vol. 91. – P. 1219–1228.
13. Hawe A., Sutter M., Jiskoot W. Extrinsic fluorescent dyes as tools for protein characterization // Pharm Res. – 2008. – Vol. 25. – P. 1487–1499.
14. Vus K., Trusova V., Gorbenko G., Sood R., Kinnunen P. ThioflavinT derivatives for the characterization of insulin and lysozyme amyloid fibrils in vitro: fluorescence and quantum-chemical studies // J. Luminesc. – 2015. – Vol. 159. – P. 284–293.
15. LeVine H. 3rd. Thioflavine T interaction with synthetic Alzheimer's disease beta-amyloid peptides: detection of amyloid aggregation in solution // Protein Sci. – 199. – Vol. 2. – P. 404-410.
16. Nilsson M.R. Techniques to study amyloid fibril formation in vitro // Methods. – 2004. – Vol. 34. – P. 151–160.
17. Groenning M. Binding mode of Thioflavin T and other molecular probes in the context of amyloid fibrils—current status // J. Chem. Biol. – 2010. – Vol. 3. – P. 1–18.
18. Foderà V., Groenning M., Vetri V., Librizzi F., Spagnolo S., Cornett C., Olsen L., van de Weert M., Leone M. Thioflavin T hydroxylation at basic pH and its effect on amyloid fibril detection // J. Phys. Chem. B. – 2008. – Vol. 112. – P. 15174–1581.
19. Mudliar N.H., Pettiwala A.M., Awasthi A.A., Singh P.K. On the molecular form of amyloid marker, Auramine O, in human insulin fibrils // J. Phys. Chem. B. – 2016. – Vol. 120. – P. 12474–12485.
20. Stsiapura V.I., Maskevich A.A., Kuzmitsky V.A., Uversky V.N., Kuznetsova I.M., Turoverov K.K. Thioflavin T as a molecular rotor: fluorescent properties of Thioflavin T in solvents with different viscosity // J. Phys. Chem B. – 2008. – Vol. 112. – P. 15893–15902.
21. Biancalana M., Koide S. Molecular mechanism of Thioflavin-T binding to amyloid fibrils // Biochim. Biophys. Acta. – 2010. – Vol. 1804. – P. 1405–1412.
22. Vus K., Trusova V., Gorbenko G., Sood R., Kirilova E., Kirilov G., Kalnina I., Kinnunen P. Fluorescence investigation of interactions between novel benzanthrone dyes and lysozyme amyloid fibrils // J. Fluoresc. – 2014. – Vol. 24. – P. 493–504.
23. Smaoui M. Computational assembly of polymorphic amyloid fibrils reveals stable aggregates // Biophys. J. – 2013. – Vol. 104. – P. 683–693.
24. Hanwell M.D., Curtis D.E., Lonie D.C., Vandermeersch T., Zurek E., Hutchison G.R. Avogadro: an advanced semantic chemical editor, visualization, and analysis platform // J. Cheminform. – 2012. – Vol. 4. – P. 17.
25. Binkley J.S., Pople J.A., Hehre W.J. Self-consistent molecular orbital methods. 21. Small split-valence basis sets for first-row elements // Am. Chem. Soc. – 1980. – P. 102. – P. 939–947.
26. Schneidman-Duhovny D., Inbar Y., Nussinov R., Wolfson H.J. PatchDock and SymmDock: servers for rigid and symmetric docking // Nucleic Acids Res. – 2005. – Vol. 33. – P. 363–367.
27. Andrusier N., Nussinov R., Wolfson H.J. FireDock: fast interaction refinement in molecular docking // Proteins. – 2007. – Vol. 69. – P. 139–159.
28. Humphrey W., Dalke A., Schulten K. VMD: Visual molecular dynamics // J. Mol. Graph. – 1996. – Vol. 14. – P. 33–38, 27–28.
29. Lakowicz J.R. Principles of fluorescence spectroscopy, 3rd edn. –New York: Springer, 2006.
30. Mishra R., Sjölander D., Hammarström P. Spectroscopic characterization of diverse amyloid fibrils in vitro by the fluorescent dye Nile red // Mol Biosyst. – 2011. – Vol. 7. – P. 1232–1240.
31. Böhme U., Scheler U. Effective charge of bovine serum albumin determined by electrophoresis NMR // Chem. Phys. Lett. – 2007. – Vol. 435. – P.342–345.
32. Mudliar N.H., Sadhu B., Pettiwala A.M., Singh P.K. Evaluation of an ultrafast molecular rotor, Auramine O, as fluorescent amyloid marker // J. Phys. Chem. B. – 2016. – Vol. 120. – P. 10496–10507.
33. Conchillo-Solé O., de Groot N.S., Avilés F.X., Vendrell J.S., Daura X., Ventura S. AGGRESCAN: a server for the prediction and evaluation of "hot spots" of aggregation in polypeptides // BMC Bioinformatics. – 2007. – Vol. 8. – P. 65.
34. Tartaglia G.G., Vendruscolo M. The Zyggregator method for predicting protein aggregation propensities // Chem. Soc. Rev. – 2008. – Vol. 37. – P. 1395–1401.
35. Linding R., Schymkowitz J., Rousseau F., Diella F., Serrano L. A comparative study of the relationship between protein structure and beta-aggregation in globular and intrinsically disordered proteins // J. Mol. Biol. – 2004. – Vol. 342. – P. 345–353.
36. Holm N.K., Jespersen S.K., Thomassen L.V., Wolff T.Y., Sehgal P., Thomsen L.A., Christiansen G., Andersen C.B., Knudsen A.D., Otzen D.E. Aggregation and fibrillation of bovine serum albumin // Biochim. Biophys. Acta. – 2007. – Vol. 1774. – P. 1128–1138.
37. Sudlow G., Birkett D.J., Wade D.N. The characterization of two specific drug binding sites on human serum albumin // Mol. Pharmacol. – 1975. – Vol. 11. – P. 824–832.
38. Vus K., Tarabara U., Kurutos A., Ryzhova O., Gorbenko G., Trusova V., Gadjev N., Deligeorgiev T. Aggregation behavior of

novel heptamethine cyanine dyes upon their binding to native and fibrillar lysozyme // Mol. Biosyst. – 2017. – Vol. 13. – P. 970–980.
39. Krebs M.R., Bromley E.H., Donald A.M. The binding of thioflavin-T to amyloid fibrils: localisation and implications // J. Struct. Biol. – 2005. – Vol. 149. – P. 30–37.
40. Bolel P., Mahapatra N., Datta S., Halder M. Modulation of accessibility of subdomain IB in the pH-dependent interaction of bovine serum albumin with Cochineal Red A: a combined view from spectroscopy and docking simulations // J. Agric. Food Chem. – 2013. – Vol. 61. – P. 4606–4613.
41. Godjayev N.M., Akyüz S., Ismailova L. The conformational properties of Glu 35 and Asp 52 of lysozyme active center // An International Journal for Physical and Engineering Sciences. – 1998. – Vol. 51. – P. 56–60.
42. Sudlow G., Birkett D.J., Wade D.N. Further characterization of specific drug binding sites on human serum albumin // Mol. Pharmacol. – 1976. – Vol. 12. – P. 1052–1061.
43. Peyrin E., Guillaume Y.C., Guinchard C. Characterization of solute binding at human serum albumin site ii and its geometry using a biochromatographic approach // Biophys. J. – 1999. – Vol. 77. – P. 1206–1212.

East Eur. J. Phys. Vol.4 No.3 (2017) 71-77 DOI:10.26565/2312-4334-2017-3-10

PACS: 42.15.Dp; 42.15.Fr

LIGHT ABERRATION IN OPTICAL ANISOTROPIC SINGLE-AXIS MEDIUM

V.M. Svishch
Kharkov National University of Radio Electronics
Science av. 14, Kharkov, Ukraine, 61166
E-mail: vladimir.svishh@rambler.ru
Received June 5, 2017

The entrainment of the light flux by a uniaxial anisotropic medium and its influence on the measurement of stellar aberration are analyzed. The influence of the entrainment of the light flux by an isotropic medium on the measurement of stellar aberration was considered by Fresnel early. The absence of such influence was confirmed by Erie's experience when filling the telescope tube with water. The formula itself was perfectly confirmed by Fizeau's experiments with moving water and the repetition of this experiment with an increase in the accuracy of measurements by Michelson, Zeeman, and others. G.A. Lorentz already on the basis of the electromagnetic theory specified the formula with allowance for the frequency dispersion of the light flux. A. Einstein made an analysis of the schemes of experiments for determining the drag coefficient, covering all possible variants of similar experiments. As a result, he obtained Fresnel and Lorentz formulas, taking into account the frequency dispersion of light, starting from the theory of relativity. The entrainment of light and its influence on the measurement of stellar aberration by a uniaxial anisotropic medium have not been considered anywhere. An analysis of such influence is carried out. The results of the analysis indicate the possibility of measuring the current value of stellar aberration using a uniaxial anisotropic medium. The concept of active light aberration is introduced. The proposed schemes of experiments of using the entrainment of a light flux by an anisotropic substance for measuring the current value of stellar aberration are investigated. It is concluded that it is possible to study the determination of the current velocity of an inertial system relative to the light flux.
KEYWORDS: light aberration, entrainment of the light flux by the medium, refractive index, optically anisotropic medium, telescope, observer speed, light speed

АБЕРАЦІЯ СВІТЛА В ОПТИЧНОМУ АНІЗОТРОПНОМУ ОДНОВІСНОМУ СЕРЕДОВИЩІ

В.М. Свищ
Харківський національний університет радіоелектроніки
пр. Науки 14, Харків, Україна, 61166

Аналізується захоплення потоку світла одновісним анізотропним середовищем та його вплив на виміри зіркової аберації. Вплив захоплення потоку світла оптично ізотропним середовищем на виміри зіркової аберації було розглянуто ще Френелєм. Відсутність такого впливу підтверджено дослідом Ері при наповненні труби телескопу водою. Сама формула захоплення була яскраво підтверджена дослідами Фізо з водою яка рухається вздовж потоку світла. Подібні досліди неодноразово повторювалися з підвищенням точності вимірів Майкельсоном, Зеєманом та іншими. Г.А. Лоренц вже на основі електромагнітної теорії уточнює формулу Френеля з урахуванням частотної дисперсії світла. А. Ейнштейн виконав аналіз схем дослідів визначення коефіцієнту захоплення, охоплюючих всі можливі варіанти подібних дослідів. В підсумку він отримав формули Френеля та Лоренца з урахуванням частотної дисперсії світла виходячи з теорії відносності. Захоплення потоку світла та його вплив на виміри зіркової аберації одновісним анізотропним середовищем з одною оптичною віссю ще ніде не розглядалося. Виконано аналіз такого впливу. Результати аналізу вказують на можливість виміру поточного значення зіркової аберації з використанням одновісного оптично анізотропного середовища. Введено поняття активної аберації світла. Досліджені запропоновані схеми дослідів застосування захоплення потоку світла одновісним анізотропним середовищем для виміру поточного значення зіркової аберації. Зроблено висновок про можливість дослідження визначення поточної швидкості інерціальної системи відносно потоку світла.
КЛЮЧОВІ СЛОВА: аберація світла, захоплення потоку світла середовищем, показник заломлення, оптично анізотропне середовище, телескоп, швидкість світла

АБЕРРАЦИЯ СВЕТА В ОПТИЧЕСКОЙ АНИЗОТРОПНОЙ ОДНООСНОЙ СРЕДЕ

В.М. Свищ
Харьковский национальный университет радиоэлектроники
пр. Науки 14, Харьков, Украина, 61166

Анализируется увлечение светового потока одноосной анизотропной средой и его влияние на измерение звездной аберрации. Влияние увлечения светового потока изотропной средой на измерение звездной аберрации было рассмотрено еще Френелем. Отсутствие такого влияния было подтверждено опытом Эри при заполнении трубы телескопа водой. Сама формула была прекрасно подтверждена опытами Физо с движущейся водой и повторением этого опыта с повышением точности измерений Майкельсоном, Зееманом и другими. Г.А. Лоренц уже на основании электромагнитной теории уточнил формулу с учетом частотной дисперсии светового потока. А. Эйнштейн сделал анализ схем опытов определения коэффициента увлечения, охватывающих все возможные варианты подобных опытов. В результате он получил формулы Френеля и Лоренца с учетом частотной дисперсии света исходя из теории относительности. Увлечение света и его влияние на измерение звездной аберрации одноосной анизотропной средой еще нигде не рассматривалось. Проведен анализ такого влияния. Результаты анализа указывают на возможность измерения текущего значения звездной аберрации при использовании одноосной анизотропной среды. Введено понятие активной аберрации света. Исследованы предложенные схемы опытов использования увлечения светового потока анизотропным веществом для измерения текущего значения

звездной аберрации. Сделан вывод о возможности исследования определения текущей скорости инерциальной системы относительно светового потока.
КЛЮЧЕВЫЕ СЛОВА: аберрация света, увлечение светового потока средой, показатель преломления, оптически анизотропная среда, телескоп, скорость наблюдателя, скорость света

Influence of the light flux carrying away by anisotropic medium on star aberration measurement was considered already by Fresnel. At such measurement light carrying away by anisotropic medium was not taken into account.

Let us analyze the influence of light carrying away by single-axis anisotropic medium on measurement of star aberration.

In 1818, Fresnel proposed theory of partial light flux carrying away by a moving substance having carrying away coefficient

$$\chi = 1 - \frac{1}{n^2}. \tag{1}$$

Based on the simplest mechanical model on full carrying away of thee the part by bodies (the part which forms its over-density as compared with the surrounding ether) he obtained correct formula [1, 2] confirmed by experiments. This formula was excellently proved by Fizeau experiment (1851) with moving water, repeated by Michelson (1886) and Zeeman (1914) with increase of measurement accuracy.

Base done lector magnetic theory G.A. Lorentz (1886) corrected the formula with the account of light flux frequency dispersion [3]. Zeeman experiments with moving rods confirmed the existence of Lorentz dispersion term.

A. Einstein highly appreciated the significance of Fizeau experiment.

«The answer to this problem is given by highly important experiment made more than half a century ago by brilliant physicist Fizeau…».

«Although its hold be noted that long before appearance of relativity theory G.A. Lorentz explained the theory of this phenomenon and justified it by purely electrodynamics method by means of certain hypothesis about electromagnetic matter structure.

However this does not diminish the evidential force of Fizeau experiment has experiment um cruces in favors of relativity theory, since Maxwell-Lorentz electrodynamics which was used as original theory do not contradict the relativity theory». «Fizeau experiment is fundamental also for the special relativity theory» [4].

A. Einstein made anal by sis based on relativity theory of three scheme variants of experiments on determination of carrying away coefficient embracing all possible variants of similar experiments. As a result, he obtained Fresnel and Lorentz formulae with the account of light frequency dispersion. This once again proved correctness oft here relativity theory [4].

W.E. Frankfurt, A.M. Frank [5] note that «in the relativity theory results of these experiments are explained simply as consequence of relativity velocity addition formula

$$c' = \frac{\frac{c}{n} \pm V}{1 \pm \frac{V}{nc}}. \tag{2}$$

Taking only terms of the first order, we obtain

$$c' = \frac{c}{n} \pm \left(1 - \frac{1}{n^2}\right) V, \tag{3}$$

(where c' is the speed of light with respect to the fixed installation and the observer). .

Although the formula has the same appearance here “partial carrying away” is the result of pure metric properties and is not connected with any assumption about substance structure or ether properties» [5].

A. Somerfield [6] investigated aberration and crystal optics based on Lorentz transformations however all these investigations and experiments related to longitudinal, as to direction of propagation, light flux carrying away but transverse carrying away was not considered.

At the same time (1818), Fresnel investigated the influence of such transverse carrying away on star aberration measuring. He considered the experiment with filling a telescope tube with water and made the conclusion about absence of influence of such filling on the value of star aberration. «Although this experiment was not yet made, but I have no doubt, that it will support this conclusion …» he wrote to Arago in 1818.

Eri made such an experiment in 1871, which confirmed permanency of star aberration angle. The analysis of such filling in was made in detail in [7].

In 1977 H. Bilger and W. Stawell conducted the experiment, wherein light propagated in the rotating optical disc

of the annular laser interferometer. [8]

Anisotropy of the electromagnetic radiation velocity space under transversal light entrainment in the rotating optical disc was investigated by V.O. Gladyshev, P.S. Tiunov, A.D. Leontiev, T.M. Gladysheva, E.A. Sharandin. By anisotropy in this case we mean the dependence of the propagation velocity of light in the optical medium on the velocity and direction of motion of the medium [9]

All this investigations are related to the light propagation in the isotropic mediums.

The main purpose of this work is to study the effect of the partial entrainment of a light flux by an optically anisotropic uniaxial substance on the measurement of stellar aberration.

THE TRANSVERSE ENTRAINMENT OF THE LIGHT FLUX BY AN ANISOTROPIC SUBSTANCE

Examine consider influence of the partial light flux carrying away by the anisotropic substance on the star aberration with different refraction indices along telescope axis and in transverse direction for an extraordinary beam.

Assume a star S be observed through an unfilled telescope (Fig. 1).

Due to star aberration because of telescope motion at speed V, its axis is directed towards O_1S_0 at the angle $\alpha_0 = \angle S - O_1 - S_0 = \angle O_2 - O_1 - B_1$ to beam $S - O_1$ of the star S. Here S_0 is aster position being watched, S – true star position. At small angles α_0 $\alpha_0 = \frac{V}{c}\sin\psi$, where c is light velocity in vacuum, V –observer's speed, ψ - angle between direction $O_1 - S$ onto star S and vector of observer's speed V.

Let us fill the telescope with optically anisotropic substance with refraction indices of an ordinary light n_o along axis O_1O_2 and radius O_2B of the telescope tube, extraordinary beam $n_e = n_o$ along O_1O_2 and $n_e \neq n_o$ along telescope tube radius O_2B in the direction of velocity V $\Delta n = n_o - n_e \neq 0$ (Fig. 2).

Now the light flux SO of the star S will get refracted on the medium border MN. Refraction angle of an ordinary light beam will be $r_o = \frac{\alpha}{n_o}$.

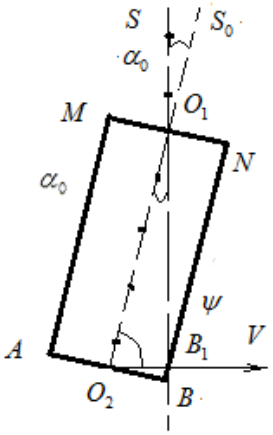

1

Fig. 1
Unfilled telescope

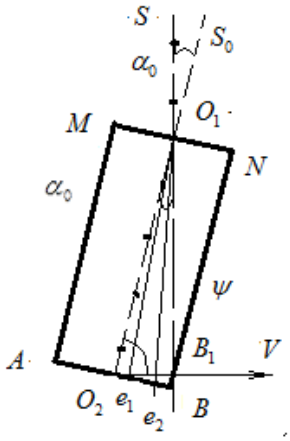

2

Fig. 2
Telescope filled with anisotropic medium

If to align the exit of an ordinary beam with the telescope cross sight reticule, then as shown by Fresnel and confirmed by Eri experiment, the aberration angle will remain as previous – α_0.

Really, if light flux carrying away by the medium with refraction index n_0 of the telescope moving at the speed V is not taken into account, then considering light flux $\overline{c}$ speeding down along axis O_1O_2 $\overline{c} = \frac{c}{n_o}$ the telescope should be inclined at the angle α $tg\alpha = \frac{O_2B}{O_1O_2}\sin\psi$ (ψ is an angle between the telescope axis and the direction of its motion speed V). Since $O_1O_2 = t\overline{c}$, $O_2B_1 = tV$ and α is small, then

$$\alpha = n_o \frac{V}{c} \sin\psi = n_o \alpha_0 , \tag{4}$$

where t is time of the light flow passing along the telescope axis O_1O_2, $\overline{c}$ – being light velocity in the medium.

On the other hand, since refraction angle $r_o = \frac{\alpha}{n_o}$ and we align the exit of the ordinary light beam with the cross sight reticule then the new aberration angle α could be

$$\alpha = n_o^2 \alpha_0 . \tag{5}$$

However, the light flux inside the telescope tube together with the medium is carried away at the speed V_u in the direction of speed V with coefficient $(1-\frac{1}{n_1^2})$ $V_u = V\ (1-\frac{1}{n_1^2})$, where n_1 is the refraction index in the direction of speed V. This is equivalent to the decrease of speed V by the value V with coefficient $(1-\frac{1}{n_1^2})$ [7,8].

Speed V_n, with the account of carrying away will become $V_n = V - V(1-\frac{1}{n_1^2}) = V\frac{1}{n_1^2}$. Substituting $V_n = V\frac{1}{n_1^2}$ in α_0 we will obtain the value of the new aberration angle α.

$$\alpha = n_o^2 \frac{V_n}{c} \sin\psi = \frac{n_o^2}{n_1^2} \frac{V}{c} \sin\psi , \tag{6}$$

$$\alpha = \frac{n_o^2}{n_1^2} \alpha_0 . \tag{7}$$

When filling in with isotropic l substance $n_o = n_1$ and $\alpha = \alpha_0$. For a no ordinary light beam also $n_o = n_1$, that is why $\alpha = \alpha_0$ is for it too.

For a next, no ordinary light beam $n_e \neq n_o$, so if to align the exit of the extraordinary light beam with the cross sight reticule, then the aberration angle will be different:

$$\alpha = \alpha_e = \frac{n_o^2}{n_1^2} \alpha_0 . \tag{8}$$

Let us denote $k = \frac{n_o^2}{n_e^2}$ and $\alpha = k\alpha_0$ then the aberration angle for an extraordinary light beam will be $\alpha_e = k\frac{V}{c}\sin\psi$;

$$\alpha_e = k\alpha_0 . \tag{9}$$

For is anisotropic substances $k = 1$ and $\alpha = \alpha_0$, but for anisotropic substances $k \neq 1$ and α_e differs from α_0.

STUDY OF THE SCHEMES OF EXPERIMENTS USING AN ANISOTROPIC SUBSTANCE TO MEASURE THE CURRENT ABERRATION VALUE

Let us consider possible variants of using this difference for determination of the star aberration angle. Then for the sake of simplicity we will regard the angle ψ being equal 90^0.

1. Let us measure the star position γ_1 by means of the "empty" telescope (fig.1) $\gamma_1 = \gamma_3 + \alpha_0$ (where γ_3 being

real star coordinate) and by means of γ_2 telescope filled with anisotropic ($n_e \neq n_o$) substance with known k (Fig.2), by the extraordinary light beam (aligning the exit of the extraordinary light beam e_2 with the telescope cross sight reticule) $\gamma_2 = \gamma_3 + \alpha_e$. The optical axis of the anisotropic substance is parallel to the telescope axis Oo. Determine the difference $\gamma_2 - \gamma_1 = \alpha_e - \alpha_0$; substituting $\alpha_e = k\alpha_0$ we obtain

$$\gamma_2 - \gamma_1 = (k-1)\alpha_0. \tag{10}$$

Hence we will determine the aberration angle α_0 of the star S

$$\alpha_0 = \frac{\gamma_2 - \gamma_1}{k-1}. \tag{11}$$

2. Let us measure the star position by means of the telescope, filled with anisotropic substance ($n_e \neq n_o$) with the known k (Fig. 2) by the ordinary light beam (with the ordinary light beam exit e1 being in the cross sight reticule) γ_4 and by the extraordinary light beam (with the extraordinary light beam exit e_2 being in the cross sight reticule) γ_5. Optical axis of the anisotropic substance is parallel to the telescope axis. Determine their difference $\gamma_5 - \gamma_4$. By analogy we obtain

$$\alpha_0 = \frac{\gamma_5 - \gamma_4}{k-1}. \tag{12}$$

3. Let us install a single–axis doubly refracting crystal 1, with crystal faces being perpendicular to its optical axis, so that optical axis of the crystal was parallel to the telescopic axis 4 (Fig. 3). We'll observe the star through the telescope aligning the star image by means of the ordinary light beam with telescope cross sight reticule 6. The star light flux will fall on the crystal face at the aberration angle α_0. In the crystal the light flux will divide into ordinary and extraordinary flows having different direction of the linear polarization. Due to different refract ion indices $n_e \neq n_o$, they will get refracted at different refraction angles.

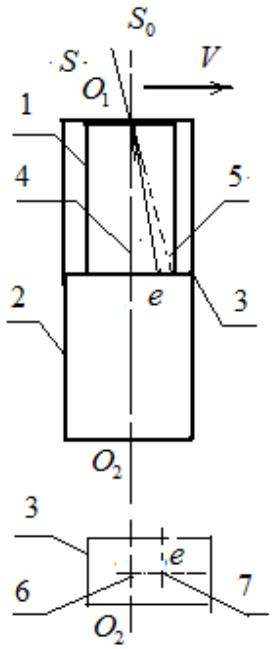

Fig.3
Telescope with single-axis crystal

The ordinary light beam refraction angle will be $r_o = \frac{\alpha_0}{n_o}$. For the extraordinary light beam refraction angler of

the single-axis doubly refracting crystal in the direction of the optical axis is equal to the ordinary light beam refraction index no and changes depending on the extraordinary light beam direction angle to the optical axis $0 \to \frac{\pi}{2}$ within $n_o \to n_e$.

Thus, the extraordinary light beam r_e fraction angler depends upon the angle of incidence α of the falling light beam. At the same time speed V_n with the account of the extraordinary light beam carrying away also depends on n_e^2 $V_n = \frac{1}{n_e^2} V$, so r_e depends upon the direction with respect to the optical axis and upon the value of the crystal motion speed (Fig. 1,2).

$$r_e = f_1(\alpha) \text{ and } r_e = f_1(V). \tag{13}$$

For a crystal with of ace perpendicular to the optical axis the refraction index of the ordinary light beam can be $r_e = r_o$ demonstrate das asp here with radius n_o, and the refraction index of the extraordinary light beam as a revolution ellipsoid with the revolution axis $n_o = n_e$ along optical axis and with axis radius n_e in the face plane. The incidence anglers small (aberration angle $\leq 200''$), so small is the refraction angle and the difference between the extraordinary light beam refraction index and the ordinary light beam refraction indexes small so it is possible to assume that

$$n_e(r_e) = n_e(\alpha) = n_o. \tag{14}$$

The main influence on the extraordinary light beam refraction angle at small r_e will be exerted by the extraordinary light beam carrying away during crystal motion perpendicular to the optical axis in the angle r_e plane where the difference $n_o - n_e$ is maximum, i.e., the difference between angles of propagation of the ordinary and extraordinary light beams will be determined in this case by the lateral speed of the telescope motion (Fig.3).

If to take into account $(n_e(\alpha) = n_o)$ and minuteness of angles r_e, r_o (Fig.3), then

$$r_e - r_o = \frac{O_2 e}{O_1 O_2}; O_2 e = t V_n; V_n = V \frac{1}{n_e^2(\alpha)}; O_2 e = tV \frac{1}{n_e^2(\alpha)}; O_2 O_1 = t\overline{c}; r_e - r_o = \frac{V}{\overline{c}} \frac{1}{n_e^2(\alpha)}; \overline{c} = \frac{c}{n_o};$$

$$\Delta_1 = \frac{n_o}{n_e^2} \alpha_0, \tag{15}$$

where $\overline{c}$ – is the speed of the ordinary light beam in the crystal, t – time of passing of the ordinary light beam along the crystal axis.

On the other hand $\Delta_1 = \frac{O_2 e}{O_1 O_2}$ and

$$\alpha_0 = \frac{n_e^2}{n_o} \frac{O_2 e}{O_1 O_2}. \tag{16}$$

Knowing O_1O_2, n_o, n_e and having measured O_2e, aberration angle α_0 can be determined.

Thus, observing the star through the telescope with a single-axis doubly refracting crystal, align the star image by means of ordinary light beams with the cross sight reticule and measure the distance O_2e between star images by the ordinary and extraordinary light beams. Knowing n_0, n_e and crystal length O_1O_2 we determine α_0, without changing the direction of the observer's motion. The aberration direction is determined by the direction of the star image shifting by extraordinary light beams in the focal plane of the telescope.

Lorentze transformation defined movement effect (second-order quantities $\triangle t$, $\triangle r$ proportional to $\frac{V^2}{c^2}$) may be ignored if measured quantities are proportional to $\frac{V}{c}$.

In all variants under consideration the current value of the star aberration can be determined without changing the direction of the observer's motion.

When observing star through the unfilled telescope the light flow does not change its direction when entering the telescope tube. To hold the star image in the cross hairs of the focal plane it has to be deflected by the aberration angle towards the telescope motion relative to the light flux of the star being observed.

In the telescope filled with isotropic medium the light flux gets refracted at the exit in to the telescope, but because of the transverse carrying away of the medium moving which is moving together with the telescope the refraction angle gets compensated, the light flux does not change the direction of its propagation and the telescope has to be deflected by the same aberration angle.

In both cases, the light flux does not change the propagation direction, and the telescope passively gets adjusted to its motion.

In the telescope filled with anisotropic medium with optical axis parallel to the telescope axis the extraordinary light beam changes its propagation direction as compared with the direction of the entry star light flux and that of the ordinary light beam in the telescope.

Active change of the extraordinary light beam direction is caused by different refraction indices of the medium along its optical axis, coinciding with the telescope axis and the direction of its motion together with the telescope.

This active aberration differs from passive aberration by the value and coincides by the direction.

Among abundance of stars one can find stars having at the given moment speed equal to observer's speed.

Aberration of their light flow for the observer is of no importance, which proves independence of the light velocity from the speed of its source. At the same time, the star and the observer can be considered as an inertial system with a source. Measuring active and passive aberration, we measure by their difference the system speed without changing the direction of the observer's motion. This gives an opportunity to investigate practical realization of devices for measuring speed of inertial systems with respect to the light flux.

CONCLUSIONS

1. When observing through the telescope filled with optically anisotropic medium by means of extraordinary light beams the aberration angle differs from the aberration angle when observing through then filled telescope or telescope filled with isotropic medium.

2. Different proportion of transverse carrying away speed of the extraordinary light beam flux and its longitudinal speed in the moving anisotropic medium, as compared with their proportions in the isotropic medium, cause difference in aberration angles in these media

3. Since anisotropic medium refraction index depends on the direction of the light flux propagation, this direction changes at the transverse motion of the anisotropic medium. The value of this change depends on the direction and speed of the medium motion.

4. In contrast to star aberration of the unfilled telescope, where there is no change of the light flow direction but passive adjustment of the moving telescoped expending on its speed takes place, when filling it with anisotropic medium the direction of the light flow propagation of the extraordinary light beams is actively changing.

5. The difference of passive and active aberration angles gives an opportunity to measure current values of star aberrations of various types (daily, yearly, century-old) and hence of various components of the telescope speed.

6. Measure mentor various speed components is possible without changing the direction of the telescope motion.

7. Active aberration gives an opportunity to investigate measurement of the transverse speed of the inertial system with respect to the light flux without change of direction of the observer's motion.

REFERENCES

1. Lakur P., Appel Ya. Historical Physics. – M-L.: GIZ, 1929.
2. Mandelstam L. Lecturesin Optics, Relativity Theory and Quantum Mechanics. – M.: Nauka, 1972.
3. Lorentz G.A. The theory of Electrons. – Leipzig. 1916.
4. Einstein A. Collection of Transactions, Vol.1. – M.: Nauka, 1963. – P. 313-315, 549.
5. Frankfurt W.I., Frank A.M. Optics of Moving Bodies. – M.: Nauka, 1972.
6. Sommerfield A. Vorlesungenuber Teoretische Physik. Rand 4. Optic von Arnold Sommerfeld. – Wisbaden, 1950.
7. Landsberg T.S. General Physics. Optic. – M.: Nauka, 1976.
8. Bilger H.R., Stowell W.K. // Phys. Rev. A. – 1977. – Vol. 16. – No.1. – P. 313–319.
9. Gladyshev V., Tiunov P., Leontev A., Gladysheva T., Sharandin E. Investigation of speed anisotropy of electromagnetic radiation in the moving environment // Journal of Technical Physics. – 2012. – Vol. 82. – No. 11. – P.54-63. (in Russian)
10. Gimmelfarb B.N. To an Explanation of Stellar Aberration in the Theory of Relativity // Physics-Uspekhi (Advances in Physical Sciences). – 1953. – Vol. 51.

EAST EUROPEAN JOURNAL OF PHYSICS
East Eur. J. Phys. Vol.4 No.3 (2017) 78-84 DOI:10.26565/2312-4334-2017-3-11

PACS: 73.63.Bd; 75.47.-m; 75.60.Ej; 75.75.Fk

COERCIVE FORCE IN THE SYSTEM OF FERROMAGNETIC GRANULES FOR HALF METAL CrO_2 WITH PERCOLATION CONDUCTIVITY

N.V. Dalakova, E.Yu. Beliayev, V.A. Horielyi
B.I. Verkin Institute for Low Temperature Physics and Engineering, NAS of Ukraine
47 Nauky Ave., 61103, Kharkov, Ukraine
e-mail: dalakova@ilt.kharkov.ua
Received August 7, 2017

Magnetic and magnetoresistive properties of several samples of compacted powders of ferromagnetic half-metal CrO_2, consisting of needle-shaped or spherical nanoparticles coated with thin dielectric shells, were investigated in wide temperature range. The temperature dependence of the coercive force $H_c(T)$ is compared with the temperature dependence of the field of maximum of positive tunneling magnetoresistance $H_p(T)$. The dependence of $H_p(T)$ was nonmonotonic one. It is found that in the low-temperature range (4.2 ÷ 70 K) the ratio $H_p \approx H_c$, expected for compacted ferromagnetic powders with particles of submicron sizes, does not fulfilled. It is assumed that the possible reason of the difference between H_p and H_c is the mismatch between the orientation of the global magnetization of the entire sample and the orientations of the magnetic moments in some part of granules that form the optimal conducting channels at low temperatures. Such a mismatch may be due to the multidomain granules are more prone to the formation of optimal conducting chains in the transport channels. That leads to a change in the mechanism of magnetization reversal in these channels and to violation of the ratio $H_p \approx H_c$.
KEY WORDS: half-metal, ferromagnets, tunneling magnetoresistance, granular systems, percolation, magnetization, coercive force

КОЭРЦИТИВНАЯ СИЛА СИСТЕМЫ ФЕРРОМАГНИТНЫХ ГРАНУЛ ПОЛОВИННОГО МЕТАЛЛА CrO_2 С ПЕРКОЛЯЦИОННЫМ ХАРАКТЕРОМ ПРОВОДИМОСТИ

Н.В. Далакова, Е.Ю. Беляев, В.А. Горелый
Физико-технический институт низких температур имени Б.И. Веркина НАН Украины
пр. Науки 47, Харьков 61103, Украина

В широкой области температур исследованы магнитные и магниторезистивные свойства нескольких прессованных порошков ферромагнитного половинного металла CrO_2, состоящих из игольчатых или сферических наночастиц, покрытых тонкими диэлектрическими оболочками. Проведено сравнение температурной зависимости коэрцитивной силы $H_c(T)$ с температурной зависимостью поля максимума положительного туннельного магнитосопротивления $H_p(T)$. Обнаружена немонотонная зависимость $H_p(T)$. Установлено, что в области низких температур (4,2 ÷ 70) K соотношение $H_p \approx H_c$, ожидаемое для прессованных ферромагнитных порошков с субмикронными размерами частиц, не выполняется. Предполагается, что возможная причина расхождения между H_p и H_c — нарушение взаимосвязи между ориентацией глобальной намагниченности всего образца и ориентациями магнитных моментов в тех гранулах, которые формируют оптимальные проводящие каналы при низких температурах. Подобное нарушение может быть связано с многодоменной структурой части гранул в транспортных каналах, что приводит к изменению механизма перемагничивания в этих каналах и нарушению соотношения $H_p \approx H_c$.
КЛЮЧЕВЫЕ СЛОВА: половинный металл, ферромагнетики, туннельное магнитосопротивление, гранулированные системы, перколяция, намагниченность, коэрцитивная сила

КОЕРЦИТИВНА СИЛА СИСТЕМИ ФЕРОМАГНІТНИХ ГРАНУЛ ПОЛОВИННОГО МЕТАЛУ CrO_2 З ПЕРКОЛЯЦІЙНИМ ХАРАКТЕРОМ ПРОВІДНОСТІ

Н.В. Далакова, Є.Ю. Біляєв, В.О. Горелий
Фізико-технічний інститут низьких температур ім. Б.І. Вєркіна НАН України
пр. Науки 47, Харків 61103, Україна

В широкому діапазоні температур було вивчено магнітні та магніторезистивні властивості декількох зразків пресованого порошку феромагнітного половинного металу CrO_2, що складається з голчастих або сферичних наночастинок, що були вкрити тонкими діелектричними оболонками. Температурна залежність коерцитивної сили $H_c(T)$ порівнюється з температурною залежністю поля максимуму позитивного тунельного магнітоопору $H_p(T)$. Залежність $H_p(T)$ була немонотонною. Встановлено що співвідношення $H_p \approx H_c$, очікуване для ущільнених феромагнітних порошків з частинками субмікронних розмірів, в низькотемпературному діапазоні (4,2 ÷ 70 K) не виконується. Передбачається, що можливою причиною різниці між H_p та H_c є невідповідність між спрямованістю глобальної намагніченості всього зразка та орієнтаціями магнітних моментів у тієї частині гранул, які утворюють оптимальні провідні канали при низьких температурах. Така невідповідність може бути пов'язана з тим, що мультідоменні гранули більш схильні до утворення оптимальних провідних ланцюгів в транспортних каналах. Це призводить до зміни механізму перемагнічування в транспортних каналах та порушення співвідношення $H_p \approx H_c$.
КЛЮЧОВІ СЛОВА: половинний метал, феромагнетики, тунельний магнітоопір, гранульовані системи, перколяція, намагніченість, коерцитивна сила.

Диоксид хрома (CrO_2) известен как половинный металл (half metal) типа I_A, у которого на уровне Ферми (E_F) имеются только электроны со спинами, направленными вверх (↑). Главным образом, это t_{2g} электроны

хрома [1]. CrO_2 имеет тетрагональную структуру типа рутила пространственной группы $P4_2/mnm$ с параметрами решетки a = 0,4422 нм и c = 0,2917 нм. Объемный (монокристаллический) CrO_2 обычно рассматривается, как ферромагнетик с заметным неаксиальным вкладом второго порядка, у которого ось c является осью легкого намагничивания. Температура Кюри диоксида хрома $T_C \approx 390$ K. Этот материал представляет интерес, как один из немногих оксидных ферромагнетиков при комнатной температуре с высоким значением спиновой поляризации. Начиная с 1968 года, высокодисперсный порошок диоксида хрома получил промышленное применение в качестве рабочего материала для магнитных носителей. В частности, диоксид хрома используется в производстве жестких дисков с большой плотностью записи информации. По этой причине огромное внимание исследователей и технологов привлекает проблема повышения коэрцитивной силы порошка CrO_2. Коэрцитивная сила H_c представляет собой значение напряженности магнитного поля, при котором намагниченность равна нулю. Чем больше коэрцитивная сила, тем выше способность материала противостоять размагничивающим полям. Как известно, максимальное значение коэрцитивной силы характерно для магнитного материала, состоящего из однодоменных частиц. Таким образом, получение порошков с высокой коэрцитивной силой сводится, в частности, к задаче синтеза однодоменных наночастиц диоксида хрома. Эту задачу можно решить, контролируя размеры и форму наночастицы путем использования малого количества модифицирующих добавок в процессе гидротермального синтеза [2].

В настоящей работе рассматривается зависимость коэрцитивной силы от температуры для нескольких прессованных порошков диоксида хрома, состоящих из наночастиц, покрытых диэлектрическими оболочками разного типа и разной толщины. Основные характеристики порошков приводятся в таблице.

Цель работы – исследование взаимосвязи между гистерезисными характеристиками магнитосопротивления и намагниченности.

Таблица

Сферические частицы имели диаметр 120 нм

№ серии	Состав порошка	частицы	Тип диэлектрической оболочки	Толщина оболочки, нм	Длина частицы нм	Толщина частицы нм	H_c, А/м (комн. темп.)
1	CrO_2	иглы	β-CrOOH	1,73	302	22,9±0,8	34387
2	CrO_2	иглы	Cr_2O_3	2,1	302	22,9±0,8	33591
3	CrO_2	сферические	β-CrOOH	3,6	–	–	11860
4	CrO_2	иглы	β-CrOOH	1,58	302	22,9±0,8	34148
5	CrO_2	иглы	β-CrOOH	~1	~240	24	41551
6	CrO_2_Fe	иглы	β-CrOOH	~1	~340	34	60576

Изменение величины коэрцитивной силы сопровождается не только изменением всех магнитных характеристик порошка CrO_2, но и изменением его магниторезистивных свойств, которые зависят от способности магнитных моментов наночастиц CrO_2 к переориентации во внешнем магнитном поле. Свойства монокристаллического CrO_2 радикально отличаются от свойств прессованных порошков CrO_2. Монокристаллический CrO_2 имеет металлический тип проводимости. Порошки CrO_2 представляют собой гранулированный материал с перколяционным характером проводимости. Перколяционная проводимость осуществляется по цепочкам, составленным из отдельных частиц/гранул. В прессованных порошках диоксида хрома, состоящих из наночастиц, покрытых тонким слоем диэлектрика (толщиной ~ 1÷4 нм), величина проводимости определяется вероятностью туннелирования носителей заряда между соседними частицами (гранулами) и зависит от толщины и свойств межгранульных диэлектрических прослоек. Такого рода проводимость называется туннельной. Собственное (intrinsic) магнитосопротивление (МС) монокристаллического CrO_2 составляет около 1% (при $H = 7{,}96\times10^5$ А/м) при комнатной температуре [3] и слабо меняется при понижении температуры. МС прессованных порошков оказывается гигантским, достигая более 30% при низких температурах и небольших полях [4, 5]. В гранулированном материале МС является несобственным (extrinsic). В этом случае вероятность туннелирования носителей заряда зависит от относительной ориентации вектора намагниченности в соседних гранулах [3] и очень чувствительна к приложенному магнитному полю. Она достигает максимального значения, когда моменты в смежных гранулах ориентированы параллельно [3]. В научной литературе такого рода туннелирование называется спин-зависящим (spin-dependent), а соответствующее магнитосопротивление называется туннельным.

Коэрцитивность прессованных порошков отчетливо проявляется в поведении туннельного МС. На рис.1 показан пример гистерезиса туннельного МС порошка CrO_2, состоящего из игольчатых частиц, покрытых слоем диэлектрика β–CrOOH толщиной 1,73 нм (таблица, порошок №1). Рис.1 демонстрирует типичное для поликристаллических оксидов переходных магнитных металлов поведение гистерезиса туннельного МС: $\Delta R(H) = [R(H)-R(0)]/R(0)$. Такое поведение полностью отражает поведение гистерезиса намагниченности [3]. А именно, в области низких полей появляются два максимума положительного МС при $H = \pm H_P$, где величина H_P соответствует коэрцитивной силе H_c, полученной из магнитных измерений. Гистерезис МС такого типа, как на

рис.1, для порошков CrO_2 обнаруживается только при достаточно высоких температурах $T > 15$ K. При $T < 15$ K наблюдается более сложный тип гистерезиса МС.

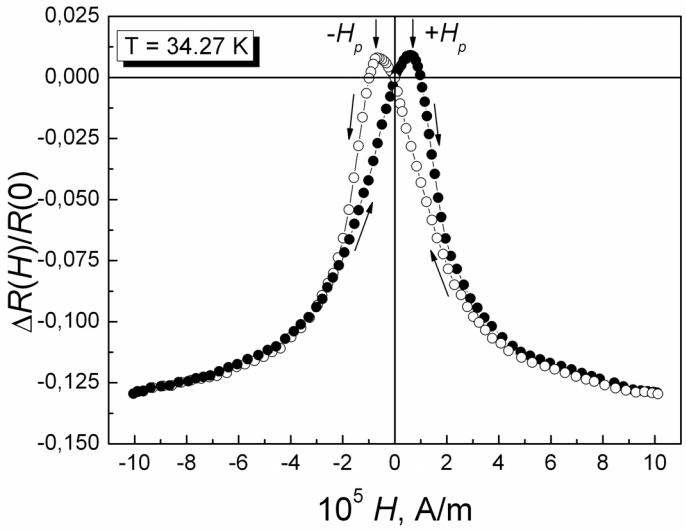

Рис.1. Гистерезис МС прессованного порошка CrO_2 (порошок № 1) при $T = 34{,}27$ K.
Стрелки указывают направление изменения магнитного поля при записи кривых МС. Поле H_p соответствует магнитному полю, при котором достигается максимальное значение сопротивления $R(H)$.

На рис.2,3 показаны гистерезисы туннельного МС и намагниченности трех образцов CrO_2, записанные при $T = 5$ K и при 20 K. Видно, что при 20 K наблюдается обычный тип гистерезиса МС. При 5 K вид гистерезиса усложняется. В этом случае наряду с двумя пиками положительного МС наблюдается дополнительное пересечение кривых $R(H)$ для прямой и обратной развертки магнитного поля в полях $H > H_p$. Второй гистерезис (при $H > H_p$) может быть связан с переключением небольшого количества перколяционных токовых каналов при вводе и выводе поля [6]. Гистерезисы МС, представленные на рис.2 и рис.3, показывают, что для образцов, состоящих из игольчатых частиц (порошки №1 и №2) $H_p \neq H_c$. При $T = 5$ K $H_p < H_c$. При $T = 20$ K $H_p > H_c$.

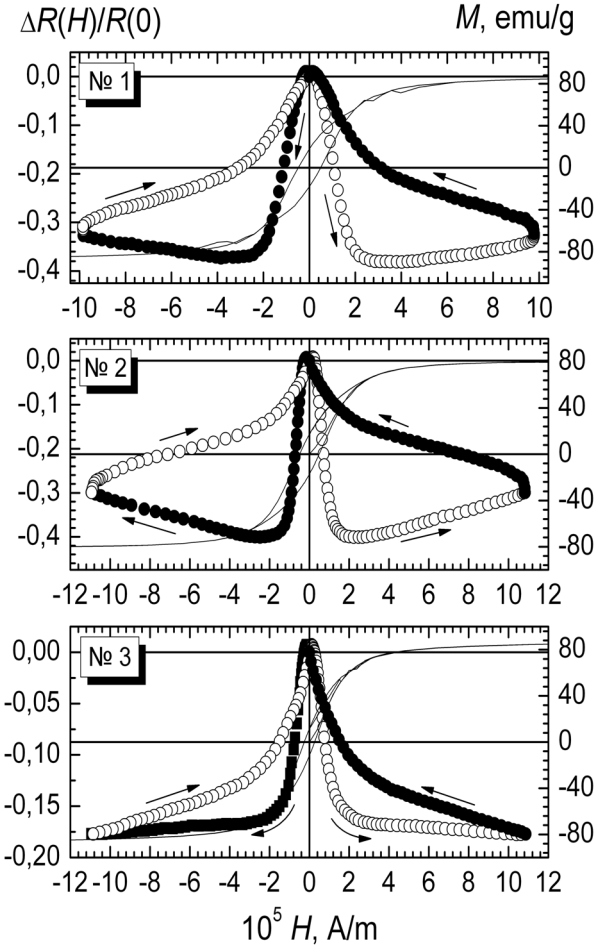

Рис.2. Гистерезисы туннельного МС трех образцов (левая ось ординат) и намагниченности (правая ось ординат) при $T = 5$ K.

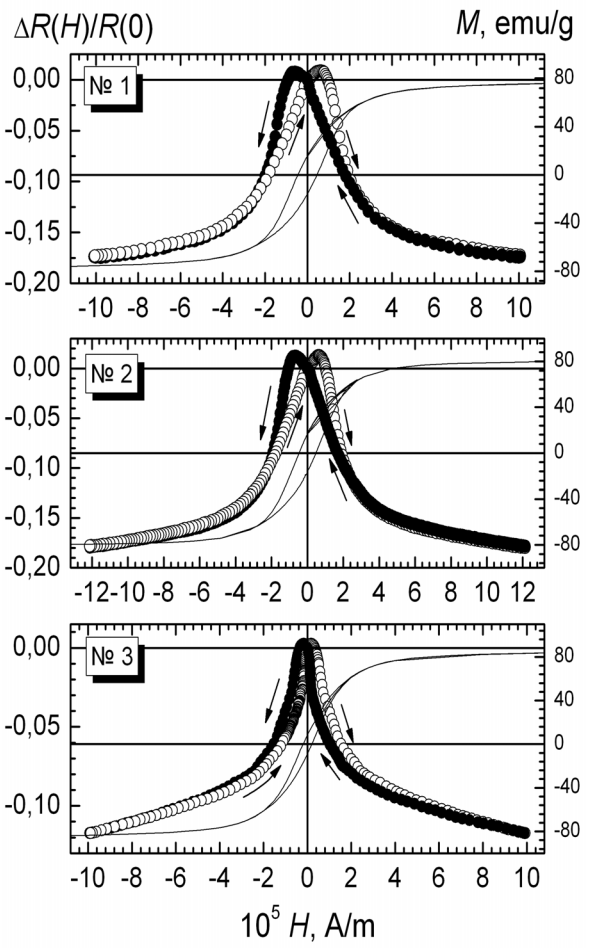

Рис.3. Гистерезисы туннельного МС трех образцов (левая ось ординат) и намагниченности (правая ось ординат) при $T = 20$ K.

Более отчетливо это различие видно на рис.4, на котором указанные зависимости построены для порошка № 2 в увеличенном масштабе. Таким образом, представляет интерес рассмотреть и проанализировать температурную зависимость коэрцитивной силы H_c и поля коэрцитивности H_p. Ранее в работах [6, 7] было обнаружено сильное отличие величин H_p и H_c в области низких температур. На рис.5 показан график зависимости $H_p(T)$ и $H_c(T)$ из работы [7]. Поведение $H_c(T)$ соответствует ожидаемому поведению для ферромагнетиков. Как известно, для однородных (однодоменных или многодоменых) ферромагнитных порошковых систем величина H_c должна быть максимальна при низких температурах и должна уменьшаться с увеличением температуры, стремясь к нулю при $T \to T_C$, что мы и наблюдаем на рис.5. В то же время зависимость $H_p(T)$ на рис.5 отвечает такому поведению только при $T > 50$ K. В целом, $H_p(T)$ ведет себя необычно.

Аномалии в поведении $H_p(T)$ заключаются в следующем: (i) немонотонное изменение поля H_p с температурой, (ii) существенное превышение величиной $H_p(T)$ соответствующих значений $H_c(T)$ в области 50 ÷100 K. С увеличением температуры при T >100 K разница между $H_p(T)$ и $H_c(T)$ заметно уменьшается. Для достаточно однородных порошковых систем отмеченные выше аномалии $H_p(T)$ представляются неожиданными. Таким образом, результаты, представленные на рис.5 показывают, что соотношение $H_p(T) \approx H_c(T)$, ожидаемое и наблюдаемое для прессованных порошков с достаточно малыми (субмикронными) размерами (включая и порошки CrO_2) [4, 5], не выполняется в широкой области температур. Рассмотрим насколько общей является наблюдаемая в [7] зависимость $H_p(T)$.

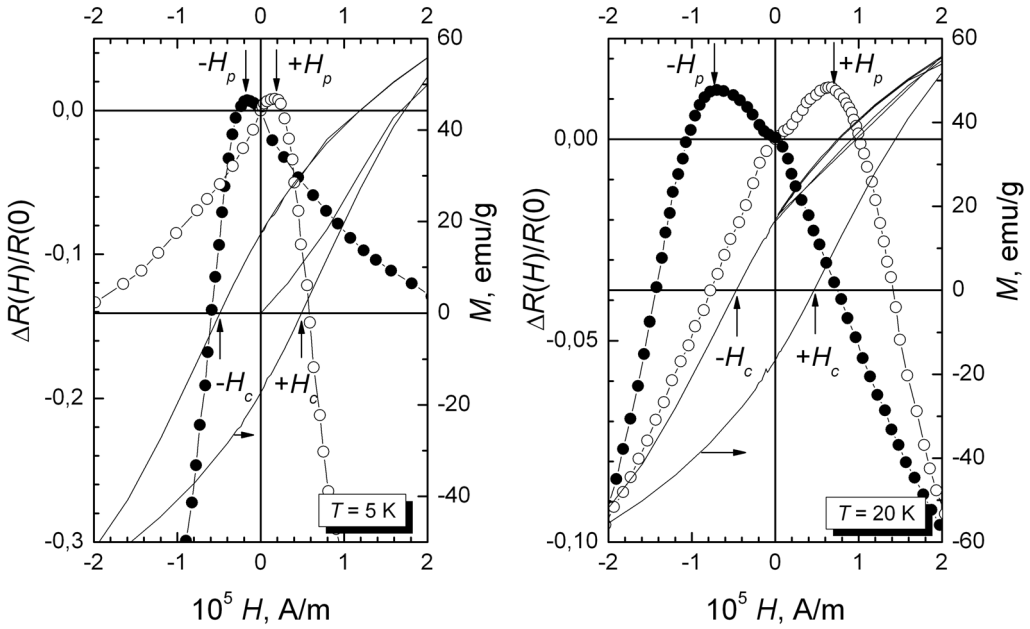

Рис.4. Гистерезисы МС (левая ось ординат) и намагниченности (правая ось ординат) образца № 2 при температурах 5 K и 20 K в области малых полей.

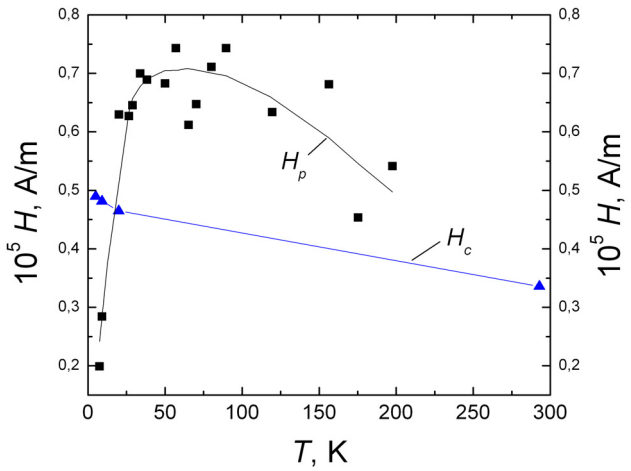

Рис.5. Температурные зависимости поля H_p (пик положительного МС) и коэрцитивной силы H_c образца № 2 [7]

ОБРАЗЦЫ И РЕЗУЛЬТАТЫ ИССЛЕДОВАНИЯ

На рис.6 показаны результаты измерения величин $H_p(T)$ и $H_c(T)$ семи образцов, представляющих собой прессованные нанопорошки диоксида хрома. Все порошки были приготовлены методом гидротермального синтеза на кафедре магнетохимии Санкт-Петербургского университета. Общие особенности использованной технологии синтеза описаны в работе [8]. Наночастицы CrO_2 были покрыты диэлектрическими оболочками, которые состояли либо из оксигидроксид хрома β-CrOOH, либо из оксида Cr_2O_3. Толщины диэлектрических оболочек указаны в таблице. Образец № 6 представлял собой твердый раствор замещения CrO_2 – Fe. Содержание железа в образце № 6 составляло 75 ммоль/(1 моль хрома).

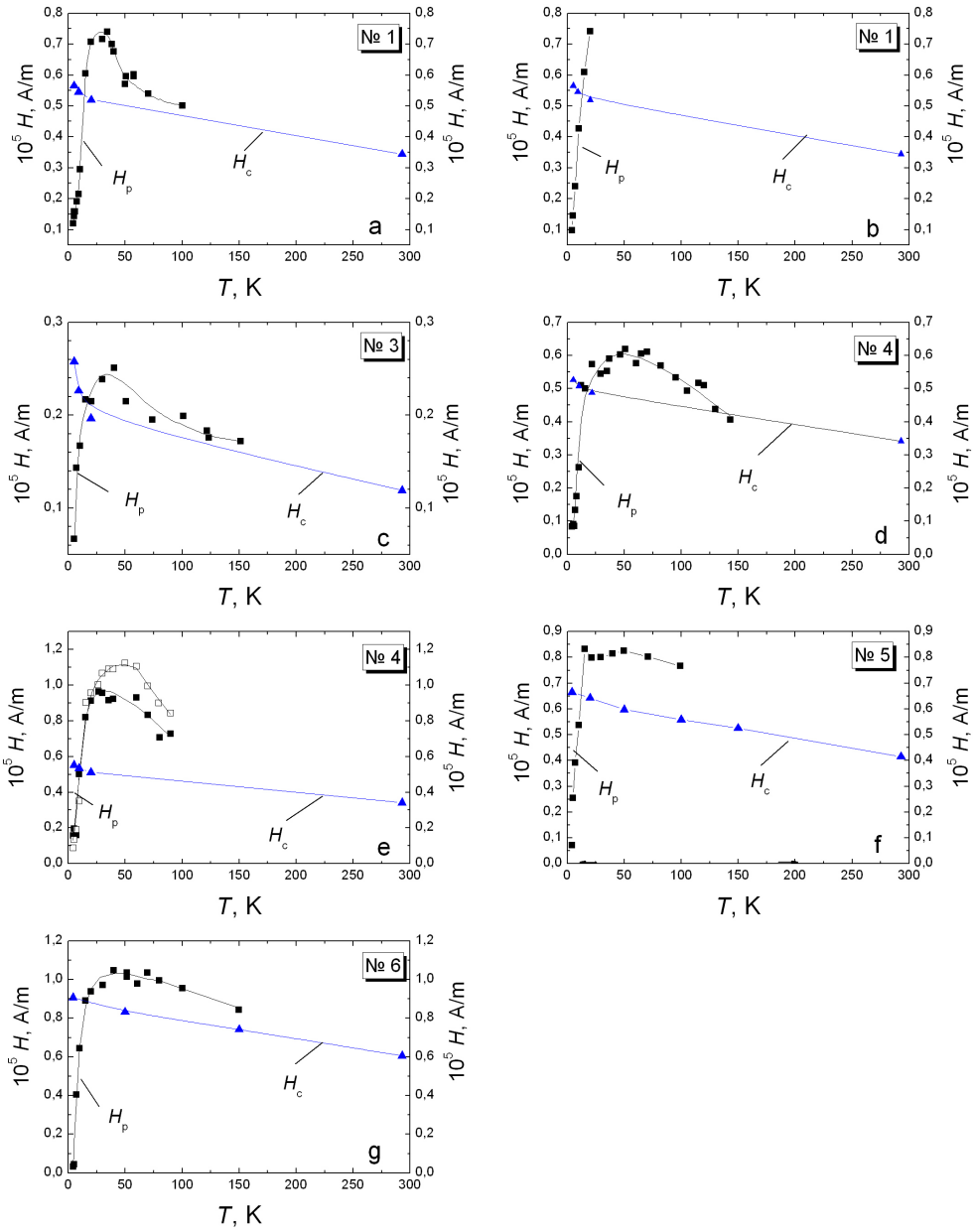

Рис.6. Температурные зависимости поля H_p (пик положительного МС) и коэрцитивной силы H_c семи различных образцов.

Номер на графике соответствует номеру образца в таблице. На рис. 6е светлые квадраты соответствуют ориентации поля перпендикулярно плоскости образца, темные квадраты – поле параллельно плоскости образца. В остальных случаях поле приложено параллельно плоскости образца.

Как видно из таблицы, примесь Fe существенно повышает коэрцитивную силу порошка H_c. В работе [9] методом мессбауэровской спектроскопии на атомах ^{57}Fe было установлено, что ионы Fe^{3+} в порошках диоксида хрома распределяются между тремя магнитными твердыми растворами. Помимо твердых растворов $Cr_{1-x}Fe_xO_2$ (это массивное вещество и обогащенный железом поверхностный слой) и включений частиц $Cr_{2-2x}Fe_{2x}O_3$ железо присутствует в оксигидроксиде хрома β-CrOOH, который входит в состав диэлектрической оболочки. Таким

образом, мы полагаем, что в образце № 6 железо присутствует в двух формах: в виде твердого раствора $Cr_{1-x}Fe_xO_2$ и в виде $Cr_{2-2x}Fe_{2x}O_3$. Первое соединение обеспечивает высокую коэрцитивную силу. Вторая фаза балластная. Она присутствует в виде отдельных малых частиц. Эти частицы антиферромагнитны или имеют намагниченность на два порядка ниже, чем у CrO_2. Фаза $Cr_{2-2x}Fe_{2x}O_3$ является диэлектрической и не дает вклада в проводимость. Концентрация железа меняется по толщине частицы. На поверхности она существенно выше, поэтому перемагничивание контролируется составом поверхности.

Из порошков посредством холодного прессования были сформированы таблетки, имеющие форму параллелепипедов с размерами 3×5×12 мм. Плотность прессованных таблеток составляла примерно 40% от рентгеновской плотности материала в случае игловидных частиц и 60% от рентгеновской плотности для сферических частиц. Следует отметить, что игольчатые частицы CrO_2 представляют собой монокристаллические образования, в большинстве своем состоящие из двух доменов. Вектор, направленный вдоль длины такой частицы, примерно совпадает с направлением тетрагональной оси *c*, которая является осью легкого намагничивания. При прессовании таблеток частицы, имеющие игольчатую форму, преимущественно ориентируются в плоскостях, перпендикулярных приложенной нагрузке. При этом ориентация частиц в плоскостях может быть довольно беспорядочной. Таким образом, для порошков с игольчатыми частицами имеется выделенное направление (параллельное вектору приложенной нагрузки или оси прессования), в котором среднее расстояние между частицами минимально. По этой причине мы полагаем, что намагничивание более легко должно происходить в случае, когда внешнее поле H направлено в плоскости образца, а поле коэрцитивности H_p должно быть анизотропным.

Все порошки были охарактеризованы посредством электронно-микроскопических, рентгеновских и магнитных исследований. Найденные параметры решетки (a = 0,4424 нм, c = 0,2916 нм) соответствовали известным данным чистого CrO_2. Значения H_p были получены из измерений гистерезисов МС. Значения H_c получены из измерений гистерезисов намагниченности. Резистивные измерения проводились по четырёхпроводной схеме в режиме заданного тока (J = 100 мкА) и выполнения закона Ома. Протокол измерений МС соответствовал обычному протоколу измерения гистерезисных кривых намагниченности в последовательности + $H_{max} \rightarrow 0 \rightarrow$ - $H_{max} \rightarrow 0 \rightarrow$ + $H_{max} \rightarrow 0$. Интервал магнитных полей при записи МС составлял ± $1{,}194\times10^6$ А/м. Скорость ввода-вывода магнитного поля составляла 16716 А/(м×сек). Измерения МС проводились с использованием вращающегося соленоида Капицы. Измерения намагниченности проводились на SQUID (Quantum Design) магнитометре. Для порошков № 1 и № 4 были измерены по два разных образца.

Зависимости $H_c(T)$ и $H_p(T)$ на рис. 6. показывают, что для всех порошков значения H_c, как и ожидается, максимальны при низких температурах и постепенно уменьшаются при $T \rightarrow T_c$. В то же время, поле H_p начинает уменьшаться с повышением температуры только при $T \geq 50$ K, как это наблюдалось ранее в работе [7]. В интервале температур 50 ÷100 K значения H_p существенно превышают H_c. Следует также отметить более высокие значения коэрцитивной силы H_c и поля H_p образца № 6 (CrO_2–Fe) по сравнению с аналогичными данными для остальных образцов и большие значения H_p в интервале температур 50 ÷ 70 K для образца № 4 на рис.6е. Результаты измерения $H_c(T)$ и $H_p(T)$ семи образцов показывают, что аномалии $H_p(T)$, которые заключаются в немонотонном поведении $H_p(T)$ и значительном превышении $H_p(T)$ значений $H_c(T)$ в интервале от 20 K до 100 K, по всей вероятности, являются общими для широкого класса ферромагнитных порошковых систем с перколяционным характером туннельной проводимости.

ОБСУЖДЕНИЕ РЕЗУЛЬТАТОВ

В работах [6, 7] наблюдаемые аномалии в поведении $H_p(T)$ объяснялись тем, что при низких температурах проводимость, и, следовательно, $R(H)$ и $R(0)$, определяются малой объемной долей гранул, формирующих «оптимальные» проводящие цепочки с максимальной вероятностью туннелирования. Как известно, количество таких цепочек непрерывно уменьшается с понижением температуры. При этом немногочисленные проводящие перколяционные каналы, дающие основной вклад в низкотемпературную проводимость, состоят в основном из многодоменных частиц [6]. Локальные величины H_c многодоменных частиц существенно меньше, чем у частиц однодоменных. Поэтому при низких температурах магнитные свойства этой части гранул могут заметно отличаться от глобальной намагниченности всего образца, измеряемой магнитометром. В частности, это может быть причиной уменьшения измеряемых величин $H_p(T)$ при достаточном понижении температуры, которое можно наблюдать на рис.5 и рис.6 при $T < 25$ K.

В работе [10], исследовано соотношение между значениями H_p и H_c порошков манганитов $La_{2/3}Sr_{1/3}MnO_3$ в зависимости от времени помола. Было показано, что увеличение времени помола приводит к уменьшению размера зерна и к формированию более однородной микроструктуры порошка. В результате исследования пяти порошков с разным размером зерна было обнаружено, что для многодоменных частиц манганитов выполняется соотношение $H_p \neq H_c$. Причем величина H_p существенно превышает H_c. Различие величин H_p и H_c уменьшается при уменьшении размеров частиц. При достаточном уменьшении размеров частиц с увеличением времени помола они становятся однодоменными, и начинает выполняется соотношение $H_p \approx H_c$. В однодоменных частицах при повышении магнитного поля магнитные моменты гранул ориентируются по полю путем

однородного вращения магнитных моментов частиц. В этом случае имеет место однозначное соответствие величины МС и измеряемой намагниченности образца, так что выполняется соотношение $H_p \approx H_c$ [10].

В многодоменных частицах перемагничивание при $H = H_c$ более легко происходит путем зарождения и роста домена с противоположным направлением магнитного момента. При этом движение доменных стенок внутри гранулы слабо влияет на спин-зависимое туннельное МС [10]. В таких условиях имеет место неравенство $H_p \neq H_c$ и отсутствует корреляция между измеряемой намагниченностью и МС. Эти представления можно применить и к образцам CrO_2 с игольчатыми (и даже округленными) частицами. Частицы (со средним диаметром 22,9 ÷ 34 нм и средней длиной 240 ÷ 340 нм) являются, несомненно, многодоменными, так как критический размер однодоменных частиц CrO_2 составляет 200 нм. Что касается порошка, состоящего из сферических частиц, то в силу некоторого разброса размера гранул, слипания некоторых гранул, что отчетливо проявлялось на микрофотографиях, снятых в просвечивающем электронном микроскопе, и по ряду других причин, нельзя исключить, что некоторые зерна были многодоменными [6].

Многие аспекты проблемы соотношения H_p и H_c, однако, до сих пор остаются неясными и требующими дальнейших исследований. В частности остается в значительной степени неясной обнаруженная в данной работе немонотонная зависимость $H_p(T)$. Кроме того, представляет интерес обнаруженная в [11] зависимость H_p от измерительного тока и от скорости ввода магнитного поля.

Авторы выражают благодарность сотрудникам кафедры магнетохимии Санкт-Петербургского Государственного Университета Осмоловской О.М. и Осмоловскому М.Г. за предоставление образцов.

СПИСОК ЛИТЕРАТУРЫ

1. Lewis S.P., Allen P.B., Sasaki T. Band structure and transport properties of CrO_2 // Phys. Rev. B. – 1997. – Vol. 55. – P.10253-10260.
2. Osmolowskaya O.M., Arkhipov D.I., Gordeev S.V., Dzidziguri E.L., Osmolowsky M.G. Synthesis of single-domain chromium dioxide nanoparticles with high coercive force // Zhurnal Obschej Khimii. – 2015. – Vol. 85. – P.1-3.
3. Ziese M. Extrinsic magnetotransport phenomena in ferromagnetic oxides // Rep. Progr. Phys. – 2002. – Vol. 65. – P.143-249.
4. Coey J.M.D. Powder Magneto-resistance // J. Appl. Phys. – 1999. – Vol. 85. – P. 5576-5581.
5. Coey J.M.D., Berkowitz A.E., Balcells Ll., Putris F.F., Barry A. Magnetoresistance of Chromium Dioxide Powder Compacts // Phys. Rev. Lett. – 1998. – Vol. 80. – P.3815-3818.
6. Belevtsev B.I., Dalakova N.V., Osmolowsky M.G., Beliayev E.Yu., Selutin A.A. Transport and magnetotransport properties of cold-pressed CrO_2 powder, prepared by hydrothermal synthesis // J. Alloys Comp. – 2009. – Vol. 479. – P.11-16.
7. Dalakova N.V., Belevtsev B.I., Beliayev E.Yu., Bludov O.M., Pashchenko V.N., Osmolowsky M.G., Osmolowskaya O.M. Resistive and magnetoresistive properties of compacted CrO_2 powders with different types of intergranular dielectric layers // Low Temperature Physics. – 2012. – Vol. 38. – P. 1422-1432.
8. Osmolovskii M.G., Kozhina I.I., Ivanova L.Yu., Baidakova O.L. Hydrothermal Synthesis of Chromium Dioxide // Russian Journal of Appl. Chem. – 2001. – Vol. 74. – P.1-6.
9. Bondarewsky S.I., Eremin V.V., Panchuk V.V., Semenov V.G., Osmolowsky M.G. Mössbauer study of the state of iron atoms in modified chromium dioxide // Fizika Tverdogo Tela (FTT). – 2016. – Vol. 68. – P.77-81.
10. Panagiotopoulos I., Moutis N., Ziese M., Bollero A. Magnetoconductance and hysteresis in milled $La_{0.67}Sr_{0.33}MnO_3$ powder compacts // J. Magn. Magn. Mater. – 2006. – Vol. 299. – P. 94-104.
11. Kolesnichenko Yu.A., Dalakova N.V., Beliayev E.Yu, Bludov O.M., Horielyi V.A., Osmolowskaya O.M., Osmolowsky M.G. Features of low-temperature tunneling magnetoresistance of pressed nanopowders of chromium dioxide CrO_2 // Low Temperature Physics. – 2017. – Vol. 43. – P.772-781.

East Eur. J. Phys. Vol.4 No.3 (2017) 85-91 DOI:10.26565/2312-4334-2017-3-12

PACS: 29.20.db, 29.27.Bd, 29.27.Fh

REDESIGN OF NESTOR STORAGE RING LATTICE

P.I. Gladkikh, A.A. Kalamaiko, I.M. Karnaukhov
National Scientific Center Kharkov Institute of Physics and Technology
1, Akademicheskaya St., Kharkiv, 61108, Ukraine
E-mail: kalamaiko@kipt.kharkiv.ua
Received August 5, 2017

NESTOR is the hard X-ray source that is under commissioning at NSC KIPT. NESTOR based on the Compton scattering of laser photons on relativistic electrons. The structure of the facility can be represented as the following components: a linear accelerator, a transport channel, a storage ring, and a laser-optical system. Electrons are stored in the storage ring for energy of 40-225 MeV, laser photons are accumulated in the optical resonator. The frequencies of laser and electron bunches are synchronized, the interaction point located in the optical resonator. The measurements showed that parameters of the manufactured bending magnets different from the design ones. The bending magnets have different field index, besides the vertical focusing forces are significantly lower than designed ones. The beam dynamics simulation showed that due to decreasing of the vertical focusing the vertical betatron frequency becomes close to the frequency of the integer resonance Q = 2, as a result the vertical motion in the ring is unstable [1]. The second reason for optimization is the need to increase the length of the drift space for optical resonator. The results of optimization are presented in this paper.
KEYWORDS: compton scattering**,** storage ring, lattice redesign, beam dynamics simulation, dynamics aperture

МОДЕРНИЗАЦИЯ СТРУКТУРЫ ФОКУСИРОВКИ НАКОПИТЕЛЬНОГО КОЛЬЦА НЕСТОР
П.И. Гладких, А.А. Каламайко, И.М. Карнаухов
Национальный научный центр «Харьковский физико-технический институт»
61108, Украина, г. Харьков, ул. Академическая, 1.
В ННЦ ХФТИ сооружается источник жесткого излучения “НЕСТОР”, основанный на комптоновском рассеянии лазерных фотонов на релятивистских электронах. Структурно установка может быть представлена в виде следующих компонентов: линейный ускоритель, канал транспортировки, накопительное кольцо, лазерно-оптическая система. Электроны накапливаются в накопительном кольце на энергию 40-225 МэВ, лазерные фотоны накапливаются в оптическом резонаторе. Частоты следования лазерных и электронных сгустков синхронизированы, точка взаимодействия находится в оптическом резонаторе. Измерения показали, что параметры изготовленных поворотных магнитов отличаются от проектных. Поворотные магниты не только имеют разные показатели спада магнитного поля, но и силы вертикальной фокусировки существенно ниже проектных. Расчеты показали, что из-за уменьшения вертикальной фокусировки частота вертикальных бетатронных колебаний становится близкой к частоте целого резонанса Q = 2, в результате чего вертикальное движение в кольце становится неустойчивым [1]. Вторая причина модернизации заключается в необходимости увеличить длину одного из дрейфовых промежутков для установки оптического резонатора. Результаты модернизации представлены в данной работе.
КЛЮЧЕВЫЕ СЛОВА: комптоновское рассеяние, накопительное кольцо, модернизация структуры фокусировки, моделирование динамики пучка, динамическая апертура

МОДЕРНІЗАЦІЯ СТРУКТУРИ ФОКУСУВАННЯ НАКОПИЧУВАЛЬНОГО КІЛЬЦЯ НЕСТОР
П.І. Гладких, А.А. Каламайко, І.М. Карнаухов
Національний науковий центр «Харківський фізико-технічний інститут»
61108, Україна, м.Харків, вул Академічна, 1.
В ННЦ ХФТІ споруджується джерело жорсткого випромінювання "НЕСТОР", засноване на комптонівському розсіюванні лазерних фотонів на релятивістських електронах. Структурно установка може бутипредставлена у вигляді наступних компонентів: лінійний прискорювач, канал транспортування, накопичувальне кільце, лазерно-оптична система. Електрони накопичуються в накопичувальному кільці на енергію 40-225 МеВ, лазерні фотони накопичуються в оптичному резонаторі. Частоти проходження лазернихі електронних згустків синхронізовані, точка взаємодії знаходиться в оптичному резонаторі. Вимірювання показали, що параметри виготовлених поворотних магнітів відрізняються від проектних. Поворотні магніти не тільки мають різні показники спаду магнітного поля, а й сили вертикального фокусування істотно нижче проектних. Розрахунки показали, що через зменшення вертикальної фокусування частота вертикальних бетатронних коливань стає близькою до частоти цілого резонансу Q = 2, в результаті чого вертикальний рух в кільці стає нестійким [1]. Друга причина модернізації полягає в необхідності збільшити довжину одного з дрейфовий проміжків для установки оптичного резонатора. Результати модернізації представлені в даній роботі.
КЛЮЧОВІ СЛОВА: комптонівське розсіювання, накопичувальне кільце, модернізація структури фокусування, моделювання динаміки пучка, динамічна апертура

Идея генерации высокоэнергетичных фотонов на основе обратного комптоновского рассеяния была предложена в 1951 - 52 Х. Мотцем [2] и К. Ландекером [3]. Затем, метод обратного комптоновского рассеяния был развит в 1963 году Ф.Р. Арутюняном и В.А. Туманяном [4], а также независимо Мильбурном [5]. Но возможности ускорительной и лазерной техники в то время не позволяли рассматривать предложенный метод для практических целей из-за очень малого поперечного сечения процесса ($\sigma_c \sim 6{,}6\times10^{-29}$ м^2).

В настоящее время достижения в области лазерной и ускорительной техники открывают новые возможности в генерации жесткого излучения высокой энергии на основе обратного комптоновского рассеяния лазерных фотонов на релятивистских электронах [6].

При однократном столкновении электронного и лазерного сгустков число рассеянных фотонов определяется светимостью L и полным сечением комптоновского рассеяния σ [7]

$$n_\gamma = L\sigma. \tag{1}$$

В лабораторной системе отсчета выражение для светимости, в случае гауссовских распределений плотностей в электронных и лазерных сгустках, имеет следующий вид [8]

$$L = \frac{n_e n_l}{2\pi\sqrt{\left(\sigma_{ze}^2+\sigma_{zl}^2\right)}\sqrt{\left(\sigma_{xe}^2+\sigma_{xl}^2\right)\cos^2\left(\varphi/2\right)+\left(\sigma_{se}^2+\sigma_{sl}^2\right)\sin^2\left(\varphi/2\right)}}, \tag{2}$$

где σ_{xe}, σ_{xl}, σ_{ze}, σ_{zl} – среднеквадратичные поперечные размеры в точке столкновения электронного и лазерного пучков, σ_{se}, σ_{sl} – среднеквадратичные продольные размеры электронного и лазерного сгустков, n_e, n_l – число электронов и фотонов в сталкивающихся пучках, φ – угол столкновения электронного и лазерного пучков.

Энергетический спектр рассеянных фотонов характеризуется максимальной энергией ε_{max}, приобретаемой фотоном при лобовом столкновении [8]

$$\varepsilon_{max} = 4\gamma^2\varepsilon_l, \tag{3}$$

где γ – Лоренц – фактор, ε_l – энергия лазерного фотона.

Принимая во внимание все вышеизложенное, для получения максимальной интенсивности необходимо создать накопительное кольцо с минимально возможными поперечными и продольными размерами электронного и лазерного сгустков в точке столкновения. Кроме того, технология должна обеспечивать минимальный угол столкновения.

Основная проблема в разработке подобной структуры заключается в большой величине энергетического разброса в электронном пучке. При комптоновском рассеянии электрон теряет значительную часть своей энергии и, вследствие стохастичности этого процесса, это приводит к росту энергетического разброса [9]. В этих условиях, для получения устойчивого движения важно обеспечить большой энергетический аксептанс накопителя. Для получения большого аксептанса в накопительном кольце необходимо добиться малого значение коэффициента упаковки орбит, т.к. его величина определяется выражением [8]:

$$\sigma_{rf} \propto \sqrt{\frac{V_{RF}}{\alpha_1}}, \tag{4}$$

где σ_{rf} - энергетический аксептанс, V_{rf} - ускоряющее ВЧ-напряжение, α_1 – линейный коэффициент упаковки орбит.

Для описания поперечного смещения пучка при больших значениях отклонения импульса необходимо также учитывать квадратичную дисперсию [10]

$$\Delta x = \eta_1 \frac{\Delta p}{p} + \eta_2 \left(\frac{\Delta p}{p}\right)^2, \tag{5}$$

где η_1 и η_2 - линейная и квадратичная дисперсия, $\frac{\Delta p}{p}$ - относительное отклонение импульса.

В случае больших значений отклонения импульса и квадратичной дисперсии, квадратичные члены начинают заметно влиять на удлинение орбиты, другими словами, коэффициент упаковки орбит становится зависимым от отклонения импульса [10].

$$\alpha = \alpha_1 + \alpha_2 \frac{\Delta p}{p}. \tag{6}$$

Когда линейный коэффициент упаковки орбит становится меньше некоторого критического значения, энергетический аксептанс накопительного кольца начинает уменьшаться [11], поэтому линейный коэффициент упаковки орбит является некоторой компромиссной величиной.

Цель данной работы заключается в проведении модернизации системы фокусировки накопительного кольца НЕСТОР и оценки интенсивности жесткого излучения с учетом реальных параметров накопительного кольца и планируемых параметров оптической системы.

ПРОЕКТНАЯ СХЕМА НАКОПИТЕЛЬНОГО КОЛЬЦА

Основные требования к фокусирующей структуре накопителя следующие:

1. Как следует из (2), для получения высокой интенсивности комптоновского рассеяния необходимо обеспечить минимальные продольные и поперечные размеры электронного и лазерного сгустков в точке взаимодействия. Поперечные размеры электронного сгустка в точке взаимодействия определяются следующим

выражением $\sigma_{xe,ze} = \sqrt{\varepsilon_{x,z}\beta_{x,z}}$, где $\varepsilon_{x,z}$ – эмитанс электронного пучка в горизонтальной (x) и вертикальной (z) плоскости, $\beta_{x,z}$ – амплитудные функции в точке взаимодействия в соответствующей плоскости. Поэтому необходимо обеспечить минимальное значение амплитудных функций в точке взаимодействия.

Продольный размер электронного сгустка σ_{se} пропорционален коэффициенту упаковки орбит $\sigma_{se} \propto \sqrt{\alpha_1 / V_{RF}}$, здесь V_{rf} - ускоряющее ВЧ-напряжение, α_1 – линейный коэффициент упаковки орбит. Таким образом, структура фокусировки должна обеспечить малое значение коэффициента упаковки орбит.

2. Количество секступольных линз должно быть достаточным для подавления хроматических эффектов и коррекции динамической апертуры.

3. Необходимо учитывать эффекты внутрипучкового рассеяния, так как на малых энергиях эти эффекты приводят к быстрой деградации электронного пучка - размеры сгустка в поперечной и продольной плоскости возрастают, что приводит к падению интенсивности рассеяния.

С учетом всего вышеизложенного была разработана схема накопительного кольца с контролируемым коэффициентом упаковки орбит (рис.1).

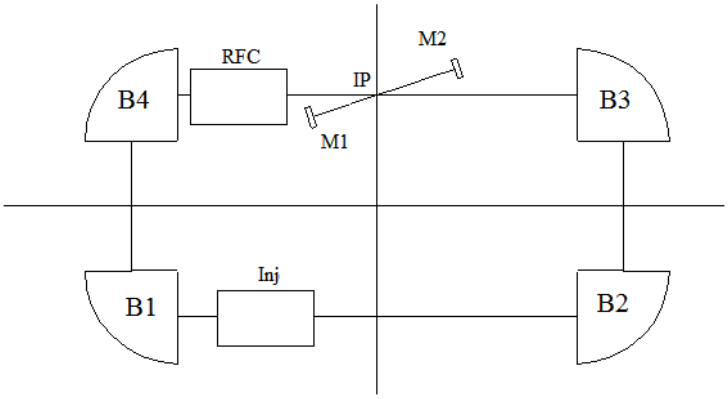

Рис. 1: Схема накопительного кольца НЕСТОР. IP – точка взаимодействия, B1-B4 – поворотные магниты, RFC – резонатор ВЧ–подпитки, Inj – ударный магнит системы инжекции, M1-M2 – зеркала оптического резонатора.

Поворотная арка это часть структуры накопителя, ограниченная поворотными магнитами, которая осуществляет поворот пучка. Поворотные арки накопительного кольца НЕСТОР представляют собой систему, состоящую из двух поворотных магнитов с двумя квадрупольными линзами, расположенными между ними. Уменьшить коэффициент упаковки орбит можно, если сделать дисперсионную функцию отрицательной на одном из поворотных магнитов поворотной арки с помощью квадрупольных линз расположенных в ней. В этом случае одна длинная прямолинейная секция (B3-B4) будет с нулевой дисперсией, дисперсионная функция на противоположной прямолинейной секции (B1-B2) будет отлична от нуля. ВЧ-резонатор (RFC) и лазерно-оптическая система (M1-M2) размещаются в секции с нулевой дисперсией, система инжекции размещается на противоположной прямолинейной секции (Inj).

В настоящее время Nd:YAG - лазеры с энергией фотонов 1,16 эВ считаются наиболее перспективными для использования в лазерно-электронных накопительных кольцах [12]. Частота следования импульсов в таких лазерах достигает сотен МГц, а средняя мощность около 10 Вт.

Примем для оценок интенсивности комптоновского рассеяния поперечные размеры лазерного пятна в точке взаимодействия равными 50 мкм, продольный размер 1,5 мм, частота следования лазерного импульса 350 МГц, средняя мощность $P \approx 10$ Вт, такой лазер излучает примерно 28 нДж ($1{,}5\times10^{11}$ фотонов) в одном импульсе. Будем считать, что на орбите накопителя находится один электронный сгусток с зарядом 2 нКл, а размеры электронного и лазерного пучков совпадают. В этом случае за одну секунду будет сгенерировано примерно 3×10^{7} фотонов.

Для увеличения интенсивности необходимо увеличивать число электронов на орбите (увеличивать число электронных сгустков) и увеличивать энергию лазерной вспышки, для чего используется оптический резонатор, в котором будет накапливаться излучение лазера. Все это позволяет достичь интенсивности жесткого излучения порядка $10^{13} - 10^{14}$ фот/сек. При энергии электронного пучка в диапазоне от 40 до 225 МэВ, можно генерировать жесткое излучение с энергией от 30 до 900 КэВ.

ПРОЕКТНАЯ СТРУКТУРА ФОКУСИРОВКИ НЕСТОР

Проектная структура фокусировки накопительного кольца НЕСТОР [13] представлена на рис.2. Периметр ускорителя составляет 15,418 м. Поворотные магниты (B1-B4) имеют радиус поворота 0,5 м, угол поворота

90°, магнитное поле на максимальной рабочей энергии электронного пучка (225 МэВ) составляет 1,5 Тл. Для обеспечения фокусировки в вертикальной плоскости поворотные магниты имеют квадрупольную составляющую магнитного поля.

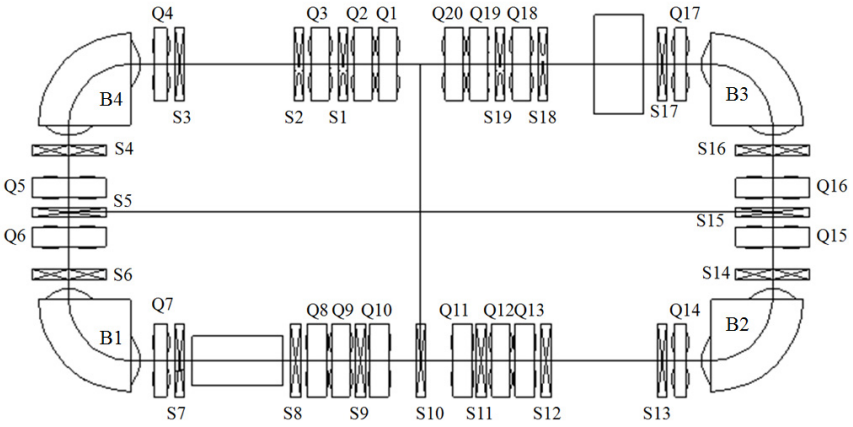

Рис.2: Структура фокусировки накопительного кольца НЕСТОР
Q1 - Q20 – квадрупольные линзы, S1 – S19 – секступольные линзы

Промежуток инжекции (B1-B2) имеет ненулевую дисперсию $\eta_1 \neq 0$, в то время как промежуток взаимодействия (B3-B4), содержащий оптический резонатор ахроматичен $\eta_1 = 0$, а в точке взаимодействия дисперсия второго порядка минимальна. С помощью квадрупольных линз (Q5, Q6, Q15, Q16) обеспечивается отрицательное значение дисперсионной функции η_1 на части траектории в поворотных арках (B4-B1, B2-B3), что позволяет получить малый коэффициент упаковки орбит $\alpha \approx 0{,}01$. Такое малое значение коэффициента упаковки орбит обеспечивает энергетический аксептанс накопителя на уровне 4%.

Для фокусировки электронного пучка в точке взаимодействия используются квадруплеты квадрупольных линз (Q1-Q4, Q17-Q20). Такая схема дает возможность получить минимальные значения горизонтальной и вертикальной амплитудных функций в точке взаимодействия. Триплеты (Q8-Q10,Q11-Q13) расположенные на промежутке инжекции, формируют необходимые амплитудные функции и частоты бетатронных колебаний. Функции фокусировки накопительного кольца «НЕСТОР» [14] показаны на рис.3а,б.

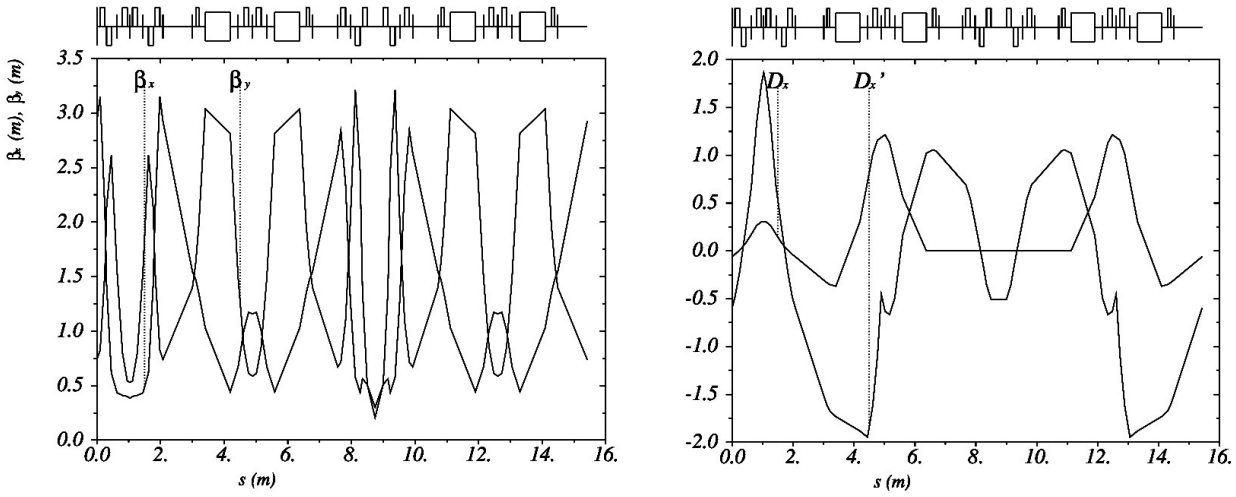

а) б)

Рис.3. Функции фокусировки накопительного кольца «НЕСТОР»
а) амплитудные функции б) дисперсионные функции

Для подавления хроматических эффектов и коррекции динамической апертуры в накопителе используется 19 секступольных линз (S1-S19). Структура фокусировки накопительного кольца спроектирована, так что бы обеспечить необходимые набеги фаз бетатронных колебаний между секступолями и минимизировать дисперсию второго порядка (η_2)в точке взаимодействия.

Проектная структура фокусировки имеет горизонтальную частоту бетатронных колебаний $Q_x = 3{,}1$, вертикальную частоту $Q_z = 2{,}15$ и коэффициент упаковки орбит $\alpha = 0{,}0096$.

МОДЕРНИЗАЦИЯ СТРУКТУРЫ ФОКУСИРОВКИ

После производства поворотных магнитов для накопителя, была проведена серия измерений их параметров с помощью датчика Холла. Измерения показали, что параметры изготовленных магнитов отличались от проектных, поворотные магниты не только имеют разные показатели спада магнитного поля, но и силы вертикальной фокусировки существенно ниже проектных.

Моделирование показало, что из-за уменьшения вертикальной фокусировки частота вертикальных бетатронных колебаний становится близкой к частоте целого резонанса Q = 2, в результате чего вертикальное движение в кольце становится неустойчивым. В таблице 1 приведены силы вертикальной фокусировки (K1) для изготовленных поворотных магнитов. Как видно из таблицы, ослабление вертикальной фокусировки ΔK1 составляет приблизительно 5-10%. В конструкции поворотных магнитов не предусмотрены корректирующие обмотки для K1.

Таблица 1

Сила вертикальной фокусировки в изготовленных поворотных магнитах (проектное значение 2.4).

Название поворотного магнита	B1	B2	B3	B4
K1, m^{-2}	2,20	2,30	2,24	2,28

Из-за того, что максимально достижимое магнитное поле в поворотных магнитах меньше проектного, максимальная рабочая энергия накопителя уменьшилась с 225 МэВ до 200 МэВ. Максимальная энергия жесткого излучения уменьшилась с 900 КэВ до 720 КэВ [15].

Вторая причина модернизации заключается в необходимости увеличить длину одного из дрейфовых промежутков от 0,45 м до 0,75 м, для установки оптического резонатора.

Для установки дополнительного монитора положения пучка на участке взаимодействия, было решено убрать две симметрично расположенные секступольные линзы (S1, S19) вместо одной из которых и был установлен монитор.

Для моделирования динамики электронного пучка использовались программные пакеты MAD-X [16] и DECA [17]. В результате модернизации промежуток взаимодействия был увеличен до 0,75 м.

Размещение магнитных элементов в накопительном кольце, за исключением триплетов на промежутке взаимодействия (Q1-Q3, Q18-Q20) осталось прежним. Силы квадрупольных линз изменены в пределах 10% от проектных.

Модернизация проходила в два этапа. На первом этапе модернизации расчет параметров структуры проводился в линейном приближении с использованием программы MAD-X. Полученная структура фокусировки полностью удовлетворяла приведенным выше требованиям. На рис.4а,б приведены амплитудные и дисперсионные функции модифицированной структуры соответственно. Значения частот бетатронных колебаний после модернизации $Q_x = 3{,}13$, $Q_z = 1{,}79$ и коэффициент упаковки орбит $\alpha \approx 0{,}01$.

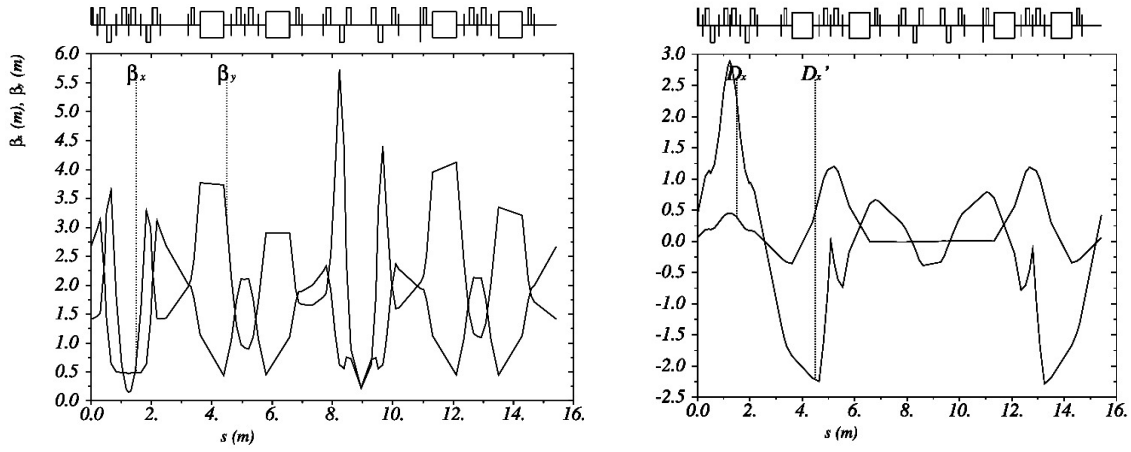

а) б)

Рис.4. Функции фокусировки накопительного кольца «НЕСТОР» после модернизации
а) амплитудные функции б) дисперсионные функции.

На втором этапе модернизации были рассчитаны силы секступольных линз (S1-S17) для подавления естественной хроматичности в накопительном кольце и проведена коррекция динамической апертуры.

После модернизации значение динамической апертуры в точке инжекции составило 38 мм в горизонтальной и 32 мм в вертикальной плоскости, что намного превышает динамическую апертуру проектного накопителя (рис. 5). Увеличенный размер динамической апертуры позволяет более эффективно инжектировать пучок в накопительное кольцо. Основные параметры накопительного кольца НЕСТОР до и после модернизации представлены в таблице 2.

Зависимость длины электронного сгустка от его энергии приведены на рис.6. Зависимость поперечных размеров электронного сгустка в точке взаимодействия от его энергии приведены на рис.7. С ростом энергии электронного пучка уменьшается влияний эффектов внутрипучкового рассеяния на его поперечные размеры.

Таблица 2

Основные параметры накопительного кольца до и после модернизации

Параметры	До модернизации	После модернизации
Q_x	3,15	3,13
Q_y	2,1	1,79
α	0,096	0,098
β_x в точке взаимодействия	0,12	0,21
β_y в точке взаимодействия	0,14	0,23

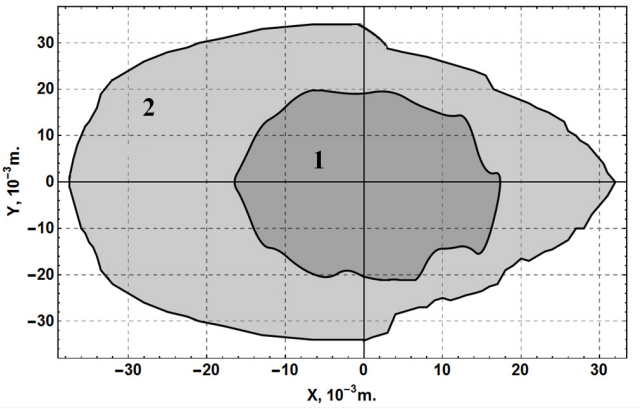

Рис.5: Динамическая апертура в точке инжекции до (1) и после (2) модернизации.

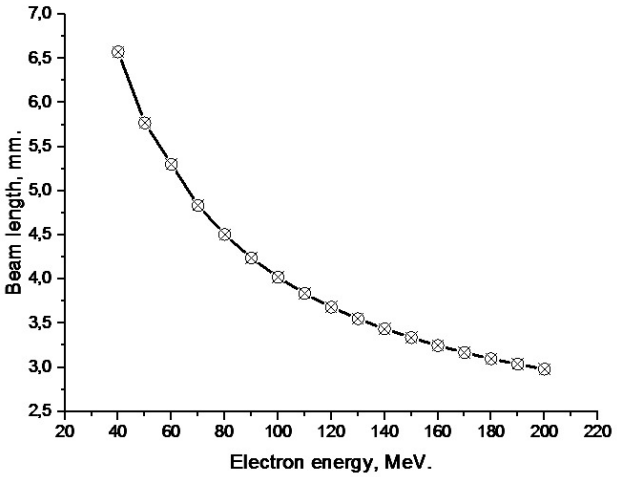

Рис.6: Зависимость продольного размера электронного сгустка от энергии

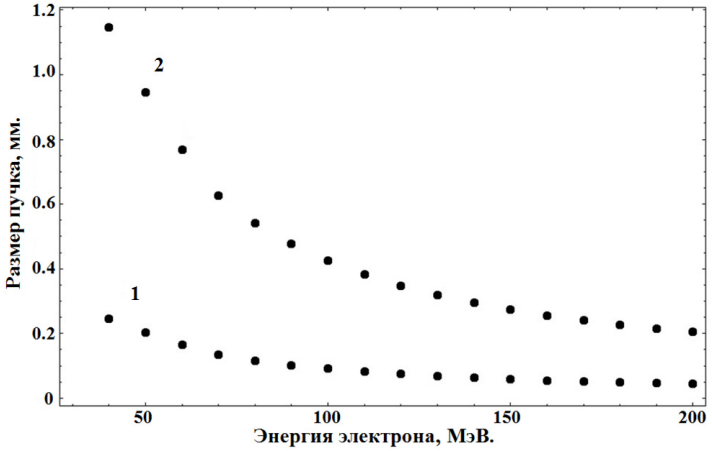

Рис.7: Зависимость поперечных размеров электронного сгустка от энергии
1 - вертикальная плоскость, 2 - горизонтальная плоскость.

Сделаем оценку интенсивности комптоновского рассеяния в накопительном кольце с учетом реальных параметров сталкивающихся пучков:

- Длиной орбиты 15,418 м (частота обращения 19,5 МГц);
- Угол столкновения φ = 12°;
- Энергия лазерного фотона ε_l = 1,16 эВ;
- Частота следования лазерного импульса 350 МГц;
- Средняя мощность лазера P ≈ 10 Вт;
- Количество фотонов в одном импульсе $1{,}5\times10^{11}$;
- На орбите накопителя находится 36 электронных сгустков (взаимодействует 18);
- Заряд в одном электронном сгустке 0,5 нКл;

• Электронный сгусток в точке встречи имеет размеры, приведенные на рис.8 и рис.9;

• Поперечные размеры лазерного сгустка в вертикальной и горизонтальной плоскости равны $\sigma_{xl} = \sigma_{zl} =$ 50 мкм;

• Продольный размер лазерного сгустка $\sigma_{sl} = 3$ мм;

• Коэффициент накопления оптического резонатора 2000.

На рис.8 приведены результаты моделирования зависимости интенсивности комптоновского рассеяния от энергии электронного пучка.

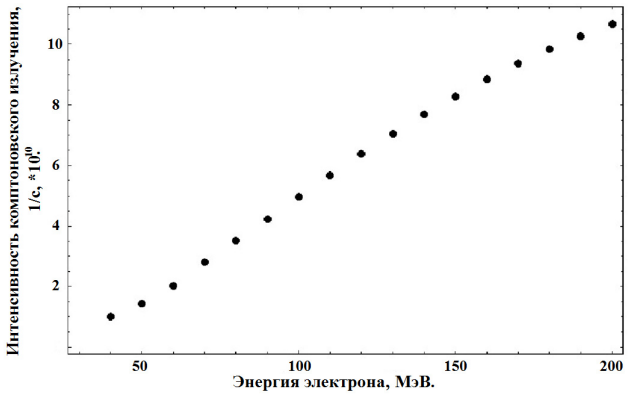

Рис.8: Зависимость интенсивности комптоновского рассеяния от энергии электронного пучка

ВЫВОДЫ

В результате модернизации структуры фокусировки накопителя НЕСТОР удалось увеличить длину дрейфового промежутка для установки оптического резонатора и решить проблемы, возникшие из-за ошибок изготовления поворотных магнитов. Все основные параметры модернизированной структуры накопительного кольца соответствуют проектным. Удалось значительно увеличить динамическую апертуру, что позволит более эффективно инжектировать электронный пучок в накопительное кольцо.

Оценки показывают, что разработанный источник позволит генерировать жесткое излучение с энергией от 30 КэВ до 720 КэВ и интенсивностью до 10^{11} фотонов в секунду.

СПИСОК ЛИТЕРАТУРЫ

1. Mytsykov A., Kalamayko A, Karnaukhov I. et al. // Modificated lattice of the Compton X-ray source NESTOR // Proceedings of IPAC 2011. – TUPC-040. – P. 1087–1089.
2. Motz H. Applications of the radiation from fast electron beams // Journal of Apply Physics. – 1951. –Vol. 22. – No. 527. – P. 527-531.
3. Landecker K. Possibility of frequency multiplication and wave amplification by means of some relativistic effects // Physical Review. – 1952. – Vol. 86. – No.6. — P. 852-855.
4. Artumanyan F., Tumanyan V. Compton effect on relativistic electrons and the possibility of generation of hard radiation // JETP. – 1963. – Vol. 44. – P. 2101.
5. Milburn R. // Thomson Scattering of Optical Radiation from an Electron Beam // Physical Review Letters. – 1963. – Vol. 10. – P. 75.
6. Casano L. et al. Laser scanning components and techniques: design considerations // Laser and Unconventional Optics Journal. – 1975. – Vol. 55. – P. 3.
7. Telnov V. Principles of photon colliders // Nuclear Instruments and Methods in Physics Research A. – 1995. – Vol. 355. – P. 3-18.
8. Luo W., Zhuo H. et al. The nonlinear effect in relativistic Compton scattering for an intense circularly polarized laser // Physica Scripta. – 2014. – Vol. 89(7). – P. 5.
9. Huang Z. Radiative cooling of relativistic electron beams // SLAC-R. – 1998. – Vol. 527. – P. 141.
10. Gladkikh P., Karnaukhov I. et. al. Physical Grounding H-100M // Internal report of NSC KIPT. – 1998. – P. 7-30.
11. Liu Lin, Cylon E.T. Goncalves da Silva Second order single particle dynamics in quasi – isochronous storage rings and its application to the LNLS – UVX ring // NIM A. – 1993. – Vol.329. – P. 9–15.
12. Pellegrini C., Robin D. Quasi – isochronous storage ring // NIM A. – 1991. – Vol. 301. – P. 27-36.
13. Zelinsky A., Shcherbakov A. et al. The Kharkov X-ray generator facility NESTOR // Proceedings of IPAC. – 2013. – P. 2253–2255.
14. Zelinsky A., Gladkikh P. et al. Investigation of injection through bending magnet fringe fields in X-rays source based on storage ring NESTOR // Proceedings of European Particle Accelerator Conference. –2004. – P. 1434.
15. Gladkikh P., Karnaukhov I. et al. The start of X-ray generator NESTOR commissioning // Problems of atomic science and technology. –2013. – Vol. 6(88). – P. 20-23.
16. Iselin F. C. The MAD Program. Physical Methods Manual // CERN/SL. –1992.
17. Gladkikh P., Strelkov M., Zelinsky A. The Application Package DECA for Calculating Cyclic Accelerators // Proceedings of PAC-93. – 1993. – P 194–196.

EAST EUROPEAN JOURNAL OF PHYSICS
East Eur. J. Phys. Vol.4 No.3 (2017) 92-96 DOI:10.26565/2312-4334-2017-3-13

PACS: 05.70. Ln; 61.72.jd. 61.72 Qq, 62.20.fg.81.30.30.Kf

ON THE PROBLEM OF MARTENSITE TETRAGONALITY NATURE

I.N. Laptev[1], O.O. Parkhomenko[1,2]
[1]*National Scientific Center "Kharkiv Institute of Physics and Technology"*
1, Akademicheskaia St., Kharkov, 61108, Ukraine
[2]*V.N. Karazin Kharkov National University*
4 Svobody Sq., Kharkov, 61022, Ukraine
e-mail: parkhomenko@kipt.kharkov.ua
Received August 11, 2017

Despite the fact that scientists have been studying the nature of the mechanism of martensite formation for almost a hundred years, these studies remain, still, relevant. In this paper, the authors present two new results related to the classical question of the role of carbon in martensite formation. If, while dissolving in the lattice, the carbon is located in the center of the octahedral emptiness, then under the influence of stresses caused by quenching or deformation, in martensite it is displaced into one of the pyramids of the constituent octahedra. The fact of the independence of the specific atomic volume of phase mismatch during martensitic transformation of iron from the carbon content was found. This fact indicates that the tetragonality of carbon steels is a function not so much of carbon as vacancies. In the pure iron the "vacancy" tetragonality can vary from 1.03 to 1.06.
KEY WORDS: martensite transformation, stress state, tetragonality , vacancies, iron, carbon

К ВОПРОСУ О ПРИРОДЕ ТЕТРАГОНАЛЬНОСТИ МАРТЕНСИТА

И.Н. Лаптев[1], А.А. Пархоменко[1,2]
[1]*Национальний научный центр «Харьковский физико-технический институт»*
ул. Академическая 1, г. Харьков 61108, Украина
[2]*Харьковский национальный университет имени В.Н. Каразина*
пл. Свободы 4, г. Харьков, 61022, Украина

Несмотря на то, что описанием природы механизма мартенситообразования ученые занимаются уже почти сто лет, эти исследования остаются, по-прежнему, актуальными. В данной работе авторы представляют два новых результата, связанные с классическим вопросом о роли углерода в МП. Если, растворяясь в решетке, углерод располагается в центре октаэдрической пустоты, то под действием напряжений, вызванных закалкой или деформацией, в мартенсите он оказывается смещенным в одну из пирамид составляющих октаэдр. Впервые обнаружен факт независимости удельного атомного объема фазового несоответствия при мартенситном превращении железа от содержания углерода. Этот факт свидетельствует о том, что тетрагональность углеродистых сталей есть функция не столько углерода сколько вакансий. В чистом железе «вакансионная» тетрагональность может меняться в пределах от 1,06 до 1,03.
КЛЮЧЕВЫЕ СЛОВА: мартенситные превращения, напряженное состояние, тетрагональность, вакансии, железо, углерод

ЩОДО ПИТАННЯ ПРИРОДИ ТЕТРАГОНАЛЬНОСТІ МАРТЕНСИТУ

І.М. Лаптєв[1], О.О. Пархоменко[1,2]
[1]*Національний науковий центр «Харківський фізико-технічний інститут»*
вул. Академична 1, м. Харків 61108, Україна
[2]*Харківський національний університет імені В.Н. Каразіна*
пл. Свободи 4, м. Харків, 61022, Україна

Не дивлячись на те, що вивченням природи мартенситоутворення вчені займаються вже майже сто років, ці дослідження залишаються як і раніше актуальними. В цій роботі автори представляють два нових результати , які пов'язані з класичним питанням щодо ролі вуглецю у у мартенситних перетвореннях. Якщо у твердому розчині кристалічної гратки вуглець знаходиться у центрі октоедрічної пустоти, то під впливом напружень, що викликані гартуванням або деформацією, у мартенситі він зміщується у бік одної з пірамід, що створюють октаедр. У роботі вперше показана незалежність питомого атомного об' єму фазової невідповідності заліза при мартенситних перетвореннях від вмісту вуглецю. Цей факт свідчить, що тетрагональність вуглецевих сталей є функцією не тільки вуглецю , але передусім-вакансій. У чистому залізі « вакансій на » тетрагональність може змінюватись у межах від 1 ,03 до 1,06.
КЛЮЧОВІ СЛОВА: мартенситні перетворення, напружений стан, тетрагональність, вакансії, залізо, вуглець

Несмотря на то, что изучением природы мартенсита ученые занимаются уже почти сто лет, вопрос о механизмах его образования и роли тетрагональности кристаллической решетки остается до конца не выясненным. В контексте данной работы, под тетрагональностью авторы понимают собственную упругую деформацию ГЦК – решетки, при ее превращении в ОЦК-структуру. Такие деформации могут создаваться сдвигом под действием механических или термических напряжений, легирования определенным элементным составом или примесями.

Эти представления о природе образования мартенсита находятся в согласии с давно забытой «релаксационной моделью» С.С. Штейнберга [1]. Подобные взгляды на природу мартенситообразования высказывали в свое время А.П. Гуляев [2], а из наших современников следует назвать С.П. Ошкадерова [3].

Уже давно открыты мартенситы в различных металах и сплавах, которые можно разделить на мартенситы

«внедрения» и мартенситы «замещения» [4]. Считается, что в углеродистых сталях за образование мартенсита отвечает углерод [5], хотя вопрос о его расположении в решетке железа до сих пор остается открытым.

Целью работы был анализ накопленных за десятилетия экспериментальных данных по изменению решеток феррита, аустенита и мартенсита в зависимости от содержания углерода, при формировании им тетрагональных искажений в железе.

АНАЛИЗ ЭКСПЕРИМЕНТАЛЬНЫХ ДАННЫХ

Наши представления о мартенсите связаны с вопросом упорядочения углерода. Мы привыкли считать, что при закалке аустенита углерод изменяет свое положение и в мартенсите он оказывается расположенным в центре ребра ОЦТ ячейки. Но ведь это положение было и есть центр октаэдра. И в аустените, и феррите углерод, растворяясь, тоже находится в центре октаэдра. Если это так, то не понятно, о каком упорядочении при образовании мартенсита идет речь. И в аустените и в феррите центр любого октаэдра одновременно принадлежит шести объемно центрированным ячейкам ортогонально ориентированным попарно. Более того, все три структуры (аустенит, феррит и мартенсит) могут быть составлены из одних октаэдров с различным соотношением диагоналей, которое изменяется в тех же пропорциях, что и тетрагональность в ОЦК и ГЦК решетках (от 1 до 1,4142). Из этого следует, что углероду, если он находится в центре октаэдра, не надо перестраиваться для образования мартенсита.

Анализ экспериментальных данных по изменению параметров решеток феррита, аустенита и мартенсита [2] и объемов элементарных ячеек этих структур, которые представлены в таблице, позволяет сделать очень важный вывод о расположении углерода в решетке железа.

Как следует из таблицы, параметр «с» возрастает прямо пропорционально росту содержания углерода в мартенсите. В тоже время, параметр «а» мартенсита слабо зависит от содержания углерода и уменьшается от 2,861Å в феррите до 2,843Å в мартенсите с 1,6 вес.% С, и с дальнейшим повышением концентрации углерода вообще остается неизменным. Иначе говоря, прямая пропорциональность с изменением содержания углерода для параметра «а», как это принято считать [6-10], не соблюдается.

Таблица

Изменения параметров кристаллических решеток феррита ($a_{м\,}$ при $C_с = 0$), мартенсита ($a_м$ и $c_м$), аустенита (a_γ), их объемов (V_α ,$V_м$,V_γ), тетрагональности (c/a), объема фазового несоответствия (ΔV) и его относительное изменение ($\Delta V/ V_м$) в зависимости от содержания углерода ($C_с$) в железе (по данным монографии [2]).

$C_с$, вес.%	a_γ, Å	$0{,}5V_\gamma$, Å^3	$a_м$, Å	$c_м$, Å	$V_м$, Å^3	c/a	$\Delta V= V_м - 0{,}5V_\gamma$, Å^3	$\Delta V/ V_м$, %
0,0	3,546	22,31	2,86	2,86	23,40	1	1,09	4,65
0,2	3,555	22,483	2,857	2.882	23,55	1,009	1,07	4,54
0,4	3,564	22,656	2,853	2,909	23,68	1,018	1,024	4,32
0,6	3,573	22,829	2,851	2,931	23,83	1,027	1,01	4,24
0,8	3,582	23,002	2,849	2,957	24,01	1,036	1,008	4,20
1,0	3,591	23,175	2,847	2,982	24,19	1,045	1,015	4,20
1,2	3,600	23,328	2,845	3,002	24,30	1, 054	0,98	4,16
1,4	3,609	23, 521	2,844	3,03	24,52	1,063	0,999	4,07
1,6	3,618	23,694	2,843	3,053	24,70	1,072	1,006	4,07
1,8	3,627	23,867	2,843	3,075	24,88	1,081	1,013	4,07
Среднее значение							1,0215	

ПРЕДЛАГАЕМАЯ МОДЕЛЬ

Если принять, что углерод в ОЦТ ячейке мартенсита располагается не в центре октаэдра (в этом положении он бы изменил параметр «а» только однажды), а в пирамиде (рис.1,2). Только в таком случае с ростом параметра «с» влияние углерода на параметр «а» будет уменьшаться, а сам параметр «а» будет сокращаться. Собственно это и есть деформация Бейна.

В таком случае, процесс упорядочения при образовании мартенсита заключается в том, что распределенный в аустените по октаэдрам углерод смещается и занимает одинаково ориентированные пирамиды в октаэдрических ячейках.

По-видимому, именно эти положения (1/3 высоты пирамиды) определяются как «тяжи» на электронограммах в сталях и сплавах, которые оказываются в, так называемых, «прекурсорных» или предмартенситных состояниях [11].

Чтобы углерод оказался смещенным в пирамиду на него должны действовать выталкивающие силы, которые могут быть либо постоянны, либо возрастать с ростом содержания углерода в железе. Тогда, в первом случае, реализовалась бы модель «универсальной тетрагональности», обусловленной только внедренным углеродом, которую предлагают авторы [12]. В такой модели, экспериментально измеряемая тетрагональность

мартенсита представляет собой усредненную по объему величину от единственной «универсальной», образованной углеродом, внедренным в ячейку железа. Во втором, тетрагональность – усредненная величина по спектру различных значений, обусловленных различным содержанием и расположением углерода в ячейке железа, а точнее – в пирамиде.

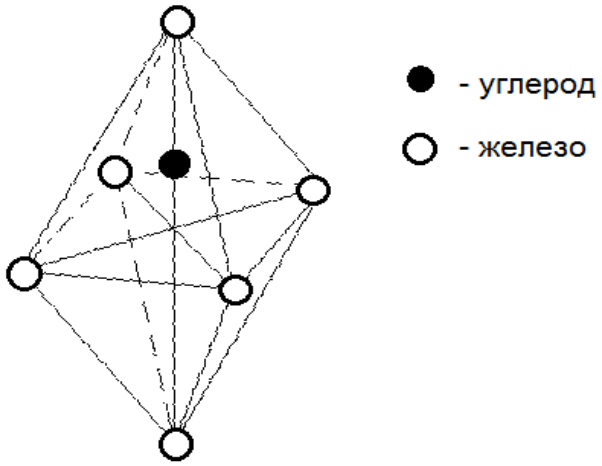

Рис.1. Наиболее вероятное положение углерода в октаэдрической поре мартенсита.

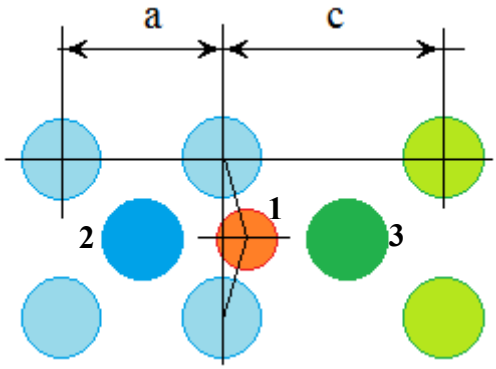

Рис.2. Формирование ОЦТ структуры в ОЦК железе.
Показано смещение атома углерода (поз.1) в октаэдрической поре ячейки железа. Плоскость рисунка соответствует плоскости (100) ОЦК структуры. Позиции 2 и 3 соответствуют центральным атомам ОЦК и ОЦТ ячеек и, следовательно, расположены над базисом. В одной с ними плоскости находится и углерод.

Эти представления и имеющиеся экспериментальные данные позволяют легко рассчитать ту тетрагональность мартенсита, которая может быть обусловлена только внедренным углеродом. Выполняя расчеты, для первого случая, мы вместо силы, выталкивающей углерод из центра октаэдра, использовали диаметр атома железа равный параметру его ОЦК решетки.

При концентрации углерода в железе в 1,6 вес.% параметр «а» в решетке ОЦТ мартенсита – 2,843Å, радиус атома углерода – 0,71Å, так что смещение атома железа составляет – 0,839Å. Сумма 2,843 + 0,8394 = 3,6824Å равна параметру «с», а отношение с/а = 1,2953 определит тетрагональность одной ячейки с одним атомом углерода. Углерод имеет ограниченную растворимость в железе. В аустените при 1148°С его содержание не может быть больше, чем 2,14 вес.%. При закалке даже с максимальным содержанием его в твердом растворе он не заполняет все октаэдрические пустоты и, по нашим оценкам, влияние одного внедренного атома углерода распространяется приблизительно на четыре - пять ближайших ячеек.

Считая, что атом углерода находится на общей для четырех ячеек оси «с» можно рассчитать усредненное значение их тетрагональности, например, для содержания углерода в железе равном 1,6 вес.%: (1,2953×1 + 1×3) / 4 = 1,0738, что находится в хорошем соответствии со значением тетрагональности, определенным экспериментально (см. таблицу - 1,072).

Оценивая параметр «с» мы не учитывали сжимающего влияния окружающей матрицы, что, безусловно, будет его уменьшать. Однако и без учета этой деформации простейшие вычисления показывают, насколько точно, предлагаемая модель, определяет положение атома углерода в решетке мартенсита.

Однако все не так просто. На самом деле не углерод определяет тетрагональность, а тетрагональность, заданная, например, уровнем термических напряжений, возникающих в процессе закалки, определяет положение углерода в ячейке железа.

Реально диаметр атома железа чуть больше 2Å. Такого же размера достигает и кратчайшее межатомное расстояние в центральной плоскости октаэдра. Это значит, что атом углерода (диаметр 1,4 Å) способен свободно разместиться в октаэрическом междоузлии. По-видимому, в аустените (температура, от которой ведется закалка, выше 900°C) он действительно располагается в центре октаэдра. Но в процессе закалки в структуре возникают градиенты термических напряжений, которые с одной стороны, порождают тетрагональные искажения решетки [13], а с другой, заставляют углерод смещаться в направлении действия градиента растяжений, занимая определенные положения в пирамиде.

Из этого следует, что углерод не является причиной образования тетрагональности в железе. С ростом содержания углерода в железе напряжения необходимые для его смещения возрастают, что ведет к подавлению процесса образования мартенсита. Этим объясняется существование остаточного аустенита и рост его массы с ростом содержания углерода (углерод – аустенитобразующий элемент).

Предлагаемая модель (рис.1,2) позволила нам правильно определить положение атома углерода в ячейке железа и утверждать теперь, что никакого универсального значения тетрагональности углерод в железе не создает. Просто в процессе закалки с ростом его содержания в железе возрастают термические напряжения (чем выше концентрация углерода, тем большее сопротивление он оказывает мартенситному превращению, поэтому температура начала образования мартенсита снижается), что приводит к росту тетрагональности системы «железо-углерод-вакансии» и большим смещениям углерода вдоль оси «c». Как следует из таблицы, углерод, в обособившемся кристалле мартенсита, способен поддерживать тетрагональность порядка 1,081 при концентрации его в железе около 1,8 об.%. При большем содержании углерода сталь должна оставаться аустенитной.

Таким образом, полученные результаты в корне меняют наши представления о месте размещения углерода в ОЦТ ячейке железа и о роли его в образовании мартенсита в сталях.

Из таблицы следует еще один удивительный факт: не смотря на то, что с ростом содержания углерода в твердом растворе и, при этом, ростом, как фазового объема аустенита, так и мартенсита, разность этих объемов (объем фазового несоответствия) остается постоянной. Действительно, как видно из таблицы, изменение величины ΔV не превышает долей кубического ангстрема на фоне объема мартенсита составляющего несколько десятков кубических ангстрем. Поскольку экспериментальные данные получены на закаленных сталях, то не вызывает сомнений, что объем фазового несоответствия никак не связан с углеродом, а обусловлен только вакансиями.

Подтверждением правильности вывода могут являться результаты экспериментальной работы [14]. Проведенная закалка чистого железа (содержание углерода 0,0015 вес.%) привела к образованию мартенсита, масса которого росла с ростом скорости закалки и достигала 100%. Без сомнения, при таком ничтожном содержании углерода он не может оказывать влияние на образование тетрагональности (если бы он был ответственным за ее образование) во всем объеме закаливаемого кристалла. Единственный «элемент» способный породить тетрагональность в объеме – вакансии.

Метод Фазовых Диаграмм Мартенситных Превращений (ФДМП) позволяет оценить «вакансионную» тетрагональность, которая может возникать в чистом железе, например, при различных скоростях закалки. В зависимости от температуры начала образования мартенсита M_s тетрагональность обособившегося мартенсита может изменяться в пределах от 1 до 1,05, сначала возрастая с ростом скорости охлаждения (от M_s ниже 900°C до M_s = 545°C), а затем понижаясь [13].

Из этого следует, что тетрагональность мартенсита является функцией не столько углерода (а в сталях, не содержащих углерод, это, без сомнения) сколько вакансий. Именно поэтому объем фазового несоответствия не меняется с изменением концентрации углерода (разумеется, при постоянной скорости охлаждения).

Любой дефект кристаллической решетки, обусловливающий появление поля внутренних деформаций с симметрией отличной от симметрии решетки, является источником внутреннего трения. Поэтому метод внутреннего трения является эффективным методом идентификации тетрагональных искажений. Если следовать [15], то одиночные вакансии не являются источником внутреннего трения, т.к. не нарушают симметрии кристалла. Тетрагональные искажения в решетке кристалла могут создавать только комплексы вакансий, начиная от дивакансий.

Исследования внутреннего трения в образцах сплава Fe-Al [16] подвергнутых γ-облучению (Co^{60}, энергия γ-квантов порядка 1,25 МэВ) обнаружили рядом с углеродным пиком Снука, дополнительный X (или R) пик, появление которого однозначно связано с образованием вакансий в сплаве.

Чтобы понять, каким образом в данном случае вакансии нарушают симметрию поля кристалла и создают тетрагональные искажения в нем, достаточно представить, что вакансия не образуется как точечный дефект, а создает комплекс, например, «углерод-вакансия», «алюминий-вакансия» либо просто – «собственный межузельный атом-вакансия». Поскольку пики разнесены, а пик Снука точно связан с углеродом, то, надо полагать, что пик X обусловлен образованием комплексов «алюминий-вакансия». Геометрически такой комплекс следует представлять как одновременное нахождение вблизи одного узла и атома и вакансии, либо просто смещенный из узла, но не покинувший свою ячейку, атом. При этом вакансия не является точечным дефектом, а представляет собой объемную деформацию растяжения. Под действием внутренних или

приложенных извне напряжений такие комплексы могут быть ориентированны в одном направлении. Объединяясь в конгломераты в волнах концентрационных неоднородностей, они будут создавать тетрагонально искаженные области кристалла (когерентные зоны предвыделений), которые, по сути, являются мартенситом [13].

Образование таких комплексов на собственных атомах, атомах внедрения и замещения обусловлено разной энергией их образования, что, в свою очередь, определяет различие температур начала и конца обособления мартенсита в сталях и сплавах.

И последнее. Рентгенографически мы все же определяем некую усредненную тетрагональность мартенсита. Однако этот спектр тетрагональностей не связан с существованием ее «универсального» значения, образуемого атомом углерода в одной ячейке железа. Такой тетрагональности не существует. Спектр возникает потому, что углерод в сталях распределяется неоднородно. Именно неоднородности его распределения и определяют разброс тетрагональностей.

ВЫВОДЫ

1) Характер изменения параметров ОЦТ решетки мартенсита указывает на то, что углерод, в мартенсите углеродистых сталей, располагается не в центре октаэдра, как это принято считать, а смещается в одну из пирамид, составляющих октаэдр.
2) Углерод не создает тетрагональность в железе. Наоборот, он тормозит ее развитие, что прямо следует из факта снижения температуры начала образования мартенсита, но в обособившемся мартенсите, он является стопором (и тем более мощным, чем выше его содержание в стали), который не позволяет системе после обособления полностью релаксировать внутренние напряжения и избавиться от тетрагональности.
3) Экспериментально измеряемая тетрагональность мартенсита углеродистых сталей - это усредненная по объему кристалла величина, которая не связана с существованием «универсальной» тетрагональности, а обусловлена только неоднородностью распределения углерода в железе.
4) Впервые обнаружен факт независимости объема фазового несоответствия при мартенситном превращении железа.
5) Неизменный объем фазового несоответствия при одинаковой скорости охлаждения, определяемый как разность объемов ОЦТ ячеек мартенсита и аустенита, свидетельствует о том, что тетрагональность углеродистых сталей есть функция не столько углерода, сколько вакансий (а вернее, деформаций и напряжений, которые они порождают в неравновесных системах). В чистом железе в обособившихся кристаллах мартенсита «вакансионная» тетрагональность может меняться в пределах от 1 до 1,05.

СПИСОК ЛИТЕРАТУРЫ

1. Schteinberg S.S. Relaxation phenomenas in martensite // Journal of technical physics – 1935. – Vol. 5. – No. 2. – P. 362 – 373.
2. Guliaev A.P. Metall Science. – M.: Oborongiz, 1963. – 185p. (In Russian)
3. Oshkaderov S.P. Phase transformation in austenite // Progress in Physics of Metals. – 2011. – Vol.12. – P.269-293. (In Russian)
4. Koval Yu.N., Lobodyuk V.A. Deformation and relaxation phenomenas during martensite transformation. – Kiev: Naukova Dumka, 2010. – 297p. (In Russian)
5. Meshkov Yu.Ya. On the problem on martensite tetragonality. // Proc. Int. Conf. “The modern problems of metal physics and physics of metallic systems” / Ed.IMF NANU, Kiev. – 25–27.05. – 2016. – P.22. (In Russian)
6. Kaminsky E.E., Percas M.D. Metal science problems. – M.: Metallurgiya, 1949. – 211p. (In Russian)
7. Arbuzov M.P. Metal physics and science problems. – Kiev: Academy of Sci. Edition. – 1955. – No. 6. – P. 3-11. (In Russian)
8. Kurdyumov G.V., The quenching and aging phenomenas in steel. – M.: Metallurgiya, 1960. – 140 p.
9. Kurdyumov G.V., Utevsky L.M., Entin R.I. Transformations in iron and steel. – M.: Nauka, 1977. – 238p. (In Russian)
10. Kurdyumov G.V., Lysak L.I. X-rays study of aging martensite // Journal of technical physics. – 1947. – Vol. 17. – P.525-531. (In Russian)
11. Lotkov. A.I, Baturin A.A. Martensite transformation in NiTi alloys // Physical mesomechanics. – 2011. – Vol.14. – No. 3. – P. 69-84. (In Russian)
12. Lobodyuk V.A., Meshkov Yu.Ya. On the problem on martensite tetragonality in carbon steel // Metal physics and new technology. – 2017. – Vol.39. – P.122-130. (In Russian)
13. Laptev I.M., Parkhomenko O.O., Tkachenko V.I. The dualism of the vacancy nature in nonequilibrium systems // East European Journal of Physics. – 2016. – No.3. – P.113-120.
14. Morozov O.P., Mirzayev D.A., Schteinberg M.M. The speed quenching impact in iron // Metal physics and Metal science. – 1987. – Vol. 32. – No. 6. – P. 1290 – 1297. (In Russian)
15. Damask A., Dins J. Point defects in metals. – M.: Mir, 1966. – 291p.
16. Rokhmanov N.Ya., Laptev I.N., Onishenko I.P., Parkhomenko O.O. Structural features of Fe-Al vacancy system // Functional Materials. – 2006. – Vol. 13. – No. 2. – P. 255-259.

blank line)
(blank line)
PACS: Here you must specify PACS codes
(blank line)

INSTRUCTIONS FOR PREPARING MANUSCRIPT (TITLE)

(blank line)

N.N. Author[1], N.N. Co-author(s)[2]

[1] *Affiliation*
[2] *Affiliation (if different from Authors affiliation)*
e-mail: corresponding_authors@mail.com
Received January 14, 2017

(blank line)

Each paper must begin with an abstract. The abstract should be typed in the same manner as the body text (see below). Please note that these Instructions are typed just like the manuscripts should be. The abstract must have at least 1000 phonetic symbols, supplying general information about the achievements, and objectives of the paper, experimental technique, methods applied, significant results and conclusions. Page layout: the text should be printed on the paper A4 format, at least 3 pages, with margins of: Top - 3, Bottom, Left and Right - 2 cm. The abstract should be presented in English (only for foreign authors), Ukraine and Russian.
KEYWORDS: there, must, be, at least, 5 keywords
(blank line)

This is introduction section. This paper contains instructions for preparing the manuscripts. The text should be prepared in .doc format (using MS Word).
(blank line)

INSTRUCTIONS

The text should be typed as follows:
• title: Times New Roman, 12 pt, ALL CAPS, bold, 1 spacing, centered;
• authors: name, initials and family names; Times New Roman, 12 pt, bold, 1 spacing, centered;
• affiliation(s): Times New Roman, 9 pt, italic, 1 spacing, centered;
• abstract: Times New Roman, 9 pt, 1 spacing, justified;
• body text: Times New Roman, 10 pt, 1 spacing, justified; paragraphs in sections should be indented right (tabulated) for 0.75 cm;
• section titles: Times New Roman, 10 pt, bold, 1 spacing, centered, without numbering, one line should be left, blank above section title;
• subsection titles: Times New Roman, 10 pt, bold, 1 spacing, centered, without numbering in accordance to the section (see below), one line should be left blank above subsection title;
• figure captions: width of the figure should be 85 or 170 mm, figures should be numbered (Fig. 1) and titled below figures using sentence format, Times New Roman, 9 pt, 1 spacing, centered (if one line) or justified (if more than one line); one line should be left blank below figure captions;
• table captions: width of the table should be 85 or 170 mm, tables should be numbered (Table 1.) and titled above tables using sentence format, Times New Roman, 10 pt, 1 spacing, centered (if one line) or justified (if more than one line), tables should be formatted with a single-line box around the outside border and single ruling lines between rows and columns; one line should be left blank below tables;
• equations: place equations centered, numbered in Arabic (1), flush right, equations should be specially prepared in MathType; one line should be left blank below and above equation.
(blank line)

Additional instructions

Numerated figures and tables should be embedded in your text and placed after they are cited. Only black and white drawings and sharp photographs are acceptable. Letters in the figures should be 3 mm high. The figures should be presented in one of the following graphic formats: jpg, gif, pcx, bmp, tif.
(blank line)

REFERENCES

Titles of journals, articles and author names in references should be given in Roman script. References should be numbered in the order of referring in the text, e.g. [1], [2-5], etc. Do not superscript your reference numbers. Cite references as in journal format. The full references should be listed in numerical order of citation in the text at the end of the paper (justified), Times New Roman, 9 pt, 1 spacing.
References should be given in the following form:

Journals

1. Holzwarth G., Eckart G. Fluid-dynamical approximation for finite Fermi systems // Nucl. Phys. - 1979. - Vol. A325. - P.1-30.

Books

2. Bertsch G.F., Broglia R.A. Oscillations in finite quantum systems. Ch. 6. - Cambridge: Cambridge University, 1994. - 150 p.

Chapters

3. Van der Woude A. The electric giant resonances // Electric and magnetic giant resonances in nuclei / Ed. by J. Speth. - Singapure: World Scientific P.C., 1991. - P. 99-232.

Conference or symposium proceedings

4. Smolanzuk R., Skalski J., Sobiczewski A. Masses and half-life of superheavy elements // Proc. of the International Workshop 24 on Gross Properties of Nuclei and Nuclear Excitations / Ed. by H. Feldmeier et al. - GSI, Darmstadt, 1996. - P.35-42.

Special Notes

1. Use International System of Units (SI system). 2. It is undesirable to use acronyms in the titles. Please define the acronym on its first use in the paper. 3. Refer to isotopes as ^{14}C, ^{3}H, ^{60}Co, etc.

Наукове видання

СХІДНО-ЄВРОПЕЙСЬКИЙ ФІЗИЧНИЙ ЖУРНАЛ

Том 4 Номер 3

EAST EUROPEAN JOURNAL OF PHYSICS

Volume 4 Number 3

Збірник наукових праць
англійською, українською, російською мовами

Коректор – Коваленко Т.О.
Технічний редактор – Гірник С.А.
Комп'ютерне верстання – Гірник С.А.

Підписано до друку 7.04.2017. Формат 60×84 /8. Папір офсетний.
Друк ризографічний.
Ум. друк. арк. 8,26. Обл.-вид. арк. 8,5
Тираж 300 пр. Зам. № Ціна договірна

61022, Харків, майдан Свободи, 4
Харківський національний університет імені В.Н. Каразіна
Видавництво

Надруковано Харківський національний університет імені В.Н. Каразіна
61022, Харків, майдан Свободи, 4, тел. +380-057-705-24-32
Свідоцтво суб'єкта видавничої справи ДК № 3367 від 13.01.09